

Anomalous Higgs couplings and collider data : some model-independent studies

By
SHANKHA BANERJEE
PHYS08201004002

Harish-Chandra Research Institute, Allahabad

*A thesis submitted to the
Board of Studies in Physical Sciences
In partial fulfillment of requirements
for the Degree of*
DOCTOR OF PHILOSOPHY
of
HOMI BHABHA NATIONAL INSTITUTE



June, 2015

STATEMENT BY AUTHOR

This dissertation has been submitted in partial fulfillment of requirements for an advanced degree at Homi Bhabha National Institute (HBNI) and is deposited in the Library to be made available to borrowers under rules of the HBNI.

Brief quotations from this dissertation are allowable without special permission, provided that accurate acknowledgement of source is made. Requests for permission for extended quotation from or reproduction of this manuscript in whole or in part may be granted by the Competent Authority of HBNI when in his or her judgment the proposed use of the material is in the interests of scholarship. In all other instances, however, permission must be obtained from the author.

Shankha Banerjee

DECLARATION

I, hereby declare that the investigation presented in the thesis has been carried out by me. The work is original and has not been submitted earlier as a whole or in part for a degree / diploma at this or any other Institution / University.

Shankha Banerjee

List of Publications arising from the thesis

Journal

1. “New Higgs interactions and recent data from the LHC and the Tevatron”, Shankha Banerjee, Satyanarayan Mukhopadhyay and Biswarup Mukhopadhyaya, JHEP **1210**, 062 (2012), [arXiv:1207.3588 [hep-ph]]
2. “Higher dimensional operators and LHC Higgs data : the role of modified kinematics”, Shankha Banerjee, Satyanarayan Mukhopadhyay and Biswarup Mukhopadhyaya, Phys. Rev. D **89**, 053010 (2014), [arXiv:1308.4860 [hep-ph]]
3. “Exploration of the Tensor Structure of the Higgs Boson Coupling to Weak Bosons in e^+e^- Collisions”, Gilad Amar, Shankha Banerjee, Stefan von Buddenbrock, Alan S. Cornell, Tanumoy Mandal, Bruce Mellado and Biswarup Mukhopadhyaya, JHEP **1502**, 128 (2015), [arXiv:1405.3957 [hep-ph]]

Others

1. “Cornering dimension-6 HVV interactions at high luminosity LHC: the role of event ratios”, Shankha Banerjee, Tanumoy Mandal, Bruce Mellado and Biswarup Mukhopadhyaya, [arXiv:1505.00226 [hep-ph]] (Accepted in JHEP)

List of Publications not contributing to the thesis

Journal

1. “Invisible Higgs Decay in a Supersymmetric Inverse Seesaw Model with Light Sneutrino Dark Matter”, Shankha Banerjee, P.S. Bhupal Dev, Subhadeep Mondal, Biswarup Mukhopadhyaya and Sourov Roy, JHEP **1310**, 221 (2013), [arXiv:1306.2143 [hep-ph]]
2. “Higgs data confronts Sequential Fourth Generation Fermions in the Higgs Triplet Model”, Shankha Banerjee, Mariana Frank and Santosh Kumar Rai, Phys. Rev. D **89**, 075005 (2014), [arXiv:1312.4249 [hep-ph]]

Others

1. “Prospects of Heavy Neutrino Searches at Future Lepton Colliders”, Shankha Banerjee, P.S. Bhupal Dev, Alejandro Ibarra, Tanumoy Mandal and Manimala Mitra, [arXiv:1503.05491 [hep-ph]]

Shankha Banerjee

To the ones I love

ACKNOWLEDGEMENTS

Firstly, I would like to thank my supervisor, Professor Biswarup Mukhopadhyaya, who has helped me at every step in my research career so far. His constructive criticisms have helped me learn many things. Also, he gave me a lot of freedom to explore new avenues and always welcomed my views and ideas. Overall, it would have been impossible to reach this stage of writing a thesis without his guidance.

I would like to extend my heartfelt thanks to Professor Sourov Roy, Professor Santosh Kumar Rai, Professor Mariana Frank and Professor Michael Spannowsky for being the best possible collaborators.

I would also like to thank my two friends and collaborators, Satyanarayan Mukhopadhyay and Tanumoy Mandal. Without their help, this thesis would not have been possible. I would also like to thank Professors Raj Gandhi, Asesh Krishna Datta, V. Ravindran and Sandhya Choubey for their constant support.

I owe a lot to Professor Bruce Mellado (ATLAS collaboration) and Professor Satyaki Bhattacharya (CMS collaboration). They helped me learn a lot about statistical techniques and ways to interpret experimental data. They have been my bridge to the world of experimental particle physics.

I would like to thank one of my close friends, Shilpi Jain who has helped me many times with insightful discussions and various technical aspects. She has been a constant support to my research career.

I thank Nabarun Chakrabarty, Ujjal Kumar Dey, Atri Bhattacharya, Saurabh Niyogi, Animesh Chatterjee, Ushoshi Maitra, Manimala Mitra, Sanjoy Biswas, Narayan Rana, Taushif Ahmed, Arghya Choudhury, Subhaditya Bhattacharya, Subhadeep Mondal, Arindam Chatterjee, Nishita Desai, Kenji Nishiwaki, Ambresh Shivaji, Pradipta Ghosh and Dhiraj Kumar Hazra, who have helped me at different stages with my research.

I would like to acknowledge the Regional Centre for Accelerator-based Particle Physics (RE-CAPP), HRI, for funding my travel when I attended schools and visited other institutes. I would also like to thank the administrative staff, the staff at the computer section and at the cluster computing facility for their immense support at various stages.

After five long years at *HRI*, I would definitely confess that this is now like my second home and I will miss not being here after a few months. I have shared many memories with my

friends Nabarun, Dibya, Animesh, Atri, Arijit, Titas, Sauri, Narayan, Taushif, Aritra, Saurabh, Satya, Ujjal, Joydeep, Sourav, Swapnamay, Masud, Sabyasachi, Paromita, Tanumoy, Madhumita, Ramesh, Sumana, Deepak, Subhronel, Arindam, Samrat, Snehbala, Eshita, Arghya, Subhadeep, Anirban Basu, Saurabh, Anushree, Manoj, Siddharth, Maguni, Ushoshi and Avinanda. The regular eat outs at restaurants and visits to movie theatres with my friends were a relief.

I have thoroughly enjoyed my course work at *HRI*, which has helped me a lot in getting prepared for my research career. I thank all my teachers at *HRI* who have helped me at different stages during my stay. I would especially like to thank Professor Ashoke Sen and Professor Rajesh Gopakumar for offering few wonderful courses.

I would like to thank Aditi Mukhopadhyaya, Korak, Professor Rukmini Dey and Atashi Das who made me feel at home at *HRI*.

I would like to extend my heartfelt gratitude to my teachers, Professor Soumitra Sengupta, IACS, Kolkata, Professor Soumen Kumar Roy, Jadavpur University, Kolkata and Professor Dhiranjan Roy, Jadavpur University, Kolkata for inculcating in me the delights of physics which made me pursue a career in research.

I would like to thank my friends Anirban, Atanu, Shreya, Siddhartha (Dasgupta), Siddhartha (Bhose), Srijit, Debolina, Upasana, Bitan and Raka. They have been my constant support.

Music is the most important way in which I can express my feelings. I would like to thank my *guruji* Shri Kalyan Mukherjee who has been extremely patient with me and has taught me melodies which will stay with me forever.

But, the most important contribution comes from my family, my parents, my maternal grandmother, my wife, my uncles and my sister Biyanka. They have supported me at every stage and believed in me. My parents never forced me to choose a career but they wanted me to pursue my dreams while they took care of everything else. My mother has been instrumental in shaping up my career. I would like to thank Anupa, my loving wife, who ignored all my tantrums and gave me encouragement to pursue my research with a calm and cool head. She is one of my best friends. I would like to thank my *late* grandparents, especially my maternal grandfather who took care of me till his last day. Most importantly, I would like to thank Bhaskarendu Sanyal (my *late* uncle) who has been a constant inspiration to me. I would like to thank my caring in-laws, who have also supported me immensely. Lastly, I would like to extend my thanks and love to my lovely furry friends *Fluffy*, Momo, Boogie, Dhonu, Kalu, Ganesh and Snowy. They have been my best stress relievers.

CONTENTS

SYNOPSIS	1
LIST OF FIGURES	4
LIST OF TABLES	7
1 INTRODUCTION	9
1.1 Introduction to the Standard Model	9
1.2 Spontaneous Symmetry Breaking and Higgs mechanism	13
1.3 Theoretical bounds on the mass of Higgs boson	16
1.4 Experimental bounds on the mass of Higgs boson	22
1.5 Motivations for physics beyond the Standard Model	24
2 High energy colliders	31
2.1 A brief review of the Large Hadron Collider	31
2.2 Detector basics	34
2.3 Modelling the simulations	38
2.4 Some relevant kinematic variables	41
3 Model-independent analysis of Higgs couplings from global fits	45
3.1 Motivation	45
3.2 New physics effects: parametrization	49
3.3 Methodology of analysis	53

3.3.1	Input data	53
3.3.2	Methodology	56
3.4	Results	59
3.5	Summary and conclusions	64
4	Constraining Higher-dimensional HVV operators	67
4.1	Motivation	67
4.2	Dimension-6 operators and electroweak precision constraints	70
4.3	Simulation framework and validation using $H \rightarrow WW^* + \geq 2j$ data	75
4.4	Modified efficiencies and signal strengths	76
4.5	Constraints using LHC Higgs data	79
4.6	Associated production and higher dimensional operators	85
4.7	Modification to kinematic distributions : examples	87
4.8	Summary and conclusions	89
5	Probing the Higher-dimensional HVV operators at the high-energy run at the LHC	93
5.1	Motivation	93
5.2	Ratios of cross-sections as chosen observables	94
5.2.1	Observable sensitive to \mathcal{O}_{WW} and \mathcal{O}_{BB} : \mathcal{R}_1	96
5.2.2	Observable sensitive to \mathcal{O}_{WW} and \mathcal{O}_W : \mathcal{R}_2	98
5.2.3	Observable sensitive to \mathcal{O}_B : \mathcal{R}_3	99
5.3	Results of the analysis	100
5.3.1	\mathcal{R}_1 @ 7+8 TeV	102
5.3.2	\mathcal{R}_1 @ 14 TeV	103
5.3.3	\mathcal{R}_2 @ 14 TeV	104
5.3.4	\mathcal{R}_3 @ 14 TeV	107
5.4	Summary and conclusions	109
6	Higher-dimensional operators at electron-positron colliders	111
6.1	Motivation	111
6.2	Effective Lagrangian Formalism	113
6.3	Phenomenology at an e^+e^- Collider	116
6.3.1	Higgs production at an e^+e^- collider	116
6.3.2	A general expression for the cross-sections	118

CONTENTS

6.3.3	Energy dependence of s and t -channel cross-sections	122
6.3.4	More information from the total rates	122
6.3.5	The effects on kinematic distributions	132
6.3.6	Discussion on relevant backgrounds	133
6.4	Likelihood Analysis for t -channel	135
6.5	Summary and Conclusions	140
7	Conclusions	143
	References for Chapter 1	147
	References for Chapter 2	151
	References for Chapter 3	153
	References for Chapter 4	159
	References for Chapter 5	163
	References for Chapter 6	171

SYNOPSIS

The Standard Model (SM) has been tested to a great accuracy and the recent discovery of the scalar boson (most likely the SM Higgs boson) at the Large Hadron Collider (LHC) by the ATLAS and the CMS collaborations establishes SM as one of the most successful theories in particle physics. However, SM is unable to answer some fundamental observations such as the existence of dark matter, massive neutrinos and the excess of baryons over anti-baryons. Besides, there are some theoretical issues like the hierarchy problem which is also unanswered by the SM. In view of such issues, most particle physicists believe in the existence of physics beyond the Standard Model (BSM). In order to constrain new physics from experimental observations, one needs to measure the couplings of the discovered particles, their decay widths and cross-sections to great precision. The discovered Higgs boson, though seemingly consistent with the SM, is still open to scrutiny for any BSM effects. For instance, the couplings of the Higgs to the other SM particles still show some departures from the SM expectations. Although the departures can very well be experimental (systematic + statistical) errors, one needs to filter out such errors to zero in on any new physics effects. Other important observables include the width of the SM Higgs. Theory predicts it to be an extremely small quantity of around ~ 4 MeV. However, this range is well below the experimental resolutions and the bound on this width is currently ~ 4 times the SM expectations from indirect measurements from the experiments. Besides, one needs to probe the Higgs self-couplings in order to make any conclusive comments on the exact nature of the Higgs boson. This will be an extremely challenging task for the experimentalists as this coupling (in the SM) is extremely tiny. Thus, we are quite far from making a final comment on the nature of the Higgs. The measurement of any non-standard (*invisible*) decay modes of the Higgs is still a possibility. In performing such studies, people generally employ two different approaches, *viz.* the model-independent approach and the model-dependent approach. The model-dependent approach is a very intricate business, where one needs to satisfy several experimental constraints and still have to comply with the model nature. Examples of these are Supersymmetric models, Extra-dimensional models, models with several representations, composite Higgs models etc. However, a class of such models are severely constrained by the experiments. The other approach, *viz.* the model-independent one, is free from any restrictions inherent to the structures of specific models. In this approach, one parametrizes the

couplings by some rescaling factors with no new Lorentz structures. One may also parametrize the theory with modified couplings with new Lorentz structures which can come from an effective theory valid up to a high cut-off scale much higher than the electroweak (EW) scale. I summarise below several projects undertaken in the above spirit.

In one of the earliest works, which came out within two weeks of the announcement of the Higgs discovery, we tried to pin down the nature of the Higgs couplings to the Standard Model (SM) particles in a very general model-independent manner. We rescaled the Higgs couplings to a pair of weak bosons and fermions, by free parameters, allowing for no new Lorentz structures in the Higgs couplings. Besides, we allowed for Higgs effective interactions with a pair of gluons (photons) to vary freely which could come from new coloured (un coloured) states in the respective loops. An arbitrary phase (absorptive) was allowed in the $Ht\bar{t}$ coupling which could show its signature in the $H\gamma\gamma$ loop mainly due to interference between the W and top loops. To make the parametrization even more general, we also kept the provision for an invisible branching ratio for the Higgs. Taking seven parameters at the same time, we constructed a χ^2 function and performed a global minimization on it, to set limits on them. Our analysis also hinted at a small but finite invisible Higgs branching ratio which has still not been ruled out by the current data. The data points used were the LHC and Tevatron signal strengths for the various Higgs decay modes.

To make the previous work more general, we allowed for new Lorentz structures in the Higgs boson couplings. To achieve such couplings, we considered dimension-6 (D6) gauge-invariant CP -even operators which enter the theory as a consequence of new physics integrated out above a cut-off scale Λ ($\mathcal{O}(\text{TeV})$). For illustrative purposes, we studied the effects of two such operators, not strongly bound by the electroweak precision test (EWPT) observables and which affect the HVV ($V = W^\pm, Z, \gamma$) vertices by bringing in momentum dependent terms through derivatives on various SM-fields. Without assuming any particular UV -completion scheme, we considered one such operator at a time and showed how the experimental cut-efficiencies get modified. This point is often neglected and SM efficiencies are assumed for global fits. We validated our Monte Carlo (MC) with ATLAS' [1] for the $H \rightarrow WW^*$ channel in the SM. Our analysis mainly focused on the vector boson fusion (VBF) channel and we found that the modification in the cut-efficiencies is the most dominant in this topology, for the operators under study. A global-fit was made to all bosonic channels using current LHC data. Bounds were put on some of these operators. We concluded that in order to see the effects of these modified efficiencies, one needs to have better statistics in the VBF channels for all the bosonic final states. Effects of two such operators on the $H \rightarrow \gamma\gamma$ channel in the VBF and associated production (VH) channels were also studied. The effects of the operators for the VH channel was found to be significantly lower than its VBF counterpart.

Several analyses have constrained the coefficients of these D6 operators to $\mathcal{O}(1) \text{ TeV}^{-2}$. A substantial improvement over them is expected in a recent approach developed by us, where we construct observables which can show the hint of such operators in the run II and run III of the LHC with integrated luminosities of 300 fb^{-1} and 3000 fb^{-1} . The idea behind this work is

that we consider ratios of rates in different channels. For instance, the branching ratio (BR) for $H \rightarrow \gamma\gamma$ is sensitive to two such operators which are thus severely constrained by the theoretical value of the BR. Some operators show flat behaviour for certain observables while are extremely sensitive to other observables. The ratio of the cross-section in the VBF channel to the cross-section in the VH channel helps us probe two such D6 operators to values of $\mathcal{O}(1) \text{ TeV}^{-2}$. The main advantage of taking ratios is that the higher order loop corrections get cancelled (at least to a substantial degree) and we are left with leading order (LO) terms without bothering about the higher order corrections. In this analysis, we make a rigorous estimate of the theoretical and statistical uncertainties on the observables. Any excess of the observables in the D6 sector above and below such uncertainty bands for the SM will clearly give us hints for such *new physics*. We show that this approach can lead to a four-fold improvement on the constraints on D6 operators.

As the LHC has too messy an environment to yield precision results, follow-up studies at e^+e^- colliders can be quite meaningful. In this regard, we also studied the effects of modified HVV ($V = W^\pm, Z, \gamma$) couplings at a future e^+e^- collider under two parametrization schemes. In one, we considered the aforementioned D6 CP -even operators. In the other, we considered the most general Lorentz invariant structure to such couplings with both CP -even and CP -odd parts. We studied two major Higgs-production channels, viz. the s -channel process, $e^+e^- \rightarrow ZH$ and the t -channel process in $e^+e^- \rightarrow \nu\bar{\nu}H$. The former has anomalous HZZ and $HZ\gamma$ vertices whereas the latter only allows an anomalous HWW vertex. We showed that, non-zero operator coefficients can closely mimic the SM-like cross-sections. We derived analytical formulae for the above cross-sections with all the relevant operators taken simultaneously. In this work, we concluded that the total rates, the ratios of the s -channel rates, t -channel rates, at different energies and also the ratios between the s - and t -channel rates at a fixed energy can be important probes in deciphering the nature of the HVV anomalous couplings. Such operators, besides affecting the HVV vertices also affect the WWV' vertices ($V' = Z, \gamma$) concomitantly. We concluded that by measuring the above rates simultaneously, we can probe the operator strengths with greater accuracy. A generator level background analysis was performed and the signal significance was computed for the operators under study. We showed that even for small values of the operator coefficients one can expect a good significance ($\gtrsim 5\sigma$). Moreover, a rigorous likelihood analysis was performed which showed that CP -odd couplings can also be probed with good significance.

Reference:

1. <https://atlas.web.cern.ch/Atlas/GROUPS/PHYSICS/CONFNOTES/ATLAS-CONF-2013-030/>

LIST OF FIGURES

1.1	Feynman diagrams of Higgs self-couplings	17
1.2	Triviality and vacuum stability bounds	19
1.3	$W_L W_L \rightarrow W_L W_L$ scattering	20
1.4	Higgs mass bound from LEP	24
1.5	One loop corrections to Higgs boson mass	27
2.1	ATLAS detector	34
2.2	CMS detector	35
2.3	Prototype particle signatures in the various detector components	36
2.4	Displaced secondary vertex	36
2.5	Transverse mass : CDF	43
3.1	Marginalised contour plots for case A ($\delta = 0$ and $\beta_W \neq \beta_Z$)	61
3.2	Marginalised contour plots for case B ($\delta \neq 0$ and $\beta_W = \beta_Z$)	62
3.3	Variation of $\Delta\chi^2$ as a function of invisible branching fraction	63
4.1	Combined efficiency of all ATLAS cuts as a function of HD-operator coefficient for different SM-like scaling	79
4.2	Percentage modification of combined efficiency of all cuts compared to the SM case, in the $H \rightarrow WW^* \rightarrow \ell^+ \nu \ell^- \bar{\nu}$ channel	80
4.3	2σ allowed regions in the $\beta - f_{WW}$ parameter space	82
4.4	68% and 95% C.L. allowed regions in the $\beta - f_{WW}$ parameter space : global fit .	83
4.5	Marginalised distributions : f_{WW} and β	84

4.6	Efficiency of cuts in VH channel with $H \rightarrow \gamma\gamma$ as a function of f_{BB}	87
4.7	Efficiency of cuts in VH channel with $H \rightarrow \gamma\gamma$ as a function of f_{WW}	88
4.8	Normalised distributions of kinematic variables for 8 TeV LHC in VBF category with $H \rightarrow \gamma\gamma$ (part I)	91
4.9	Normalised distributions of kinematic variables for 8 TeV LHC in VBF category with $H \rightarrow \gamma\gamma$ (part II)	92
5.1	Higgs production cross-sections at 14 TeV for VBF and VH categories as functions of HD-operators	96
5.2	Higgs BRs in bosonic channels as functions of HD-operators	97
5.3	\mathcal{R}_1 versus f_{WW}/Λ^2 (TeV ⁻²) @ 8 TeV (using ATLAS + CMS signal strengths)	104
5.4	\mathcal{R}_1 versus f_{WW}/Λ^2 (TeV ⁻²) @ 14 TeV and 3000 fb ⁻¹	105
5.5	\mathcal{R}_2 versus (a) f_{WW}/Λ^2 (TeV ⁻²) and (b) f_W/Λ^2 (TeV ⁻²) @ 14 TeV and 3000 fb ⁻¹	106
5.6	\mathcal{R}_3 versus f_B/Λ^2 (TeV ⁻²) @ 14 TeV and 3000 fb ⁻¹	107
6.1	s and t -channel Feynman diagrams for Higgs production @ e^+e^- colliders	116
6.2	Invariant mass distributions of $\nu\bar{\nu}$ for $e^+e^- \rightarrow \nu\bar{\nu}H$ @ $\sqrt{s} = 300$ GeV	119
6.3	Normalised distributions of the Higgs energy for the s and t -channels	121
6.4	σ^s for $e^+e^- \rightarrow ZH$ and $\sigma^{t,ac}$ for $e^+e^- \rightarrow \nu\bar{\nu}H$ as functions of the CME	123
6.5	Variations of σ_{ZH}^s and $\sigma_{\nu\bar{\nu}H}^{t,ac}$ as functions of the HD-operator coefficients (one parameter at a time) at a fixed energy and their ratios at two energies for $\kappa = 1$	124
6.6	Variations of σ_{ZH}^s and $\sigma_{\nu\bar{\nu}H}^{t,ac}$ as functions of the HD-operator coefficients (one parameter at a time) at a fixed energy and their ratios at two energies for $\kappa = 0.8$	125
6.7	Variations of $\sigma(e^+e^- \rightarrow W^+W^-)$ as functions of the HD-operator coefficients (one parameter at a time)	126
6.8	Variations of σ_s^{300} for $e^+e^- \rightarrow Zh$ as functions of two parameters at a time	128
6.9	Variations of $\sigma_t^{300,ac}$ for $e^+e^- \rightarrow \nu\bar{\nu}h$ as functions of two parameters at a time	129
6.10	Allowed parameter space for $\sigma_{\nu\bar{\nu}H}^{t,ac}$ within 10% of its SM value with all parameters varied	130
6.11	Normalised kinematic distributions $(1/\sigma)d\sigma^s/d \cos \theta$ for the s and t channels of Higgs production	131
6.12	Significance (S/\sqrt{B}) as functions of f_i/Λ^2 for $\kappa = 1$ at $\sqrt{s} = 300$ GeV	134
6.13	Normalised kinematic distributions of Higgs momentum and the angle of the Higgs with the beam-axis at $\sqrt{s} = 250$ GeV.	137
6.14	2D histograms showing the correlation of the t -channel Higgs momentum and the angle of the Higgs with the beam-axis	137

6.15 Median significance values for likelihood analyses done with both one dimensional and two dimensional distributions 139

LIST OF TABLES

1.1	Quantum numbers of quarks and leptons	12
3.1	$H \rightarrow \gamma\gamma$ signal strengths for ATLAS and CMS	54
3.2	$H \rightarrow ZZ^*$ signal strengths for ATLAS and CMS	54
3.3	$H \rightarrow WW^*$ signal strengths for ATLAS and CMS	54
3.4	$H \rightarrow b\bar{b}$ signal strengths for ATLAS and CMS	55
3.5	$H \rightarrow \tau^+\tau^-$ signal strengths for ATLAS and CMS	55
3.6	Tevatron Higgs signal strengths	55
3.7	Best-fit values of the various parameters in the three cases considered. In cases A and C, δ has been fixed at 0 (indicated with a '*'). In cases B and C, the relation $\beta_W = \beta_Z$ has been imposed, and their values have been restricted within precision constraints.	59
4.1	Comparison of experimental cut efficiencies I : ATLAS versus our MC	75
4.2	Comparison of experimental cut efficiencies II	76
4.3	Higgs signal strengths : ATLAS and CMS	81
4.4	Cuts for VH channel in $H \rightarrow \gamma\gamma$ final state (ATLAS)	86
5.1	Higgs BR , total decay width and their uncertainties in bosonic channels	101
5.2	Higgs production Cross-sections and their theory uncertainties in different channels @ 14 TeV LHC	101
5.3	Number of surviving events in various final states after selection cuts @ 14 TeV LHC and 3000 fb^{-1} luminosity	101

5.4	Systematic uncertainties used	102
5.5	Higgs signal strengths ($7 + 8$ TeV) in $\gamma\gamma$ and WW^* channels in ggF production mode : ATLAS and CMS	103
5.6	Table summarising allowed ranges of HD-operator coefficients	108
6.1	$\nu\bar{\nu}H$ cross-section for three benchmark points in the parameter space	118
6.2	Signal and background cross-sections for two different final states, $b\bar{b}l^+l^-$ and $b\bar{b} + \cancel{E}$	134

Chapter 1

INTRODUCTION

1.1 Introduction to the Standard Model

The Standard Model (SM) of particle physics [1] has been profoundly successful in explaining the behavioural patterns of practically all known elementary particles and three of the four fundamental interactions in nature. To start with, the matter sector is comprised of elementary spin- $\frac{1}{2}$ particles known as fermions. The *visible* spectrum of particles in the SM includes the *six* quarks and the *three* charged leptons. With each charged lepton, one also has an associated *invisible* particle, *viz.*, a neutrino. Neutrinos carry no electric charge and are massless in the original SM¹. Moreover, the spin-1 particles mediating the interactions among the matter sector are called gauge bosons. The particles mediating strong interaction are termed gluons (g). Gluons are massless, eight in number and are electrically neutral. However, they carry a separate quantum number, *viz.*, *colour*. Weak interaction is mediated by three massive gauge bosons, *viz.*, W^\pm and Z . Finally, electromagnetic interaction is mediated by the massless gauge boson named photon (γ) and forms the subject matter of quantum electrodynamics (QED).

The SM is a renormalizable local quantum field theory based on the gauge group $SU(3)_C \times SU(2)_L \times U(1)_Y$, each describing a fundamental force in nature. The action for strong

¹Experiments have disfavoured this claim and now neutrinos are known to be massive with masses in the sub-electron volts range. However, their absolute masses are still to be determined.

interaction is locally invariant under an $SU(3)_C$ group, where C signifies the *colour* quantum number. The theory of strong interaction is termed quantum chromodynamics (QCD). The framework describing electromagnetic and weak interactions is governed by the $SU(2)_L \times U(1)_Y$ gauge group, where L signifies couplings to only left-handed fermions and Y is a quantum number termed as the hypercharge (the implications of these three gauge groups will be discussed below in some detail). The fourth fundamental interaction, *viz.*, gravitational interaction among elementary particles only becomes relevant near the Planck energy scale (10^{19} GeV).

We start the mathematical formulation of SM by describing the classical electroweak Lagrangian obeying local gauge invariance

$$\mathcal{L}_{EW} = \mathcal{L}_{gauge} + \mathcal{L}_{matter}^f, \quad (1.1)$$

$$\text{where } \mathcal{L}_{gauge} = -\frac{1}{4}W_{\mu\nu}^a W^{\mu\nu,a} - \frac{1}{4}B_{\mu\nu}B^{\mu\nu} \quad \text{and} \quad \mathcal{L}_{matter}^f = i\bar{\psi}\gamma_\mu D^\mu\psi \quad (1.2)$$

Here, \mathcal{L}_{gauge} represents the gauge kinetic terms and also includes self-interactions between the non-abelian gauge fields ($W_{\mu\nu}^a$). The gauge field strengths of the electroweak sector are defined as

$$\begin{aligned} W_{\mu\nu}^a &= \partial_\mu W_\nu^a - \partial_\nu W_\mu^a - g\epsilon^{abc}W_\mu^b W_\nu^c \\ B_{\mu\nu} &= \partial_\mu B_\nu - \partial_\nu B_\mu, \end{aligned} \quad (1.3)$$

where g , a and ϵ^{abc} are respectively the gauge coupling, gauge index and the structure constants of the $SU(2)_L$ gauge group.

The second part of the electroweak Lagrangian, *i.e.*, \mathcal{L}_{matter}^f represents both kinetic terms and interactions of the fermion fields, ψ . D_μ is the covariant derivative which acts on these fields and is designed to preserve gauge invariance and is defined as

$$D_\mu \equiv \partial_\mu + ig\frac{\sigma^a}{2}W_\mu^a + ig'\frac{Y}{2}B_\mu, \quad (1.4)$$

where g' is the $U(1)_Y$ gauge coupling and σ^a s (with $a = 1, 2, 3$) are the three Pauli matrices. $T^a = \sigma^a/2$ are the three generators of $SU(2)_L$ and Y is the hypercharge of $U(1)_Y$. With these

definitions at hand, we present the algebra followed by the electroweak sector

$$[T^a, T^b] = i\epsilon^{abc}T^c; \quad [T^a, Y] = 0; \quad [Y, Y] = 0 \quad (1.5)$$

By defining $T^\pm = T^1 \pm iT^2$, the charged physical fields as $W_\mu^\pm = \frac{1}{\sqrt{2}}(W_\mu^1 \mp iW_\mu^2)$ and the neutral physical fields as

$$\begin{pmatrix} Z_\mu \\ A_\mu \end{pmatrix} = \begin{pmatrix} \cos \theta_w & -\sin \theta_w \\ \sin \theta_w & \cos \theta_w \end{pmatrix} \begin{pmatrix} W_\mu^3 \\ B_\mu \end{pmatrix}, \quad (1.6)$$

one can rewrite the covariant derivative in terms of the physical fields as

$$D_\mu = \partial_\mu + i\frac{g}{\sqrt{2}}(T^+W_\mu^+ + T^-W_\mu^-) + ig_Z(T^3 - Q\sin^2\theta)Z_\mu + ieQA_\mu, \quad (1.7)$$

where θ_w is the weak mixing angle, called the Weinberg angle defined as $\sin \theta_w = \frac{g'}{\sqrt{g^2+g'^2}}$ and $\cos \theta_w = \frac{g}{\sqrt{g^2+g'^2}}$, $g_Z = \frac{g}{\cos \theta_w}$, $Q = T^3 + \frac{Y}{2}$ and $e = g \sin \theta_w = g' \cos \theta_w$. Q and e are respectively the charge and coupling strength of the electromagnetic interaction and T^3 are the eigenvalues of the third component of $SU(2)_L$ generators.

One of the most remarkable facets of SM is that it differentiates between weak interactions of the left and right-handed fermions (the left and right handed projections of a field ψ are defined as $\psi_L = \frac{1}{2}(1 - \gamma_5)\psi$ and $\psi_R = \frac{1}{2}(1 + \gamma_5)\psi$ respectively) by respectively grouping them under $SU(2)$ doublets and singlets. The quark doublets and singlets in the SM are denoted as

$$\begin{pmatrix} u \\ d \end{pmatrix}_L, u_R, d_R, \begin{pmatrix} c \\ s \end{pmatrix}_L, c_R, s_R, \begin{pmatrix} t \\ b \end{pmatrix}_L, t_R, b_R \quad (1.8)$$

and the lepton sector is denoted by

$$\begin{pmatrix} \nu_e \\ e \end{pmatrix}_L, e_R, \begin{pmatrix} \nu_\mu \\ \mu \end{pmatrix}_L, \mu_R, \begin{pmatrix} \nu_\tau \\ \tau \end{pmatrix}_L, \tau_R \quad (1.9)$$

Due to historic reasons, the right handed neutrino singlets, ν_{RS} are not included in the SM. The quantum numbers of these fermion fields are tabulated in Table 1.1.

After discussing the electroweak sector, we briefly review the strong sector, *viz.*, the

Particle	T_3	Y	Q
$\nu_{eL}, \nu_{\mu L}, \nu_{\tau L}$	$+\frac{1}{2}$	-1	0
e_L, μ_L, τ_L	$-\frac{1}{2}$	-1	-1
e_R, μ_R, τ_R	0	-2	-1
u_L, c_L, t_L	$+\frac{1}{2}$	$+\frac{1}{3}$	$+\frac{2}{3}$
u_R, c_R, t_R	0	$+\frac{2}{3}$	$+\frac{2}{3}$
d_L, s_L, b_L	$-\frac{1}{2}$	$+\frac{1}{3}$	$-\frac{1}{3}$
d_R, s_R, b_R	0	$-\frac{2}{3}$	$-\frac{1}{3}$

Table 1.1: The quantum numbers of the three generations of quarks and leptons. The hypercharge of these particles are computed using the Gell-Mann-Nishijima relation, $Q = T_3 + \frac{Y}{2}$. We must note that each quark has a colour quantum number three and hence is threefold degenerate in electroweak interactions. All the leptons however, have no colour quantum number.

$SU(3)_C$ sector of SM. The QCD Lagrangian is given by

$$\mathcal{L}_{QCD} = -\frac{1}{4}G_{\mu\nu}^a G^{a,\mu\nu} + g_s \sum_{i=u,d,c,s,b,t} \bar{q}_i \gamma_\mu t^a q_i G_\mu^a, \quad (1.10)$$

where g_s is the strong coupling constant, t^a s are the generators of the $SU(3)_C$ group with a being the colour index varying between 1 and 8, G_μ^a are the gluon fields and $G_{\mu\nu}^a$ are the gluon field strengths defined as

$$G_{\mu\nu}^a = \partial_\mu G_\nu^a - \partial_\nu G_\mu^a - g_s f^{abc} G_\mu^b G_\nu^c, \quad (1.11)$$

where f^{abc} are the structure constants of the $SU(3)_C$ group which follows the algebra

$$[t^a, t^b] = i f^{abc} t^c \quad (1.12)$$

We must mention here that like photon, gluons are also massless because of local gauge invariance. However, an important difference in the strong sector is that, unlike the photon, which is electrically neutral, the gluons are charged under the $SU(3)_C$ gauge group and hence have self-interactions because of the non-abelian nature of the theory.

Till now, we have postponed any discussion on the masses of the fermions and gauge bosons. Gauge symmetry prohibits any explicit mass terms for the gauge fields. However, the short-range weak interactions require W^\pm and Z to be massive. For the fermions too, we can

not write gauge invariant mass terms like $M\bar{\psi}\psi$ simply because the left and right handed components of these fields transform differently under the $SU(2)_L \times U(1)_Y$ gauge groups and such terms mix the left and right handed components. However, experiments have already shown all quarks and charged leptons to have masses. Hence, the mechanism for mass generation in the SM is a matter of special concern. The existence of massive particles in the SM implies that the electroweak symmetry must somehow be broken. This is achieved through the concept of spontaneous symmetry breaking (SSB) [2]. In an SSB, even though the Lagrangian is gauge invariant, by choosing an arbitrary vacuum, the symmetry is broken. An SSB is also shown to be renormalizable [3] and hence gives successful predictions as a quantum field theory by generating masses for gauge bosons and fermions. In SM, the Glashow-Salam-Weinberg (GSW) [4] model achieves spontaneous breaking of the electroweak sector by postulating a complex $SU(2)_L$ doublet scalar field. This field takes an appropriate vacuum expectation value (v_{ev}) which then spontaneously breaks the electroweak symmetry. In the following section, we discuss the scheme indicated above.

1.2 Spontaneous Symmetry Breaking and Higgs mechanism

We know that electric charge is conserved, hence implying that the electromagnetic gauge group, $U(1)_{EM}$ is unbroken. Therefore, SSB must achieve the task of breaking the electroweak gauge group such that we finally obtain

$$SU(2)_L \times U(1)_Y \xrightarrow{SSB} U(1)_{EM} \quad (1.13)$$

To attain the goal of breaking the electroweak gauge group spontaneously, one introduces a complex $SU(2)_L$ doublet scalar Φ with hypercharge $Y_\Phi = +1$, defined as

$$\Phi = \begin{pmatrix} \phi^+ \\ \phi^0 \end{pmatrix} = \frac{1}{\sqrt{2}} \begin{pmatrix} \phi_1 + i\phi_2 \\ \phi_3 + i\phi_4 \end{pmatrix} \quad (1.14)$$

The Lagrangian density for this scalar field Φ is given as

$$\mathcal{L}_{scalar} = (D_\mu \Phi)^\dagger (D^\mu \Phi) - V(\Phi^\dagger, \Phi), \quad (1.15)$$

with the scalar potential $V(\Phi^\dagger, \Phi)$ defined as

$$V(\Phi^\dagger, \Phi) = -\mu^2 \Phi^\dagger \Phi + \lambda (\Phi^\dagger \Phi)^2 \quad (1.16)$$

For $\mu^2 > 0$ and $\lambda > 0$, the potential $V(\Phi^\dagger, \Phi)$ has degenerate minima at

$$\Phi^\dagger \Phi = \frac{1}{2}(\phi_1^2 + \phi_2^2 + \phi_3^2 + \phi_4^2) = \frac{v^2}{2}; \quad v = \sqrt{\frac{\mu^2}{\lambda}} \quad (1.17)$$

Without any loss of generality, one can exploit the freedom of $SU(2)_L$ gauge invariance in choosing the vev of Φ to be real and entirely along the electrically neutral component, ϕ_3 . This choice thus translates into $\phi_1 = \phi_2 = \phi_4 = 0$ and $\phi_3 = v^2$ and achieves the spontaneous breaking of the $SU(2)_L \times U(1)_Y$ symmetry. Thus, $\Phi(x)$ can now be expanded about this particular vacuum

$$\Phi_0 = \langle 0 | \Phi | 0 \rangle = \frac{1}{\sqrt{2}} \begin{pmatrix} 0 \\ v \end{pmatrix} \quad (1.18)$$

One can then write

$$\Phi = \frac{1}{\sqrt{2}} \begin{pmatrix} 0 \\ v + H \end{pmatrix}, \quad (1.19)$$

where H is the Higgs field. On comparing with Eq. 1.14, one can see that the four degrees of freedom have been traded off by just one physical field, H . This was achieved by expressing the field as

$$\Phi = e^{iT \cdot \theta(x)/v} \begin{pmatrix} 0 \\ \frac{v+H}{\sqrt{2}} \end{pmatrix} \quad (1.20)$$

and considering small perturbations such that one can identify $(\phi_1, \phi_2, \phi_3, \phi_4)$ with $(\theta_2, \theta_1, v + H, -\theta_3)$. By exploiting the $SU(2)$ invariance of \mathcal{L}_{scalar} , one can gauge away the three massless *Goldstone* boson fields, θ_i ($i = 1, 2, 3$) by the transformation

$$\Phi \rightarrow e^{-iT \cdot \theta(x)/v} \Phi \quad (1.21)$$

to obtain Eq. 1.19. This particular choice of vacuum thus breaks the $SU(2)_L \times U(1)_Y$ symmetry. By plugging this in Eq. 1.15, the kinetic term generates masses for the W^\pm , Z and γ .

$$M_W = \frac{1}{2}vg; \quad M_Z = \frac{1}{2}v\sqrt{g^2 + g'^2}; \quad M_\gamma = 0 \quad (1.22)$$

Hence, the Lagrangian now describes *three* massive gauge fields (W^\pm and Z), *one* massless gauge field (γ) and *one* massive scalar (H). The gauge fields have thus “*eaten up*” the Goldstone bosons and have become massive. The scalar degrees of freedom have been converted to the longitudinal degrees of freedom of the massive gauge bosons. This mechanism is known as the *Higgs-Brout-Englert-Guralnik-Hagen-Kibble mechanism*, or more commonly as the *Higgs mechanism* [5]. We must note that out of the four generators T and Y of $SU(2)_L \times U(1)_Y$, only the combination $Q = T^3 + \frac{Y}{2}$ obeys the unbroken symmetry. The other three indeed break this symmetry and generate massive gauge bosons as we have shown.

The effective theory of weak interactions at low energies implies $v = (\sqrt{2}G_F)^{-1/2} \simeq 246$ GeV, where G_F is the Fermi constant ($G_F = 1.1663787 \times 10^{-5}$ GeV⁻²). By considering the experimental inputs of v and θ_w ($\sin \theta_w \simeq 0.23$), the masses of the W^\pm and Z bosons were accurately predicted by the model. The photon remaining massless implies that the gauge group $U(1)_{EM}$ remains unbroken after the SSB.

Till now, we have reserved our discussion to generation of masses for the weak bosons only. However, the fermion masses are also generated by the Higgs field Φ , but in a completely different fashion. To achieve this goal, one has to define two different terms for the *up*-type ($T^3 = +\frac{1}{2}$) and *down*-type ($T^3 = -\frac{1}{2}$) fermions, in the Lagrangian as follows

$$\mathcal{L}_{Yukawa} = -y_d \bar{\psi}_L \cdot \Phi \psi_R - y_u \bar{\psi}_L \cdot \tilde{\Phi} \psi_R + h.c., \quad (1.23)$$

where y_u, y_d represents the Yukawa couplings of all quarks and leptons with $T^3 = +\frac{1}{2}$ and $-\frac{1}{2}$ respectively and $\tilde{\Phi}$ is the conjugate of Φ defined as

$$\tilde{\Phi} = i\sigma_2 \Phi^\dagger = \begin{pmatrix} \phi^0 \\ -\phi^- \end{pmatrix}, \quad (1.24)$$

with σ_2 being a Pauli matrix. ψ_L and ψ_R are the fermion fields which are respectively the $SU(2)_L$ doublets and singlets. After the SSB, *i.e.*, after the Higgs field receives a v ev, the fermions get

masses. For instance for the top-quark, one gets

$$\mathcal{L}_{Yukawa}^t = -\frac{y_t}{\sqrt{2}}(v + H)\bar{t}t, \quad (1.25)$$

where the first term, $y_t v / \sqrt{2}$ can be interpreted as the top-quark mass, M_t . We must however note that, in the SM, the Yukawa couplings are free parameters. This completes our discussion on SSB and the generation of masses for the quarks, charged leptons and weak bosons.

1.3 Theoretical bounds on the mass of Higgs boson

The subject of this thesis is to find the bounds on the Higgs boson couplings in various model-independent beyond the SM (BSM) scenarios. It must be mentioned that when there is no new physics between the electroweak scale and the *grand unification* (GUT) scale (10^{16} GeV), many theoretical bounds can be obtained on the Higgs boson mass. However, these constraints are often invalidated on the introduction of some yet unknown new physics above the electroweak scale and much below the GUT scale. In this section, we will review a few indirect theoretical constraints on the Higgs mass in the minimal SM scenario. For more detailed reviews see for instance Refs. [6–8]. The most important constraints are as follows :

- **Triviality bound :** Let us consider the one-loop radiative corrections to the Higgs quartic coupling. Considering only the tree-level Feynman diagram and the one-loop corrections to Higgs self-coupling as shown in Fig. 1.1, one can express the evolution of the quartic coupling as

$$\frac{d\lambda}{dt} = \frac{3\lambda^2}{4\pi^2} + \text{higher-order corrections}, \quad (1.26)$$

where $t = \ln(Q^2/Q_0^2)$, with Q being the effective energy scale of the theory and Q_0 being some reference scale, say for instance the electroweak scale v . The higher-order terms come from the one loop diagrams of the ϕ^4 theory. One can easily solve this and obtain, at the one-loop level

$$\lambda(Q) = \frac{\lambda(v)}{1 - \frac{3\lambda(v)}{4\pi^2} \ln\left(\frac{Q^2}{v^2}\right)} \quad (1.27)$$

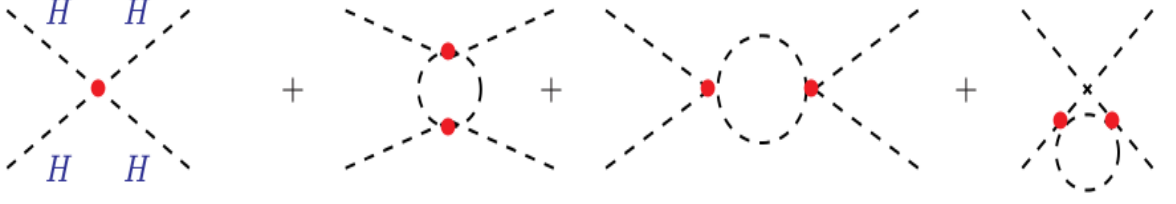


Figure 1.1: Feynman diagrams for the tree-level and one-loop level Higgs self couplings.

One observes that when $Q^2 \ll v^2$, then $\lambda(Q^2) \rightarrow 0$. This is the point, where there are no self interactions and the theory is said to be *trivial* [9]. However, when $Q^2 \gg v^2$, then $\lambda(Q^2) \rightarrow \infty$ and the point where $\lambda(Q^2)$ becomes infinity is called the *Landau pole*. The energy at which this phenomenon occurs is $\Lambda_C = ve^{8\pi^2 v^2/3M_H^2}$.

Thus, by demanding λ to be finite, one obtains an approximate upper bound on the Higgs mass as

$$M_H < \frac{8\pi^2 v^2}{3 \ln(\Lambda^2/v^2)}, \quad (1.28)$$

where Λ is the energy of the new-physics scale. If there is no new physics between the electroweak scale and the GUT scale, then by demanding $\Lambda \simeq 10^{16}$ GeV, one obtains

$$M_H < 160 \text{ GeV} \quad (1.29)$$

This description is only correct when the one loop evolution of Eq. 1.26 accurately describes the theory at large λ . For large λ , the non-perturbative higher-order terms must be explicitly incorporated.

The above discussion is relevant only for a pure scalar theory. However, as we know, the scalar Higgs boson in the SM has couplings to fermions as well as gauge bosons over and above its self interactions. Keeping these in mind, and considering the effect of only the top quark among the fermions, the evolution equation for the quartic coupling needs to be modified as follows [10]

$$\frac{d\lambda}{dt} = \frac{1}{16\pi^2} \left[12\lambda^2 + 12\lambda g_t^2 - 12g_t^4 - \frac{3}{2}\lambda(3g^2 + g'^2) + \frac{3}{16}(2g^4 + (g^2 + g'^2)^2) \right], \quad (1.30)$$

where $g_t = -\frac{M_t}{v}$. By demanding the theory to be perturbative, *i.e.*, λ to be finite at energy scales below the GUT scale, one obtains an upper bound on the Higgs mass as a function of M_t . Hence, for $M_t = 175$ GeV, one obtains $M_H < 170$ GeV.

- **Vacuum Stability bound :** A lower bound on the Higgs boson mass can be derived by requiring that SSB actually takes place, *i.e.*, $V(v) < V(0)$. This is equivalent to demanding that the quartic coupling λ remains positive at all energy scales Q . If λ becomes negative, then the potential will be unbounded from below and will not have a minima, rendering the theory meaningless. For small λ , *i.e.* $\lambda \ll g_t, g, g'$, Eq. 1.30 can be approximately written as

$$\frac{d\lambda}{dt} = \frac{1}{16\pi^2} \left[-12g_t^4 + \frac{3}{16}(2g^4 + (g^2 + g'^2)^2) \right], \quad (1.31)$$

which can be solved to yield

$$\lambda(Q) = \lambda(v) + \frac{1}{16\pi^2} \left[-12g_t^4 + \frac{3}{16}(2g^4 + (g^2 + g'^2)^2) \right] \ln \left(\frac{Q^2}{v^2} \right) \quad (1.32)$$

By demanding $\lambda(Q) > 0$, one obtains a lower bound on the Higgs boson as

$$M_H^2 > \frac{v^2}{8\pi^2} \left[-12g_t^4 + \frac{3}{16}(2g^4 + (g^2 + g'^2)^2) \right] \ln \left(\frac{Q^2}{v^2} \right) \quad (1.33)$$

For a cut-off energy scale as high as the GUT scale, one obtains $M_H \gtrsim 130$ GeV. However, if the theory is valid up to a cut-off scale of say, a TeV, then $M_H \gtrsim 70$ GeV. We must note that these limits are derived by assuming that the electroweak vacuum is absolutely stable. However, even in the minimal SM, for certain values of M_t and M_H ², the vacuum can be metastable with the lifetime greater than the age of the universe [11]. The obtained bound on M_H , can hence be much weaker if one relaxes the criteria of absolute stability.

Hence, we get a rough picture of the upper and lower bounds on the Higgs boson mass solely from *triviality* and *stability* arguments. These are summarised in Fig. 1.2, where the top mass is assumed to be 175 GeV.

²The latest bound on M_t from a combination of data from the Tevatron and the Large Hadron Collider (LHC) [12] is $M_t = 173.34 \pm 0.27$ (stat) ± 0.71 (syst) GeV. A scalar boson was recently discovered by the ATLAS and CMS collaborations and till now is shown to be consistent with the SM expectations at 2σ confidence level. Its mass is measured to be $\sim 125 - 126$ GeV [13].

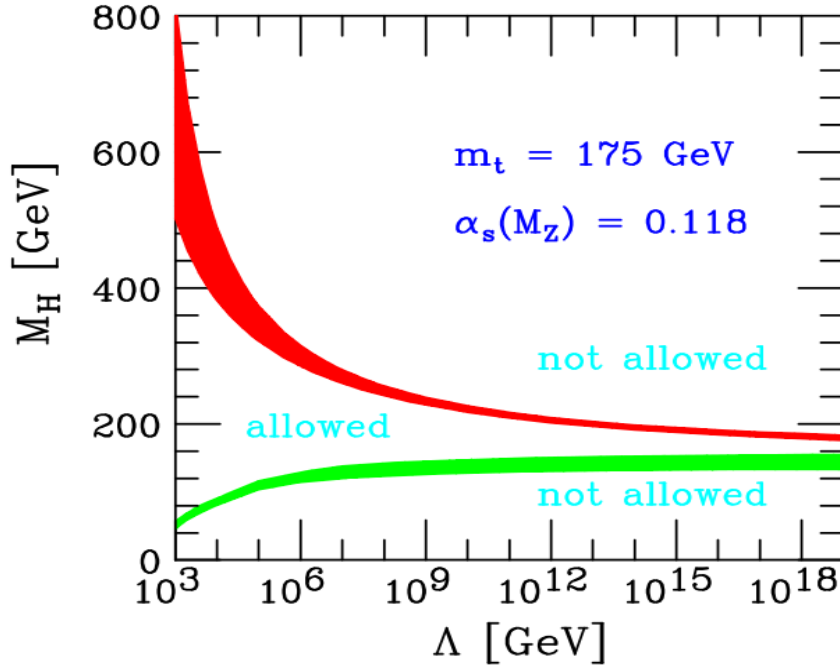


Figure 1.2: Triviality (upper) bound and vacuum stability (lower) bound on the Higgs boson mass as a function of the new physics scale Λ for a top quark mass $M_t = 175 \pm 6$ GeV and $\alpha_s(M_Z) = 0.118 \pm 0.002$. The allowed region lies between the bands and the coloured bands illustrate the impact of various uncertainties. (figure courtesy Ref. [14].)

- Bound from perturbative unitarity :** The Fermi theory was abandoned as it violated unitarity at energies close to the Fermi scale. This led the scientific community to the idea of massive gauge bosons. However, there is still a problem of unitarity violation in SM, but at a scale considerably higher than the Fermi scale. The interactions of the longitudinal components of the massive gauge bosons increase with momenta, implying that these scattering cross-sections increase with the centre of mass energy \sqrt{s} and at some energy scale, unitarity is violated. Here, we will discuss this aspect by studying the scattering process $W_L^+ W_L^- \rightarrow W_L^+ W_L^-$ at high energies (W_L being the longitudinal component of W), as an example [15]. Fig. 1.3 shows some of the Feynman diagrams for this process (the s and t channel exchange of γ and Z are not shown). At high energies, one can approximate the gauge bosons W^\pm, Z as the Goldstone bosons θ^\pm, θ^0 (the Goldstone

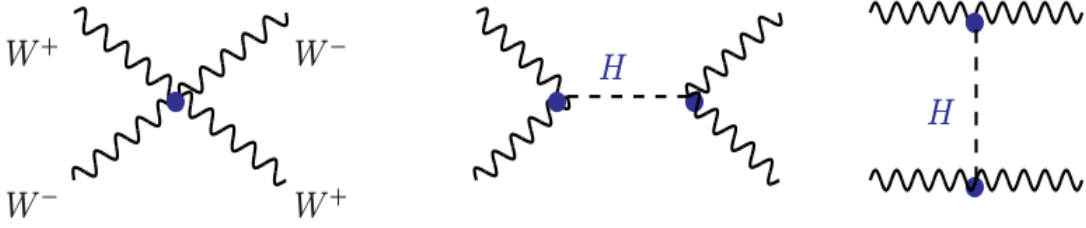


Figure 1.3: Some Feynman diagrams for $W_L W_L \rightarrow W_L W_L$ scattering at high energies.

bosons are responsible for the longitudinal components of the massive gauge bosons as has been discussed above). This is called the *equivalence theorem*.

If one further wants to compute scattering cross-sections using the *equivalence theorem*, one would require to write down the Feynman rules involving the Goldstone bosons and the Higgs boson. By defining $\theta_{\pm} = \frac{1}{2}(\theta_1 \pm i\theta_2)$, one obtains,

$$V(\theta_1, \theta_2, \theta_3, H) = \frac{2M_H^2}{v^2} \theta_+ \theta_- \theta_+ \theta_- + \frac{2M_H^2}{v} H \theta_+ \theta_- + \dots, \quad (1.34)$$

which is the charged Goldstone boson coupling to Higgs. Along the same lines, one can compute the neutral Goldstone boson couplings to Higgs. Hence, now in terms of the Goldstone bosons, one can compute the scattering amplitude of the process, say $W_L^+ W_L^- \rightarrow W_L^+ W_L^-$ at very high energies, $\sqrt{s} \gg M_W$. This can be expanded in terms of the partial waves as

$$A = -\left[2 \frac{M_H^2}{v^2} + \left(\frac{M_H^2}{v} \right)^2 \frac{1}{s - M_H^2} + \left(\frac{M_H^2}{v} \right)^2 \frac{1}{t - M_H^2} \right] = 16\pi \sum_{l=0}^{\infty} (2l+1) P_l(\cos \theta) a_l, \quad (1.35)$$

where s, t, u are the Mandelstam variables in the centre of mass frame of the charged Goldstone bosons. l are the orbital angular momenta and P_l are the Legendre polynomials of the scattering angle θ .

The scattering cross-section can then be expressed as

$$\sigma = \int d\Omega \frac{|A|^2}{64\pi^2 s} = \frac{16\pi}{s} \sum_l (2l+1) |a_l|^2, \quad (1.36)$$

and this can violate unitarity. The *optical theorem* tells us that for asymptotically free fields, the scattering cross-section is given as

$$\sigma = \frac{1}{s} \text{Im}(A(\theta = 0)) \Rightarrow \frac{16\pi}{s} (2l + 1) |a_l|^2 = \frac{1}{s} 16\pi (2l + 1) a_l, \quad (1.37)$$

where we have used $P_l(\cos \theta = 1) = 1$. Hence, this condition can be rewritten as

$$(\text{Re}(a_l))^2 + (\text{Im}(a_l))^2 = \text{Im}(a_l) \Rightarrow |\text{Re}(a_l)| < \frac{1}{2} \quad (1.38)$$

This basically boils down to a constraint described by a circle in the plane $\text{Re}(a_l)$ and $\text{Im}(a_l)$ about $a_l = (0, 1/2)$ with radius = $1/2$ units. By taking the $J = 0$ partial wave for the amplitude A , one obtains

$$a_0 = \frac{1}{16\pi s} \int_s^0 dt |A| = -\frac{M_H^2}{16\pi v^2} \left[2 + \frac{M_H^2}{s - M_H^2} - \frac{M_H^2}{s} \ln \left(1 + \frac{s}{M_H^2} \right) \right] \quad (1.39)$$

If one assumes the Higgs boson mass to be much smaller than the centre of mass energy \sqrt{s} , one gets

$$a_0 \xrightarrow{s \gg M_H^2} -\frac{M_H^2}{8\pi v^2} \quad (1.40)$$

Hence, by imposing the unitarity condition of Eq. 1.38, one has

$$M_H \lesssim 870 \text{ GeV} \quad (1.41)$$

However, the discussion will be incomplete if we do not mention the other scattering processes. By considering the full basis of scattering processes at high energies, *viz.*, $(W_L^+ W_L^-, \frac{1}{\sqrt{2}} Z_L Z_L, \frac{1}{\sqrt{2}} H H, Z_L H, W_L^+ H, W_L^- H)$, where $\frac{1}{\sqrt{2}}$ accounts for the identical particles,

the coefficient of the $J = 0$ partial wave, a_0 takes the form

$$a_0 \propto \frac{M_H^2}{v^2} \begin{pmatrix} 1 & \frac{\sqrt{2}}{4} & \frac{\sqrt{2}}{4} & 0 & 0 & 0 \\ \frac{\sqrt{2}}{4} & \frac{3}{4} & \frac{1}{4} & 0 & 0 & 0 \\ \frac{\sqrt{2}}{4} & \frac{1}{4} & \frac{3}{4} & 0 & 0 & 0 \\ 0 & 0 & 0 & \frac{1}{2} & 0 & 0 \\ 0 & 0 & 0 & 0 & \frac{1}{2} & 0 \\ 0 & 0 & 0 & 0 & 0 & \frac{1}{2} \end{pmatrix} \quad (1.42)$$

By demanding that the largest eigenvalue of a_0 satisfies unitarity constraint, one obtains [16]

$$M_H \lesssim 710 \text{ GeV} \quad (1.43)$$

However, one must note that to put bounds on M_H from the above argument, one must assume that SM remains perturbative and that the higher-order corrections are not large. Hence the unitarity argument is termed the *tree-level (perturbative) unitarity*.

1.4 Experimental bounds on the mass of Higgs boson

The LHC has finally discovered a boson. Its exact nature is still to be confirmed with a series of experiments on its couplings to other SM particles, its self-coupling, parity, spin, decays to *invisible* particles etc. However, by now one knows that it is *similar* to the SM-higgs. Its mass is measured to be 125.09 ± 0.21 (stat.) ± 0.11 (syst.) GeV from a combined measurement by the CMS and ATLAS collaborations [13] in the $H \rightarrow \gamma\gamma$ and $H \rightarrow ZZ^* \rightarrow 4\ell$ channels. But before the advent of the LHC, the Large Electron-Positron Collider (LEP) also provided indirect bounds on the Higgs boson mass from the measurement of electroweak precision observables which we briefly discuss below

- **Indirect limits from Electroweak Radiative correction :** The SM Higgs boson enters into the one-loop radiative corrections and hence its mass can be bound by the electroweak precision measurements. The ρ parameter (defined at the tree level as $\rho = \frac{M_W^2}{M_Z^2 \cos^2 \theta_w} = 1$) gets radiative corrections at the loop level. Hence, by taking into account its correction

due to Higgs, one obtains

$$\rho = 1 - \frac{11g^2}{96\pi^2} \tan^2 \theta_w \ln\left(\frac{M_H}{M_W}\right) \quad (1.44)$$

The dependence of ρ on M_H being logarithmic in nature, only gives us a weak bound on it. On the other hand, the *top*-quark contributes quadratically to several electroweak observables including the ρ parameter and hence is strongly bound from such measurements. It has been shown in Ref. [17] that at one-loop all electroweak parameters have at most a logarithmic dependence on M_H . This is called the *screening theorem*. All electroweak corrections involving the Higgs boson have the general form

$$g^2 \left(\ln\left(\frac{M_H}{M_W}\right) + g^2 \frac{M_H^2}{M_W^2} \right), \quad (1.45)$$

i.e., the quadratic terms in M_H are additionally screened by a factor of g^2 . Hence from precision measurements of EW observables at LEP and at the Stanford Linear Collider (SLC), direct measurements of M_W and M_t at the Tevatron and the measurements of neutrino scattering experiments, one gets an upper bound on the Higgs boson mass from the effect of radiative corrections as

$$M_H < 280 \text{ GeV at } 95\% \text{ CL} \quad (1.46)$$

Since this bound arises from loop corrections, any unknown new physics contributing to the loop can circumvent this.

- **Bound from LEP :** Combining the results of the four LEP collaborations, no significant excess was seen above the SM background and one obtained a lower bound of

$$M_H > 114.4 \text{ GeV at } 95 \% \text{ CL} \quad (1.47)$$

from the non-observation of a signal, as shown in Fig. 1.4. The expected limit was $M_H > 115.3 \text{ GeV}$.

- **Bound from Tevatron :** Tevatron presented its results in 2012 and excluded $100 \text{ GeV} < M_H < 103 \text{ GeV}$ and $147 \text{ GeV} < M_H < 180 \text{ GeV}$ at 95% CL [19]. Besides, Tevatron also saw a 3σ excess in the range $115 \text{ GeV} < M_H < 140 \text{ GeV}$ specially in the $H \rightarrow b\bar{b}$

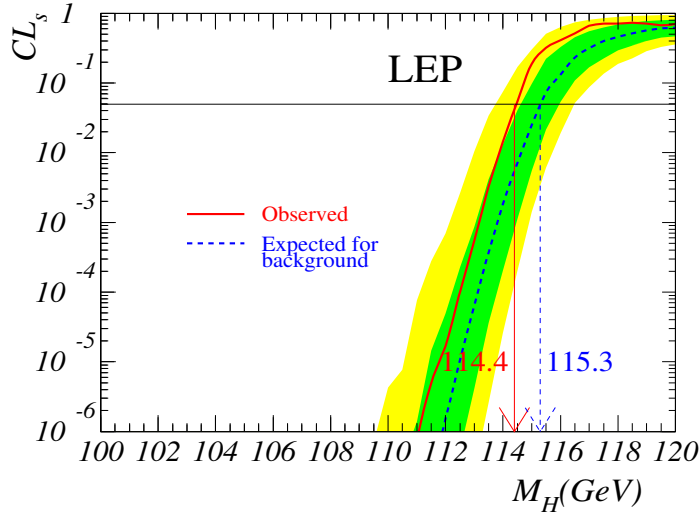


Figure 1.4: Confidence Level CL_s for the signal+background hypothesis in Higgs production at LEP2. The solid/red line is for the observation, the dashed line is the median background expectation, the darkgrey/green and lightgrey/yellow shaded bands around the median expected line correspond to the 68% and 95% simulated probability bands. The intersection of the horizontal line at $CL_s = 0.05$ with the observed curve defines the 95% CL lower bound for M_H ; from Ref. [18]

channel [20].

1.5 Motivations for physics beyond the Standard Model

Even though SM has been hugely successful as a theory of elementary particles, still it is plagued by certain limitations. There are numerous experimental observations unsupported by this theory and there are also few theoretical limitations. In this section, we briefly review the most striking discrepancies, both from theory and experiments, which makes it necessary to call for BSM physics.

- **Observation of neutrino masses and mixing :** The SM particle spectrum consists of three massless left-handed neutrinos. Even though direct detection of neutrinos are extremely difficult because of their feeble interaction with matter, however, in the late 1960s, J.N. Bahcall and R. Davis Jr. discovered a phenomenon called neutrino oscillations [21] in which they found a deficit in the flux of solar neutrinos as predicted by the *Standard*

Solar Model. In 1998, the Super-Kamiokande collaboration [22] published their results stating that neutrinos oscillate from one flavour eigenstate to another while travelling through atmosphere or through matter. Later, in 2001, the Sudbury Neutrino Observatory (SNO) also concluded that neutrinos change flavour [23]. The mechanism is based on basic quantum mechanics and requires the neutrinos to be massive [24]. Even though these experiments suggest the neutrinos to be massive, we are yet unaware of their absolute masses, because the oscillations are only sensitive to the mass squared differences of neutrinos having different mass eigenstates. In 2005, the KamLAND collaboration predicted a mass squared difference between the first two mass eigenstates, $\Delta m_{12}^2 \simeq 7.9 \times 10^{-5} \text{ eV}^2$ [25]. Later, Δm_{32}^2 was measured to be $2.7 \times 10^{-3} \text{ eV}^2$. Even more recently, non-zero neutrino mixing angles have also been determined. For instance the Daya Bay experiment measured $\sin^2\theta_{13} = 0.092 \pm 0.016 \text{ (stat)} \pm 0.005 \text{ (syst)}$ in a three neutrino framework [26]. As an aside, we must note that we are still unaware of the nature of neutrinos, whether they are *Dirac* or *Majorana* fermions. There are several extensions of the SM in which neutrinos obtain masses. The most popular approach is the *seesaw* mechanism where one needs to add massive right handed neutrinos to the SM sector in order to generate tiny masses for them.

- **Dark Matter :** Besides ordinary matter, or the matter that is known to contribute 4.9% of the total mass-energy in the universe, 26.8% of the universe is known to have contributions from some yet unknown gravitating particles known as *dark matter*. Dark matter was hypothesized when astrophysicists found a discrepancy in the mass of large astronomical objects when measured by their gravitational interaction than when determined by the observation of visible stars, dust and gas. It was first hypothesized by J. Oort in 1932 and F. Zwicky in 1933 [27]. The evidence of dark matter could be seen from the velocity distribution curves of spiral galaxies (as a function of the distance from the centre). Even though from observed matter, classical mechanics predicts the velocity distribution to decrease with increase in radial distance from the centre of the spiral galaxy, the velocity is seen to have a rather flat behaviour. This was first shown by V. Rubin in 1960-1970 [28]. Afterwards various other astrophysical observations like the gravitational lensing of background objects by galaxy clusters like the Bullet cluster or the temperature distribution of hot gas in galaxies and clusters of galaxies, also showed the existence of dark matter. More recently, the anisotropy patterns in the cosmic microwave background radiations (CMBR) suggests the existence of dark matter. It is not yet clear

as to the nature of dark matter. There are several hypothesis including dark matter to be sub-atomic particles. Various extensions of the SM which incorporate a *dark matter-like* candidate are now being studied extensively. Every model has to satisfy the criteria of a dark relic abundance, *i.e.*, $h^2\Omega_{DM} = 0.1123 \pm 0.0035$ and the limits from the direct detection experiments.

- **Dark Energy** : The remaining 68.3% of the universe is comprised of the even more elusive *dark energy*. Dark energy is an unknown form of energy which supposedly tends to accelerate the universe [29]. The two proposed forms of dark energy are the cosmological constant Λ which arises in Einstein's field equation designed to achieve a *static universe* and some scalar fields whose energy density can vary in spacetime.
- **Baryogenesis** : Besides, SM is unable to provide the reason for the *baryon asymmetry* in nature, *i.e.*, there is an observable difference between the baryonic matter and the anti-baryonic matter in the universe. Theoretically, this can be achieved by a set of rules listed by A.D. Sakharov [30]
 - Baryon number violation
 - C -symmetry and CP -symmetry violation
 - Interactions out of *thermal equilibrium*

Even though, the SM allows for CP violation and baryogenesis in SM requires the electroweak symmetry breaking (EWSB) to be a first order phase transition, still the observed amount of baryon asymmetry can not be explained in SM.

- **The naturalness problem** : The SM faces problems when one tries to compute the radiative corrections to M_H . This is termed as the *fine-tuning* problem. Several loop diagrams involving fermions, gauge bosons and the Higgs itself, contribute to the one-loop correction to M_H (see Fig. 1.5). Even though we noted that the Higgs contributes mostly logarithmically to the EW corrections, it shows a very different nature while trying to compute its own mass correction at the loop level. For instance at the one-loop level, M_H can be written in terms of the bare mass M_H^0 (the mass occurring in the unrenormalised SM Lagrangian) as

$$M_H^2 = (M_H^0)^2 + \frac{3\Lambda^2}{8\pi^2 v^2} [M_H^2 + 2M_W^2 + M_Z^2 - 4M_t^2], \quad (1.48)$$

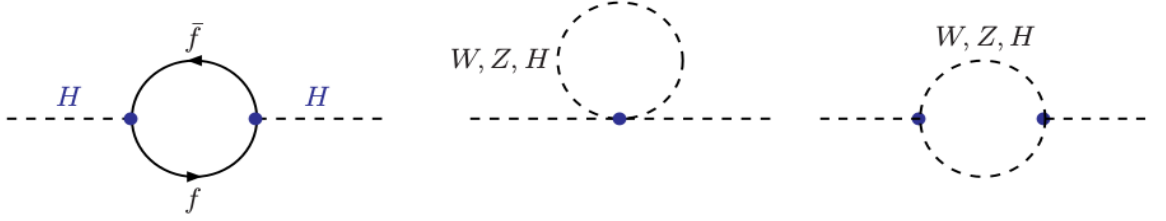


Figure 1.5: Feynman diagrams for the one-loop corrections to the SM Higgs boson mass.

where Λ is the cut-off scale for the loop momentum. Only the top quark contribution has been shown here. Here, the Higgs is thus shown to have a quadratic divergence in its mass. If the cut-off Λ is as large as the GUT scale, one needs a fine tuning of 16 digits between M_H^0 and the radiative corrections, in order to have a physical Higgs boson mass of the order of the EWSB scale. This is termed as the *naturalness* problem or the *fine-tuning* problem. Thus, in order to achieve a Higgs mass consistent with the experimental predictions and to maintain a perturbative theory, one needs to add counter-terms to M_H^2 such that the divergences cancel out. Veltman, gave a solution [31], stating that by choosing the Higgs mass to be

$$M_H^2 = 4M_t^2 - 2M_W^2 - M_Z^2, \quad (1.49)$$

one could cancel the quadratic divergence and restore the prediction of a Higgs mass at the EWSB scale. However, the above condition only works for the one-loop correction. For a general loop order, the correction to the Higgs mass is given as [32]

$$\Lambda^2 \sum_{n=0}^{\infty} c_n(\lambda_i) \ln^n(\Lambda/Q), \quad (1.50)$$

where Q is the renormalisation scale. The higher-order c_n s have more powers of $1/(16\pi^2)$ and hence are more suppressed. The Veltman condition requires the fine-tuning to work at all orders in the perturbation theory. But as various c_n terms are independent, there is no obvious solution for M_H . So this might imply that the Veltman condition is not so useful and can not solve the fine-tuning problem. But, this problem of fine-tuning is a major problem only for large scales where new physics (NP) might arise.

There are however some beautiful theories beyond the SM which can cure this problem of a quadratically divergent Higgs boson mass. One of the most lucrative candidates to achieve this is the theory of supersymmetry, a spacetime symmetry of the integer-spin bosons and the half-integer spin fermions (for a detailed review on supersymmetry, see for instance Ref. [33]). Besides, supersymmetry also provides possible candidates for dark matter and also provides a solution to the baryon asymmetry problem in nature (for a review see Ref. [34]).

- **Flavour problem and family structure** : The *flavour problem* in SM refers to the unexplained hierarchy in masses of the fermions. In the quark sector, the mass ranges from 2.3 MeV for the *up*-quark to around 173.2 GeV for the *top*-quark. The discrepancy is also massive in the lepton sector where the masses vary from sub-eV range for the neutrinos to about 1.77 GeV for the τ lepton. All the fermions are categorised as generations with higher generations having greater masses. Besides, the generation of fermion masses in SM is somewhat *ad-hoc* and not as theoretically motivated as the generation of masses for the gauge bosons.

The Cabibbo-Kobayashi-Maskawa (CKM) matrix is a unitary matrix which parametrizes the mixing of the *six* quarks in terms of three angles and one phase. Like the masses, the mixings are also shown to follow a generational structure.

- **Lack of insight on quantum gravity** : SM describes three of the four fundamental interactions in nature but is unable to incorporate gravity as a quantum theory. In an attempt to use the general prescriptions of quantum field theory to the force of gravity, one obtains a non-renormalizable theory. However, there exists two remarkable theories where gravity is quantised. In the more popular *string theory*, an attempt is made to unify gravity with the other fundamental interactions. However, the subject *loop quantum gravity* makes no attempt for such grand unification of all fundamental forces and attempts to quantize the gravitational field keeping it away from the other fundamental forces in nature.

Apart from these reasons, there are several other motivations for studying physics beyond the SM. For instance, as we will see in the next few chapters, even though the discovered scalar boson has properties very similar to the SM Higgs, there are still avenues to explore, before we rule out even some small trace of new physics in its behaviour and properties. A conjecture is that the discovered Higgs is part of a wider particle spectrum, for instance the particle spectra

allowed in supersymmetry, extra dimensional models, extended gauge sectors, grand unified theories etc. Another mode of thought is that the couplings of the Higgs bosons might vary slightly from their SM-expectations and that the Higgs can also have some non-standard decay modes. This is the main theme of the thesis, i.e. to study the Higgs coupling variations in a model-independent framework. In the major part of this thesis, we show the allowed variations in the couplings of the Higgs in the perspective of the Large Hadron Collider (LHC). Later in the thesis, however, we even show how such coupling variations can be probed at electron-positron colliders.

Chapter 2

High energy colliders

2.1 A brief review of the Large Hadron Collider

The Large Hadron Collider (LHC) located in CERN, Geneva, is the highest energy accelerator ever built. It is a proton-proton collider consisting of a 27 km underground storage ring. Superconducting magnets are used to accelerate the colliding protons. The circumference of this accelerator spans a wide region along the border of Switzerland and France. The LHC is designed to run at a centre-of-mass energy (CME) going up to 14 Tera electron volts (TeV), with each beam accelerated at a maximum of 7 TeV. The run I of the LHC, till 2014, has been able to accelerate the protons to a CME of 8 TeV. The discovery of the erstwhile elusive Higgs boson was made public by two experimental collaborations at the LHC in July, 2012, when the protons collided at a CME of 7 TeV. Later, the statistics were improved and the data on Higgs were further consolidated. The LHC is also designed to study heavy-ion physics during part of its run-time. Before the LHC started running, the highest energy collider was the Tevatron which is a proton-antiproton collider in Fermilab, Batavia, Illinois. There, the maximum CME attained was 1.96 TeV. One major achievement of the Tevatron was the discovery of the top quark.

Hadron colliders differ from electron-positron colliders in several aspects. An important distinction is that in an e^+e^- collider, the CME of the colliding particles is spread out at best by

a small fraction, due to initial state radiation and beam-beam interactions, whereas for colliding protons or anti-protons, only a fraction of the initial beam energies is carried by the partons (quarks and gluons). Effectively, the CME of the colliding particles in a hadron collider is of the order of a few TeVs, which is the maximum energy scale that can be attained at the current run of the LHC. Future colliders with CME close to a hundred TeV are now also contemplated as follow-ups of the LHC experiment. It should also be noted that, in spite of their capacity to generate a wide variety of events, hadron colliders produce more backgrounds via strong interaction, which makes it even more challenging to distinguish any new physics. However, while discussing hadron colliders, one must mention one of their major advantages over e^+e^- colliders. In circular colliders, the beams always lose energy because of their acceleration. This relativistic phenomenon is termed *synchrotron radiation*, which is given as

$$\Delta E \propto \frac{1}{R} \left(\frac{E}{m} \right)^4, \quad (2.1)$$

where ΔE is the energy loss per cycle, R is the radius of the colliding machine, E/m is the relativistic factor γ , with E being the beam energy and m being the mass of the particle. Hence, to minimise energy loss, either R should be large or m should be large. Proton being about 2000 times heavier than an electron, undergo much lower energy loss per turn compared to electrons.

Apart from the CME, the other important parameter for a collider is the instantaneous luminosity, which is defined as the number of particles passing each other per unit time through unit transverse area at the interaction point. However, in reality, bunches of particles cross each other. If there are n_1 and n_2 particles in each bunch in beam 1 and beam 2 respectively, then if the frequency of the beam crossing is f and the transverse profile of the beams is A , the instantaneous luminosity scales as

$$\mathcal{L} \propto f n_1 n_2 / A \quad (2.2)$$

The instantaneous luminosity is often given in units of $\text{cm}^{-2} \text{s}^{-1}$. The reaction rate, *i.e.*, the number of scattering events per unit time is given as

$$R(s) = \sigma(s) \times \mathcal{L}, \quad (2.3)$$

where $\sigma(s)$ is the total scattering cross-section and is a function of the partonic CME, \hat{s} . Even though the conventional unit for cross-section is cm^2 , but for subatomic particles, this is too big

a unit. The commonplace unit of cross-section in particle physics is a barn, where $1 \text{ cm}^2 = 10^{24} \text{ barn} = 10^{36} \text{ pb}$, etc. Hence, even for luminosity, it is convenient to translate to such units.

In practice, many times while presenting results, the experiments report an integrated luminosity over a large period of time, say a year. For the 7 TeV run of the LHC, they managed an integrated luminosity of $\sim 5 \text{ fb}^{-1}$ and for the 8 TeV run, the accumulated luminosity for the entire period reached close to 20 fb^{-1} . For the run II of the LHC, the planned integrated luminosity reach is $\sim 300 \text{ fb}^{-1}$. There is a further plan for a high luminosity run at the LHC (HL-LHC), which might at the end, achieve an integrated luminosity of 3000 fb^{-1} .

A discussion on LHC would be incomplete without mentioning the various experiments in its ambit. There are seven primary experiments at the LHC, *viz.*, **ATLAS** (A Toroidal LHC Apparatus) [1], **CMS** (Compact Muon Solenoid) [2], **ALICE** (A Large Ion Collider Experiment), **LHCb** (Large Hadron Collider beauty), **TOTEM** (TOTAL cross section, Elastic scattering and diffraction dissociation Measurement at the LHC), **LHCf** (Large Hadron Collider forward) and **MoEDAL** (Monopole and Exotics Detector at the LHC). The ATLAS and CMS experiments are the largest general purpose experiments searching for a vast range of new physics over and above studies on the Higgs boson and the top quark. ALICE is a heavy-ion detector and is designed to study the quark-gluon plasma phase. LHCb is designed to study the slight difference between matter and anti-matter by studying the physics of the bottom-quark. The ATLAS, CMS, ALICE and LHCb detectors sit in huge underground caverns on the LHC ring.

The ATLAS detector is the largest volume particle detector being 46 m long, 25 m high and 25 m wide. It weighs 7000 tonnes and sits 100 m below the ground in an underground cavern near the CERN main entrance. ATLAS uses a very sophisticated online trigger system deciding which events to record and which to discard. A schematic diagram of the ATLAS detector is shown in Fig. 2.1

The Compact Muon Solenoid (CMS) detector is another general purpose detector with dimensions $21 \text{ m} \times 15 \text{ m} \times 15 \text{ m}$. The speciality of this detector is that it is built around a huge solenoid magnet in the shape of a cylindrical coil of superconducting cable, which generates a magnetic field of 4 tesla, about 100,000 times that of the earth's magnetic field. This field is confined by a steel "yoke" that forms the bulk of the detector and weighs 14,000 tonnes. The schematic representation of the CMS detector is shown in Fig. 2.2

Both the ATLAS and CMS experiments are designed to study the standard model (SM) (with special emphasis on the Higgs boson), search for extra spatial dimensions and possible

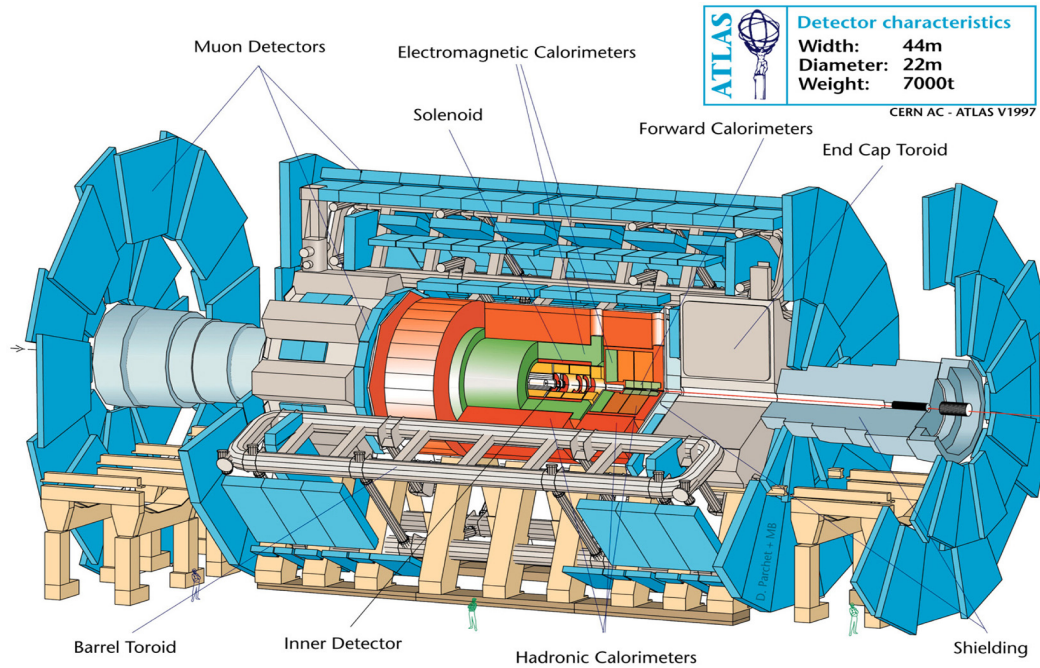


Figure 2.1: Schematic view of the ATLAS detector (figure courtesy [3].)

particles that can be constituents for the elusive dark matter. Besides, these two experiments are also taking part in looking for various signals of physics beyond the standard model (BSM).

The TOTEM and LHCf are the smallest experiments at the LHC. They focus on “forward particles”, *i.e.*, protons or heavy ions brushing past each other. MoEDAL is the seventh experiment at the LHC which is looking for the very elusive magnetic monopole particles [5,6].

In section 2.2, we discuss the different components of a general purpose detector required for detecting particles. In section 2.3, we briefly discuss how we model our simulations to mimic the detector effects. Finally in section 2.4, we discuss a few kinematic variables which are a must in studying physics at hadron colliders.

2.2 Detector basics

Hadron colliders like LHC and Tevatron, are built up of several components, each one specific to the detection of some definite class of particles (for a detailed review on the aspects of collider physics, one can look into Ref. [7]). By looking at the tracks in the tracking chambers or the

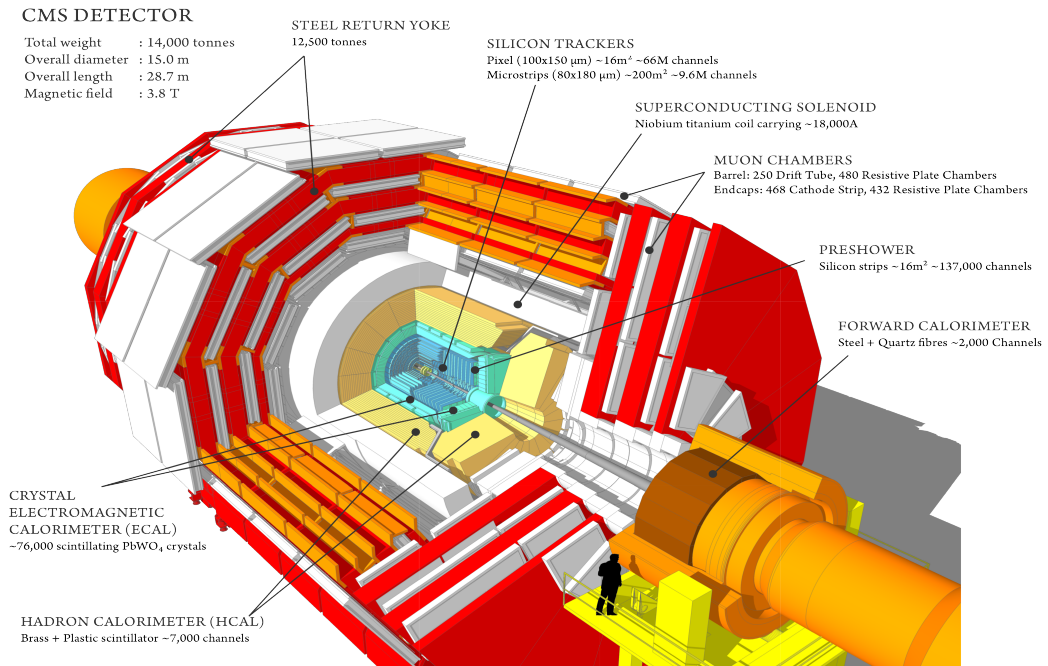


Figure 2.2: Schematic view of the CMS detector (figure courtesy [4].)

energy deposits in the calorimeters, one can understand the nature of the collisions. As the major part of this thesis deals with studying BSM physics by looking at events with final states comprising of leptons, jets, photons and missing transverse energy, it is important to mention the various components of the general purpose detectors (like ATLAS and CMS) which measure the energies, momenta, charges, interaction vertices etc. of such final state particles. Most of the particles in the SM Lagrangian are not seen by the detectors. Heavy particles like W^\pm , Z and t , promptly decay to leptons and quarks with lifetimes around $1/(2 \text{ GeV}) \approx 3.3 \times 10^{-25}$ seconds. Here, the widths of these particles are about 2 GeV [8] ($\Gamma_W = 2.085 \pm 0.042$, $\Gamma_Z = 2.4952 \pm 0.0023$ GeV and $\Gamma_t = 2.0 \pm 0.5$ GeV). The quarks also fragment to colour-singlet hadrons because of QCD confinement [9], at a time scale of $t_h \sim 1/\Lambda_{QCD} \approx (1/200 \text{ MeV}) \approx 3.3 \times 10^{-24}$ seconds. The stable particles, such as the electrons, positrons, jets and photons show up as energy deposits or charged tracks (except photons). In Fig. 2.3, we show a prototype for a general purpose detector. The major components of a detector can broadly be categorised as follows

- **Vertex detector** : This is the innermost component of a detector. When there are more

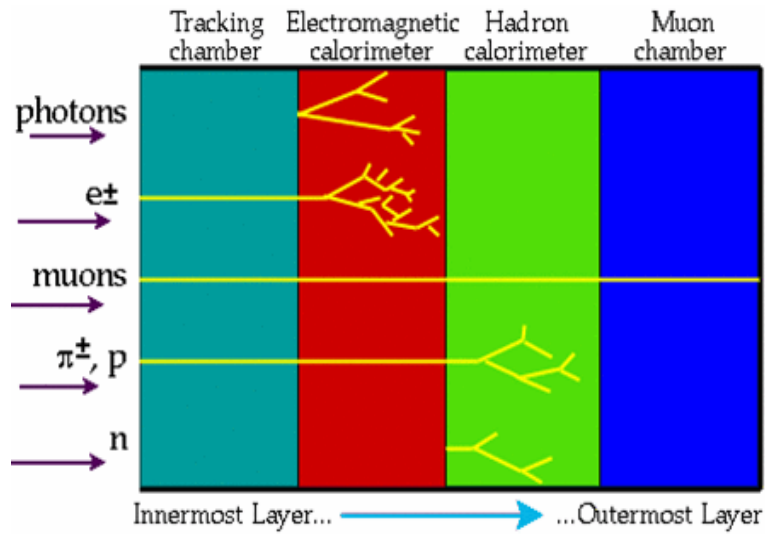


Figure 2.3: Prototype of particle signatures in the various detector components (figure courtesy Ref. [7]).

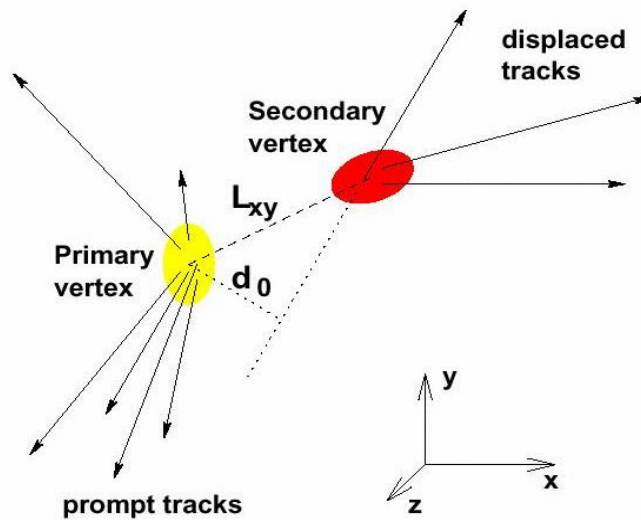


Figure 2.4: An illustrative event leading to a displaced secondary vertex (figure courtesy Ref. [7]).

than two charged tracks, it is possible to reconstruct a secondary decay vertex (an illustrative case is shown in Fig. 2.4). If the decaying particle travels very fast then the decay products will be collimated with a typical angle of separation, $\theta \approx \gamma^{-1} = m/E$. The im-

parameter d_0 (as shown in Fig. 2.4) can be approximately written as $d_0 \approx L_{xy}\theta$, where L_{xy} is the distance between the primary and secondary vertices. This quantity is crucial in determining the displaced vertex. For the ATLAS detector, the resolution of the impact parameter is parametrized as [10]

$$\Delta d_0 = 11 \oplus \frac{73}{(p_T/GeV) \sqrt{\sin \theta}} \mu m, \quad (2.4)$$

where p_T is the transverse momentum of the decaying particle and \oplus implies summation in quadrature. However, if there is only one charged track, then also it is possible to resolve a secondary vertex along the longitudinal direction alone. The resolution in this case is worse and can be approximated as [10]

$$\Delta z_0 = 87 \oplus \frac{115}{(p_T/GeV) \sqrt{\sin^3 \theta}} \mu m. \quad (2.5)$$

- **Tracking chamber :** The tracking chamber is the component of a general purpose detector, tracing out the trajectories of charged particles and also measuring their energy losses. For both ATLAS and CMS experiments, the pseudo-rapidity (discussed in section 2.4) coverage for the tracking chamber is up to around $|\eta| \simeq 2.5$. One of the major features of the tracking chamber is that, one can estimate a particle's momentum by measuring its curvature. The magnetic fields ($|\vec{B}|$) at the ATLAS and CMS detectors are respectively 2 and 4 Teslas. So, by assuming unit charge for a particle (or using the information for the charge Q , from some other source), the particle's momentum $|\vec{p}|$ can be measured as

$$\kappa \equiv \frac{1}{\rho} \propto \frac{QB}{|\vec{p}|} \quad (2.6)$$

Another feature of the tracking chamber is the possibility of measuring the energy loss of a particle as it traverses the detector. Using the Bethe-Bloch formula, the energy loss by excitation and ionisation is given as

$$\frac{dE}{dx} \propto \left(\frac{Q}{\beta}\right)^2, \quad (2.7)$$

where $\beta = v/c$ is the speed of the particle. Thus, one can find the mass of the particle from $|\vec{p}|$ and β . These measurements are possible if one knows the value of Q . How-

ever, without such knowledge, some additional information like the time-of-flight of the particle might be necessary for its identification.

- **Electromagnetic Calorimeter (ECAL) :** Just after the tracking chamber, is the electromagnetic calorimeter (ECAL). This part of the detector is used to measure the energies of the electrons, positrons and the photons. In a typical event, there are many e^- , e^+ and γ in the final states, mostly due to cascades of electromagnetic showers due to bremsstrahlung and also due to pair production. With an increase in the depth of the medium, the number of such particles increases exponentially. Because the measured incident energy is proportional to the total number (N) of such particles impinging on these detectors, the energy resolution must be characterised by $(1/\sqrt{N})$. The pseudo-rapidity coverage of the ECAL for ATLAS and CMS is at least $|\eta_{e,\gamma}| \simeq 3$.
- **Hadron Calorimeter (HCAL) :** Next is the hadron calorimeter (HCAL). This functions somewhat similarly to an ECAL, in principle. It measures the energy of the high energy incident hadrons. The pseudo-rapidity coverage for this part of the detector is $|\eta_h| \simeq 5$.
- **Muon Chamber :** High energy muons have a comparatively larger lifetime and hence the muon chambers are kept in the outer layers of the detectors. Muon is approximately 200 times heavier than an electron and is the only particle which is not stopped by the calorimeters and the tracker. The muon chambers, with the help of magnets, measure the momentum of a muon by measuring its curvature.

2.3 Modelling the simulations

In an attempt to mimic the experimental results, it is necessary to include resolution effects to the energies and momenta for the various final state particles. A part of this project deals with such collider analysis, where modelling the detector effects becomes important. We have mostly used the detector resolutions modelled on ATLAS [11]. In some parts, we have not explicitly used the detector effects in our Monte Carlo codes, but have used the standard package DELPHES [12].

The energy resolutions for the electrons/positrons, photons and jets are discussed below

- **For electrons/positrons, photons and jets :** The energy resolution, $\sigma(E)$ of e^- , e^+ , γ and

jets (j) are modelled according to a single Gaussian distribution.

$$\frac{\sigma(E)}{E} = \frac{a}{\sqrt{E}} \oplus b \oplus \frac{c}{E}, \quad (2.8)$$

where a is the stochastic term, essentially coming due to photostatistics and hence σ is proportional to \sqrt{E} for this term, b is the constant term, which is due to energy leakage from the back of the crystal and crystal to crystal inter-calibration errors and c is the noise term, which includes the electronic noise. a, b and c can depend strongly on the pseudo-rapidity, $|\eta|$. We must note that the three terms are added in quadrature.

We list the values of these parameters for CMS and ATLAS as follows :

1. **For e^-, e^+, γ :**

For CMS :

$$(a, b, c) = \begin{cases} (0.030 \text{ GeV}^{1/2}, 0.005, 200 \text{ MeV}), & |\eta| < 1.5, \\ (0.055 \text{ GeV}^{1/2}, 0.005, 600 \text{ MeV}), & 1.5 < |\eta| < 2.5 \end{cases}$$

For ATLAS :

$$(a, b, c) = \begin{cases} (0.11 \text{ GeV}^{1/2}, 0.007, 250 \text{ MeV}), & |\eta| < 1.5, \\ (0.13 \text{ GeV}^{1/2}, 0.007, 250 \text{ MeV}), & 1.5 < |\eta| < 2.5 \end{cases}$$

2. **For jets :**

For CMS :

$$(a, b, c) = \begin{cases} (0.70 \text{ GeV}^{1/2}, 0.08, < 1 \text{ GeV}), & |\eta| < 1.5, \\ (1.00 \text{ GeV}^{1/2}, 0.10, < 1 \text{ GeV}), & 1.5 < |\eta| < 3.0, \\ (1.00 \text{ GeV}^{1/2}, 0.10, < 1 \text{ GeV}), & 3.0 < |\eta| < 5.0 \end{cases}$$

For ATLAS :

$$(a, b, c) = \begin{cases} (0.65 \text{ GeV}^{1/2}, 0.027, 4 \text{ GeV}), & |\eta| < 1.5, \\ (1.10 \text{ GeV}^{1/2}, 0.01, 6.5 \text{ GeV}), & 1.5 < |\eta| < 3.0, \\ (1.00 \text{ GeV}^{1/2}, 0.05, 10 \text{ GeV}), & 3.0 < |\eta| < 5.0 \end{cases}$$

- **For muons :** The transverse momentum resolution for the muons is modelled according to a single Gaussian distribution.

$$\frac{\sigma(p_T)}{p_T} = \begin{cases} a, & p_T < 100 \text{ GeV} \\ a + b \log \frac{p_T}{100 \text{ GeV}}, & p_T > 100 \text{ GeV} \end{cases}$$

Following are the values of the parameters (a, b) for CMS and ATLAS :

For CMS:

$$(a, b) = \begin{cases} (0.008, 0.037), & |\eta| < 1.5, \\ (0.020, 0.050), & 1.5 < |\eta| < 3.0 \end{cases}$$

For ATLAS:

$$(a, b) = \begin{cases} (0.02, 0.08), & |\eta| < 1.5, \\ (0.03, 0.06), & 1.5 < |\eta| < 3.0 \end{cases}$$

- **For unclustered particles :** In order to find a realistic estimate for the missing transverse energy, besides requiring the transverse momenta of all the stable visible particles, it is also necessary to consider those particles (clusters of particles) which are not identifiable as jets, electrons, muons or photons because they do not satisfy the stipulated triggers for any of them. They are calorimeter clusters with $p_T > 0.5 \text{ GeV}$ and $|\eta| < 5$. These particles are called unclustered objects. Their x and y components are smeared independently using

the same Gaussian width

$$\sigma(E_{x(y)}^{Uncl.}) = \alpha \sqrt{\sum_i E_T^{(Uncl.)_i}}, \quad (2.9)$$

where $\alpha = 0.55$ is obtained with the study of minimum bias events, i is the unclustered object index and $E_T^{(Uncl.)_i}$ is the *transverse energy* (discussed in the next section) of the i^{th} object.

One must note that in order to obtain the ‘‘corrected’’ energies or transverse momenta using the resolution values, it is essential to generate a Gaussian random number [13] for each case, multiply it with the resolution and add it to the energy/transverse momentum that one obtains from energy-momentum conservation.

2.4 Some relevant kinematic variables

Unlike in e^-e^+ colliders, in a hadron collider, the partonic centre-of-mass (CM) frame is different from the lab frame of the collider because each parton only carries a fraction of the energy of the initial beam. The parton CM frame, is hence, boosted with respect to the lab frame along the beam direction. Below, we discuss some frequently used kinematic variables

- **Parton level CME ($\sqrt{\hat{s}}$)** : In a hadron collider, the four-momenta of two colliding hadrons (protons or anti-protons) A and B are typically represented as $P_A = (E_A, 0, 0, p_A)$ and $P_B = (E_A, 0, 0, -p_A)$ in the lab frame. However, during the actual collision, the partons carry only a fraction of the beam energies. If x_1 and x_2 are the momenta fractions for the two beams, then the two partons carry four momenta $p_1 = x_1 P_A$ and $p_2 = x_2 P_B$. Thus, in the lab frame, the parton system moves with a four momentum $P_{cm} = [(x_1 + x_2)E_A, 0, 0, (x_1 - x_2)p_A]$. Hence, we see that the parton CM frame is boosted with respect to the lab frame with a speed $|\vec{\beta}_{cm}| = \frac{|\vec{p}|}{E} = (x_1 - x_2)/(x_1 + x_2)$ or a rapidity $y_{cm} = \frac{1}{2} \ln \frac{x_1}{x_2}$. If the total hadronic CME is denoted as $\sqrt{S} = 2E_A$, then the partonic CME is $\sqrt{\hat{s}} = \sqrt{x_1 x_2 S}$.
- **Transverse momentum (p_T), azimuthal angle (ϕ) and transverse energy (E_T)** : Since the relative motion between the hadron lab frame and the parton CM frame is along the longitudinal (\vec{z}) direction, it is thus convenient to work with variables which are invariant

under boosts along this direction. The phase space element can be written in terms of the cylindrical coordinates as

$$\frac{d^3\vec{p}}{E} = dp_x dp_y \frac{dp_z}{E} = p_T dp_T d\phi \frac{dp_z}{E}, \quad (2.10)$$

where ϕ is the azimuthal angle about the \vec{z} axis and $p_T = \sqrt{p_x^2 + p_y^2} = p \sin \theta$ is the transverse momentum (θ is the polar angle). Both p_T and ϕ are independent of boosts along the longitudinal axis. Another, variable used frequently in collider analyses is the transverse energy defined as $E_T = \sqrt{m^2 + p_T^2}$, where m is the mass of the particle.

- **Rapidity(y) and pseudorapidity(η)** : The *rapidity*, y , of a particle is defined as

$$y = \frac{1}{2} \ln \frac{E + p_z}{E - p_z} \quad (2.11)$$

This variable represents the level of boost of the parton CM frame with respect to the hadron lab frame. However, when a particle is travelling very fast or when its mass is negligible such that $E \approx |\vec{p}|$, then one defines the quantity pseudorapidity as

$$y \xrightarrow{E \approx |\vec{p}|} \frac{1}{2} \ln \frac{1 + \cos \theta}{1 - \cos \theta} = \ln \cot \frac{\theta}{2} \equiv \eta. \quad (2.12)$$

η varies in the range $-\infty < \eta < \infty$ and has a one-to-one correspondence to the polar angle, θ . Since, both rapidity and pseudorapidity are additive under longitudinal boosts, it can be shown that the rapidity (pseudorapidity) difference between two particles is a frame invariant quantity, *i.e.*, $\Delta y = y'_2 - y'_1 = y_2 - y_1$, where $y_1, y_2 (y'_1, y'_2)$ are the rapidities of two particles in two frames related by a boost in the *longitudinal* direction.

- **Transverse mass (M_T)** : Let us consider the process $W \rightarrow e\nu$ as an example. As we know, neutrinos cannot be directly observed by the detectors and one can only estimate their missing transverse momentum from the imbalance of the observed transverse momentum

$$\vec{p}_T = - \sum \vec{p}_T(\text{observed}) \quad (2.13)$$

Because the neutrinos are almost massless, their missing transverse energy, $\cancel{E}_T \approx |\cancel{p}_T|$. One can not define the invariant mass of the $e\nu$ system (the invariant mass of two particles

a and b is defined as $m_{ab} = (p_a + p_b)^2$ because one does not have the information on p_z . Hence, to overcome this limitation, one defines a transverse mass variable for the $e\nu$ system as

$$m_{e\nu T}^2 = (E_{eT} + E_{\nu T})^2 - (\vec{p}_{eT} + \vec{p}_{\nu T})^2 \approx 2\vec{p}_{eT} \cdot \vec{p}_{\nu T} \approx 2E_{eT}E_{\nu T}(1 - \cos\phi_{e\nu}), \quad (2.14)$$

where $\phi_{e\nu}$ is the opening angle between the electron and the neutrino in the transverse plane. The transverse mass variable is invariant under longitudinal boosts and reaches its maxima $m_{e\nu T}^{max} = m_{e\nu}$ when $p_e = p_\nu$. In general the transverse mass varies in the range

$$0 \leq m_{e\nu T} \leq m_{e\nu} \quad (2.15)$$

However, in reality due to the finite width of W , the transverse mass distribution extends beyond $m_{e\nu} = M_W$. The CDF collaboration measured the mass of W using the transverse mass variable [14] as shown in Fig. 2.5.

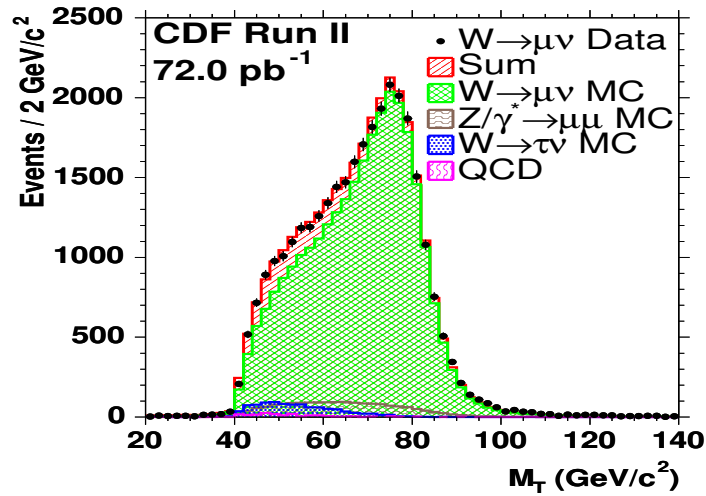


Figure 2.5: Transverse mass distribution for the process $W \rightarrow \mu\nu$ as seen by the CDF collaboration at Tevatron (figure courtesy Ref. [14]).

- **Isolation (ΔR)** : One frequently comes across the kinematic variable, ΔR , which quanti-

defines the separation between two particles in the $\eta - \phi$ plane. It is defined as

$$\Delta R = \sqrt{\Delta\eta^2 + \Delta\phi^2}. \quad (2.16)$$

Another practical motivation for the introduction of ΔR is that it provides a definition for hadronic jets (for a review on jet algorithms, see Ref. [15]) where ΔR defines the cone size of a jet formed by multiple hadrons within a cone-radius of ΔR about the jet axis.

Chapter 3

Model-independent analysis of Higgs couplings from global fits¹

3.1 Motivation

The standard electroweak model (SM) [1, 2] has been validated to a great extent by the recent discovery of the Higgs boson in 2012 by the ATLAS and CMS groups at the Large Hadron Collider (LHC) [3, 4]. Most properties of the newly discovered particle are quite consistent with those of the Higgs boson predicted in the SM. The run I of the LHC has predicted most of the couplings of the Higgs to both gauge bosons and fermions. A closer examination is, and will be, on in the next run which has just began. However, this boson brings along with it numerous theoretical issues, for instance the hierarchy problem. Besides, the experimental observation of dark matter also suggests that SM can not be the most complete theory. For instance, SM predicts the masses of the neutrinos to be zero which is experimentally disfavoured. At least two of the neutrinos have masses. These experimental results make one ponder as to what lies outside the SM. To look for any hints for physics beyond the SM (BSM), both experimentalists

¹This chapter is based on the paper *New Higgs interactions and recent data from the LHC and the Tevatron* by Shankha Banerjee, Satyanarayan Mukhopadhyay and Biswarup Mukhopadhyaya, JHEP **1210**, 062 (2012), [arXiv:1207.3588 [hep-ph]]

and phenomenologists are trying to explore all possible avenues in understanding the nature of the Higgs boson. The belief is that, some new physics may be lurking amongst the measured properties of the Higgs boson. As a start both the ATLAS and CMS collaborations have looked at the spin and parity of the discovered boson and the SM seems to be consistent.

First of all, the SM predicts a CP-even boson with spin 0. Deviation from this nature will be a clear indication for BSM physics. The Landau-Yang theorem [5] forbids a spin-1 particle decaying to two spin 1 particles. As the observed boson is seen to decay to a pair of photons, a spin-1 boson is immediately ruled out. There have also been speculations of this boson being a spin-2 resonance. The spin-parity structure of this boson has been studied in great detail in the $H \rightarrow ZZ^*, Z\gamma^*, \gamma^*\gamma^* \rightarrow 4\ell$, $H \rightarrow WW^* \rightarrow \ell\nu\ell\nu$ and the $H \rightarrow \gamma\gamma$ channels [6] ($\ell = e, \mu$). Some of these analyses have ruled out a large class of spin-2 models at more than 99% CL [6, 7].

Physicists thus tend to concur that both the CMS and ATLAS collaborations have found a spin-zero bosonic resonance of mass 125 - 126 GeV. However, the issue of whether it is exactly the Higgs boson predicted by the SM is still somewhat open. This question can be settled by the close examination of accumulating data over a longer period, thus revealing not only the complete picture of the electroweak symmetry breaking sector but also any secret message of new physics buried within the available results.

Any departure from SM predictions in the observed scalar is ultimately reflected in its interactions with pairs of fermions or weak gauge bosons, and also the loop-induced effective couplings to photon and gluon pairs. However, these interactions are rather intricately twined in the calculation of rates for various final states into which the Higgs can decay. The trace of non-standard physics there can be looked for in two ways— either in the context of specific theories where the different new couplings are all dictated by the model parameters, or in a phenomenological, model-independent analysis of as general a nature as possible. We attempt to add the present investigation in the second direction, to the already growing volume of extant studies in the light of the data piling up [8–16].

We start by assuming that the $SU(2)_L \times U(1)_Y$ gauge invariance holds at the energy scale under scrutiny. Under such circumstances, the aforementioned interactions of the Higgs boson can be different from the SM expectations due to (a) the observed scalar having admixtures with other states, or (b) the presence of additional, gauge invariant effective operators which contribute to the same couplings. In either case, a renormalisation of the SM couplings may take place, and interactions with new Lorentz structure may also appear. Only the former possibility

is addressed in the present chapter.

The modification of the SM couplings of the Higgs is subject to various experimental constraints, the severest of them often coming from electroweak precision observables. Our purpose is to investigate, within such constraints, how much allowance for departure of various interaction strengths from the SM values can be made by the currently observed rates in different final states, as found from a global fit of these strengths based on chi-squared minimisation. The available best fits for the rates in different channels, scaled by the corresponding SM expectations, are our inputs, and we use them to obtain the widest allowed ranges for various modified couplings as well as an invisible decay width, with the hope that this will guide us to the direction where new physics may lie.

We start by assuming that the Higgs (or, to be more precise, the observed boson, to which we refer here as the Higgs) can differ from the SM expectations in all respects— couplings with $T_3 = +1/2$ and $T_3 = -1/2$ fermions (the departures being different in the two cases), couplings with both W - and Z -boson pairs (again with potentially different deviations), and also the effective couplings to photon and gluon pairs, where additional effects over and above the modified fermion and boson couplings are included as possibilities. While the modifications mentioned above can be described in terms of a given framework (such as a chiral Lagrangian), we deliberately take them as completely free and independent parameters, to make our study free of any theoretical bias. Besides, it is also assumed at the beginning that the Higgs can have a finite invisible decay width. We use the CMS [17–22] as well as ATLAS [23–28] results in various channels for both the 2011 (7 TeV) and 2012 (8 TeV) runs. Results from the Tevatron, wherever available, are also used as data points in obtaining the least-square fits [29].

As has been already mentioned, a number of similar investigations have appeared in the literature [8–16]. Though they are all instructive, the present study may be of particular use in the following respects:

- We start by taking *all* of the couplings, tree-level as well as loop-induced, to be unrelated and free parameters. The couplings to up- and down-type quarks, as also those to W - and Z -pairs, are allowed to be different at the same time. Most earlier studies (except, for example, Refs. [8] and [9]) have not allowed uncorrelated variation of HWW and HZZ interactions, albeit in a gauge-invariant fashion; also, some of them set the interactions with up- and down-type quarks to identical value.
- We investigate the effect of an arbitrary phase in the fermion pair couplings, relative to

the W -pair couplings, which is also varied as a free parameter in obtaining the global fits. We have retained this arbitrary phase only in the top coupling (we discuss this in the next section) which alters the interaction term between the top and the W -loops in the $H \rightarrow \gamma\gamma$ decay width.

- We do not restrict ourselves by assuming the anomalous interactions to arise from some underlying scenario like a chiral Lagrangian, which implies concomitant variation of different couplings.
- We take into account the possibility that the effective Hgg and $H\gamma\gamma$ couplings are modified due to effects other than non-standard interactions of the Higgs with W - and fermion pairs. Furthermore, the possibility of loop-induced Higgs decays being modified differently due to both coloured and colourless fermions running in the loops is taken into consideration. We keep the modifications due to these two different effects separate and uncorrelated.
- An invisible decay width for the Higgs is allowed as a free parameter.
- We parametrize all new physics effects at the coupling level (excepting for the invisible width, where we take the width as a free parameter, for the sake of model-independence). This is in contrast to cases where branching ratios of the Higgs into some channels are taken as free parameters, which results in various new physics effects getting entangled, since branching ratios also involve the total decay width of the Higgs, where all (modified) interactions contribute.
- In obtaining the 2σ ranges of allowed values for various couplings, we have not fixed the remaining parameters at their SM values or at their global best fits corresponding to the minimum of the χ^2 function. We have marginalised over the remaining *nuisance* parameters in order to obtain the 2σ allowed ranges. This makes our analysis completely unbiased, from the angle of physics beyond the SM.
- Even in channels where the gluon fusion channel for Higgs production dominates, the vector boson fusion (VBF) and the WH/ZH associated production channels contaminate the rates to varying degrees. Also, the VBF and associated channels have both HWW - and HZZ -induced contributions. These warrant a careful treatment if one is allowing

uncorrelated deviations from SM in the HWW and HZZ interactions. Such issues have been taken into account in our analysis.

- In cases where the best fit values for various rates come with asymmetric error-bars, the asymmetry is retained in the analysis that follows.

In section 3.2, we outline our parametrization of the various new physics effects mentioned above, and discuss the motivations of their origin. The details of input data sets from the LHC and the Tevatron used in our global numerical analysis, and the methodology adopted have been described in section 3.3. We discuss our results of the best-fit values obtained and the allowed confidence intervals for the various parameters in section 3.4. We summarise and conclude in section 3.5.

3.2 New physics effects: parametrization

In this section, we describe the parameters used to encapsulate any likely new physics effect hidden within the data on the Higgs. We also outline the motivations for choosing these parameters, and indicate the ranges over which we let them vary to obtain their favoured locations in the light of observations till date.

Fermion couplings

Classifying all $T_3 = +1/2$ fermions as u , and all $T_3 = -1/2$ fermions as d , we assume

$$\begin{aligned}\mathcal{A}_{H\bar{u}u}^{eff} &= e^{i\delta} \alpha_u \mathcal{A}_{H\bar{u}u}^{eff,SM} \\ \mathcal{A}_{H\bar{d}d}^{eff} &= \alpha_d \mathcal{A}_{H\bar{d}d}^{eff,SM}\end{aligned}\tag{3.1}$$

where $\mathcal{A}_{H\bar{u}u}^{eff}$ ($\mathcal{A}_{H\bar{d}d}^{eff}$) denotes the amplitude for the $H\bar{u}u$ ($H\bar{d}d$) coupling. This parametrization implicitly assumes the couplings of H to all fermions to be proportional to their masses. The assumed difference in interaction strengths to up-and down-type fermions include the possibility of H being part of a scenario containing more than one doublets, including the supersymmetric case. In general, a relative phase between the couplings is assumed. A phase in the $Ht\bar{t}$ effective coupling can arise due to imaginary (absorptive) parts coming from loop diagrams for the transition where some of the intermediate SM states in the loop graphs, being lighter than the

Higgs boson, can go on-shell. For example, a heavy W' like gauge boson having $W'tb$ type couplings can give rise to additional contributions to the $Ht\bar{t}$ effective coupling, via a triangle loop involving two b-quarks, where the b-quarks can go on-shell inside the loop. This would then give rise to an imaginary part in the effective interaction. This phase allows various degrees of interference among fermion loops, and between the fermion and W -boson loops, for example, in the decay $H \rightarrow \gamma\gamma$. As will be seen in the next section, we perform a scan over the phase δ like we do over α_u and α_d . Even in cases where we neglect a non-trivial phase, we allow α_u and α_d to be both positive and negative, in order to account for constructive as well as destructive interferences. Moreover, the phase δ enters seriously into Higgs phenomenology only via the top quark couplings. Therefore, nothing is affected by dropping it for the first two families, in case it is subject to any constraints from flavour physics.

There are essentially no limits on $|\alpha_u|$ and $|\alpha_d|$ from earlier data, except those from perturbativity of the Yukawa couplings. Keeping this in mind, we take the maximum value of $|\alpha_u|$ to be 2 (keeping the top quark Yukawa coupling in mind), while $|\alpha_d|$ is *prima facie* allowed to lie all the way upto 40. However, even before the full analysis is done, we find that the rate for $H \rightarrow \gamma\gamma$ for large $|\alpha_d|$ gets suppressed well below limits admissible by current observations, as the $b\bar{b}$ mode then dominates overwhelmingly. With this in view, we also limit the maximum value of $|\alpha_d|$ to 2 in our final analysis. Since this renders the contribution of all $T_3 = -1/2$ SM fermions to $\Gamma(H \rightarrow \gamma\gamma)$ negligibly small, we also do not miss anything by dropping the phase in α_d . Note that the same consideration prevents us from taking seriously regions of the parameter space, where the b-quark loop contributes substantially to the gluon fusion channel of Higgs production. Thus we do not expect the phase in $Hb\bar{b}$ coupling, too, to affect Higgs production cross-sections.

Gauge boson pair couplings

We parametrize the interactions of the observed scalar to a pair of weak gauge bosons as

$$\begin{aligned}\mathcal{L}_{HWW}^{eff} &= \beta_W \frac{2m_W^2}{v} HW_\mu^+ W^{\mu-} \\ \mathcal{L}_{HZZ}^{eff} &= \beta_Z \frac{m_Z^2}{v} HZ_\mu Z^\mu\end{aligned}\tag{3.2}$$

where the Lorentz structure of the interaction has been tentatively taken to be the same as in the standard model. Such anomalous interactions can arise if, again, the Higgs has admixtures

of other doublets or scalars in some other representations of SU(2), and also via loop effects in specific models.

Clearly, one faces precision electroweak constraints here, in particular, for $\beta_W \neq \beta_Z$, which entails a breakdown of custodial SU(2), and is thus restricted by the T-parameter. Such anomalous couplings can arise, for example, from gauge invariant effective operators, an example being [30]

$$\mathcal{O}_{\Phi,1} = \frac{f_{\Phi,1}}{\Lambda^2} (D_\mu \Phi)^\dagger \Phi \Phi^\dagger (D_\mu \Phi) \quad (3.3)$$

where Φ is a set of SU(2) doublet scalars, out of which H is the lightest mass eigenstate, and Λ is the scale below which the effective operator is defined. This operator in itself gives rise to unequal β_W and β_Z . However, taking this operator alone, precision constraints yield the limits [30, 31]

$$0.991 \lesssim \beta_W \lesssim 1.001 \quad (3.4)$$

$$0.997 \lesssim \beta_Z \lesssim 1.028 \quad (3.5)$$

It is hardly expected to see any appreciable effects of such variation on observable rates, and we do not include the bounds given by Eqns. 3.4, 3.5 in our global fits. However, one can have less constrained couplings if one includes other effective operators which, however, give rise to additional HWW and HZZ interactions involving derivatives. We do not rule out such possibilities, but neglect the effects of derivative couplings for the time being, and vary β_W and β_Z between 0 and 2, in a purely phenomenological way. An analysis including the derivative couplings is presented in the subsequent chapters. We also consider the case where $\beta_W = \beta_Z \equiv \beta$, thereby restoring tree-level custodial invariance. In this case, for a Higgs mass of 125 GeV, electroweak precision constraints restrict β in the range [8]

$$0.84 \leq \beta^2 \leq 1.4 \quad (3.6)$$

Effective gluon-gluon and photon-photon couplings

The gluon fusion channel is the dominant production mode for a Higgs of mass around 125 GeV, and is overwhelmingly driven by the top quark loop. Therefore, a departure of α_u from unity will be reflected in the production cross-section (though the phase δ will be ineffectual).

Similarly, the two-photon amplitude has contributions from both fermion- and W -induced loops. Thus the parameter β_W also dictates the rate for the two-photon final state.

This is, however, not the entire story. Both of the aforementioned loop-induced processes can have modified contributions, beyond the coverage of the α - and β -parameters, if additional states contribute in the loops. The most obvious example is the contribution of Kaluza-Klein towers in theories with extra compact dimensions, where fermions and/or gauge bosons propagate in the bulk. Due to such (and perhaps other) possibilities, it is necessary in a general study to include an additional parameter to properly quantify new physics effects in the gluon fusion channel. For the two-photon amplitude, this parameter can well be different, since new physics can be quite different in the coloured and non-coloured sectors.

With this in view, we parametrize the gluon-gluon-Higgs and Higgs-photon-photon effective lagrangians as follows:

$$\begin{aligned}\mathcal{L}_{gg}^{eff} &= -x_g f(\alpha_u) \frac{\alpha_s}{12\pi v} H G_{\mu\nu}^a G^{a\mu\nu} \\ \mathcal{L}_{\gamma\gamma}^{eff} &= -x_\gamma g(\alpha_u, \alpha_d, \beta_W, \delta) \frac{\alpha_{em}}{8\pi v} H F_{\mu\nu} F^{\mu\nu}\end{aligned}\quad (3.7)$$

where x_g and x_γ encapsulate the overall modification due to new intermediate states in the two cases ². The functions $f(\alpha_u)$ and $g(\alpha_u, \alpha_d, \beta_W, \delta)$ encapsulate the modifications of these couplings due to fermion and W -boson loops. We shall discuss their detailed forms in the next section when we discuss the departures of the Higgs production and decay widths from their SM values in detail. Since there is no restriction till now on x_g and x_γ , we let each of them vary from 0.2 to 3.0. The lower and upper bounds have been set keeping in mind that we do not have too much room for varying them beyond a range, and still being consistent with the data.

Invisible width

Since the earlier analyses of the 2011 data have led to different conclusions about a possible invisible width of the Higgs [10–13], we keep this possibility alive in our analysis. Such an invisible width can occur if, for example, the Higgs serves as a portal to a ‘dark matter’ sector. The exact expression of the width in terms of the coupling to the dark sector will require one to know the nature of the invisible particle(s), for example, whether they are scalars or spin-1/2

²This is just one way of parametrizing the effects of new states. It could be parametrized alternatively adding terms of the form $x_g H G_{\mu\nu}^a G^{a\mu\nu}$ or $x_\gamma H F_{\mu\nu} F^{\mu\nu}$ to the SM Lagrangian. It is straightforward to translate the limits obtained using one convention into those using the other.

objects. In order to be model-independent, we take as a free parameter the *invisible width* Γ_{inv} , which is independent of the nature of the invisible state, and is also not entangled with other new physics effects.

Since there is very little guideline on the range over which Γ_{inv} should be varied in order to obtain the value corresponding to the minimum of chi-squared, we start from ϵ , the invisible branching ratio, and let it vary between 0 and 1. In each case, the invisible width is expressed as

$$\Gamma_{inv} = \frac{\epsilon}{1 - \epsilon} \sum \Gamma_{vis} \quad (3.8)$$

where $\sum \Gamma_{vis}$ is the total decay width into all visible channels.

3.3 Methodology of analysis

3.3.1 Input data

Tables 3.1,3.2,3.3,3.4,3.5 and 3.6 contain the details of all the data points used in our analysis. This includes the combination of 7 TeV (with 5.1 fb^{-1} data) and 8 TeV (with 19.7 fb^{-1} data) results from CMS [3, 17–22] in all channels, namely, $\gamma\gamma$, $ZZ^* \rightarrow 4\ell$, $WW^* \rightarrow \ell\ell\nu\nu$, $\tau^+\tau^-$ and $b\bar{b}$. For the ATLAS experiment [4, 23–28], results for all the aforementioned channels are available as similar 7 + 8 TeV combinations. The integrated luminosities for ATLAS are 4.5 fb^{-1} and 20.3 fb^{-1} for the 7 and 8 TeV runs respectively. We have considered the exclusive signal strengths for the $\gamma\gamma$, $ZZ^* \rightarrow 4\ell$, $WW^* \rightarrow 2\ell 2\nu$ and $\tau\bar{\tau}$ channels in different production modes. However, for the $b\bar{b}$ mode, we have considered the results pertaining to the associated production (VH) modes because the results in the gluon fusion channel are not presented by the experimental collaborations due to excessive QCD backgrounds. For the $b\bar{b}$ channel, the VBF and $t\bar{t}H$ production modes are also being looked at by the experimental collaborations. However, given poor statistics in such channels, we only consider the VH production mode. Furthermore, we have used the Tevatron (combined CDF and DØ) results for WW^* , $\gamma\gamma$, $b\bar{b}$ and $\tau\bar{\tau}$, for an integrated luminosity of up to 10 fb^{-1} [29]. Thus we have thirty two input data points altogether for our global analysis. All the SM production cross-sections and decay widths for the Higgs have been taken from the results reported by the LHC Higgs Cross Section Working Group [32].

Channel	Signal strength (μ)		Production mode					
	<i>ATLAS</i>	<i>CMS</i>	<i>ggF</i>	<i>VBF</i>	<i>WH</i>	<i>ZH</i>	<i>VH</i>	<i>t\bar{t}H</i>
μ_{ggF}	1.32 ± 0.38	$1.12^{+0.37}_{-0.32}$	100%	-	-	-	-	-
μ_{VBF}	0.8 ± 0.7	$1.58^{+0.77}_{-0.68}$	-	100%	-	-	-	-
μ_{WH}	1.0 ± 1.6	-	-	-	100%	-	-	-
μ_{ZH}	$0.1^{+3.7}_{-0.1}$	-	-	-	-	100%	-	-
μ_{VH}	-	$-0.16^{+1.16}_{-0.79}$	-	-	-	-	100%	-
$\mu_{t\bar{t}H}$	$1.3^{+2.6}_{-1.8}$	$2.69^{+2.51}_{-1.81}$	-	-	-	-	-	100%

Table 3.1: Signal strengths of $H \rightarrow \gamma\gamma$ channel as recorded by ATLAS [23, 28] and CMS [17, 22] collaborations after 7+8 TeV run of LHC with $\sim 25 \text{ fb}^{-1}$ of luminosity. Contribution from each production modes are shown in Columns 4-9. $M_H = 125.36$ (124.7) GeV as measured in this channel by ATLAS (CMS).

Channel	Signal strength (μ)		Production mode		
	<i>ATLAS</i>	<i>CMS</i>	<i>ggF</i>	<i>VBF</i>	<i>VH</i>
$\mu_{ggF+bbH+t\bar{t}H}$	$1.66^{+0.52}_{-0.44}$	-	$\sim 100\%$	-	-
$\mu_{ggF+t\bar{t}H}$	-	$0.80^{+0.46}_{-0.36}$	$\sim 100\%$	-	-
μ_{VBF+VH}	$0.26^{+1.64}_{-0.94}$	$1.7^{+2.2}_{-2.1}$	-	$\sim 60\%$	$\sim 40\%$

Table 3.2: Signal strengths of $H \rightarrow ZZ^*$ channel as recorded by ATLAS [24, 28] and CMS [18, 22] collaborations after 7+8 TeV run of LHC with $\sim 25 \text{ fb}^{-1}$ of luminosity. Contribution from each production modes are shown in Columns 4-6. $M_H = 125.36$ (125.6) GeV as measured in this channel by ATLAS (CMS).

Channel	Signal strength (μ)		Production mode		
	<i>ATLAS</i>	<i>CMS</i>	<i>ggF</i>	<i>VBF</i>	<i>WH</i>
μ_{ggF}	$1.02^{+0.29}_{-0.26}$	-	100%	-	-
μ_{VBF}	$1.27^{+0.53}_{-0.45}$	-	-	100%	-
$\mu_{0/1 \text{ jet}}$	-	$0.74^{+0.22}_{-0.20}$	$\sim 97\%$	$\sim 3\%$	-
$\mu_{VBF\text{-tag}}$	-	$0.60^{+0.57}_{-0.46}$	$\sim 18\%$	$\sim 82\%$	-
$\mu_{WH\text{-tag}(3\ell 3\nu)}$	-	$0.56^{+1.27}_{-0.95}$	-	-	$\sim 100\%$

Table 3.3: Signal strengths of $H \rightarrow WW^*$ channel as recorded by ATLAS [25, 28] and CMS [19, 22] collaborations after 7+8 TeV run of LHC with $\sim 25 \text{ fb}^{-1}$ of luminosity. Contribution from each production modes are shown in Columns 4-6. $M_H = 125.36$ (125.6) GeV as measured in this channel by ATLAS (CMS).

In calculating the modifications of various branching ratios of the Higgs, we have used

Channel	Signal strength (μ)		Production mode	
	<i>ATLAS</i>	<i>CMS</i>	<i>WH</i>	<i>ZH</i>
μ_{ZH}	$0.05^{+0.52}_{-0.49}$	0.92 ± 0.62	-	100%
μ_{WH}	$1.11^{+0.65}_{-0.61}$	1.1 ± 0.9	100%	-

Table 3.4: Signal strengths of $H \rightarrow b\bar{b}$ channel as recorded by ATLAS [26, 28] and CMS [20, 22] collaborations after 7+8 TeV run of LHC with $\sim 25 \text{ fb}^{-1}$ of luminosity. Contribution from each production modes are shown in columns 4-5. $M_H = 125 \text{ GeV}$ for both ATLAS and CMS.

Channel	Signal strength (μ)		Production mode		
	<i>ATLAS</i>	<i>CMS</i>	<i>ggF</i>	<i>VBF</i>	<i>VH</i>
μ_{ggF}	$2.0^{+1.47}_{-1.17}$	-	100 %	-	-
μ_{VBF+VH}	$1.24^{+0.58}_{-0.54}$	-	-	$\sim 60\%$	$\sim 40\%$
μ_{0-jet}	-	0.34 ± 1.09	$\sim 96.9\%$	$\sim 1.0\%$	~ 2.1
μ_{1-jet}	-	1.07 ± 0.46	$\sim 75.7\%$	$\sim 14\%$	$\sim 10.3\%$
$\mu_{VBF-tag}$	-	0.94 ± 0.41	$\sim 19.6\%$	$\sim 80.4\%$	-
μ_{VH-tag}	-	-0.33 ± 1.02	-	-	$\sim 100\%$

Table 3.5: Signal strengths of $H \rightarrow \tau^+\tau^-$ channel as recorded by ATLAS [27, 28] and CMS [21, 22] collaborations after 7+8 TeV run of LHC with 25 fb^{-1} of luminosity. Contribution from each production modes are shown in Columns 4-6. $M_H = 125.36 (125) \text{ GeV}$ as measured in this channel by ATLAS (CMS).

Channel	Signal strength (μ)	Production mode		
	<i>Tevatron</i>	<i>ggF</i>	<i>VBF</i>	<i>VH</i>
$\mu_{\gamma\gamma}$	$5.97^{+3.39}_{-3.12}$	$\sim 78\%$	$\sim 5\%$	$\sim 17\%$
μ_{WW^*}	$0.94^{+0.85}_{-0.83}$	$\sim 78\%$	$\sim 5\%$	$\sim 17\%$
$\mu_{b\bar{b}}$	$1.59^{+0.69}_{-0.72}$	-	-	100%
$\mu_{\tau^+\tau^-}$	$1.68^{+2.28}_{-1.68}$	$\sim 78\%$	$\sim 5\%$	$\sim 17\%$

Table 3.6: Signal strengths of $H \rightarrow \gamma\gamma, WW^*, b\bar{b}$ and $\tau^+\tau^-$ channels as recorded by CDF and *D0* collaborations at the Tevatron with $\sim 10 \text{ fb}^{-1}$ of luminosity at $\sqrt{s} = 1.96 \text{ TeV}$ [29]. Contribution from each production modes are shown in Columns 4-6. $M_H = 125 \text{ GeV}$.

$m_t = 173.5 \text{ GeV}$, $m_b = 4.7 \text{ GeV}$, $m_\tau = 1.777 \text{ GeV}$ and $m_W = 80.385 \text{ GeV}$ [33]. The combined best fit value for the Higgs mass (m_H) reported by the CMS and ATLAS collaborations is $125.09 \pm 0.21 \text{ (stat.)} \pm 0.11 \text{ (syst.) GeV}$ [34]. For our present analysis, we have used $m_H = 125 \text{ GeV}$. For the Tevatron analysis also, $m_H = 125 \text{ GeV}$ has been used, following combined CDF

and D0 analysis as reported in Ref. [29].

3.3.2 Methodology

Experimental collaborations have reported various signal strengths, which are defined as $\hat{\mu}_i = \sigma_i^{obs}/\sigma_i^{SM}$, with σ_i as the respective uncertainty. Here, σ_i^{obs} refers to the observed signal cross-section for a particular Higgs mass, while σ_i^{SM} is the signal cross-section for an SM Higgs with the same mass. We calculate the corresponding values of μ_i for various points in the space spanned by the parameters in terms of which we have tried to capture the departure of the Higgs interactions from their SM values, as explained in the previous section. One can express μ_i as

$$\mu_i = R_i^{prod} \times R_i^{decay} / R^{width} \quad (3.9)$$

where R_i^{prod} , R_i^{decay} and R^{width} are the factors modifying the corresponding SM production cross-sections, decay width in a particular channel, and the total decay width of the Higgs respectively. Whenever a particular final state has contributions from various production modes, i , the signal strengths have been combined by weighting with the cross-sections in the i^{th} mode as [12, 35]

$$\mu_{combined} = \sum_i S_i \mu_i, \quad (3.10)$$

where S_i is the contribution to the total cross section for the i^{th} production mode. The values of S_i are tabulated in Tables 3.1–3.6.

The relevant production mechanisms at the LHC and Tevatron for the various channels are listed below:

- For $\gamma\gamma$, $ZZ^* \rightarrow 4\ell$, $WW^* \rightarrow \ell\ell\nu\nu$ and $\tau^+\tau^-$, one has to include all the available production processes as mentioned in Tables 3.1,3.2,3.3,3.4,3.5 and 3.6
- The associated WH and ZH production channels can lead to $b\bar{b}$ final states that can be well separated from backgrounds. The VBF and $t\bar{t}H$ production modes for the $b\bar{b}$ final state has poor statistics [36] and hence are ignored in the present analysis.

In the most general case, the production cross-sections in the gluon fusion (ggF), associated production with a Z (ZH), associated production with W^\pm (WH) and associated production

with $t\bar{t}$ ($t\bar{t}H$) are modified by the factors $x_g^2\alpha_u^2$ (R_{ggF}), β_Z^2 (R_{ZH}), β_W^2 (R_{WH}) and α_u^2 ($R_{t\bar{t}H}$) respectively. In the vector boson fusion (VBF) channel, the corresponding factor is given by

$$R_{VBF} \simeq \frac{3\beta_W^2 + \beta_Z^2}{4} \quad (3.11)$$

The factor R_{VBF} requires some explanation. In order to obtain this, first of all, we have used the fact that the interference of the WW -fusion and the ZZ -fusion diagrams is of the order of 1%, and can therefore be ignored in our calculation. Secondly, the WW -fusion contribution to the total cross-section is roughly 3 times that of the ZZ -fusion contribution. For details on this point we refer the reader to Ref. [37]. We have cross-checked these facts for the LHC energies using the VBF@NNLO code of Bolzoni *et al* [38].

For channels in which special kinematic selection criteria are used, one also needs to include the corresponding efficiency factors (as we will discuss in the next chapter).

Next, we consider the Higgs decay widths in the channels under study. The Higgs decay widths in the ZZ^* , WW^* , $\tau\bar{\tau}$, $b\bar{b}$, $c\bar{c}$ and gg channels get multiplied by $\beta_Z^2, \beta_W^2, \alpha_d^2, \alpha_d^2, \alpha_u^2$ and $x_g^2\alpha_u^2$ respectively. In the loop-induced $\gamma\gamma$ channel, the contribution due to the top quark and W -boson loops (and a small contribution due to the bottom and tau loops) to the Higgs decay width is modified by the factor given by

$$R_{\gamma\gamma} = x_\gamma^2 \frac{|\frac{4}{3}\alpha_u e^{i\delta} A_{1/2}^H(\tau_t) + \frac{1}{3}\alpha_d A_{1/2}^H(\tau_b) + \alpha_d A_{1/2}^H(\tau_\tau) + \beta_W A_1^H(\tau_W)|^2}{|\frac{4}{3}A_{1/2}^H(\tau_t) + \frac{1}{3}A_{1/2}^H(\tau_b) + A_{1/2}^H(\tau_\tau) + A_1^H(\tau_W)|^2} \quad (3.12)$$

The form factors for the spin- $\frac{1}{2}$ and spin-1 particles are respectively given by [37]

$$\begin{aligned} A_{1/2}^H(\tau_i) &= 2[\tau_i + (\tau_i - 1)f(\tau_i)]\tau_i^{-2} \\ A_1^H(\tau_i) &= -[2\tau_i^2 + 3\tau_i + 3(2\tau_i - 1)f(\tau_i)]\tau_i^{-2} \end{aligned} \quad (3.13)$$

Here, the function $f(\tau_i)$, for $\tau_i \leq 1$ is expressed as,

$$f(\tau_i) = (\sin^{-1} \sqrt{\tau_i})^2 \quad (3.14)$$

while, for $\tau_i > 1$, it is given by

$$f(\tau_i) = -\frac{1}{4} \left[\log \frac{1 + \sqrt{1 - \tau_i^{-1}}}{1 - \sqrt{1 - \tau_i^{-1}}} - i\pi \right]^2 \quad (3.15)$$

In the above equations τ_i denotes the ratio $m_H^2/4m_i^2$, with $i = f, W$. The electromagnetic constant in the couplings must be taken at $q^2 = 0$ as both the photons are real.

Here, we must admit that the modification in the $H \rightarrow Z\gamma$ partial decay width has been ignored because for $m_H = 125$ GeV, the branching ratio of $H \rightarrow Z\gamma = 1.54 \times 10^{-3}$. Also because the measured signal strength, $\mu_{Z\gamma}$ is extremely poor as has been seen by both ATLAS and CMS [39], we do not consider this channel in the fits. For completeness, we have kept the SM decay width in constructing our total decay width. In future if this channel is better explored, we will then have to incorporate the full analysis.

With the values of μ_i thus calculated for various points in the parameter space, we first obtain the best fit values for these parameters (up to 7 at a time) corresponding to the global minimum of the function χ^2 , defined as

$$\chi^2 = \sum_i \frac{(\mu_i - \hat{\mu}_i)^2}{\sigma_i^2} \quad (3.16)$$

Note that the experimental collaborations, in some cases, have reported asymmetric error bars on the data. In order to include such error bars in the above definition, we use the following prescription. If $(\mu_i - \hat{\mu}_i) > 0$, we use the positive error bar σ_i^+ , while if $(\mu_i - \hat{\mu}_i) < 0$, we use the negative error bar σ_i^- [40]. Note that, in cases for which we have combined more than one experimental data points to obtain a single input data, we obtained the average signal strength $\bar{\mu}$ and the corresponding uncertainty $\bar{\sigma}$ using the following relations:

$$\begin{aligned} \frac{1}{\bar{\sigma}^2} &= \sum_i \frac{1}{\sigma_i^2} \\ \frac{\bar{\mu}}{\bar{\sigma}^2} &= \sum_i \frac{\hat{\mu}_i}{\sigma_i^2} \end{aligned} \quad (3.17)$$

We have used the above method in combining different contributions to the theoretically calculated μ values, for example, while combining the contributions of $WH \rightarrow l\nu b\bar{b}$, $ZH \rightarrow$

$l^+l^-b\bar{b}$ and $ZH \rightarrow \nu\bar{\nu}b\bar{b}$ to associated Higgs production with gauge bosons and the subsequent decay of the Higgs to a bottom pair [32, 41]. Such combinations were necessitated by the fact that the experimental collaborations have reported a single signal strength value in the $b\bar{b}$ channel.

After obtaining the best-fit values for the parameters by minimizing the χ^2 function, we consider two-dimensional contours for various pairs of them about the global minimum by marginalising over the remaining ones. The contours are drawn for 68.3% and 95.4% confidence intervals. The various values of $\Delta\chi^2$ for the 68.3% and 95.4% confidence intervals as a function of the number of degrees of freedom, are tabulated, for example, in Refs. [42–45].

3.4 Results

We obtain the χ^2 fits in three different cases. In the first case (case A), the phase δ is set to zero, and the seven remaining parameters are varied across the pre-decided ranges, as described in section 2. In the second case (case B), we try to see the effects of the phase, and set $\beta_W = \beta_Z$ in the process. The same exercise is done in the third case, but with the phase set to zero again. The simplification in the last two cases is done because $\beta_W \neq \beta_Z$ amounts to the breaking of custodial SU(2) at the tree-level, and is subject to rather stringent constraints from precision electroweak observables. Though we go beyond these constraints in the first case, assuming the simultaneous existence of more than one gauge-invariant effective interactions at the same time, we desist from such speculative exercise in cases B and C, and keep $\beta_W = \beta_Z$ within the most stringent precision electroweak limits. It should be noted that the phase δ does not affect the loop-induced contribution to the T -parameter, since it cancels in the relevant self-energy diagrams. Table 3.7 contains the best fit values of various parameters in the three cases.

Case	β_W	β_Z	α_u	α_d	x_g	x_γ	ϵ	δ
A	1.00	1.08	1.00	1.00	1.00	0.99	0.00	0*
B	1.00	1.00	1.00	1.00	1.01	0.96	0.00	0.81
C	1.00	1.00	1.02	1.00	1.00	1.06	0.00	0*

Table 3.7: Best-fit values of the various parameters in the three cases considered. In cases A and C, δ has been fixed at 0 (indicated with a '*'). In cases B and C, the relation $\beta_W = \beta_Z$ has been imposed, and their values have been restricted within precision constraints.

The minimum values of χ^2, χ_{min}^2 are 18.5985, 18.5985 and 18.5986 for cases A, B and C

respectively. The value of χ^2 with the parameters set to their SM expectations is 18.6152. Note that, the number of degrees of freedom (for cases A and B) in our fits is 25, since we have 32 input data points, and 7 parameters. However, for case C the number of degrees of freedom is 26, since $\beta_W = \beta_Z$ and $\delta = 0$. We present the 68.3% and 95.4% confidence interval contours for various pairs of parameters about χ_{min}^2 , for cases A and B, in Figures 3.1 and 3.2 respectively. As mentioned before, while drawing these contours, we have marginalised over the remaining parameters. In this connection, we note that the consistency of our methodology has been checked by also performing a two parameter fit of the data (with the parameters pertaining to the overall modifications of the fermion and gauge couplings), and our results in that case agree with those presented in recent literature.

Let us first consider the case with $\delta = 0$ and $\beta_W \neq \beta_Z$. First of all, there is a global tendency in the experimental results reported so far by ATLAS and CMS to be more or less consistent with the SM at the 1σ level. The celebrated $H \rightarrow \gamma\gamma$ excess from the 2012 data is now not there anymore. As is clear from Tables 3.2 and 3.3, there is a slight excess in the central value of $H \rightarrow ZZ^* \rightarrow 4\ell$ for the ggF channel in ATLAS and a little deficit in the $H \rightarrow WW^* \rightarrow 2\ell 2\nu$ for the 0/1-jet tagged category in CMS. These are most probably statistical fluctuations and with improved statistics might become more consistent with the SM. The fermionic channels like $H \rightarrow b\bar{b}$ and $H \rightarrow \tau\bar{\tau}$ still have significant uncertainties. The least-square minimisation inevitably yields a best fit for β_Z higher than that of β_W for case A. Since this causes one to go beyond the most stringent of precision constraints, one has to admit that such a best fit central value favours the simultaneous presence of more than one gauge-invariant anomalous WW/ZZ interactions for the Higgs. It should, of course, be kept in mind that one has to wait for the accumulation of more data before a final verdict can be spelt on this.

As far as the best fit values for the parameters multiplying the fermionic couplings are concerned, we find that both α_u and α_d are overlapping with the SM expectations. However, negative values of the fermionic couplings are still allowed at the 2σ CL as can be seen in Fig. 3.1, which brings out the global picture more clearly than just the best-fit values. To completely rule out such possibilities the $Ht\bar{t}$ coupling needs to be measured very precisely. Recently, the ATLAS and CMS collaborations have proposed several channels, for instance the single top production in association with the Higgs and a light jet is very sensitive to the sign of the top- yukawa coupling [46]. Thus, to be completely general, we varied the fermionic couplings in the range -2.0 to 2.0 . We also note that, from contours involving α_u and α_d in Figure 3.1 and α_u in Figure 3.2, it is clear that values close to zero of these two parameters

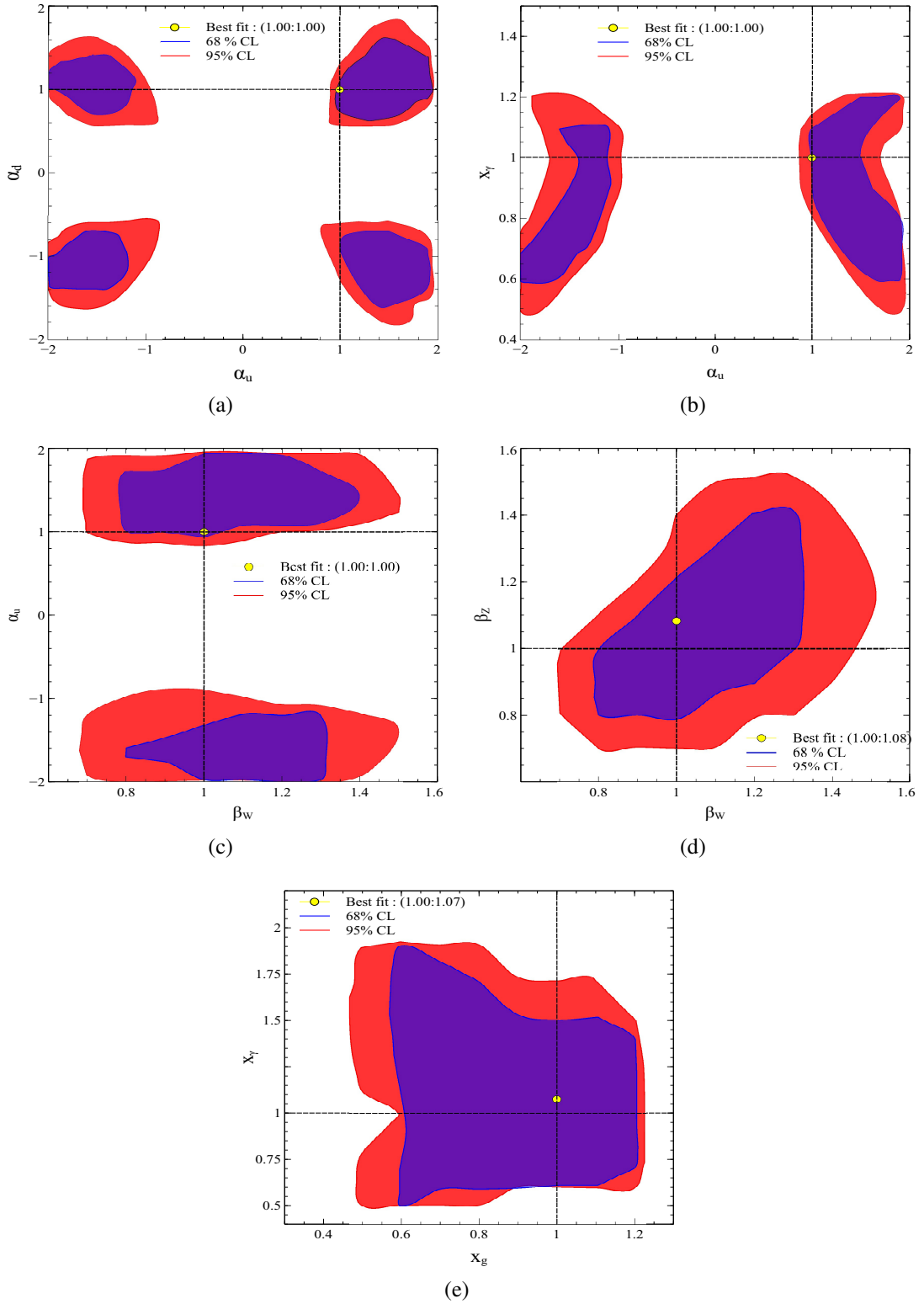


Figure 3.1: Two-dimensional contour plots for 68% (blue) and 95% (red) confidence intervals, for case A, where the rest of the parameters have been marginalised. The best-fit point is also marked separately by a yellow point. In this case $\delta = 0$ and $\beta_w \neq \beta_z$. The intersection of the horizontal and vertical dashed lines denotes the SM values.

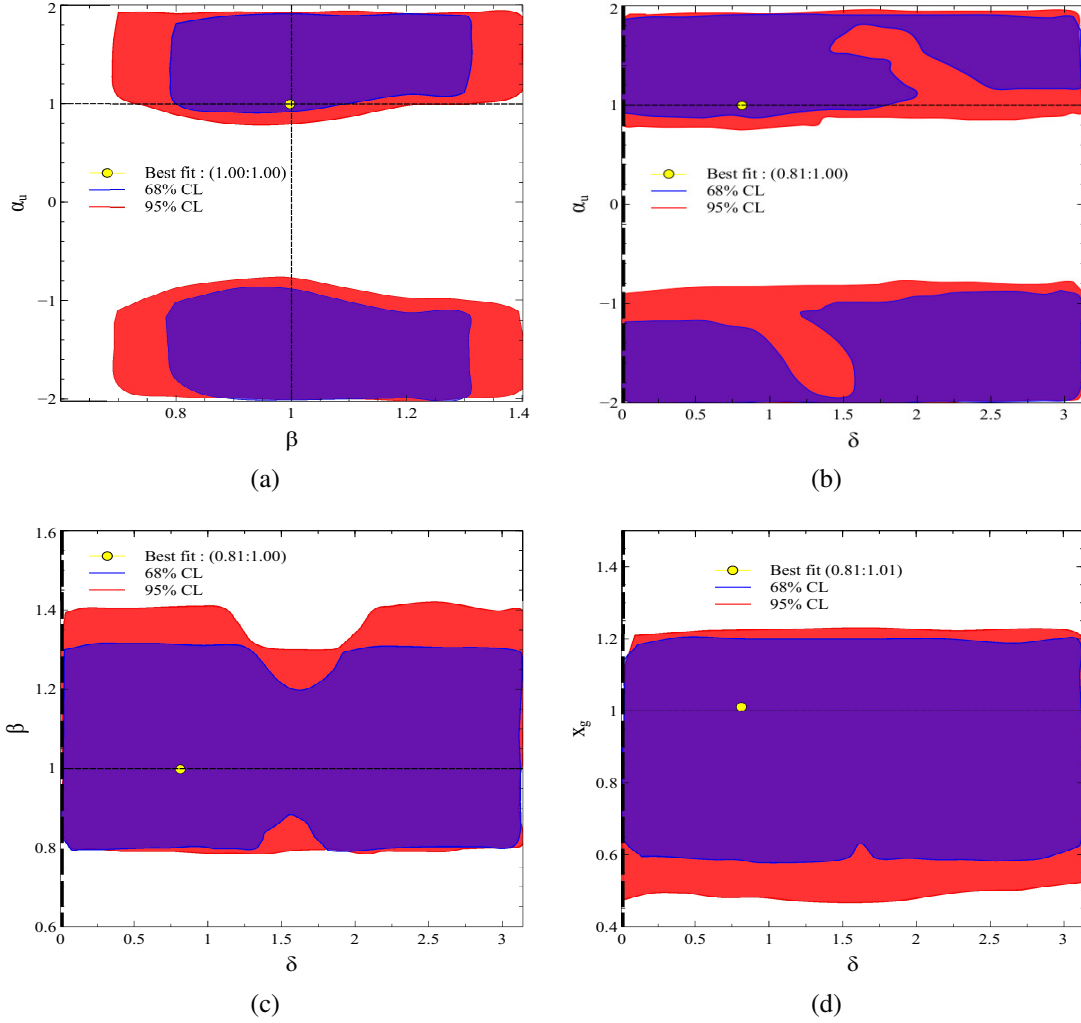


Figure 3.2: Two-dimensional contour plots for 68% (blue) and 95% (red) confidence intervals, for case B, where the rest of the parameters have been marginalised. The best-fit point is also marked separately by a yellow point. In this case has been varied in the range $\{0, \pi\}$, whereas $0.92 \leq \beta \leq 1.18$, with $\beta \equiv \beta_W = \beta_Z$. The intersection of the horizontal and vertical dashed lines denotes the SM values.

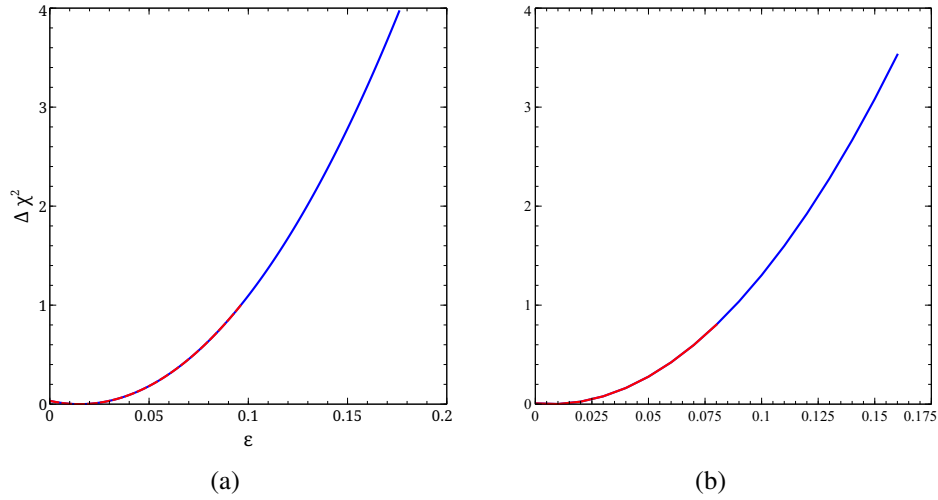


Figure 3.3: Variation of the χ^2 function with the invisible branching fraction of H (ϵ) in cases A (left panel) and B (right panel). In case A, $\delta = 0$ and $\beta_W \neq \beta_Z$, whereas in case B, δ has been varied in the range $\{0, \pi\}$ and $0.92 \leq \beta \leq 1.18$, with $\beta \equiv \beta_W = \beta_Z$.

are clearly disfavoured. This, therefore, should severely constrain fermiophobic models for the Higgs [47].

We also find the best-fit values for x_g and x_γ to be very much consistent with the SM expectations. However, at 2σ , values varying from the SM expectations are also allowed. This suggests that not only is the presence of new coloured or electrically charged states coupling to the Higgs plausible, but that the number of states contributing to the gluon fusion process can be different from those contributing to the $\gamma\gamma$ decay mode. However, if we see the uncertainties in the diphoton mode to shrink considerably in the run II of the LHC, then such possibilities will diminish.

In both cases A and B, we find that the best-fit value of the invisible branching ratio is almost zero. However, at 2σ CL, values of 15-17% are allowed at present if we do not marginalise over the other parameters. Marginalising over the other parameters will yield bigger allowed regions at 2σ CL. So, in order to measure such invisible modes, the Higgs total decay width needs to be measured to a really good precision, which seems to be a very challenging task for the LHC. The most recent searches predicts an indirect upper bound of ~ 17 MeV on the Higgs width [48] from its off-shell production and decay to four leptons or two leptons plus two neutrinos. We demonstrate the variation of the χ^2 function with ϵ , in cases A and B, with rest of the parameters fixed at their best-fit values, in Figure 3.3.

The interesting feature to be noted is that the phase δ is allowed to assume values as large as 0.81 in the best fit. Once this non-trivial phase is there, the 95% confidence level contours of all other anomalous interactions tend to include the SM values. The 2σ allowed regions involving δ include all values from 0 through π , and we have to wait for more data to have a clearer picture about the occurrence of this phase.

3.5 Summary and conclusions

The attempt in this study is to see how much scope of new physics is contained within the data on Higgs search, taking into account not only the results available from 7 and 8 TeV runs of the LHC (at $\sim 25 \text{ fb}^{-1}$ integrated luminosity) but also the full data set of the Tevatron. We have taken a completely model-independent stand, without any bias of correlation between the anomalous Higgs couplings of $T_3 = +1/2$ and $-1/2$ fermions, as well as the W - and Z -couplings. We have, in addition accounted for additional states contributing to the effective interaction of the Higgs with photon and gluon pairs. Since such contributions can come through different sets of states for the gg and $\gamma\gamma$ pairs, we assign a separate uncorrelated parameter for each of these processes. Furthermore, we have taken into account an arbitrary phase in the top-pair coupling with respect to that from a W -pair, which can in principle non-trivially affect the loop-induced decay $H \rightarrow \gamma\gamma$. Last but not the least, a non-vanishing width for the Higgs decaying into invisible final states is kept as a free parameter in our global fit.

Our study takes into account not only the contributions to all final states from the dominant gluon fusion channel but also the VBF and all associated production subprocesses. The present study is nonetheless based on certain simplifying assumptions. These include, for example, the same cut efficiencies taken in final states where more than one production channels are involved, which can be improved as and when the efficiencies are published by the experimental collaborations. However, we have weighted the signal strengths by the cross-sections in the different production modes.

The fits for the minimum of χ^2 over seven-parameter scans, for three sets of combinations, yield the best fit values of each. Subsequently, 68% and 95% confidence level contours for various parameters have been presented, where all other parameters have been marginalised over a wide range.

The most important conclusion we draw is that it is still a bit too early to say that signals

reveal *the standard model Higgs*, since the 2σ contours allow departure from the SM values. A few general trends that show up are

- A fermiophobic Higgs is by and large disfavoured.
- There is in general the hint of a relative sign between the couplings to the up-type fermion and the gauge boson pairs. This is true at the 2σ level.
- A non-trivial phase in the top-quark coupling can have a rather important role. Interestingly, the SM values of the remaining parameters still tend to get included within the 2σ contours once this phase is turned on. In fact the best-fit values of the remaining parameters are consistent with unity.
- It still seems possible to accommodate an invisible decay width of the Higgs at the 2σ confidence level. In particular, it can be between 15-17% at 2σ CL, when marginalisation is not done over the remaining parameters. Marginalising over the other parameters will yield larger bounds for ϵ .

Data from the LHC are currently in a state of flux, and therefore the numerical results on which our analysis is based can change with growing statistics. However, while the trends pointed out by us might change as more accurate data become available, the rather general approach used by us should continue to serve as a template for future analyses.

Chapter 4

Constraining Higher-dimensional HVV operators¹

4.1 Motivation

In the previous chapter, we mainly studied by how much the Higgs couplings, scaled by arbitrary values but with the same Lorentz structure, are allowed to deviate from the corresponding standard model values. We also tried to see what fraction of the Higgs decay width can be due to hitherto unknown particles, also called the “invisible” particles, which can not be detected in the detectors save for their imprint in the form of missing energy. This whole exercise was performed in a model-independent manner and by assuming that the Lorentz structure of the modified Higgs couplings are exactly as those in SM. After the discovery of the new scalar with a mass around 125 GeV at the Large Hadron Collider (LHC) [1, 2], there have been numerous studies attempting to pin down its properties, namely, its spin-parity and its couplings to standard model (SM) particles [3–8]. The bosonic decay modes of this particle have been

¹This chapter is based on the paper *Higher dimensional operators and LHC Higgs data : the role of modified kinematics* by Shankha Banerjee, Satyanarayan Mukhopadhyay and Biswarup Mukhopadhyaya, Phys. Rev. D **89**, 053010 (2014), [arXiv:1308.4860 [hep-ph]]

analyzed with greater precision than the fermionic modes by both the ATLAS and CMS collaborations, since the latter requires much more statistics and possibly the application of new search strategies. The signal-strengths reported in various channels by the experiments are broadly consistent with the SM predictions within about two standard deviations, and a preliminary analysis of spin-parity using the $ZZ^* \rightarrow 4\ell$ channel suggests that a CP-even scalar hypothesis is favoured over other alternatives [9]. Therefore, the accumulating evidence is in favour of an SM-like ($J^{PC} = 0^{++}$) Higgs boson, and we are going to assume so henceforth.

Global fits of the Higgs data have been used by both experimentalists and theorists to derive bounds on possible deviations from the SM. Such deviations in the Higgs couplings can be parametrized either by including a multiplicative (or additive) constant to the SM coupling (as has been demonstrated in the previous chapter), or by including new Lorentz structures not present in the renormalizable SM Lagrangian. In the framework of the SM as an effective field theory valid below a cut-off scale Λ , higher-dimensional operators involving the SM fields and invariant under the SM gauge group can be used to capture possible new physics effects. A complete list of such operators has been written down in Ref. [10], while a minimal basis has been obtained rather recently in Ref. [11]. Such an approach is valid as long as there is no new light degree of freedom coupled to the SM sector below the scale Λ . Null results in LHC searches for new particles provide some motivation for this approach, although the presence of new particles charged under the SM gauge group is still viable even with masses around the electroweak symmetry breaking scale. Henceforth, we assume that there is no such new state, and work with the SM Lagrangian supplemented with dimension-6 operators involving SM gauge bosons and the SM Higgs doublet. As is well-known, although there exists one possible dimension-5 operator, it plays a role only in the generation of neutrino masses.

Electroweak precision measurements constrain the overall strength of the operators involving SM electroweak gauge bosons [12, 13]. However, such constraints come from one-loop contributions of these operators to the self-energy diagrams of the gauge-bosons, parametrized in terms of the so-called oblique corrections [14, 15]. In contrast, the Higgs boson couplings to W, Z or photon pairs can be affected at the tree level itself by a class of such operators, and therefore, it is possible to impose stronger constraints on their co-efficients using the already accumulated LHC Higgs data. This fact has been observed in several studies performing global fits to the Higgs data, and deriving limits on the operator co-efficients [16–19]. However, in most cases, these studies make an important assumption, namely, that the efficiencies of experimental cuts used for various final states are the same as the corresponding efficiencies in

the SM case. To understand where the efficiency of experimental cuts enter the global fits, let us recall that the global fits are performed by comparing the experimentally observed signal strength ($\hat{\mu}_{X\bar{X}}$) in a channel $X\bar{X}$ with the corresponding signal strength predicted by a particular framework beyond the standard model (BSM), $\mu_{X\bar{X}}$, which is defined as

$$\mu_{X\bar{X}} = \frac{\left[\sigma(pp \rightarrow H) \times \text{BR}(H \rightarrow X\bar{X}) \times \epsilon_{X\bar{X}} \right]_{\text{BSM}}}{\left[\sigma(pp \rightarrow H) \times \text{BR}(H \rightarrow X\bar{X}) \times \epsilon_{X\bar{X}} \right]_{\text{SM}}}, \quad (4.1)$$

where, $\epsilon_{X\bar{X}}$ denotes the efficiency of the experimental cuts applied to select a particular final state. Although the assumption that $(\epsilon_{X\bar{X}})_{\text{BSM}} = (\epsilon_{X\bar{X}})_{\text{SM}}$ can be justified if the Higgs couplings only receive a multiplicative modification to the SM one, it is not *a priori* clear whether such an assumption holds after the inclusion of dimension-6 operators. This is because these operators bring in new Lorentz structures to the Higgs-gauge boson couplings, which in turn modify the distributions of kinematic variables on which these cuts are imposed. Some of these distributions have been used in earlier studies, with special emphasis on the spin-parity determination of the newly discovered particle [20–22]. In this chapter, we assume $J^{PC} = 0^{++}$ for this particle, and investigate how additional interaction terms with gauge boson pairs, gauge invariant and of higher dimension, affect Higgs phenomenology. With this in view, we subject the contributions of the additional operators to the cuts used on specific final states. Thus we demonstrate through rigorous Monte Carlo simulations how much the efficiencies can get modified, and to what extent they alter the bounds on the operator co-efficients. We use LHC Higgs search studies in the WW^* and $\gamma\gamma$ channels as examples, implement the cuts used by the ATLAS collaboration in our toy detector simulation, and determine the modified efficiencies for two such dimension-6 operators¹. We also simultaneously allow the modification of the SM coupling to the weak gauge bosons by a multiplicative constant, keeping the custodial $SU(2)$ symmetry intact. It should be mentioned that generically more than one higher-dimensional operator can be present in the effective low-energy theory with different coupling strengths. In that sense, our study with one operator considered at a time is illustrative, and focuses on the important effect of new Lorentz structures in the cut efficiencies. Moreover, the method developed here is of general utility in studying all possible higher-dimensional operators.

This chapter is organized as follows. In section 4.2, we describe the higher dimensional operators considered, the modified Higgs-gauge boson couplings that they lead to, and con-

¹For an analysis of the modified efficiencies in the ZZ^* channel, we refer the readers to Ref. [23].

straints on them from electroweak precision tests. In section 4.3, we describe the set-up of our Monte-Carlo simulation, including its validation against the ATLAS Higgs search studies in the WW^* channel. The modified decay widths, cross-sections and efficiencies are presented in section 4.4, including simple parametrizations of each of these. Section 4.5 is devoted to the re-evaluation of constraints on these operators using a fit to the Higgs data in bosonic channels, while in section 4.6 we study the modified efficiencies in the associated production of Higgs. In section 4.7 we show the modifications to certain kinematic observables in presence of the new operators. We summarize our findings in section 4.8.

4.2 Dimension-6 operators and electroweak precision constraints

In order to see any possible deviations from the SM in the Higgs sector, we will follow the effective field theory (EFT) framework. We assume that the SM is a low-energy effective theory of a more complete perturbation theory valid below a cut-off scale Λ . In the present study, we are concerned mainly with the Higgs sector. The first order corrections to the Higgs sector will come from gauge invariant dimension 6 operators as there is only one dimension-5 operator which contributes to the neutrino masses. The relevant additional Lorentz structures in HVV interactions are necessarily of dimensions higher than four. If they arise as a consequence of integrating out physics at a higher scale, all such operators will have to be invariant under $SU(2)_L \times U(1)_Y$. A general classification of such operators is found in the literature [10–13]. The lowest order CP-conserving operators which are relevant for Higgs phenomenology are

- Operators which contain the Higgs doublet Φ and its derivatives:

$$O_{\Phi,1} = (D_\mu \Phi)^\dagger \Phi \Phi^\dagger (D^\mu \Phi); \quad O_{\Phi,2} = \frac{1}{2} \partial_\mu (\Phi^\dagger \Phi) \partial^\mu (\Phi^\dagger \Phi); \quad O_{\Phi,3} = \frac{1}{3} (\Phi^\dagger \Phi)^3 \quad (4.2)$$

- Those containing the Higgs doublet Φ (or its derivatives) and the bosonic field strengths
:

$$O_{GG} = \Phi^\dagger \Phi G_{\mu\nu}^a G^{a\mu\nu}; \quad O_{BW} = \Phi^\dagger \hat{B}_{\mu\nu} \hat{W}^{\mu\nu} \Phi; \quad O_{WW} = \Phi^\dagger \hat{W}_{\mu\nu} \hat{W}^{\mu\nu} \Phi$$

$$O_W = (D_\mu \Phi)^\dagger \hat{W}^{\mu\nu} (D_\nu \Phi); \quad O_{BB} = \Phi^\dagger \hat{B}_{\mu\nu} \hat{B}^{\mu\nu} \Phi; \quad O_B = (D_\mu \Phi)^\dagger \hat{B}^{\mu\nu} (D_\nu \Phi), \quad (4.3)$$

where $\hat{W}^{\mu\nu} = i \frac{g}{2} \sigma_a W^{a\mu\nu}$ and $\hat{B}^{\mu\nu} = i \frac{g'}{2} B^{\mu\nu}$ and g, g' are respectively the $SU(2)_L$ and $U(1)_Y$ gauge couplings. $W_{\mu\nu}^a = \partial_\mu W_\nu^a - \partial_\nu W_\mu^a - g \epsilon^{abc} W_\mu^b W_\nu^c$, $B_{\mu\nu} = \partial_\mu B_\nu - \partial_\nu B_\mu$ and $G_{\mu\nu}^a = \partial_\mu G_\nu^a - \partial_\nu G_\mu^a - g_s f^{abc} G_\mu^b G_\nu^c$. The Higgs doublet is denoted by Φ and its covariant derivative is given as $D_\mu \Phi = (\partial_\mu + \frac{i}{2} g' B_\mu + i g \frac{\sigma_a}{2} W_\mu^a) \Phi$.

Following are the properties of the aforementioned HDOs:

- $O_{\Phi,1}$: Does not preserve custodial symmetry and is therefore severely constrained by the T -parameter (or equivalently the ρ parameter). It modifies the SM HZZ and HWW couplings by unequal multiplicative factors.
- $O_{\Phi,2}$: Preserves custodial symmetry and modifies the SM HZZ and HWW couplings by multiplicative factors. This operator modifies the Higgs self-interaction as well.
- $O_{\Phi,3}$: Modifies only the Higgs self-interaction.
- O_{GG} : Introduces HGG coupling which is same in structure as the SM effective HGG coupling. Since our discussion in this chapter is limited to the context of VBF and VH production modes and as we will also not consider the gluonic decay mode of the Higgs, we will not discuss this operator any further.
- O_{BW} : Drives the tree-level $Z \leftrightarrow \gamma$ mixing and is therefore highly constrained by the electroweak precision test (EWPT) data [18].
- O_{WW}, O_W, O_{BB}, O_B : Modifies the HVV couplings by introducing new Lorentz structure in the Lagrangian. They are not severely constrained by the EWPT data [16, 17].

The Lagrangian in the presence of the above operators can be generally expressed as :

$$\mathcal{L} \supset \beta \left(\frac{2m_W^2}{v} H W_\mu^+ W^{\mu-} + \frac{m_Z^2}{v} H Z_\mu Z^\mu \right) + \sum_i \frac{f_i}{\Lambda^2} O_i, \quad (4.4)$$

where in addition to the D6 operators, we also allow for the SM-like HWW and HZZ couplings to be scaled by a factor β , keeping in sync with the previous chapter. No operator of the form

\mathcal{O}_{GG} is assumed to exist since we are presently concerned with Higgs interactions with a pair of electroweak vector bosons only. $\mathcal{O}_{\Phi,1}$ is severely constrained by the T-parameter (or equivalently the ρ parameter), as it alters the HZZ and HWW couplings by unequal multiplicative factors. As far as $HVV(V = W, Z)$ interactions are concerned, $\mathcal{O}_{\Phi,2}$ only scales the standard model couplings, without bringing in any new Lorentz structure. It also alters the Higgs self-coupling, something that is the sole consequence of $\mathcal{O}_{\Phi,3}$ as well.

In view of the above, we focus on the four operators \mathcal{O}_{WW} , \mathcal{O}_{BB} , \mathcal{O}_W and \mathcal{O}_B . We do not include the operator $\mathcal{O}_{BW} = \Phi^\dagger \hat{B}_{\mu\nu} \hat{W}^{\mu\nu} \Phi$ in the present analysis, because it mixes the Z and γ fields at the tree level, violates custodial symmetry (by contributing only to the Z -boson mass) and is highly constrained by the S and T -parameters at the tree level [17].

The finally evolving effective interactions that affect the Higgs sector are

$$\begin{aligned} \mathcal{L}_{eff} = & g_{HWW}^{(1)} (W_{\mu\nu}^+ W^{-\mu} \partial^\nu H + h.c.) + g_{HWW}^{(2)} H W_{\mu\nu}^+ W^{-\mu\nu} \\ & + g_{HZZ}^{(1)} Z_{\mu\nu} Z^\mu \partial^\nu H + g_{HZZ}^{(2)} H Z_{\mu\nu} Z^{\mu\nu} \\ & + g_{HZ\gamma}^{(1)} A_{\mu\nu} Z^\mu \partial^\nu H + g_{HZ\gamma}^{(2)} H A_{\mu\nu} Z^{\mu\nu} + g_{H\gamma\gamma} H A_{\mu\nu} A^{\mu\nu}, \end{aligned} \quad (4.5)$$

where

$$\begin{aligned} g_{HWW}^{(1)} &= \left(\frac{gM_W}{\Lambda^2} \right) \frac{f_W}{2}; & g_{HWW}^{(2)} &= - \left(\frac{gM_W}{\Lambda^2} \right) f_{WW} \\ g_{HZZ}^{(1)} &= \left(\frac{gM_W}{\Lambda^2} \right) \frac{c^2 f_W + s^2 f_B}{2c^2}; & g_{HZZ}^{(2)} &= - \left(\frac{gM_W}{\Lambda^2} \right) \frac{s^4 f_{BB} + c^4 f_{WW}}{2c^2} \\ g_{HZ\gamma}^{(1)} &= \left(\frac{gM_W}{\Lambda^2} \right) \frac{s(f_W - f_B)}{2c}; & g_{HZ\gamma}^{(2)} &= \left(\frac{gM_W}{\Lambda^2} \right) \frac{s(s^2 f_{BB} - c^2 f_{WW})}{c} \\ g_{H\gamma\gamma} &= - \left(\frac{gM_W}{\Lambda^2} \right) \frac{s^2(f_{BB} + f_{WW})}{2} \end{aligned} \quad (4.6)$$

with $s(c)$ being the sine (cosine) of the Weinberg angle. Besides, the operators \mathcal{O}_W , \mathcal{O}_B and \mathcal{O}_{WWV} also contribute to the anomalous triple gauge boson interactions which can be summarised as

$$\begin{aligned} \mathcal{L}_{WWV} = & - i g_{WWV} \left\{ g_1^V (W_{\mu\nu}^+ W^{-\mu} V^\nu - W_\mu^+ V_\nu W^{-\mu\nu}) + \kappa_V W_\mu^+ W_\nu^- V^{\mu\nu} + \frac{\lambda_V}{M_W^2} W_{\mu\nu}^+ W^{-\nu\rho} V_\rho^\mu \right\}, \end{aligned} \quad (4.7)$$

where $g_{WW\gamma} = g s$, $g_{WWZ} = g c$, $\kappa_V = 1 + \Delta\kappa_V$ and $g_1^Z = 1 + \Delta g_1^Z$ with

$$\begin{aligned}\Delta\kappa_\gamma &= \frac{M_W^2}{2\Lambda^2} (f_W + f_B); & \lambda_\gamma = \lambda_Z &= \frac{3g^2 M_W^2}{2\Lambda^2} f_{WWW} \\ \Delta g_1^Z &= \frac{M_W^2}{2c^2 \Lambda^2} f_W; & \Delta\kappa_Z &= \frac{M_W^2}{2c^2 \Lambda^2} (c^2 f_W - s^2 f_B)\end{aligned}\quad (4.8)$$

The already existing limits on the various operators discussed above operators are found in numerous references [16, 17, 19]. Even within their current limits, these operators are shown to modify the efficiencies of the various experimental cuts for certain final states at the LHC [23]. The question we address in the rest of this chapter is : are the modified efficiencies significant and can they alter the results of global fits of the parameters to data ? How do we parametrize such efficiencies in terms of the operator coefficients ?

To illustrate the modification of experimental cut-efficiencies on including new Lorentz structures in Higgs-gauge boson interactions (henceforth called HVV interactions) we take O_{WW} and O_{BB} as examples.

As discussed before, we include the possibility of having the HWW and HZZ couplings modified by the same factor β , assuming custodial invariance. Since generically, in presence of an arbitrary number of extra scalar singlets or doublets, $\beta \leq 1$ [24], we scan the range $0 < \beta \leq 1$ in our analysis. One of the goals of this study is to determine to what extent β can be different from its SM value of 1, while including new dimension-6 operators. Taking these two modifications into account, the Lagrangian in the Higgs sector becomes

$$\mathcal{L} = \mathcal{L}_{SM}(\beta) + \frac{f_{WW}}{\Lambda^2} O_{WW} + \frac{f_{BB}}{\Lambda^2} O_{BB}, \quad (4.9)$$

where, the operators O_{WW} and O_{BB} are given by equation 4.3. The Higgs couplings in \mathcal{L}_{SM} to fermions and gluons are not modified.

The interaction terms involving the derivatives of the gauge fields bring in momentum dependent vertices, which are responsible for the modified kinematics in Higgs boson production via weak-boson fusion and associated production with a W or a Z , as well as the decay of the Higgs particle to electroweak gauge boson final states. The kinematics is affected most when the new interactions appear in both the production and decay processes, an example of which we shall discuss in sections 4.3 and 4.4. We should remark here that in $g_{H\gamma\gamma}$, only the new tree-level terms generated due to O_{WW} and O_{BB} have been considered. There will be addi-

tional contributions coming from the W boson loop (apart from the SM contribution modified by the inclusion of β , which we take into account), since now the HWW coupling also involves momentum-dependent terms. However, on naive power-counting in the number of loops and derivatives, these contributions are sub-leading, and the new divergences arising from this loop diagram will be cancelled by the next higher-order terms in the derivative expansion². With the current level of precision in the data, such terms can be safely neglected. Finally, though we have noted the new contribution to the $HZ\gamma$ vertex for completeness, there is no data in this channel so far, and therefore, the effect of the modification to this channel is sub-dominant.

The operators O_{WW} and O_{BB} contribute to the so-called Peskin-Takeuchi STU parameters [14, 15], and are therefore constrained by electroweak precision data [12, 13]. Following Ref. [13], the bounds at 95% C.L., taking one operator at a time, are given by

$$\begin{aligned} -24 \text{ TeV}^{-2} &< \frac{f_{WW}}{\Lambda^2} < 14 \text{ TeV}^{-2} \\ -79 \text{ TeV}^{-2} &< \frac{f_{BB}}{\Lambda^2} < 47 \text{ TeV}^{-2}. \end{aligned} \tag{4.10}$$

These bounds can change once we include the factor β . However, as we shall see, the Higgs data puts much stronger constraints on these two operators compared to the precision data, and therefore, we do not consider modifications to the precision constraints in this study.

We note in passing that since the inclusion of the higher-dimensional operators in equation 4.4 modifies the HWW and HZZ vertices from their corresponding SM values, this will spoil the unitarity of $V_L V_L \rightarrow V_L V_L$ ($V = W, Z$) scattering amplitudes at high energies. For the values of operator coefficients allowed by the current Higgs data, the violation of unitarity appears at energies of a few TeV, with the exact value depending upon the specific choice of operators [25]. Since the higher-dimensional operators themselves arise from integrating out heavy fields of mass $\mathcal{O}(\Lambda)$ (for weakly coupled ultra-violet completions), one expects in general that the presence of these new degrees of freedom in the UV completion will eventually restore the unitarity of the full theory at high energies.

²We thank Adam Falkowski for clarifying this point.

Cut	ATLAS efficiency	Our MC efficiency
$N_{b-jet} = 0$	0.68-0.76 (0.72)	0.74
$p_T^{tot} < 45$	0.81-0.93 (0.87)	0.88
$Z \rightarrow \tau\tau$ veto	0.86-1.00 (0.92)	0.95
$ \Delta y_{jj} > 2.8$	0.45-0.51 (0.48)	0.50
$m_{jj} > 500$	0.61-0.64 (0.62)	0.53
No jets in y gap	0.82-0.86 (0.84)	0.81
Both l in y gap	0.94-1.00 (0.97)	0.95
$m_{ll} < 60$	0.87-0.93 (0.90)	0.95
$ \Delta\phi_{ll} < 1.8$	0.89-0.96 (0.93)	0.92

Table 4.1: Comparison of the efficiencies of experimental cuts on the signal cross-section in the $H \rightarrow WW^* \rightarrow \ell^+ \nu \ell^- \bar{\nu}$ channel, for the $N_{jet} \geq 2$ category, demanding different flavour leptons ($e^+ \mu^- + \mu^+ e^-$) in the final state. The signal cross-section here refers to the sum of VBF and VH processes. The ATLAS numbers have been taken from Ref. [26], for which we show the 1σ range (the central value is written within brackets).

4.3 Simulation framework and validation using

$H \rightarrow WW^* + \geq 2j$ data

As noted in the previous section, we expect in general significant modifications to the kinematics in processes where the new Lorentz structures appear both in the production and decay vertices. An example of such a process is the production of Higgs boson via VBF and its subsequent decay to WW^* . The ATLAS collaboration has presented a detailed analysis of such a scenario in the $WW^* \rightarrow \ell^+ \nu \ell^- \bar{\nu}$ channel ($\ell = \{e, \mu\}$) in Ref. [26] using the 8 TeV, 20 fb^{-1} data. The response of SM-type interactions to all the individual cuts can be readily checked from this analysis, which thus provides a much needed calibration for the simulation with additional operators. Therefore, we use this channel to set-up and validate our Monte Carlo as well as our detector simulation code.

We have used `FeynRules` [27] to extract the Feynman rules from the Lagrangian in equation 4.4, `MadGraph-5` [28] to generate the parton level events, `Pythia-6` [29] for parton shower and hadronization, and our own detector simulation code for analyzing the hadron-level events. Jet formation and underlying events have been simulated within the `Pythia` framework.

In the study of Higgs boson decaying to WW^* , followed by the semi-leptonic decay of the W 's, the ATLAS collaboration has considered three categories, namely, the production of Higgs in association with 0, 1, and ≥ 2 jets. In this part of the study, we consider only the

Cut	ATLAS efficiency	Our MC efficiency
$N_{b-jet} = 0$	0.69-0.77 (0.73)	0.73
$p_T^{tot} < 45$	0.84-0.95 (0.89)	0.87
$ \Delta y_{jj} > 2.8$	0.45-0.50 (0.48)	0.50
$m_{jj} > 500$	0.65-0.71 (0.68)	0.57
No jets in y gap	0.82-0.89 (0.85)	0.81
Both l in y gap	0.92-1.00 (0.96)	0.93
$m_{ll} < 60$	0.85-0.93 (0.89)	0.94
$ \Delta\phi_{ll} < 1.8$	0.88-0.97 (0.92)	0.90

Table 4.2: Same as table 4.1, for same-flavour leptons in the final state ($e^+e^- + \mu^+\mu^-$).

≥ 2 -jet category. According to Ref. [26], vector-boson fusion (VBF) and associated production with W or Z (called VH) are considered as signals in this category. For the WW^* final state, the VBF channel is picked out in the ATLAS analysis, by requiring a high invariant mass for the two leading jets in the forward region. The gluon-fusion production of Higgs is considered as a background. For a detailed description of the experimental cuts used, we refer the reader to Ref. [26]. To validate our Monte Carlo (MC) simulation, in tables 4.1 and 4.2, we compare the efficiencies of each of the experimental cuts obtained by our MC in the SM case, with the numbers reported by ATLAS, in the same and opposite flavour dilepton sub-categories respectively. As we can see from this comparison, our simulations agree with the ATLAS simulation to within 5% for all cuts except the one on m_{jj} , for which the difference is $\sim 15\%$. Our simulation shows a lower efficiency for this cut compared to ATLAS, and a possible reason for this is our inadequate modelling of detector effects for jets. Since the purpose of this part of the study is the overall validation of our MC, and in the subsequent sections we concentrate on the modification of efficiencies after including the dimension-6 operators within our own MC set-up, this difference is not expected to alter our main conclusions.

4.4 Modified efficiencies and signal strengths

After the validation of our MC simulation framework in the previous section, we are now in a position to determine the modified cut-efficiencies ($(\epsilon_{X\bar{X}})_{\text{BSM}}$ in equation 4.1) and signal strengths $\mu_{X\bar{X}}$ using the Lagrangian in equation 4.9. We first do so in the WW^* channel for the ≥ 2 -jet category considered in section 4.3, by including only the operator \mathcal{O}_{WW} , where we expect the maximum modification. The efficiency then is a function of the parameters β and

f_{WW} , and is given by

$$\epsilon_{WW^*+\geq 2\text{-jets}}(\beta, f_{WW}) = \frac{[\sigma(pp \rightarrow H)_{\text{VBF+VH}} \times \text{BR}(H \rightarrow WW^*)]_{\text{After Cuts}}}{[\sigma(pp \rightarrow H)_{\text{VBF+VH}} \times \text{BR}(H \rightarrow WW^*)]_{\text{Before Cuts}}}. \quad (4.11)$$

The theoretically calculated efficiencies are assumed here to be independent of radiative corrections. We evaluate the cross-sections before and after cuts by scanning over the parameters β and f_{WW} , and since they are found to be smooth functions of these parameters even after detector level simulations, we can parametrize them by simple polynomial functions of β and f_{WW} . The Higgs boson partial decay widths in the WW^* , ZZ^* , $\gamma\gamma$ and $Z\gamma$ channels are also functions of these two variables, while in the rest of the channels the partial widths are the same as in the SM. Since higher-order corrections are small in the aforementioned bosonic channels [30], we compute them at tree level, while for all other channels we have used the NNLO predictions from Ref. [31] for a Higgs mass of 125 GeV. The tree-level partial widths (in GeV) in these channels are rather accurately parametrized by the following expressions :

$$\begin{aligned} \Gamma_{H \rightarrow WW^*} &= 8.61 \times 10^{-4} \beta^2 + 8.51 \times 10^{-6} \beta f_{WW} + 2.95 \times 10^{-8} f_{WW}^2 \\ \Gamma_{H \rightarrow ZZ^*} &= 9.28 \times 10^{-5} \beta^2 + 4.77 \times 10^{-7} \beta f_{WW} + 1.00 \times 10^{-9} f_{WW}^2 \\ \Gamma_{H \rightarrow \gamma\gamma} &= 8.59 \times 10^{-7} - 8.04 \times 10^{-6} \beta - 4.36 \times 10^{-6} f_{WW} \\ &\quad + 1.77 \times 10^{-5} \beta^2 + 1.98 \times 10^{-5} \beta f_{WW} + 5.68 \times 10^{-6} f_{WW}^2 \\ \Gamma_{H \rightarrow Z\gamma} &= 3.75 \times 10^{-8} - 7.91 \times 10^{-7} \beta - 5.65 \times 10^{-7} f_{WW} \\ &\quad + 7.12 \times 10^{-6} \beta^2 + 1.06 \times 10^{-5} \beta f_{WW} + 3.82 \times 10^{-6} f_{WW}^2 \end{aligned} \quad (4.12)$$

For the above formulae and all subsequent ones involving f_{WW} , we have used a reference scale of $\Lambda = 1$ TeV, and for a different choice of the cut-off, the coefficients should be re-scaled according to the power of f_{WW} involved. Adding all the contributions, the total Higgs boson width becomes

$$\begin{aligned} \Gamma_{\text{tot}} &= [3.07 - 7.82 \times 10^{-3} \beta - 4.37 \times 10^{-3} f_{WW} \\ &\quad + 0.97 \beta^2 + 3.67 \times 10^{-2} \beta f_{WW} + 8.76 \times 10^{-3} f_{WW}^2] \times 10^{-3} \text{GeV}. \end{aligned} \quad (4.13)$$

Similarly, the tree-level total cross-section for the VBF and VH processes at 8 TeV LHC, before the application of selection cuts, can be expressed as follows

$$\sigma_{pp \rightarrow H+2\text{-jets}}(\text{VBF} + \text{VH}) = (2.0432\beta^2 - 0.0330\beta f_{WW} + 0.0030f_{WW}^2) \text{ pb}. \quad (4.14)$$

By performing a scan over the (β, f_{WW}) parameter space, we compute the combined efficiency (defined in equation 4.11) of the basic trigger level cuts on jets and leptons as well as the subsequent ATLAS cuts listed in tables 4.1 and 4.2, and it is well-fit by the following function

$$\epsilon_{WW^*+\geq 2\text{-jets}} = \frac{50.98\beta^4 + 121.76\beta^3 f_{WW} + 22.85\beta^2 f_{WW}^2 + 0.15\beta f_{WW}^3 + 0.01f_{WW}^4}{1601.43\beta^4 + 3796.63\beta^3 f_{WW} + 666.79\beta^2 f_{WW}^2 - 1.98\beta f_{WW}^3 + 0.73f_{WW}^4}. \quad (4.15)$$

In figure 4.1 we show the variation of $\epsilon_{WW^*+\geq 2\text{-jets}}$ as a function of f_{WW} for different values of β . The red (solid), green (dashed) and black (dot-dashed) curves correspond to $\beta = 1, 0.5$ and 0.1 respectively. For $f_{WW} = 0$, we recover the SM efficiency ($\epsilon_{\text{SM}} \simeq 0.032$) for all values of β . This fact confirms our expectation that only the introduction of new Lorentz structures changes the efficiencies, and a scaling of the SM coupling alone by the factor β does not. However, as we can see from this figure, although the overall features of the three curves are similar, for different values of β , the change in slopes are markedly different. Within the range of f_{WW} shown in this figure, for $\beta = 0.5$, the efficiency can reduce from its SM value by up to a factor of 2.5 or more, while for $\beta = 0.1$, it can drop by up to a factor of 3.

Combining equations 4.11 –4.15, we can now evaluate the signal strength μ for the $H \rightarrow WW^*$ mode in the ≥ 2 -jets category, for any value of β and f_{WW} . We emphasise that this calculation of the signal strength takes into account all the effects of the experimental cuts, and the resulting modification of their efficiencies compared to the SM case. This is one of our main results. In figure 4.2 we show the percentage difference of ϵ_{BSM} and ϵ_{SM} in this channel in the $\beta - f_{WW}$ plane. The ranges of the parameters have been restricted to a region consistent at 95% C.L., with the signal strength measured in this channel by ATLAS ($\hat{\mu} = 1.27^{+0.53}_{-0.45}$) [26]. For comparison, we also show the allowed region at 95% C.L. (grey shaded region to the right of the dashed curve), with the assumption $\epsilon_{\text{BSM}} = \epsilon_{\text{SM}}$. It is clear that taking the efficiency modification into account significantly changes the parameter space allowed by the measurement in this channel. As we can also see from this figure, if this channel is considered on its own, the allowed region includes parameter points where the change in efficiency can be as large as

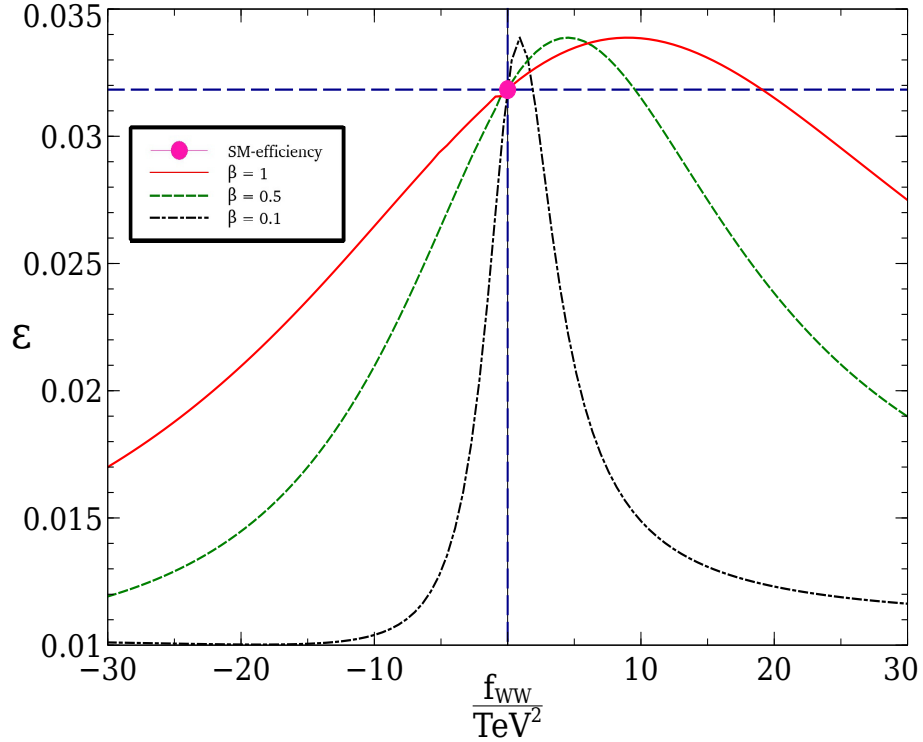


Figure 4.1: The combined efficiency of all ATLAS cuts (ϵ) as a function of f_{WW} for different values of β , in the $H \rightarrow WW^* \rightarrow \ell^+ \nu \ell^- \bar{\nu}$ channel (≥ 2 -jets category) at 8 TeV LHC.

60%. Therefore, in a completely rigorous global analysis of the data, this modification should be taken into account.

4.5 Constraints using LHC Higgs data

In the previous section, we have seen that the operator \mathcal{O}_{WW} significantly modifies the final state kinematics in the $H + 2$ -jets channel (with $H \rightarrow WW^*$) and that a large region in the $\beta - f_{WW}$ parameter space is allowed by the current ATLAS measurement in this particular final state. However, the signal strengths in other bosonic channels are modified by \mathcal{O}_{WW} as well. In this section, we therefore study the modifications to the inclusive $H \rightarrow WW^*$, $H \rightarrow ZZ^*$ and $H \rightarrow \gamma\gamma$ channels in presence of non-zero β and f_{WW} , and determine the most stringent possible constraints on these parameters. Before performing a global analysis with all the data

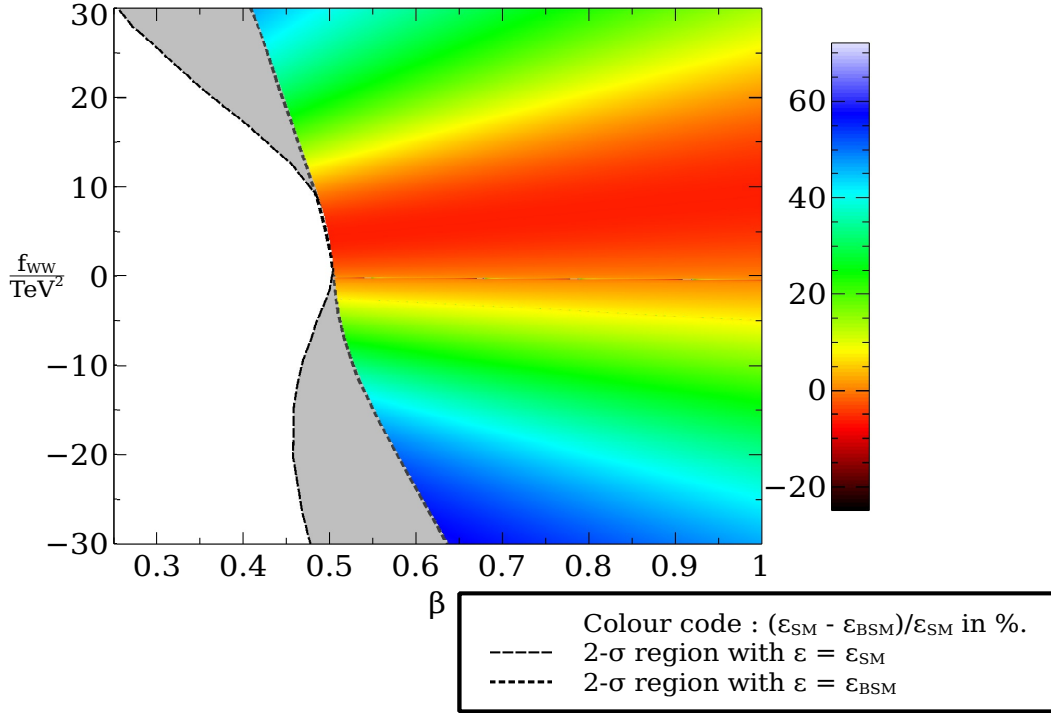


Figure 4.2: Percentage modification of the combined efficiency of all cuts compared to the SM case, in the $H \rightarrow WW^* \rightarrow \ell^+ \nu \ell^- \bar{\nu}$ channel for the ≥ 2 -jets category at 8 TeV LHC. Only the region allowed at 95% C.L. after imposing the ATLAS signal-strength constraint in this channel is shown. For comparison, we also show the allowed region at 95% C.L. (grey shaded region to the right of the dashed curve), with the assumption $\epsilon_{BSM} = \epsilon_{SM}$.

taken together, we first analyze the constraints coming from each channel separately, in order to acquire a qualitative understanding. The signal strengths measured by the ATLAS and CMS collaborations, and a combination of the two experiments (assuming they are statistically independent) are shown in table 4.3. For the $H \rightarrow WW^* + 2$ -jets channel, only the ATLAS result is available at present.

A measurement of the inclusive cross-section at 8 TeV LHC in the WW^* channel has also been reported by ATLAS, after unfolding all detector effects, and it is found to be (for $m_H = 125$ GeV) [26]

$$\sigma(pp \rightarrow H) \times \text{BR}(H \rightarrow WW^*) = 5.11_{-1.15}^{+1.22} \text{ pb}, \quad (4.16)$$

Channel	ATLAS	CMS	Combined
$H \rightarrow \gamma\gamma$	1.17 ± 0.27	1.12 ± 0.24	1.14 ± 0.18
$H \rightarrow WW^*$	$1.09^{+0.23}_{-0.21}$	0.83 ± 0.21	0.95 ± 0.15
$H \rightarrow ZZ^*$	$1.44^{+0.40}_{-0.33}$	1.00 ± 0.29	1.17 ± 0.23
$H \rightarrow WW^* + 2\text{-jets}$	$1.27^{+0.53}_{-0.45}$	NA	NA

Table 4.3: Signal strengths measured by the ATLAS and CMS collaborations, and a combination of the two experiments (assuming they are statistically independent) for the bosonic final states. For the $H \rightarrow WW^* + 2\text{-jets}$ channel, only the ATLAS result is available at present.

which is slightly more than the expected SM cross-section (4.8 ± 0.7 pb), but consistent with it within the uncertainties. We find that this measurement of the inclusive cross-section puts a severe constraint in the $\beta - f_{WW}$ parameter space, and the 2σ allowed region after imposing this requirement is shown in figure 4.3. In the allowed region, to the right of the red (dashed) curve, f_{WW}/Λ^2 can be in the range $[-18 : 21]$ TeV^{-2} , while β is restricted to the range $[0.75 : 1.0]$. As we can see from equation 4.12, the relative magnitudes of the β^2 , βf_{WW} and f_{WW}^2 terms are similar for both $\Gamma_{H \rightarrow WW^*}$ and $\Gamma_{H \rightarrow ZZ^*}$. Therefore, their deviations from the SM will restrict β and f_{WW} in a similar range as well, especially since the signal strength measurements in both these channels have similar errors at the moment. Hence, we do not show the effect of the ZZ^* channel separately, although it is included in our global fit to the data in bosonic channels.

As seen in equation 4.5, O_{WW} also affects the $H\gamma\gamma$ coupling, and therefore, the inclusive signal-strength measured in this channel. Since gluon fusion is the dominant production mechanism for this mode, and we do not find significant deviations in the kinematics if the momentum-dependent couplings appear only in the decay vertices, an appreciable change in the cut-efficiency factor is not expected for this channel, and we do not include a modified ϵ_{BSM} . In figure 4.3, along with the inclusive total cross-section constraint in the WW^* channel discussed above, we show the 2σ region, allowed by the combined signal strength measurement by ATLAS and CMS, $\hat{\mu}_{\gamma\gamma} = 1.14 \pm 0.18$. Only the two blue-shaded regions are allowed by the current data, restricting the values of f_{WW} to two narrow bands. For example, for $\beta = 1$ the allowed values of $f_{WW}/(1 \text{ TeV}^2)$ are in the two sub-regions $[-3.05, -2.46]$ and $[-0.25, 0.35]$. It is interesting to note that the intermediate region $-2.46 < f_{WW}/(1 \text{ TeV}^2) < -0.25$ is not allowed by the 2σ constraint. This is because, from equation 4.12, we can see that $\Gamma_{H \rightarrow \gamma\gamma}$ has a minimum at $f = -1.36$ for $\beta = 1$. Therefore, in this intermediate region around the minimum, the signal strength becomes lower than the 2σ allowed lowest value. Similarly, for $\beta = 0.1$, the allowed ranges for $f_{WW}/(1 \text{ TeV}^2)$ are $[-1.39, -0.85]$ and $[1.24, 1.80]$, and the minimum of $\Gamma_{H \rightarrow \gamma\gamma}$ is at

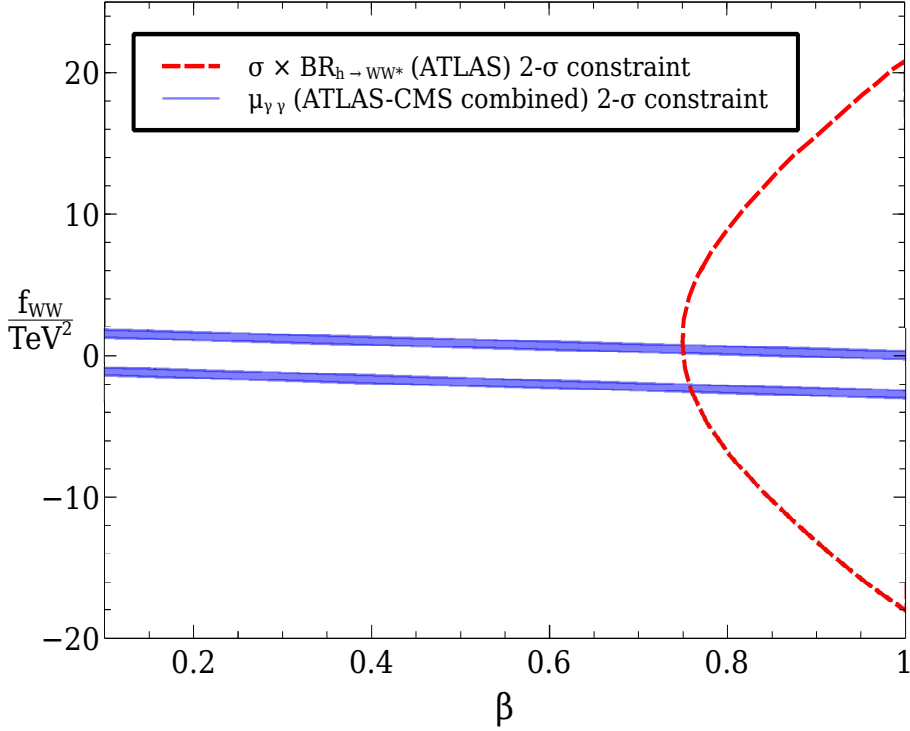


Figure 4.3: 2σ allowed regions in the $\beta - f_{WW}$ parameter space, after imposing the inclusive $\sigma(pp \rightarrow H) \times \text{BR}(H \rightarrow WW^*)$ cross-section measurement by ATLAS (to the right of the red dashed curve), and the combined ATLAS and CMS signal strength constraint in the $\gamma\gamma$ channel (blue-shaded bands).

$f = 0.21$. Since the operator \mathcal{O}_{BB} modifies the $H\gamma\gamma$ coupling in exactly the same form as \mathcal{O}_{WW} (see equation 4.6), these constraints on f_{WW} from the $\gamma\gamma$ data also apply to f_{BB} . The modified cut efficiencies in the VH channel in presence of \mathcal{O}_{BB} are studied in section 4.6.

As we can see from equation 4.12, for the $\gamma\gamma$ partial width, the contribution from \mathcal{O}_{WW} is comparable in magnitude to the loop-induced W-boson contribution, and therefore, values of β as small as 0.1 with $|f_{WW}/(1 \text{ TeV}^2)| < 2$ are allowed by this constraint. This is not true for the WW^* inclusive cross-section constraint, where, the SM-like term contributes 2 orders of magnitude higher (see $\Gamma_{H \rightarrow WW^*}$ in equation 4.12), thereby restricting β to 0.75. Therefore, by comparing the $\gamma\gamma$ and WW^* inclusive constraints taken separately, we can learn that while large values of f_{WW} is disallowed by the former, small values of β are ruled out by the latter. A combination of all the constraints brings us to the global analysis using the data in the bosonic channels (see table 4.3), the result of which is presented in figure 4.4. The constraints on each

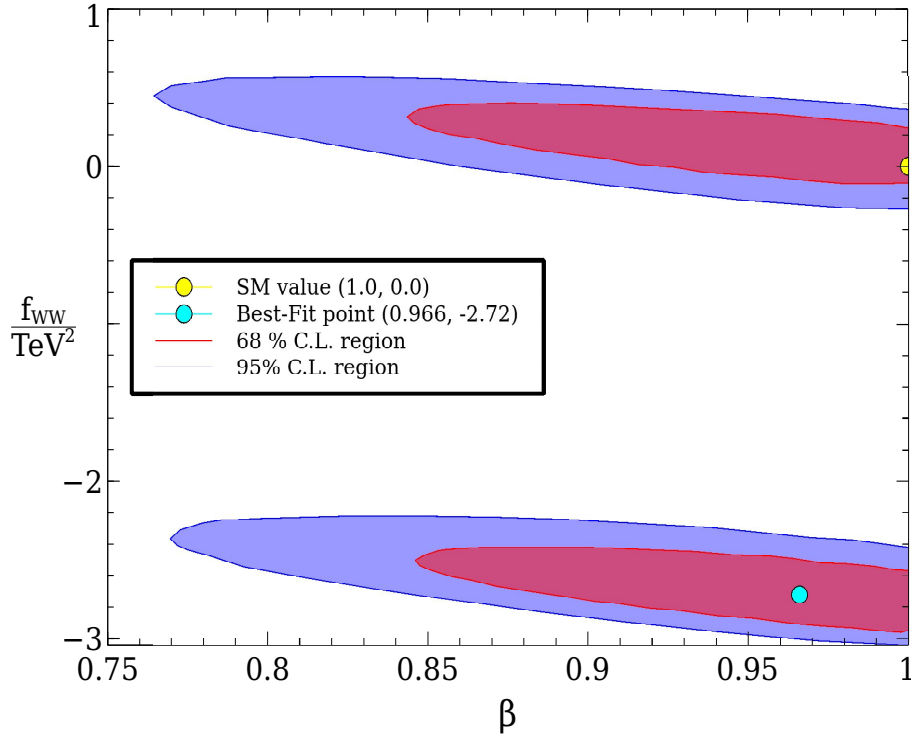


Figure 4.4: 68% and 95% C.L. allowed regions in the $\beta - f_{WW}$ parameter space, after performing a global fit using the data in all bosonic channels given in table 4.3. The best-fit and SM points are also shown.

of the parameters coming from the global fit is now easily understood in terms of the arguments given above. The best fit point corresponds to $\beta = 0.97$ and $f_{WW}/(1 \text{ TeV}^2) = -2.72$, which are very close to the SM point. However, there is still a small room for new physics effects described by O_{WW} and β , as can be seen from the allowed regions at the 2σ level. We also show in figure 4.5 the $\Delta\chi^2$ distributions as a function of f_{WW} and β , after marginalizing over β and f_{WW} respectively. From this figure, we obtain the allowed range for β as

$$0.8 \leq \beta \leq 1.0 \quad 95\% \text{ C.L., marginalized over } f_{WW}. \quad (4.17)$$

Similarly, the allowed range for f_{WW} is found to be

$$\frac{f_{WW}}{\text{TeV}^2} \in [-3.02, -2.31] \cup [-0.20, 0.48] \quad 95\% \text{ C.L., marginalized over } \beta. \quad (4.18)$$

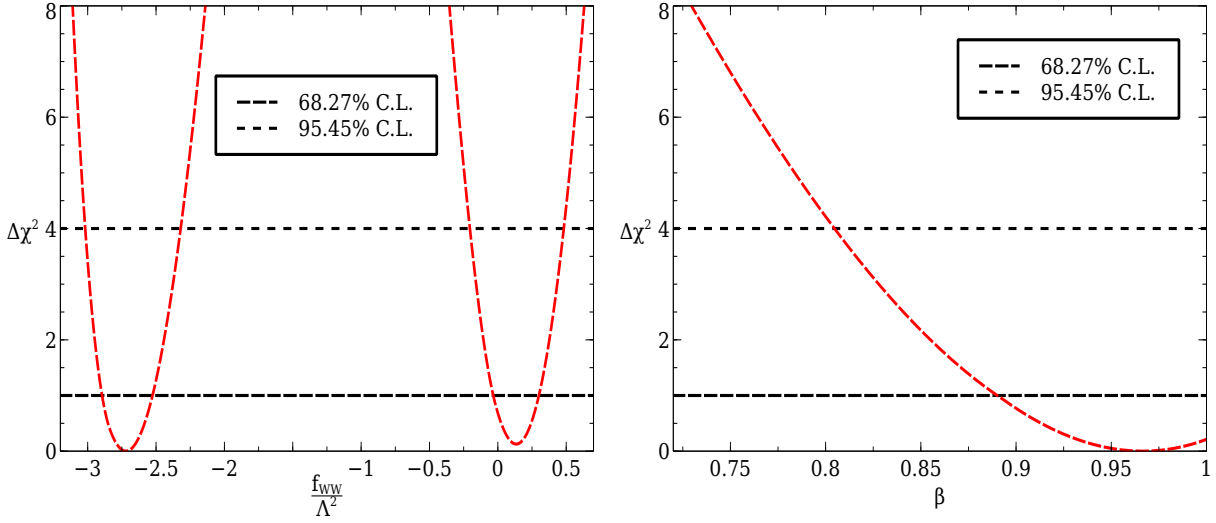


Figure 4.5: $\Delta\chi^2$ distributions as a function of f_{WW} (left) and β (right), after marginalizing over β and f_{WW} respectively. The allowed ranges at 68% and 95% C.L. are also shown by the horizontal dashed lines.

As far as the dimension-six operator \mathcal{O}_{WW} is concerned, this bound tells us that for a suppression scale $\Lambda = 1$ TeV, the co-efficient f_{WW} cannot be smaller than ~ -3 , or, in other words, if $f_{WW} = \mathcal{O}(1)$, $\Lambda \gtrsim 600$ GeV. This result is consistent with the present LHC direct search bounds on the mass of new coloured or uncoloured particles charged under the electroweak gauge group.

Two points are worth mentioning here. Firstly, it is true that the apparently allowed range of f_{WW} after fitting the data suggest rather modest change in cut efficiencies due to the presence of the additional operator. Still we consider the general demonstration of altered efficiencies over a range of the parameter space, quite substantially different in some cases, to be useful. Such altered efficiencies may plague our results, if, for example, over-constraining of f_{WW} has taken place because of event migration. Moreover, in our global fit, we could only include the modified cut efficiencies in the $WW^* + \geq 2$ -jets channel, and not in the other important bosonic channels like $\gamma\gamma$, ZZ^* and WW^* (inclusive), as the detailed information on the cut-flows for the latter channels are not yet presented by the experimental collaborations. Thus the 95% C.L. allowed regions obtained by a global fit with our current set-up is very similar to the region obtained using SM efficiencies. Once the detailed information of experimental cut-flows in all

channels is available, our method can be extended to perform a fully rigorous global analysis. Secondly, even within the ‘apparently allowed’ range, it is worthwhile to look for modification in kinematic distributions due to the additional operators. For example, variables used in Boosted Decision Trees (BDT) can still bear the stamp of the higher-dimensional operators, as we shall see in section 4.7.

4.6 Associated production and higher dimensional operators

In section 4.4, we studied the change in efficiencies of the cuts used by ATLAS in the $H \rightarrow WW^*$ channel (≥ 2 -jet category), in presence of non-zero β and f_{WW} . These cuts were tailored to primarily select VBF events. In this section, we study the modification of cut-efficiencies in the associated production (VH) channel, in presence of O_{WW} as well as O_{BB} , taking their effects one at a time. As the operator O_{BB} only modifies the HZZ and $H\gamma\gamma$ vertices, but not the HWW vertex (see equations 4.5, 4.6), its effect in the VBF channel is not significant³. We do not show the modification of efficiencies for the $H \rightarrow ZZ^*$ channel in the VH category, mainly because the cuts given in the corresponding experimental papers are not so transparently provided when compared to the WW^* and $\gamma\gamma$ final states.

Thus we focus here on the VH production of Higgs, where the Higgs decays to two photons and the vector boson (W or Z) decays hadronically. We closely follow the cuts used by ATLAS (see table 4.4) and study modifications to their efficiencies. The photon isolation criteria have been required to be $\Delta R_{\gamma\gamma} \geq 0.3$, $\Delta R_{\gamma j} \geq 0.4$ and $\Delta R_{\gamma l} \geq 0.4$, where j and l denote jets and leptons (e, μ), and $\Delta R_{ij} = \sqrt{(\eta_i - \eta_j)^2 + (\phi_i - \phi_j)^2}$, η and ϕ being the pseudorapidity and azimuthal angle respectively. In addition, a photon is considered isolated only if the total transverse energy around it in a cone of size $\Delta R = 0.4$ is less than 6 GeV. For further details on the cuts, we refer the reader to references [7, 32]. As in equation 4.11, we define the efficiency for this channel as a function of β and f (f_{WW} or f_{BB}) as

$$\epsilon_{\gamma\gamma+2\text{-jets}(VH)}(\beta, f_{WW/BB}) = \frac{\left[\sigma(pp \rightarrow H)_{VH, V \rightarrow jj} \times \text{BR}(H \rightarrow \gamma\gamma) \right]_{\text{After Cuts}}}{\left[\sigma(pp \rightarrow H)_{VH, V \rightarrow jj} \times \text{BR}(H \rightarrow \gamma\gamma) \right]_{\text{Before Cuts}}}. \quad (4.19)$$

³In the SM, the WW -fusion diagram contributes roughly 3 times to the VBF Higgs production cross-section, compared to the ZZ -fusion diagram, while the interference term is negligible ($\sim 1\%$) [30].

⁴ p_T , is the diphoton transverse momentum orthogonal to the diphoton thrust axis in the transverse plane, as defined later in section 4.7.

$100 \text{ GeV} < m_{\gamma\gamma} < 160 \text{ GeV}$
$60 \text{ GeV} < m_{jj} < 110 \text{ GeV}$
$ \Delta y_{jj} < 3.5$
$ \Delta \eta_{\gamma\gamma, jj} < 1$
$p_{T_i} > 70 \text{ GeV}^4$

Table 4.4: Cuts used for the VH channel with $H \rightarrow \gamma\gamma$ and $V \rightarrow jj$ in the low mass two-jet category (ATLAS). See references [7, 32] for details.

By performing a scan over the $(\beta, f_{WW/BB})$ parameter space, we obtain the combined efficiencies (for \mathcal{O}_{BB} and \mathcal{O}_{WW}) of the isolation cuts and the ATLAS cuts in table 4.4 and they are well fit by the following functions :

$$\epsilon_{\gamma\gamma+2\text{-jets}(VH)}(\beta, f_{BB}) = \frac{(3.75\beta^2 + 2.66\beta f_{BB} + 0.47f_{BB}^2)(0.15 - 1.34\beta + 0.01f_{BB} - 1.22\beta^2 - 0.05\beta f_{BB} - 1.3 \times 10^{-11} f_{BB}^2)}{(5.20\beta^2 + 3.68\beta f_{BB} + 0.65f_{BB}^2)(2.05 - 18.76\beta + 0.06f_{BB} - 17.57\beta^2 - 0.65\beta f_{BB} - 1.4 \times 10^{-10} f_{BB}^2)}, \quad (4.20)$$

$$\epsilon_{\gamma\gamma+2\text{-jets}(VH)}(\beta, f_{WW}) = \frac{(15.46\beta^2 - 1.33\beta f_{WW} + 0.05f_{WW}^2)(0.03 - 0.35\beta + 0.05f_{WW} - 8.88\beta^2 + 61.25\beta f_{WW} - 15.31f_{WW}^2)}{(0.64\beta^2 - 4.12\beta f_{WW} + 1.03f_{WW}^2)(-1.33 + 11.22\beta + 0.22f_{WW} - 4346.94\beta^2 + 392.44\beta f_{WW} - 14.86f_{WW}^2)}. \quad (4.21)$$

In equations 4.20 and 4.21, the denominator and the numerator represent $\sigma_{prod}^{VH} \times B.R.(H \rightarrow \gamma\gamma)$, before and after all the cuts respectively, and some common numerical factors between the two, like the total Higgs decay width have been cancelled out.

In figures 4.6 and 4.7, we show the variation of $\epsilon_{\gamma\gamma+2\text{-jets}(VH)}$ as a function of f_{BB} and f_{WW} respectively for different values of β . The red (solid), green (dashed) and black (dot-dashed) curves correspond to $\beta = 1, 0.5$ and 0.1 respectively. For $f_{BB} = 0$ or $f_{WW} = 0$ we recover the SM efficiency ($\epsilon_{SM} \sim 0.053$) in both the cases for all values of β . Within the range of f_{BB} shown in figure 4.6, the efficiency for $\beta = 0.5$ can change from its SM value by up to 8.7%, while for $\beta = 0.1$, it can increase by up to 19.7%. On the other hand, for the range of f_{WW} shown in figure 4.7, for $\beta = 0.5$ ($\beta = 0.1$), the efficiency can increase from its SM value by up to 14.7% (13.9%). Thus our overall conclusion is that the modification of cut efficiencies in the VH production mode is in general less pronounced than in the VBF Higgs production with $H \rightarrow WW^*$.

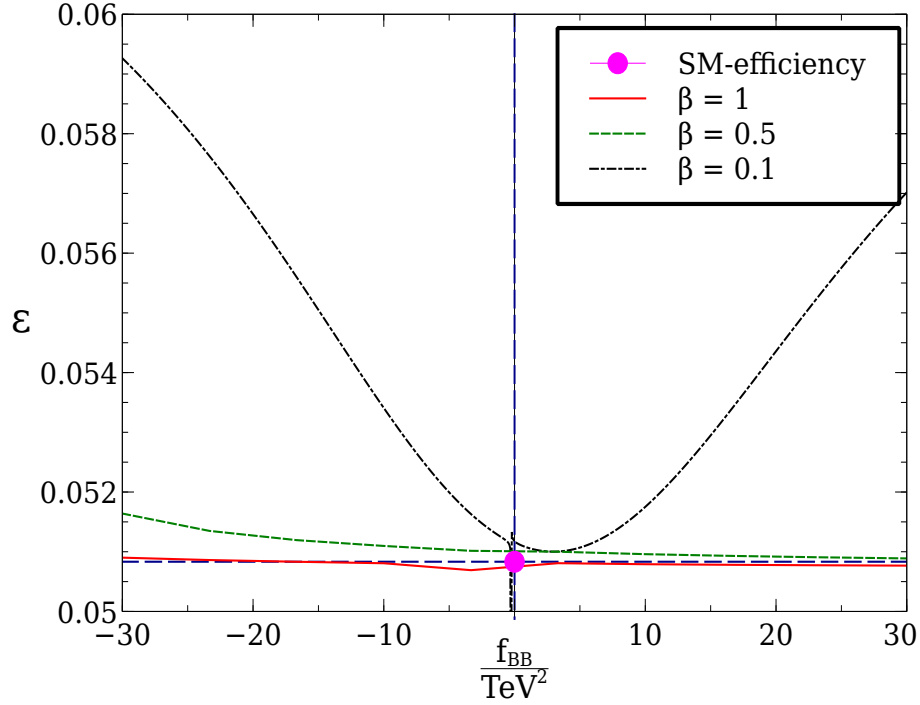


Figure 4.6: The combined efficiency of all ATLAS cuts (ϵ) as a function of f_{BB} for different values of β , in the $H \rightarrow \gamma\gamma$ channel (VH category) at 8 TeV LHC.

4.7 Modification to kinematic distributions : examples

Since the modifications of cut efficiencies discussed so far originate from changes in kinematic distributions, in this section, we explore some of these distributions in the presence of higher dimensional operators. Study of differential distributions is the next step in experimental analysis of the Higgs sector, and preliminary results with the current data have already been presented in Ref [33]. As an example we choose the diphoton channel in the VBF category [7, 32], and consider the operator \mathcal{O}_{WW} for illustration. All the distributions are shown after applying the standard trigger and isolation cuts for jets and photons. The kinematic variables considered are :

1. $\sqrt{\vec{p}_{Tj_1} \cdot \vec{p}_{Tj_2}}$, where j_1 and j_2 are the two tagged jets ordered in terms of their transverse momenta.
2. $|\Delta\eta_{j_1j_2}| = |\eta_{j_1} - \eta_{j_2}|$.
3. The invariant mass of the two tagged jets, $m_{j_1j_2}$. For this as well as the distributions listed

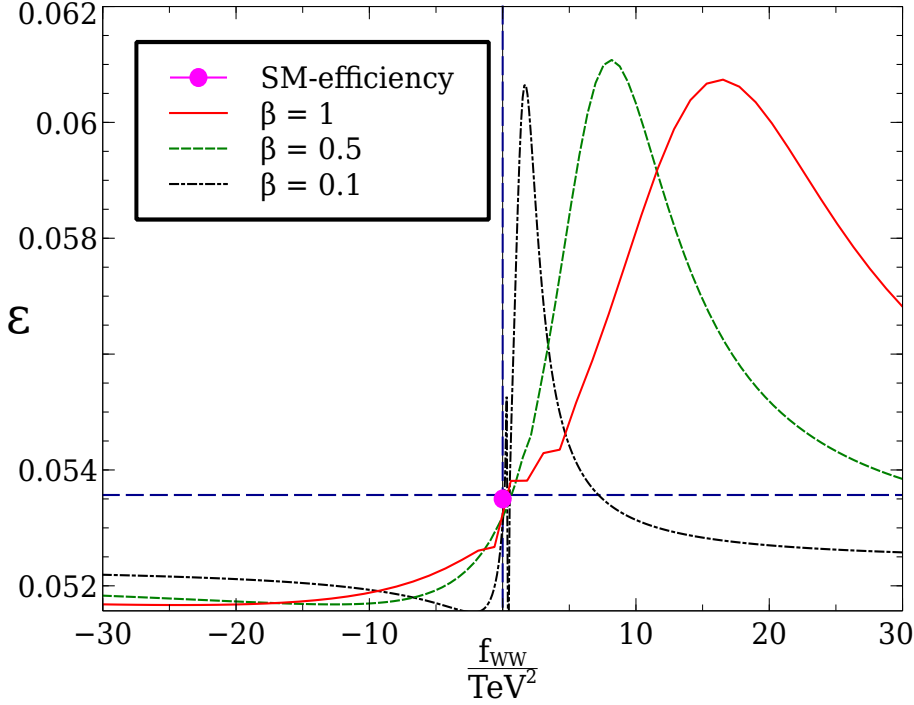


Figure 4.7: The combined efficiency of all ATLAS cuts (ϵ) as a function of f_{WW} for different values of β , in the $H \rightarrow \gamma\gamma$ channel (VH category) at 8 TeV LHC.

below, the cut $|\Delta\eta_{j_1 j_2}| > 2.8$ (see Ref. [34]) is imposed.

4. $p_{T_i} = |\vec{p}_T^{\gamma\gamma} \times \hat{t}|$, where $\hat{t} = \frac{\vec{p}_T^{\gamma 1} - \vec{p}_T^{\gamma 2}}{|\vec{p}_T^{\gamma 1} - \vec{p}_T^{\gamma 2}|}$ is the transverse thrust, $\vec{p}_T^{\gamma 1}$, $\vec{p}_T^{\gamma 2}$ are the transverse momenta of the two isolated photons and $\vec{p}_T^{\gamma\gamma} = \vec{p}_T^{\gamma 1} + \vec{p}_T^{\gamma 2}$ is the transverse momentum of the diphoton system [7,32]. This and the subsequent distributions are subjected to the cuts $m_{j_1 j_2} > 400$ GeV and $\Delta\phi_{\gamma\gamma, j_1 j_2} > 2.6$, where $\Delta\phi_{\gamma\gamma, j_1 j_2}$ is the azimuthal angle separation between the diphoton system and the system of the two tagged jets. The criterion of no hadronic activity in the rapidity gap between the two tagged jets is also imposed [34].
5. $\eta^* = \eta_{\gamma\gamma} - \frac{\eta_{j_1} + \eta_{j_2}}{2}$, where $\eta_{\gamma\gamma}$ is the pseudorapidity of the diphoton system.
6. $\Delta R_{\min}^{\gamma j}$ is the minimal ΔR between a photon and a tagged jet.

The last five kinematic variables form a subset of the inputs for the Boosted Decision Tree (BDT) employed by ATLAS for studying this channel [7, 32].

Figure 4.8 shows the normalised distributions in the above six variables for $\beta = 1$ and $f_{WW} = 0, \pm 10$ at the 8 TeV LHC. The values $f_{WW} = \pm 10$ are chosen for illustrative purpose only, since, as seen in section 4.5, although they are allowed by the LHC data in the WW^* channel, the current measurement in the $\gamma\gamma$ channel restricts f_{WW} to smaller values. Therefore, in figure 4.9 we show the aforementioned distributions in the SM, and for the parameters $\{\beta, f_{WW}\} = \{0.8, -3\}$ the latter being within the 2σ allowed range of the global fit (see figure 4.5). For both the above figures, the cut-off scale has been chosen as $\Lambda = 1$ TeV. We note that the distributions of $|\Delta\eta_{j_1 j_2}|$ have two peaks. The peak at $|\Delta\eta_{j_1 j_2}| = 0$ is due to VH contamination. Moreover, the relative heights of the two peaks change on introducing higher dimensional operators.

4.8 Summary and conclusions

We have considered some illustrative dimension-6 operators for HVV interactions, and their potential contributions to the Higgs data, in conjunction with the SM-like operators. Parametrizing the strength of the additional interactions by f (f_{WW}/f_{BB}), and the simultaneous modification to the SM-like couplings to W and Z bosons by β , we show, after a detailed cut-based Monte Carlo analysis, how the efficiencies of different acceptance cuts are altered for various values of f and β . We find that in general there can be substantial modification of this kind, which underscores the importance of a detailed study of the effect of all such additional operators on the kinematics of various final states. When one further imposes the constraints on the (f, β) space as resulting from a global fit of the LHC data available till date, the f -parameters are in general restricted to rather modest values while β is restricted to be in the range $[0.8, 1]$. Thus the effects of cuts in the diboson channels may not be drastically different, unless there is ground for relaxing their constraints. In general, the VBF channel is more sensitive to the higher-dimensional operators than the gluon-fusion and VH production modes. We also present several kinematic distributions, some of which are used in BDT analyses, which can potentially bring out signatures of the new operators, even with moderate strength.

It should be remembered here that our analysis is purely phenomenological and data-driven; the assumption of any specific ultraviolet (UV) completion is deliberately avoided. In a specific UV completion scheme, more than one higher-dimensional operator relevant at the

LHC scale may be generated, which can affect some of our conclusions. For example, with additional operators present, a situation as restrictive as indicated by figure 4.3 may not arise due to the accidental cancellation of different contributions. However, studying one operator at a time gives us valuable insight on how it typically affects various observables in the Higgs sector — an insight that is lost in the introduction of all operators of a given dimension simultaneously. In this spirit, we have explored two operators which can most significantly modify the interaction of the Higgs with a pair of electroweak gauge bosons. The other operators which have not been shown as examples, will also modify the experimental cut-efficiencies, though in different degrees. The next chapter deals with all such operators from such a standpoint, and aims to identify some more ways of probing them.

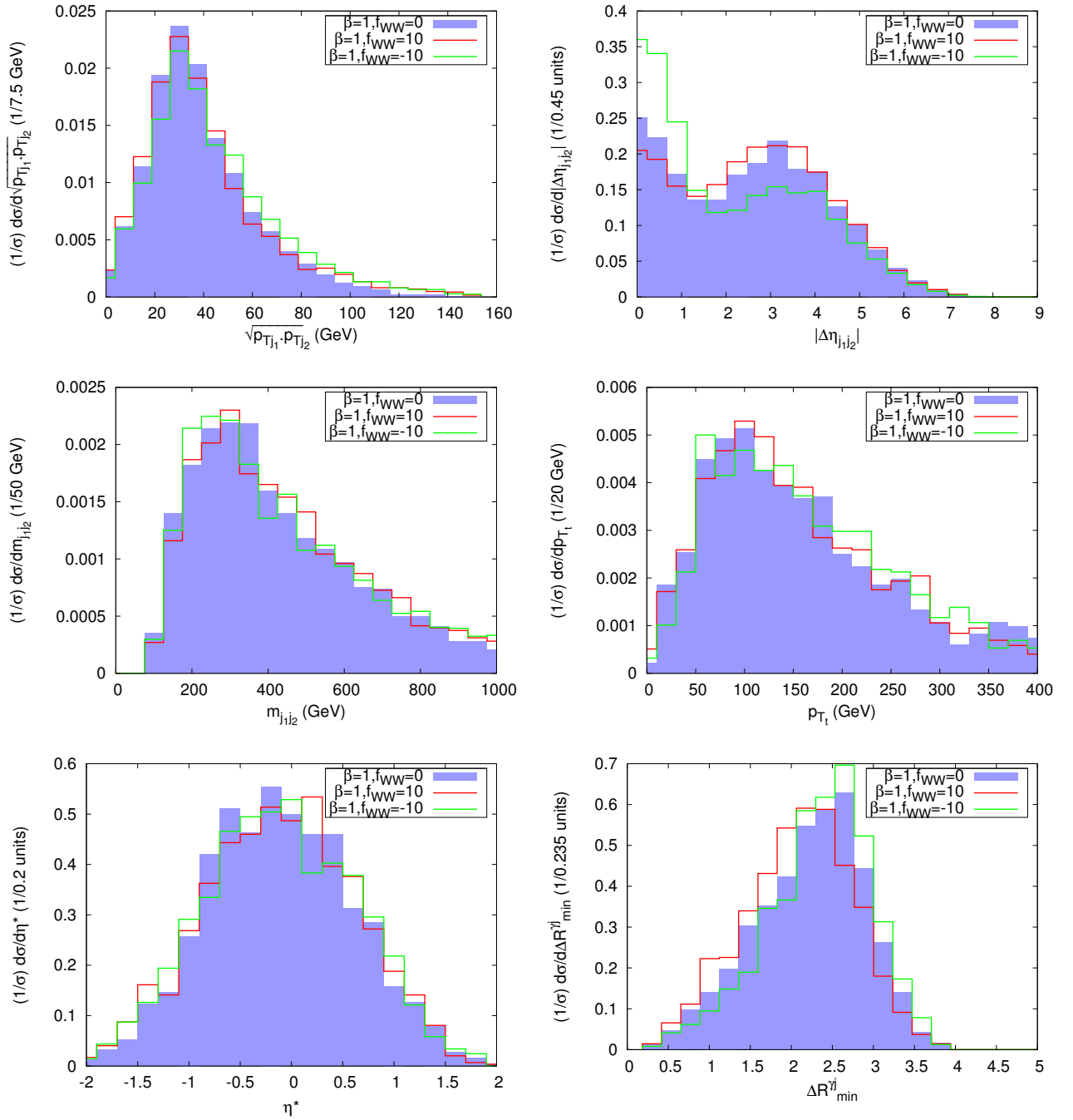


Figure 4.8: Normalised distributions in various kinematic variables for 8 TeV LHC, top row : $\sqrt{\vec{p}_{Tj_1} \cdot \vec{p}_{Tj_2}}$ (left) and $|\Delta\eta_{j_1j_2}|$ (right); middle row : $m_{j_1j_2}$ (left) and p_{T_i} (right); bottom row : η^* (left) and ΔR_{\min}^j (right), for the parameter points $\{\beta = 1, f_{WW} = 0\}$ (shaded blue region), $\{\beta = 1, f_{WW} = 10\}$ (solid red line) and $\{\beta = 1, f_{WW} = -10\}$ (solid green line). The cut-off scale chosen is $\Lambda = 1$ TeV.

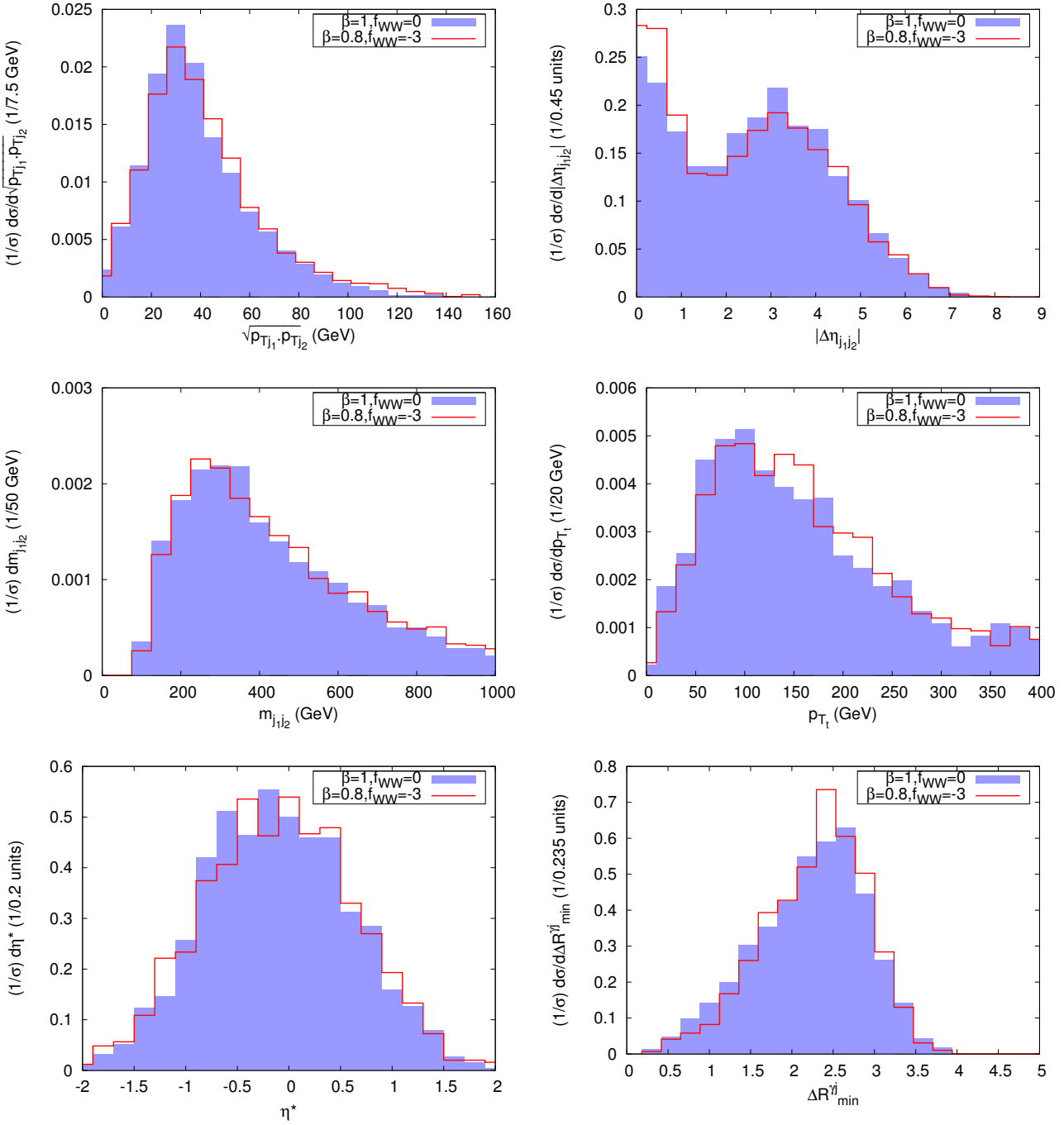


Figure 4.9: Normalised distributions in various kinematic variables for 8 TeV LHC, top row : $\sqrt{\vec{p}_{Tj_1} \cdot \vec{p}_{Tj_2}}$ (left) and $|\Delta\eta_{j_1j_2}|$ (right); middle row : $m_{j_1j_2}$ (left) and p_{T_i} (right); bottom row : η^* (left) and ΔR_{\min}^{yj} (right), for the parameter points $\{\beta = 1, f_{WW} = 0\}$ (shaded blue region) and $\{\beta = 0.8, f_{WW} = -3\}$ (solid red line). The cut-off scale chosen is $\Lambda = 1$ TeV. Both the parameter points are allowed by the current data at 95% C.L.

Chapter 5

Probing the Higher-dimensional HVV operators at the high-energy run at the LHC¹

5.1 Motivation

In the last two chapters, we have tried to put bounds on the Higgs couplings from the data available from the run I of the LHC. From the previous chapter, we have also seen that the coupling coefficients which come about from the higher-dimensional operators are instrumental in changing the experimental cut efficiencies [1, 2]. Hence, we showed that it is very important to consider the effects of such modified efficiencies when one is doing fits of these parameters to the experimental data. Constraints on such terms have already been studied, using precision electroweak data as well as global fits of the current Higgs data [1–37]. Many studies have considered anomalous Higgs couplings in context of future e^+e^- colliders [38–43] and ep colliders [44]. The general conclusion that several (though not all) of the gauge invariant, dimension-6 HVV terms can at most have coefficients $\sim 5 \text{ TeV}^{-2}$ [2–37, 45]. It still remains to be seen whether such small coefficients can be discerned with some ingeniously constructed kinematic

¹This chapter is based on the paper *Cornering dimension-6 HVV interactions at high luminosity LHC: the role of event ratios* by Shankha Banerjee, Tanumoy Mandal, Bruce Mellado and Biswaryp Mukhopadhyaya, [arXiv:1505.00226 [hep-ph]] (Submitted for publication)

distributions. Some work has nonetheless been done to study such distributions [44, 46–49], in terms of either the gauge invariant operators themselves or the structures finally ensuing from them. At the same time, it is of interest to see if meaningful constraints do arise from the study of total rates at the LHC. The essence of any probe of these anomalous couplings, however, lies in pinning them down to much smaller values using the 14 TeV runs, as common sense suggests the manifestation, if any, of new physics through Higher Dimensional Operators (HDO's) with small coefficients only.

We show here that the relative rates of events of different kinds in the Higgs data can allow us to probe such effective interactions to levels of smallness not deemed testable otherwise. This happens through (a) the cancellation of theoretical uncertainties, and (b) the fact that some ratios have the numerators and denominators shifting in opposite directions, driven by the additional interactions. Thus the cherished scheme of finding traces of new physics in Higgs phenomenology can be buttressed with one more brick. The list of the Higher-dimensional operators and their effective couplings have already been discussed in chapter 4.2. In Sec. 5.2, we introduce three ratios of cross-sections as our observables. The results of our analysis are explained in Sec. 5.3. We summarise and conclude in Sec. 5.4.

The question we address in the rest of this chapter is: can these limits be improved in the next run(s) through careful measurement of the ratios of total rates in different channels? as we shall see below, the answer is in the affirmative.

5.2 Ratios of cross-sections as chosen observables

The four HDOs under consideration affect Higgs production as well as its decays, albeit to various degrees. For example, HDO-dependent single Higgs production processes are in association with vector bosons (VH) *i.e.* $pp \rightarrow VH$ (where $V = \{W, Z\}$) and vector-boson fusion (VBF). We show the production cross-sections in these channels at 14 TeV in Fig. 5.1, as functions of the four operator coefficients (f_i) taken one at a time.² The relevant decay channels which are dependent on such operators are $H \rightarrow WW^*, ZZ^*, \gamma\gamma, Z\gamma$. Fig. 5.2 contains these branching ratios (BR) as functions of the four coefficients under consideration.

The VBF and VH rates are sensitive to f_{WW} and f_W , but depend very weakly on f_{BB} and

²We have used CTEQ6L1 parton distribution functions (PDFs) by setting the factorization (μ_F) and renormalization scales (μ_R) at the Higgs mass ($M_H = 125$ GeV).

f_B , while the cross-section $\sigma(pp \rightarrow WH)$, is completely independent of f_{BB} and f_B . The HDO effects in $H \rightarrow \gamma\gamma$ and $H \rightarrow Z\gamma$ for $f_i \sim O(1)$ is of the same order as the loop-induced SM contribution unlike in the case of the HW and HZZ couplings. Therefore, $BR_{H \rightarrow \gamma\gamma}$ becomes highly sensitive to f_{WW} and f_{BB} . Consequently, the 7+8 TeV data already restrict their magnitudes to small values of the order of $\lesssim 5 \text{ TeV}^{-2}$. The limits on f_W and f_B , however, are relatively weaker, even after simultaneous imposition of constraints from electroweak precision data and LHC results.

Based on the above information, we set out to find observables which are sensitive to $f_i \lesssim 5 \text{ TeV}^{-2}$ in the High luminosity run at the LHC. It is not completely clear yet how much of statistics is required to probe such small values with various event shape variables. On the other hand, the more straightforward observables, namely, total rates in various channels, are also fraught with statistical, systematic and theoretical uncertainties which must be reduced as far as possible when precision is at a premium.

An approach that is helpful is looking at ratios of cross-sections in different channels. In this chapter, we invoke two kinds of ratios. First, we take ratios of events in two different final states arising from a Higgs produced via the same channel (in our case, gluon fusion). Such a ratio enables one to get rid of correlated theoretical uncertainties (CThU) such as those in PDF and renormalisation/factorisation scales. They also cancel the uncertainty in total width which is correlated in the calculation of BRs into the two final states. Secondly, we consider the ratio of rates for the same final state for two different production channels (such as VBF and VH). Although the uncertainty in the BR cancels here, the theoretical uncertainties at the production level do not. Moreover, since the final state is same in this case, some systematic uncertainties which are correlated (related to identification, isolation, trigger etc.) will also get cancelled. However, this is helpful in another manner. For some of the operators, the f_i -dependent shifts with respect to the SM are in opposite direction for the numerator and the denominator in such ratios. The result is that the net deviation adds up, as shown in subsection 5.2.2. We shall see that the use of both these kinds of ratios (including those involving the channel $Z\gamma$ can capture the HDO coefficients at a level unprecedented, going down to values where new physics can show up.

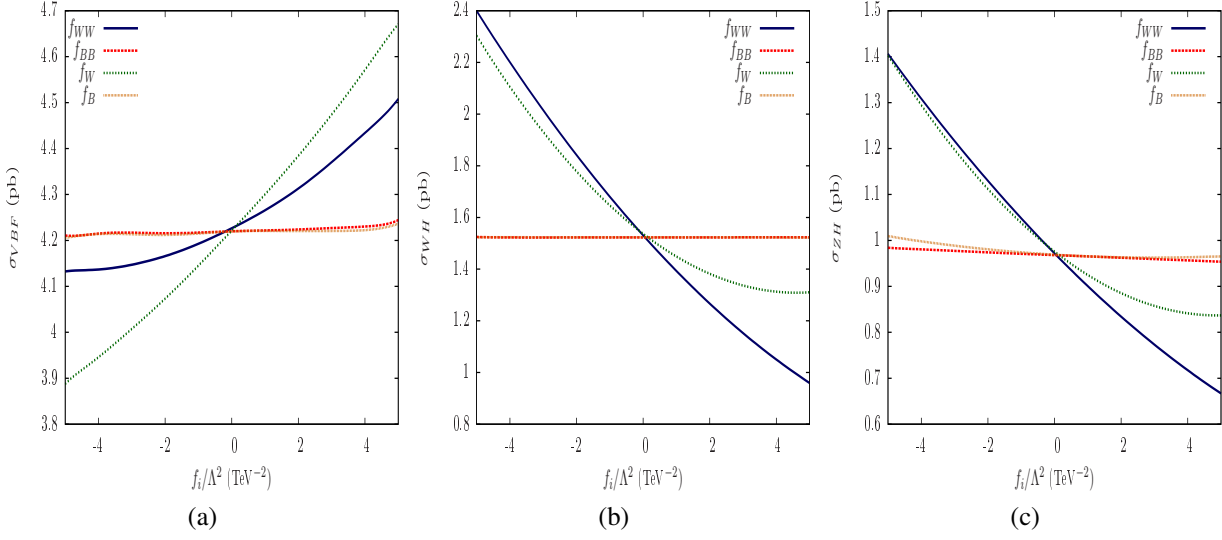


Figure 5.1: Higgs production cross-sections for the VBF and VH channels in presence of HDOs at 14 TeV. Here the operators are varied one at a time.

5.2.1 Observable sensitive to O_{WW} and O_{BB} : \mathcal{R}_1

As has been noted earlier, $\text{BR}_{H \rightarrow \gamma\gamma}$ (Fig. 5.2c) is highly sensitive to two of the operators, namely, O_{BB} and O_{WW} . Therefore, we propose to probe them in the $\gamma\gamma$ channel, with the Higgs produced through gluon-gluon fusion (ggF). This final state is clean for reconstruction, and has high statistics. We should mention here that if we consider the simultaneous presence of more than one operators, then there is a “blind-direction” in the parameter space $f_{WW} \approx -f_{BB}$ where $\text{BR}_{H \rightarrow \gamma\gamma}$ mimics the SM value. This is because the higher-dimensional part of the $H\gamma\gamma$ vertex is proportional to $f_{WW} + f_{BB}$. Also, for the non-trivial range $f_{WW} = f_{BB} \approx -3$, $\text{BR}_{H \rightarrow \gamma\gamma}$ mimics the SM value, due to parabolic dependence of the diphoton rate on the HDO coefficients. Therefore, the Higgs produced through ggF followed by its decay to $\gamma\gamma$ cannot be used alone to probe these two ‘special’ regions of the parameter space. We construct the observable

$$\mathcal{R}_1(f_i) = \frac{\sigma_{ggF} \times \text{BR}_{H \rightarrow \gamma\gamma}(f_i)}{\sigma_{ggF} \times \text{BR}_{H \rightarrow WW^* \rightarrow 2\ell 2\nu}(f_i)}, \quad (5.1)$$

where $\ell = e, \mu$ and f_i 's are the operator coefficients. As explained earlier, the CThU in production as well as total width cancels here; so does the K -factor in the production rate. Clearly, \mathcal{R}_1

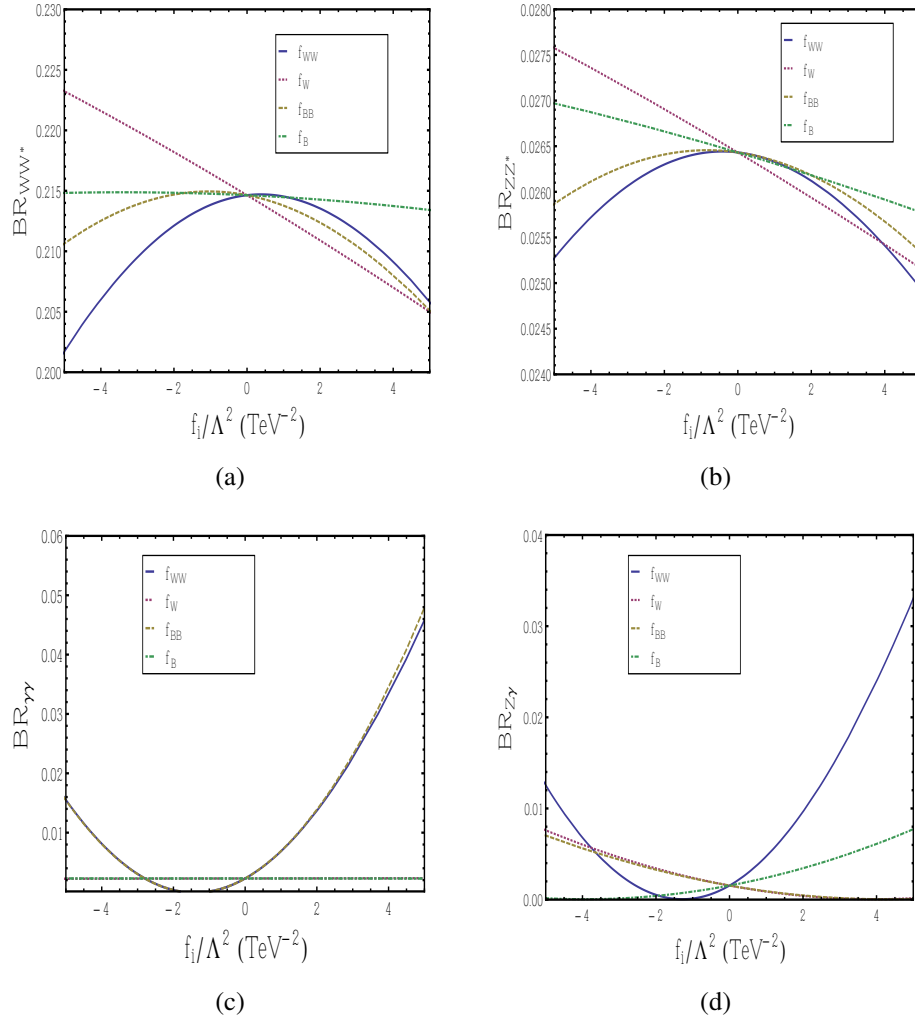


Figure 5.2: Branching ratios of $H \rightarrow WW^*, ZZ^*, \gamma\gamma, Z\gamma$ in presence of HDOs. The operators are varied one at a time.

can also be expressed as the ratio of two signal strengths as follows,

$$\mathcal{R}_1(f_i) = \frac{\mu_{\gamma\gamma}^{\text{ggF}}(f_i)}{\mu_{WW^*}^{\text{ggF}}(f_i)} \times \frac{(\sigma_{\text{ggF}} \times \text{BR}_{H \rightarrow \gamma\gamma})^{\text{SM}}}{(\sigma_{\text{ggF}} \times \text{BR}_{H \rightarrow WW^* \rightarrow 2\ell 2\nu})^{\text{SM}}}. \quad (5.2)$$

Therefore, already measured $\gamma\gamma$ and WW^* signal strengths can be used to constrain the operator coefficients affecting the ratio \mathcal{R}_1 . The efficiency of acceptance cuts does not affect the results, for values of f_{WW} and f_{BB} which are of relevance here because for such small values of the parameter coefficients the change in experimental cut-efficiencies is negligible. On top of that, for the ggF production mode, these operators only affect the decay vertices and hence the cut-efficiencies are but modified by a very small extent. We must also note that in defining \mathcal{R}_1 a full jet-veto (0-jet category) has been demanded for both the numerator and the denominator to reduce the uncertainties related to the different jet-requirement in the final state. Besides, in the denominator, the WW^* pair is considered to decay into both same flavour ($ee + \mu\mu$) and different flavour ($e\mu + \mu e$) final states to improve the statistics.

5.2.2 Observable sensitive to O_{WW} and O_W : \mathcal{R}_2

It turns out that the f_{WW} and f_W affect (to one's advantage) the ratio of events in a particular Higgs decay mode in the VBF and VH channels. This captures the new physics at the production level. By considering the same final states from Higgs decay, some theoretical uncertainties in the decay part cancels out. The production level uncertainties, including the K -factors, however, do not cancel here. In our calculation, the next-to-next-to leading order (NNLO) K -factors have been assumed to be the same as in the SM, expecting that the presence of HDO does not effect the K -factors much. For precise estimate of the observed ratio, one of course has to incorporate the modified cut efficiencies due to the new operators, though such modifications may be small. The other, important advantage in taking the above kind of ratio is that, for not-too-large f_{WW} or f_W (in the range $[-5, +5]$), the deviations of the VBF and VH cross-sections are in opposite directions. The generic deviation for the rate in any channel can be parametrized as

$$\sigma_{\text{prod.}}^{\text{HDO}} = \sigma_{\text{prod.}}^{\text{SM}} \times (1 + \delta_{\text{prod.}}). \quad (5.3)$$

From Fig. 5.1a, δ_{VBF} is positive in the range $f_{WW}, f_W > 0$. On the other hand, in the same region of the parameter space, δ_{VH} is negative as evident from Figs. 5.1b and 5.1c. Hence, on taking

the ratio $\sigma_{\text{VBF}}^{\text{HDO}}/\sigma_{\text{VH}}^{\text{HDO}}$, the deviation from SM is

$$\frac{\sigma_{\text{VBF}}}{\sigma_{\text{VH}}} = \frac{\sigma_{\text{VBF}}^{\text{SM}}}{\sigma_{\text{VH}}^{\text{SM}}} \times \left(1 + \delta_{\text{VBF}} - \delta_{\text{VH}} + \mathcal{O}(\delta^2)\right). \quad (5.4)$$

Thus this ratio further accentuates the deviation from SM behaviour. As an example, if we consider the parameter choice $f_W = 2$, then $\delta_{\text{VBF}} \approx 3.6\%$ and $\delta_{\text{VH}} \approx 10\%$. However, from the ratio, the combined $\delta_{\text{VBF}+\text{VH}} \approx 15\%$, which is a clear indication of why we should consider such ratios. We thus define our next observable

$$\mathcal{R}_2(f_i) = \frac{\sigma_{\text{VBF}}(f_i) \times \text{BR}_{H \rightarrow \gamma\gamma}(f_i)}{\sigma_{\text{VH}}(f_i) \times \text{BR}_{H \rightarrow \gamma\gamma}(f_i) \times \text{BR}_{W \rightarrow \ell\nu}}, \quad (5.5)$$

where the $\gamma\gamma$ final state has been chosen because of its clean character and reconstructibility of the Higgs mass. It should be remembered, however, that f_{WW}, f_{BB} in the range -3 to 0 causes the diphoton branching ratio to undergo a further dip. This can adversely affect the statistics, and thus the high luminosity run is required for an exhaustive scan of the admissible ranges of the above coefficients.

5.2.3 Observable sensitive to O_B : \mathcal{R}_3

The operator O_B is sensitive to $H \rightarrow ZZ^*$ and $H \rightarrow Z\gamma$. In the former mode, the sensitivity of f_B is limited (see the green curve in Fig. 5.2b) and can be appreciable only for larger f_B . The partial decay width $\Gamma_{H \rightarrow Z\gamma}$, on the other hand is rather sensitive to all the four operators under study (Fig. 5.2d), primarily due to the fact that the new $HZ\gamma$ vertex contributes practically as the same order as in the SM. However, the present statistics in this channel is poor [50,51]. We use it for the 14 TeV 3000 fb⁻¹ run to constrain f_B only, for which other channels fail. In the same spirit as for \mathcal{R}_1 , we thus define our third observable

$$\mathcal{R}_3(f_i) = \frac{\sigma_{\text{ggF}} \times \text{BR}_{H \rightarrow Z\gamma \rightarrow 2\ell\gamma}(f_i)}{\sigma_{\text{ggF}} \times \text{BR}_{H \rightarrow WW^* \rightarrow 2\ell 2\nu}(f_i)}, \quad (5.6)$$

where $\ell = e, \mu$ and here again the CThU cancels. Here also, we must note that in defining \mathcal{R}_3 a full jet-veto has been demanded for both the numerator and the denominator. For the numerator, the Z boson's decay to both an electron pair and a muon pair is considered. Besides, in the denominator, the WW^* pair is taken to decay similar to the \mathcal{R}_1 case.

5.3 Results of the analysis

For our subsequent collider analysis, the chain we have used is as follows - first we have implemented the relevant dimension-6 interaction terms as shown in Eq. (4.5) in FEYNRULES [52], and generated the Universal FeynRules Output (UFO) [53] model files. These UFO model files have been used in the MONTE-CARLO (MC) event generator MADGRAPH [54] to generate event samples. Next, the parton-showering and hadronisation are performed using PYTHIA [55] and finally detector level analyses is carried using DELPHES [56].

Before we discuss the phenomenological aspects of the aforementioned observables, we re-iterate below the various kinds of uncertainties considered. The two major classes of observables where these uncertainties arise are as follows:

- Same production channel but different final states:

In such cases (as in \mathcal{R}_1 and \mathcal{R}_3), the correlated uncertainties lie in PDF+ α_s , QCD-scale and in the total Higgs decay width, Γ_H . However, uncertainties in the partial decay widths are uncorrelated.³ Statistical uncertainties for distinct final states are always uncorrelated and are retained in our analysis. We also assume some systematic uncertainties, whenever shown, to be fully uncorrelated. All surviving uncertainties are added in quadrature to estimate total uncertainties related to our observables.

- Different production channels but same final state:

For such observables (\mathcal{R}_2 in our definition), the only correlated uncertainty is in $\text{BR}_{H \rightarrow \gamma\gamma}$. All other uncertainties are uncorrelated and hence are added in quadrature (including the uncertainties in the numerator and the denominator of the ratio \mathcal{R}_2). Beside the already mentioned theoretical uncertainties, we also encounter some additional theoretical uncertainty related to the QCD-scale in the WH mode, which we separately discuss in subsection 5.3.3.

We further assume that the percentage uncertainties remain same even after the inclusion of the anomalous couplings. In order to illustrate how the uncertainties are taken into consideration, we list the theoretical uncertainties related to relevant Higgs BR and total width in Table 5.1, and related to various production cross-sections in Table 5.2. In Table 5.3, number

³We must mention here that $\Gamma_{H \rightarrow \gamma\gamma}$ and $\Gamma_{H \rightarrow Z\gamma}$ have tiny correlations with $\Gamma_{H \rightarrow WW^*}$ because of the W -boson loop in the former two cases. However, in this present analysis we neglect such small correlations and consider these partial decay widths to be mostly uncorrelated

SM Quantity	Value	+ve uncert. %	-ve uncert. %
$\text{BR}_{H \rightarrow \gamma\gamma}$	2.28×10^{-3}	+4.99	-4.89
$\text{BR}_{H \rightarrow WW^*}$	2.15×10^{-1}	+4.26	-4.20
$\text{BR}_{W \rightarrow e\nu_e}$	1.07×10^{-1}	+0.16	-0.16
$\text{BR}_{W \rightarrow \mu\nu_\mu}$	1.06×10^{-1}	+0.15	-0.15
$\text{BR}_{H \rightarrow Z\gamma}$	1.54×10^{-3}	+9.01	-8.83
$\text{BR}_{Z \rightarrow ee}$	3.36×10^{-2}	+0.004	-0.004
$\text{BR}_{Z \rightarrow \mu\mu}$	3.37×10^{-2}	+0.007	-0.007
Total Γ_H	4.07 MeV	+3.97	-3.94

Table 5.1: $\text{BR}_{H \rightarrow \gamma\gamma}$, $\text{BR}_{H \rightarrow WW^*}$, $\text{BR}_{H \rightarrow Z\gamma}$, $\text{BR}_{W \rightarrow \ell\nu}$, $\text{BR}_{Z \rightarrow \ell\ell}$ and total Higgs width Γ_H (MeV) and their % uncertainties for a Higgs of mass 125 GeV ($m_W = 80.385$ GeV and $m_Z = 91.1876$ GeV). These numbers are taken from the LHC Higgs Cross Section Working Group page [57].

Process	σ (pb)	+QCD-Scale %	-QCD-Scale %	+(PDF+ α_s) %	-(PDF+ α_s) %
ggF	49.47	+7.5	-8.0	+7.2	-6.0
VBF	4.233	+0.4	-0.5	+3.3	-3.3
WH	1.522	+0.8	-1.6	+3.2	-3.2
ZH	0.969	+4.0	-3.9	+3.5	-3.5

Table 5.2: The cross-sections of relevant Higgs production ($m_H = 125$ GeV) channels and their QCD-Scale and PDF+ α_s uncertainties in %. These numbers are again taken from the LHC Higgs Cross Section Working Group page [57].

	\mathcal{R}_1	\mathcal{R}_2	\mathcal{R}_3
Numerator	47724 ($\gamma\gamma$ in ggF)	194 ($\gamma\gamma$ in VBF)	1989 ($Z\gamma$ in ggF)
Denominator	40850 (WW^* in ggF)	238 ($\gamma\gamma$ in WH)	40850 (WW^* in ggF)

Table 5.3: Number of surviving events (taken from Refs. [58, 59]) after the selection cuts in the SM at 14 TeV with 3000 fb^{-1} integrated luminosity. These numbers are used to compute the statistical uncertainties (which goes as σ/\sqrt{N} , where σ is the cross-section and N is the number of surviving events after all selection cuts. Here, we have taken N to be twice of the numbers reported in the table to approximately include the contribution from CMS) related to the numerator and denominator of the three observables. Number of events in the VBF ($\gamma\gamma$) channel is computed by applying a fixed p_T -cut (keeping other cuts are same as in Ref. [58]) of 50 GeV on both the tagged jets instead of η -dependent jet selection cuts as used in the same reference. Number of events for $\gamma\gamma$ in \mathcal{R}_1 , $Z\gamma$ in \mathcal{R}_3 and WW^* for \mathcal{R}_1 and \mathcal{R}_3 are obtained after putting 0-jet veto and demanding only ggF events. In all these cases contamination from secondary production modes have been considered.

	\mathcal{R}_1	\mathcal{R}_2	\mathcal{R}_3
Numerator	2.5% ($\gamma\gamma$ in ggF)	9.1% ($\gamma\gamma$ in VBF)	3.1% ($Z\gamma$ in ggF)
Denominator	3.4% (WW^* in ggF)	5.0% ($\gamma\gamma$ in WH)	2.8% (WW^* in ggF)

Table 5.4: Systematic uncertainties used in our analysis to compute the total uncertainties related to the three observables. The numbers shown here are combination of various types of relevant systematic uncertainties added in quadrature taken from Refs. [50, 60, 61].

of surviving events after the selection cuts in the SM at 14 TeV with 3000 fb^{-1} integrated luminosity. These numbers are taken from Refs. [58, 59] except for the $\gamma\gamma$ channel in the VBF production mode, which we estimate by applying a fixed p_T -cut (keeping other cuts are same as in Ref. [58] of 50 GeV on both the tagged jets instead of η -dependent jet selection cuts as used in the same reference. We also use some systematic uncertainties in our analysis as listed in Table 5.4 (Refs. [50, 60, 61]). In all these cases, we have considered the effects of signal contamination as given in Refs. [58, 59]. While computing the statistical uncertainties, the number of ATLAS events have been doubled to roughly take into account the contribution from CMS. In the future, it is quite expected, various systematic uncertainties will reduce by improving their modelling. In order to be conservative, we have used various important uncorrelated systematic uncertainties as used in Refs. [50, 60, 61] for 7+8 TeV analysis. For the observable \mathcal{R}_1 , since we are applying same jet veto (*i.e.* 0-jet category), the systematic uncertainties related to the jet energy scale, jet vertex fraction etc. will not be present. On the other hand, due to the different final state, systematic uncertainties related to the photon and lepton identification and isolation, missing energy trigger etc. will remain. In a similar fashion, for \mathcal{R}_2 and \mathcal{R}_3 various correlated systematic uncertainties will cancel between their respective numerator and denominator.

Next, we consider the ratio \mathcal{R}_1 in the light of both the existing data and those predicted for the high energy run. For \mathcal{R}_2 and \mathcal{R}_3 , only a discussion in terms of 14 TeV rates is relevant, as the currently available results have insufficient statistics on these.

5.3.1 \mathcal{R}_1 @ 7+8 TeV

Before predicting the bounds from the 14 TeV HL run, let us form an idea about the constraints from the 7+8 TeV Higgs data from ATLAS and CMS. The $\gamma\gamma$ [60, 62] and WW^* [61, 63] channels are used for this. We compute all the surviving correlated theory errors and subtract them in quadrature from the errors in the numerator and denominator of the ratio \mathcal{R}_1 , *viz.* $\mathcal{R}_1^{num.} =$

Experiment	$\mu(H \rightarrow \gamma\gamma)$ in ggF	$\mu(H \rightarrow WW^* \rightarrow 2\ell\cancel{E}_T)$ in ggF
ATLAS (@ 7+8 TeV)	$1.32^{+0.38}_{-0.38}$	$1.02^{+0.29}_{-0.26}$
CMS (@ 7+8 TeV)	$1.12^{+0.37}_{-0.32}$	$0.75^{+0.29}_{-0.23}$
Combined	1.21 ± 0.26	0.88 ± 0.19

Table 5.5: Measured Higgs Signal strengths in the $\gamma\gamma$ and WW^* modes where Higgs is produced through ggF channel using $\sqrt{s} = 7 + 8$ TeV data by ATLAS [60, 61] and CMS [62, 64].

$\mu_{H \rightarrow \gamma\gamma}^{ggF} \times (\sigma_{ggF} \times BR_{H \rightarrow \gamma\gamma})^{SM}$ and $\mathcal{R}_1^{den.} = \mu_{H \rightarrow WW^*}^{ggF} \times (\sigma_{ggF} \times BR_{H \rightarrow WW^*})^{SM} \times \sum_{\ell} BR_{W \rightarrow \ell\nu_\ell}^2$.⁴ In Fig. 5.3, the red line is the theoretically computed \mathcal{R}_1 which is independent of the centre of mass energy since \mathcal{R}_1 is actually a ratio of two BRs. The outer (light green) band shows the uncertainty comprising of the uncorrelated theoretical, statistical and systematic parts and the inner (dark green) band represents the total uncorrelated theory uncertainty. The black dashed line gives the experimental central value of \mathcal{R}_1 . The ratio, \mathcal{R}_1 is almost completely dominated by $BR_{H \rightarrow \gamma\gamma}$ (since $BR_{H \rightarrow WW^*}$ is not so sensitive on HDOs) and therefore highly sensitive to the operators O_{WW} and O_{BB} . The parabolic nature of the $BR_{H \rightarrow \gamma\gamma}$ as functions of f_{WW} and f_{BB} leads to two disjoint allowed ranges of $f_{WW} = f_{BB} \approx [-3.32, -2.91] \cup [0.12, 0.57]$ as shown in Fig. 5.3. We should mention that the region between these two allowed ranges shows extremely low values of $BR_{H \rightarrow \gamma\gamma}$ because of destructive interference between the SM and HDO might leads to poor statistics. If both O_{WW} and O_{BB} are present simultaneously with almost equal magnitude and opposite signs, the observable \mathcal{R}_1 closely mimics the SM expectation, and to probe that ‘special’ region of parameter space we need to go for other observable like \mathcal{R}_2 . The operators O_W and O_B are mostly insensitive to this observable mainly because $BR_{\gamma\gamma}$ is independent of these operators and the dependence of BR_{WW^*} on all four operators is comparatively weak (see Fig. 5.2a).

5.3.2 \mathcal{R}_1 @ 14 TeV

Next, we present a projected study of \mathcal{R}_1 for the 14 TeV run at 3000 fb^{-1} of integrated luminosity. It should be noted here that the systematic uncertainties used here are for the 8 TeV run and we have assumed that they will not change significantly for the HL-LHC at 14 TeV. The inner bands, more clearly noticeable in the Fig. 5.4b, contain only the uncorrelated theoretical

⁴For instance, the error associated with combined (ATLAS+CMS) $\mu^{ggF}(H \rightarrow \gamma\gamma)$ *i.e.* ± 0.26 consists of theoretical, statistical and systematic uncertainties and, by subtracting the CThU (± 0.13) in quadrature we get (± 0.22) which will finally contribute to the uncertainty related to the numerator of \mathcal{R}_1 .

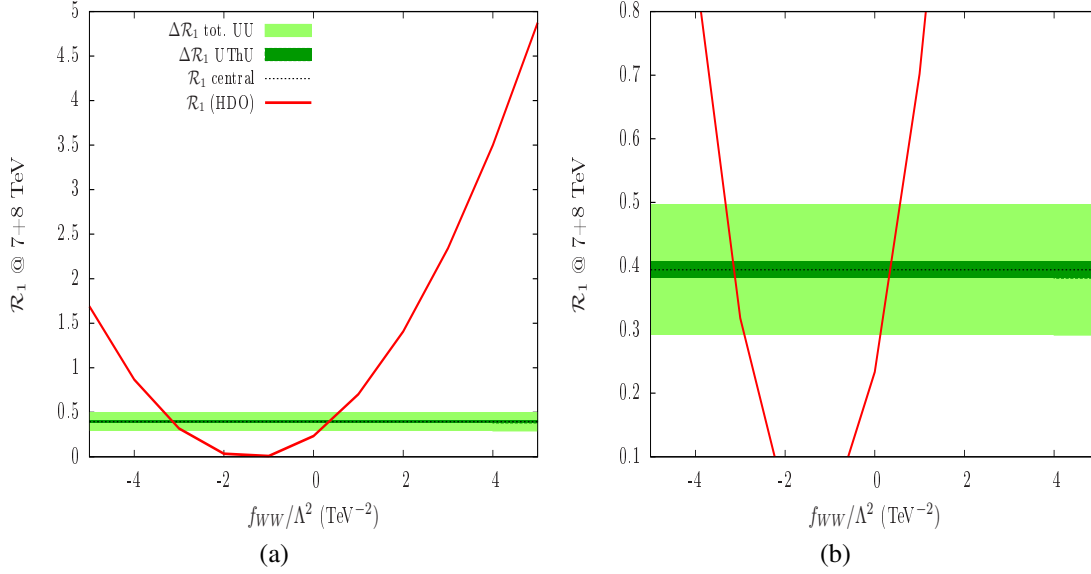


Figure 5.3: (a) \mathcal{R}_1 versus f_{WW}/Λ^2 (TeV^{-2}) and (b) same plot in magnified scale. Plots (a) and (b) are identical for f_{BB}/Λ^2 . The red line is the theoretical expectation in presence of HDOs. The inner band (dark green) shows the uncorrelated theoretical uncertainty (UThU) and the outer (light green) band shows the total surviving uncorrelated uncertainty (UU) (uncorrelated theoretical + statistical + systematic) at 7+8 TeV computed using the $\mu_{\gamma\gamma}$ and μ_{WW^*} (CMS+ATLAS) results. The black dotted line is the corresponding central value.

errors, while the statistical and systematic errors are compounded in the outer bands. Clearly, the uncertainty gets reduced, as compared to \mathcal{R}_1 (@ 7 + 8 TeV), and we get an even smaller window around f_{WW} and $f_{BB} \approx [-2.75, -2.66] \cup [-0.06, 0.03] \text{TeV}^{-2}$ as shown in Fig. 5.4. The difference in this case is that the projected band is around the SM in contrast to what was shown for the 7+8 TeV case, where the ratio of the experimental signal strengths was treated as the reference.

5.3.3 \mathcal{R}_2 @ 14 TeV

We now show the potential of \mathcal{R}_2 in deriving bounds on some of the operator coefficients at 14 TeV. As is evident from Eq. (5.5), this ratio has the capacity to probe \mathcal{O}_W which cannot be constrained from \mathcal{R}_1 . On the other hand, the operator \mathcal{O}_{BB} , though amenable to probe via \mathcal{R}_1 , fails to show any marked effect on \mathcal{R}_2 because $\text{BR}_{H \rightarrow \gamma\gamma}$ gets cancelled in the ratio as defined by us. Also, \mathcal{O}_{BB} does not modify σ_{WH} but, \mathcal{R}_2 is however sensitive to the operator \mathcal{O}_{WW} as both

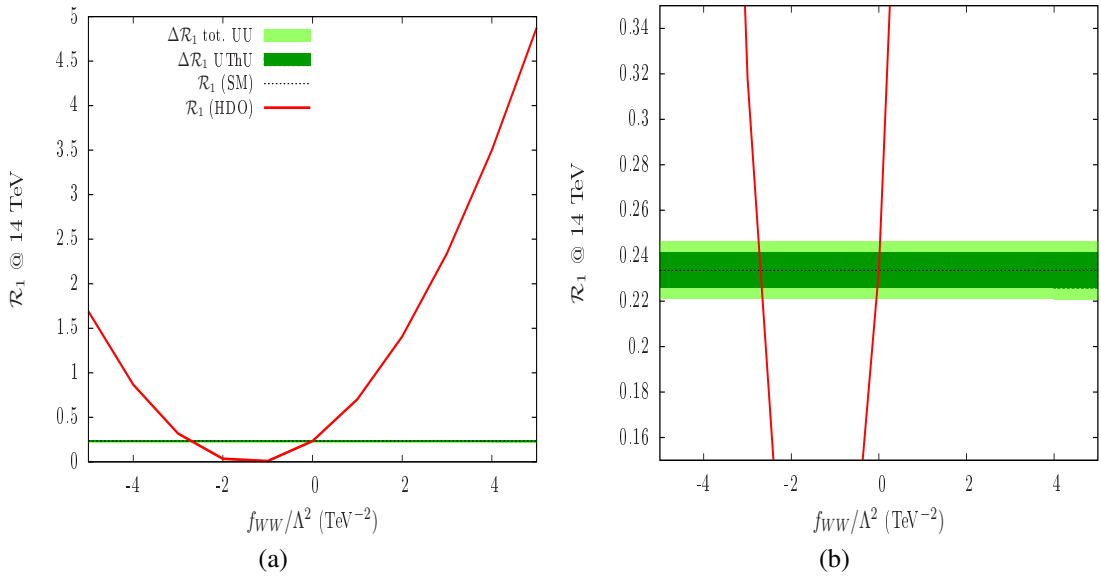


Figure 5.4: (a) \mathcal{R}_1 versus f_{WW}/Λ^2 (TeV^{-2}) and (b) same plot in magnified scale. Plots (a) and (b) are identical for f_{BB}/Λ^2 . The red line is the theoretical expectation in presence of HDOs. The inner band (dark green) shows the uncorrelated theoretical uncertainty (UThU) and the outer band (light green) shows total uncorrelated uncertainty (UU) (uncorrelated theoretical + statistical + systematic) at 14 TeV with 3000 fb^{-1} integrated luminosity. The black dotted line is the corresponding central value.

σ_{VBF} and σ_{WH} are sensitive to this.

By closely following the ATLAS analyses in the context of high luminosity LHC run, we have used a trigger cut of 50 GeV on jet p_T , instead of using η -dependent p_T cut for jets as used in Ref. [58]. The reason is that, a flat cut on the p_T will most certainly give us a less pessimistic number of final state events than that for the η dependent p_T cuts and performs as good as the η -dependent cut to suppress the background. So, we estimate a slightly larger number of events, *i.e.* we obtain a better efficiency to the cuts for the flat p_T case as compared to what is predicted by ATLAS. For the WH production mode, we use a matched sample with $WH+0, 1, 2$ jets with the W decaying leptonically. Finally we demand samples with a maximum of one jet in our analysis. In selecting this 0 + 1 jet sample, from a matched two jet sample, we encounter another theoretical scale uncertainty as described in Ref. [65]. We have estimated

this uncertainty as follows:

$$\Delta^{th.} = \frac{\sigma(pp \rightarrow WH + \geq 2 \text{ jets})}{\sigma^{NNLO}(pp \rightarrow WH)} \Big|_{m_H} \times \Delta\sigma(pp \rightarrow WH + \geq 2 \text{ jets})(\mu_F, \mu_R), \quad (5.7)$$

where $\Delta\sigma(pp \rightarrow WH + \geq 2 \text{ jets})$ is the maximum deviation of the exclusive 2-jet cross-section computed at $\mu_F = \mu_R = m_H$ from the ones computed by varying μ_F and μ_R between $m_H/2$ and $2m_H$.

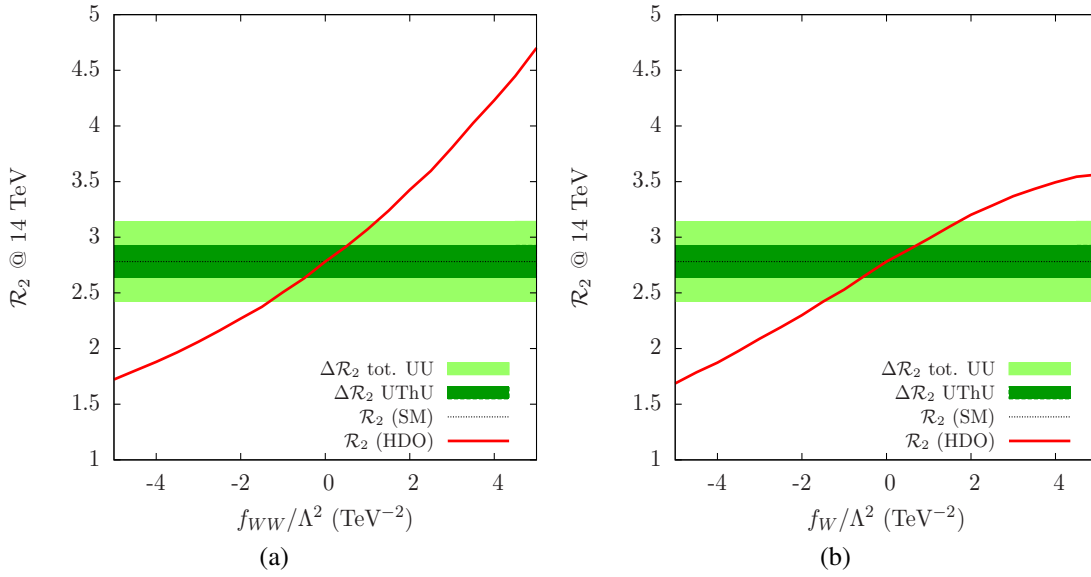


Figure 5.5: The ratio, \mathcal{R}_2 versus (a) $f_{WW}/\Lambda^2 (\text{TeV}^{-2})$, (b) $f_W/\Lambda^2 (\text{TeV}^{-2})$ for the 14 TeV analysis with 3000 fb^{-1} . The red line is the theoretical expectation in presence of HDOs. The inner band (dark green) shows the uncorrelated theoretical uncertainty due to PDF+ α_s , QCD-scale and $\Delta^{th.}$ which is defined in Eq. (5.7). The outer band (light green) shows the uncertainties due to the statistical, systematic compounded with the uncorrelated theoretical part. The black dotted line is the corresponding SM value.

In constructing \mathcal{R}_2 , we include the modified cut-efficiencies [45, 66] for both the VBF and WH channels. Even though we stick to small values of f_i where the modification in such efficiencies from the SM-values are small, we still incorporate these to make the study more rigorous. In computing the statistical uncertainties, we took the relevant numbers from the 14 TeV projected study done by ATLAS (see Refs. [58, 59]). Besides, we also suggest tagging a single jet for VBF , which reduces the statistical uncertainty by a factor of $\sqrt{2}$ [67]. In Fig. 5.5, we present \mathcal{R}_2 as a function of the f_{WW} and f_W taken one at a time for an integrated luminosity of

$\mathcal{L} = 3000 \text{ fb}^{-1}$. The outer band (light green) shows the uncertainties due to the statistical, systematic compounded with the uncorrelated theoretical part. The central black dashed line shows the SM expectation for \mathcal{R}_2 . We can see in Fig. 5.5 that very small values of HDO coefficients can be probed by measuring the observable \mathcal{R}_2 . For f_{WW} , one can corner the allowed region to a small window of $[-1.32, +1.21]$ and for f_W the range would be $[-1.51, +1.72]$. Predicting the observability of such small values in the parameter coefficients is definitely an improvement on existing knowledge.

5.3.4 \mathcal{R}_3 @ 14 TeV

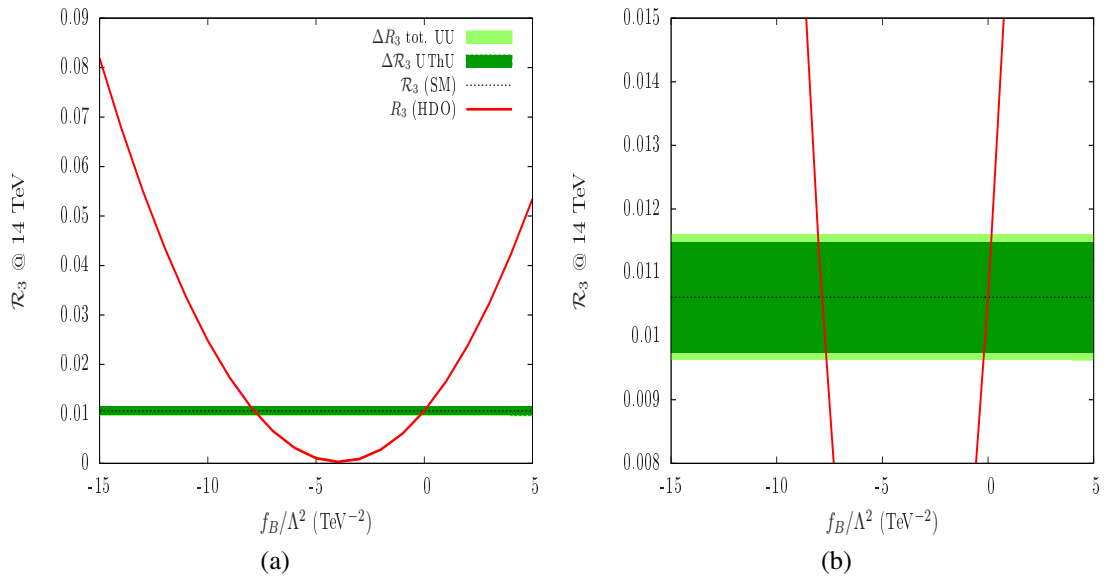


Figure 5.6: The ratio, \mathcal{R}_3 versus f_B/Λ^2 (TeV⁻²) at 14 TeV with 3000 fb⁻¹. The red line is the theoretical expectation in presence of HDOs. The inner band (dark green) shows the uncorrelated theoretical uncertainty (UThU) and the outer band (light green) shows the total uncorrelated uncertainty (UU) due to statistical, systematic and the uncorrelated theoretical part. These uncertainty bands are for \mathcal{R}_3 at 14 TeV. The black dotted line is the corresponding SM value.

The operator O_B appears only in the HZZ and $HZ\gamma$ couplings, As seen in Fig. 5.2b, the sensitivity of O_B is too low and hence $H \rightarrow ZZ^*$ will not give a proper bound on f_B/Λ^2 . Recent experiment by ATLAS (CMS) puts bounds on the observed signal strength of $H \rightarrow Z\gamma$ at about 11 (9.5) times the SM expectation at 95% confidence level [50, 51]. Instead of using these weak signal strengths, we perform an analogous projected study of \mathcal{R}_3 at 14 TeV

Observables	O_{WW}	O_{BB}	O_W	O_B
\mathcal{R}_1 @ 7+8 TeV	$[-3.32, -2.91]$ \cup $[+0.12, +0.57]$	$[-3.32, -2.91]$ \cup $[+0.12, +0.57]$	Not bounded	Not bounded
\mathcal{R}_1 @ 14 TeV	$[-2.75, -2.66]$ \cup $[-0.06, +0.03]$	$[-2.75, -2.66]$ \cup $[-0.06, +0.03]$	Not bounded	Not bounded
\mathcal{R}_2 @ 14 TeV	$[-1.32, +1.21]$	Not bounded	$[-1.51, +1.72]$	Not bounded
\mathcal{R}_3 @ 14 TeV	Not used	Not used	Not used	$[-8.04, -7.63]$ \cup $[-0.21, +0.17]$

Table 5.6: We summarize our obtained allowed region of the coefficients of HDOs using the three observables.

in the same spirit as \mathcal{R}_1 at 14 TeV. From Fig. 5.6, we find that the projected bounds on f_B/Λ^2 is $[-8.04, -7.63] \cup [-0.21, +0.17]$. The region in between is again inaccessible due to poor statistics, as in this region, $\text{BR}_{H \rightarrow Z\gamma}$ becomes insignificant, the reasons being similar to those mentioned for $H \rightarrow \gamma\gamma$. The inner band (dark green) includes the uncorrelated theoretical uncertainties due to the partial decay widths of $H \rightarrow Z\gamma$ and $H \rightarrow WW^*$. The outer band (light green), in addition to the theoretical uncertainties, contains the statistical and systematic uncertainties. The statistical uncertainties were computed by doubling the number of events as shown in Table 5.3 to approximately incorporate the CMS data. As discussed earlier, a few types of correlated systematic uncertainties related to the uncertainty in luminosity, lepton identification and isolation etc. will get cancelled in the ratio \mathcal{R}_3 . On the other hand, photon identification, isolation etc. uncertainties will be retained in the analysis.

In Table 5.6, we summarize our obtained region of the parameter space allowed using three ratios, \mathcal{R}_1 , \mathcal{R}_2 and \mathcal{R}_3 . We present \mathcal{R}_1 using combined ATLAS+CMS data for 7+8 TeV run. We also present a projected study for all three observables at 14 TeV with an integrated luminosity of 3000 fb^{-1} . The allowed regions on f_{WW} and f_{BB} shrink at the 14 TeV 3000 fb^{-1} run as compared to the current data. Using the ratio, \mathcal{R}_2 one can also put bounds on f_{WW} and f_W . As mentioned earlier, there is a ‘special’ region of parameter space where \mathcal{R}_1 mimics the SM expectation, therefore, \mathcal{R}_2 can also be used to infer the presence of O_{WW} with ‘special’ values of coefficient f_{WW} . The operator O_B does not show any appreciable sensitivity in any production of Higgs or its decay except in the $\text{BR}_{H \rightarrow Z\gamma}$. Therefore, the ratio \mathcal{R}_3 is constructed to constrain f_B by a significant amount, as evident from Table 5.6.

5.4 Summary and conclusions

We have investigated how well one can constrain dimension-6 gauge-invariant operators inducing anomalous HVV interactions. Probing the gauge invariant operators individually, we feel, are important, since they can point at any new physics above the electroweak symmetry breaking scale. While the operators contributing to $H \rightarrow \gamma\gamma$ are subjected to the hitherto strongest limits using the (7+8) TeV data, the remaining ones are relatively loosely constrained, in spite of the bounds coming from precision electroweak observables. At any rate, it is necessary to reduce uncertainties as much as possible, since any realistically conceived new physics is likely to generate such operators with coefficients no greater than $\approx O(1) \text{ TeV}^{-2}$. We show that a good opportunity to probe them at this level, and improve spectacularly over the existing constraints, arises if event ratios in various channels are carefully studied. These include both ratios of events in different final states with the same Higgs production channel and those where a Higgs produced by different production modes ends up decaying into the same final state. While a majority of the theoretical uncertainties cancel in the former category, the latter allow us to probe those cases where some dimension-6 operators shift the rates in the numerator and the denominator in opposite directions. We find that, after a thorough consideration of all uncertainties, all the couplings can be pinned down to intervals of width $\approx O(1) \text{ TeV}^{-2}$ on using 3000 fb^{-1} of integrated luminosity at 14 TeV. Even with 300 fb^{-1} , improvement over existing constraints is clearly expected, and the results are more uncertainty-free than in any other hitherto applied method. However, we must mention here that this approach should be complemented with the study of differential distributions as well, as suggested widely in works cited above.

Chapter 6

Higher-dimensional operators at electron-positron colliders¹

6.1 Motivation

We have discussed several strategies of probing non-standard Higgs interactions at a hadron collider, namely, the LHC. In view of the cumulative demand for a closer probe on the HVV couplings (and of course the couplings to other SM particles), another desirable endeavour, however, is to build an electron-positron collider which provides a clean environment for precise measurements of Higgs interaction strengths. An important step in this context is of course to develop a Higgs factory (at $\sqrt{s} \approx 250 - 300$ GeV). Such a machine will not only produce the Higgs boson copiously near resonance, but is also the first step before an e^+e^- machine at even higher energies is developed. In this chapter, we incorporate some observations regarding the signatures of anomalous HVV couplings, manifest through higher dimensional operators (HDOs), at a Higgs factory. Other studies performed for an e^+e^- machine can be found in [1]. This possibility has been explained in the context of an ep collider too [2, 3].

¹ This chapter is based on the paper *Exploration of the Tensor Structure of the Higgs Boson Coupling to Weak Bosons in e^+e^- Collisions* by Gilad Amar, Shankha Banerjee, Stefan von Buddenbrock, Alan S. Cornell, Tanumoy Mandal, Bruce Mellado and Biswarup Mukhopadhyaya, JHEP **1502**, 128 (2015), [arXiv:1405.3957 [hep-ph]]

As already stated, if the couplings arise through physics at a scale higher than that of electroweak symmetry breaking, then the resulting higher-dimensional effective interactions are expected to be gauge invariant. Such interactions have not only been identified, but constraints on their coefficients have also been obtained from the LHC data [4–9]. In view of such analyses, the coefficients are often restricted to such values where many cherished kinematic distributions may fail to reveal their footprints. In the current study, we point out some features which influence the detectability (or otherwise) of the higher-dimensional couplings at a Higgs factory. At the same time, we emphasise some possible measurements that can elicit their signatures even for relatively small coefficients of such operators.

We concentrate on two Higgs production channels, namely, $e^+e^- \rightarrow ZH$ (the s -channel process) and $e^+e^- \rightarrow \nu\bar{\nu}H$ (the t -channel process, which we separate with the help of a simple kinematic cut around the Higgs boson energy). In principle, the HDOs that will constitute our report can influence the rates in both channels. In contrast, the most obvious kinematic distributions, namely, those based on the angular dependence of matrix elements, drawn with moderate values of their coefficients do not show a perceptible difference with respect to the SM situation. Keeping this in view, we underscore the following points here:

1. The s -channel process has substantial rates at ≤ 300 GeV or thereabout. We show, through an analysis of the production amplitude squared, why one cannot expect significantly different angular distributions in this channel at such energies, if one uses moderate values of the operator coefficients.
2. The t -channel process can have appreciable production rates at high energies (\approx a TeV), too. Because of the production of two neutrinos in the final state, this process provides limited phase-space for the exploration of the tensor structure of the HWW coupling. Here it is attempted to exploit the full kinematics of the Higgs boson by means of a correlated two-dimensional likelihood analysis.
3. We show that, given such impediment, it is possible to uncover signatures of the aforementioned BSM operators through measurements of rates at two different energies, which also cancels many systematic uncertainties. In general, the energy dependence of the rates can be sensitive to anomalous couplings.
4. The very fact that the additional operators should be electroweak gauge invariant imply not only higher-dimensional HVV interactions ($V = W, Z, \gamma$) but also anomalous WWW

interactions ($V = Z, \gamma$) whose strengths are related to the former. We show that the concomitant variations in Higgs production and W -pair production at Higgs factories may elicit the presence of such BSM interactions.

5. We also show that if the centre-of-mass energy (CME) of the colliding particles is ≈ 500 GeV or more, then even moderate values of the operator coefficients can show some differences in the kinematic distributions.
6. Lastly, we perform the analysis in a framework that allows one to retain all the gauge-invariant operators at the same time.

The gauge invariant operators are discussed in section 4.2. A slightly different formalism is discussed in section 6.2. In section 6.3, we take up the s and t -channel Higgs production cross-sections in turn, and explain why one cannot expect too much out of kinematic distributions at Higgs factory energies, so long as the BSM coupling coefficients are subject to constraints imposed by the LHC data. Their detectable signatures through event ratios at two energies, and also via the simultaneous measurement of W -pair production are predicted in section 6.3. A likelihood analysis and some related issues, mostly in terms of the phenomenological forms to which all new couplings reduce, are found in section 6.4. We summarise our conclusions in section 6.5.

6.2 Effective Lagrangian Formalism

In this chapter, we adopt two types of effective Lagrangian parametrizations which are commonly used in the literature to probe the anomalous HVV (where $V = W, Z, \gamma$) interactions. In one parametrization, we take the most general set of dimension-6 gauge invariant operators which give rise to such anomalous HVV interactions. In the other one, we parametrize the HVV vertices with the most general Lorentz invariant structure. Although, this formalism is not the most transparent one from the viewpoint of the gauge structure of the theory, it is rather simple and more experiment-friendly. Both formalisms modify the HVV vertices by introducing non-standard momentum-dependent terms.

We assume that the SM is a low-energy effective theory of a more complete perturbation theory valid below a cut-off scale Λ . In the present study, we are concerned mainly with the Higgs sector. The first order corrections to the Higgs sector will come from gauge invariant

dimension 6 operators as there is only one dimension-5 operator which contributes to the neutrino masses. The relevant additional Lorentz structures in HVV interactions are necessarily of dimensions higher than four. If they arise as a consequence of integrating out physics at a higher scale, all such operators will have to be invariant under $SU(2)_L \times U(1)_Y$. A general classification of such operators is found in the literature [10–13]. The lowest order CP-conserving operators which are relevant for Higgs phenomenology are discussed in section 4.2.

Hence for the Higgs sector, we will choose our basis as $O_i \in \{O_{WW}, O_W, O_{BB}, O_B\}$. In the presence of the above operators, the Lagrangian is parametrised as

$$\mathcal{L} = \kappa \left(\frac{2m_W^2}{v} HW_\mu^+ W^{\mu-} + \frac{m_Z^2}{v} HZ_\mu Z^\mu \right) + \sum_i \frac{f_i}{\Lambda^2} O_i \quad (6.1)$$

where κ is the scale factor of the SM-like coupling (please note that a different notation β has been used in chapters 3 and 4), something which needs to be accounted for when considering BSM physics. f_i is a dimensionless coefficient which denotes the strength of the i^{th} operator and Λ is the cut-off scale above which new physics must appear. We keep κ to be the same for the HWW and HZZ couplings so that there is no unacceptable contribution to the ρ -parameter. Another operator considered in this chapter is $O_{WWW} = Tr[\hat{W}_{\mu\nu} \hat{W}^{\nu\rho} \hat{W}_\rho^\mu]$. This only affects the triple gauge boson couplings and does not affect the Higgs sector.

The effective Lagrangian which affects the Higgs sector is discussed in equation 4.5 in section 4.2.

The operators O_W , O_B and O_{WWW} contribute to the anomalous triple gauge boson interactions. The interactions are also summarised in equation 4.7 in section 4.2.

The possibility of modified cut efficiencies in the presence of such operators have been discussed in great detail in chapter 4.

All of the aforementioned HDOs lead essentially to one effective coupling (each for HWW and HZZ), when CP-violation is neglected. These can be alternatively used in a phenomenological way for example, the $H(k)W_\mu^+(p)W_\nu^-(q)$ vertex can be parametrised as [14]:

$$i\Gamma^{\mu\nu}(p, q)\epsilon_\mu(p)\epsilon_\nu^*(q), \quad (6.2)$$

where deviations from the SM form of $\Gamma_{SM}^{\mu\nu}(p, q) = -gM_W g^{\mu\nu}$ would indicate the presence of BSM physics. These BSM deviations, including CP-violating ones (not considered among the

gauge invariant operators), can be specified as

$$\Gamma_{\mu\nu}^{BSM}(p, q) = \frac{g}{M_W} [\lambda(p_\nu q_\mu - p_\nu q_\mu) + \lambda' \epsilon_{\mu\nu\rho\sigma} p^\rho q^\sigma], \quad (6.3)$$

where λ and λ' are the effective strengths for the anomalous CP-conserving and CP-violating operators respectively.

Precise identification of the non-vanishing nature of λ, λ' is a challenging task. If ever accomplished, it can tell us whether the modification in HVV -couplings are CP -conserving or CP -violating in nature and, if both are present, what their relative proportion is. Here we analyse the process $e^+e^- \rightarrow H\nu\bar{\nu}$ and see if there is any BSM physics involved by incorporating a likelihood analysis of the SM hypothesis tested against BSM hypotheses.

A few comments are in order on the two ways of parametrizing the anomalous Higgs couplings. The latter, of course, encapsulates all possible modified Lorentz invariant couplings in the lowest possible order, including both CP -conserving and CP -violating ones, in the coefficients λ and λ' respectively. All of the anomalous HWW and HZZ couplings listed in the gauge-invariant formulation reduce basically to one term if one confines oneself to a CP -conserving scenario. Thus we can say that the latter parametrization shows us a rather ‘economic’ way of relating the anomalous HVV interactions to collider phenomenology. On the other hand, the process of relating the anomalous couplings to specific effective interactions is more transparent from the viewpoint of gauge structures when one uses the gauge invariant HDOs. It paves an easier path towards understanding the ultraviolet completion of the scenario. In addition to this, the formulation in terms of gauge-invariant operators relates the anomalous HWW and HZZ interactions. One finds, in this way, a pattern in the departure of the ZH and $\nu\bar{\nu}H$ final state production rates from the corresponding SM prediction. Finally, some of the gauge-invariant operators lead simultaneously to anomalous triple gauge boson interactions. There is thus an associated variation in the ZH , $\nu\bar{\nu}H$ and W^+W^- production rates as well as in the kinematic distributions associated with each final state. Such an association enables one to use various pieces of data to determine each new operator.

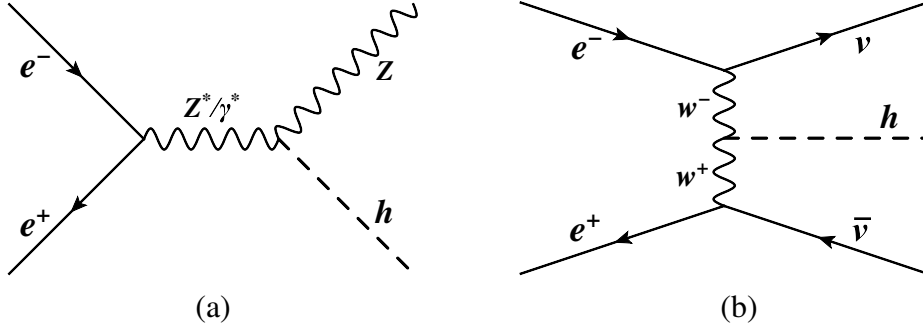


Figure 6.1: (a) s -channel Feynman diagrams (b) t -channel Feynman Diagram.

6.3 Phenomenology at an e^+e^- Collider

In this section, we discuss various important Higgs production mechanisms through HVV vertices at an e^+e^- collider. For the collider phenomenology, we have implemented the Lagrangians of Eqs. (4.5) and (4.7) in FeynRules [15] to generate Universal FeynRules Model (UFO) [16] files suitable for interfacing with MadGraph [17]. We also use FORM [18] to compute many cross-sections analytically.

6.3.1 Higgs production at an e^+e^- collider

We concentrate on two main Higgs production mechanisms *viz.* $e^+e^- \rightarrow ZH$ and $e^+e^- \rightarrow \nu\bar{\nu}H$, at an e^+e^- collider with energies ranging from 250 GeV to 500 GeV. The $e^+e^- \rightarrow ZH$ channel includes only the s -channel processes – $e^+e^- \rightarrow Z^*/\gamma^* \rightarrow ZH$ (shown in Fig. 6.1(a)). Whereas $e^+e^- \rightarrow \nu\bar{\nu}H$ includes both the s -channel processes, $e^+e^- \rightarrow Z^*/\gamma^* \rightarrow ZH \rightarrow \nu\bar{\nu}H$ as well as the t -channel process $e^+e^- \rightarrow \nu\bar{\nu}W^*W^* \rightarrow \nu\bar{\nu}H$ (WW fusion process as shown in Fig. 6.1(b)).

The s and t -channel processes have different kinematics and hence are affected differently by the inclusion of the HDOs. Moreover, the t -channel process allows us to explore the tensor structure of the HWW vertex alone, free from any contamination from the HZZ and $HZ\gamma$ vertices. On the other hand, the s -channel process is free from any contamination due to the HWW vertex. Hence, the measurement of the s -channel contribution will shed light on the tensorial nature of the HZZ and $HZ\gamma$ vertices. We, therefore, analyse the s and t -channel processes separately to shed more light on the anomalous behaviour of the HVV vertices. We separate the s -channel (t -channel) contribution from the $e^+e^- \rightarrow \nu\bar{\nu}H$ events by applying a simple kinematic

cut on the Higgs energy (E_H) as follows:

$$E_H\text{-cut: } \left| E_H - \frac{s + M_H^2 - M_Z^2}{2\sqrt{s}} \right| \leq \Delta \quad \left(E_H^c\text{-cut: } \left| E_H - \frac{s + M_H^2 - M_Z^2}{2\sqrt{s}} \right| \geq \Delta \right), \quad (6.4)$$

where \sqrt{s} is the CME of the two colliding e^+e^- beams and Δ is an energy-window around E_H . Here, E_H^c -cut is complementary to the E_H -cut. We use $\Delta = 5$ GeV throughout our analysis². We must mention here that for the rest of this chapter the s -channel process will be studied at the ZH level without any cuts, unless otherwise specified. One can easily get an estimate of the cross-section for any decay modes of Z by multiplying the appropriate BR. This is because for the $e^+e^- \rightarrow l^+l^-H$ channel, a simple invariant mass cut on the two leptons about the Z boson mass will separate the s -channel to a very high degree. For $e^+e^- \rightarrow \nu\bar{\nu}H$, on the other hand, the cut on E_H separates the s and t -channels. The s -channel contribution surviving the cut is found to be very close to what one would have found from the rate for l^+l^-H , through a scaling of BRs. One is thus confident that the E_H -cut is effective in minimising mutual contamination of the s and t -channel contributions.

It should also be mentioned here that the effects of beam energy spread are not taken into account in Eq. 6.4 for simplification. While we present the basic ideas of distinguishing anomalous interactions of the Higgs, the relevant energy window for precision studies has to factor in the effects of bremsstrahlung as well as beamstrahlung (depending on whether the Higgs factory is a circular or a linear collider).

In Table 6.1, we show the effect of the E_H -cut on the $\nu\bar{\nu}H$ channel in the SM and in presence of HDOs for one benchmark point, BP1 ($\kappa = 1, f_{WW} = -3, f_W = 8, f_{BB} = -4, f_B = 3$) which closely mimics the SM cross-section. The E_H -cut keeps almost all the s -channel contribution but the E_H^c -cut cuts out a small portion around E_H from the t -channel contribution. Therefore, the s -channel cross-sections after this cut increase slightly from their without-cut values due to this small t -channel contamination. On the other hand, the t -channel cross-sections after cut decrease slightly from their without-cut values. We also estimate the interference between the s and t -channel diagrams and present the numbers in Table 6.1. Interference contribution is expected to be tiny in the \sqrt{s} region sufficiently away from the s -channel threshold energy

²Typical values of Δ can be estimated from the energy uncertainties of the b -jets coming from the Higgs decay. The jet energy uncertainty ΔE_{jet} (1σ) of a jet having energy E_{jet} are related as, $\Delta E_{jet}/E_{jet} \lesssim 0.3/\sqrt{E_{jet}}$ at the ILC [19]. For example, if there are two b -jets each with energy 100 GeV, the total uncertainty in their energy measurement is $\sqrt{2 \times (0.3 \times \sqrt{100})^2} \sim 4$ GeV (added in quadrature).

\sqrt{s} (GeV)	Benchmark point	$\sigma_{\nu\bar{\nu}H}^{tot}$ (fb)	$\sigma_{\nu\bar{\nu}H}^s$ (fb)	$\sigma_{\nu\bar{\nu}H}^t$ (fb)	$\sigma_{\nu\bar{\nu}H}^{int}$ (fb)	$\sigma_{\nu\bar{\nu}H}^{s,ac}$ (fb)	$\sigma_{\nu\bar{\nu}H}^{t,ac}$ (fb)
300	SM	52.43	36.35	17.83	-1.75	37.24	15.19
	BP1	52.11	35.29	18.83	-2.01	36.76	15.35
500	SM	84.80	11.64	74.07	-1.11	11.93	72.83
	BP1	87.38	7.37	81.50	-1.49	7.83	79.55

Table 6.1: We show the total $\nu\bar{\nu}H$ cross-section ($\sigma_{\nu\bar{\nu}H}^{tot}$), only s -channel cross-section ($\sigma_{\nu\bar{\nu}H}^s$), only t -channel cross-section ($\sigma_{\nu\bar{\nu}H}^t$) and their interference contribution ($\sigma_{\nu\bar{\nu}H}^{int}$) for the SM ($\kappa = 1, f_{WW} = 0, f_W = 0, f_{BB} = 0, f_B = 0$) and for HDO benchmark point BP1 ($\kappa = 1, f_{WW} = -3, f_W = 8, f_{BB} = -4, f_B = 3$) for two different CMEs. We also present the s ($\sigma_{\nu\bar{\nu}H}^{s,ac}$) and t -channel ($\sigma_{\nu\bar{\nu}H}^{t,ac}$) cross-sections separated from the $\nu\bar{\nu}H$ events after applying the cut defined in Eq. 6.4. The superscript ac means after cut.

($M_H + M_Z$) ≈ 226 GeV. We find that the interference contribution is only $\sim 3.5\%$ of the total cross-section for $\sqrt{s} = 300$ GeV, in the SM. This re-affirms the statement at the end of the previous paragraph. We also note that the inclusion of HDOs with moderate values of coefficients does not affect this contribution much. Hence, by neglecting the interference term, we approximate the total $\nu\bar{\nu}H$ cross-section as

$$\sigma_{\nu\bar{\nu}H}^{tot} \approx \sigma_{ZH} \times BR_{Z \rightarrow \nu\bar{\nu}} + \sigma_{\nu\bar{\nu}H}^t, \quad (6.5)$$

where σ_{ZH} is the s -channel cross section and $BR_{Z \rightarrow \nu\bar{\nu}}$ is the invisible branching fraction ($\approx 20\%$) of the Z -boson.

Fig. 6.2 shows the invariant mass distribution of the neutrino pair for the process $e^+e^- \rightarrow \nu\bar{\nu}H$ at $\sqrt{s} = 300$ GeV and for the benchmark point BP1. We separately show the distributions for the total process (which includes the s and t channels as well as the interference) and also the s and t channels separately. In an inset plot we show the distribution due to this interference. This clearly shows that it is negligible when compared to the s and t channel contributions. This nature generally holds for the parameter space under consideration.

6.3.2 A general expression for the cross-sections

In this analysis, we keep $\kappa, f_{WW}/\text{TeV}^2, f_W/\text{TeV}^2, f_{BB}/\text{TeV}^2$ and f_B/TeV^2 as free parameters. The HWW vertex depends on three parameters (κ, f_{WW} and f_W) whereas the HZZ and the $HZ\gamma$ vertices depend on five parameters ($\kappa, f_{WW}, f_W, f_{BB}$ and f_B). The κ dependence enters the

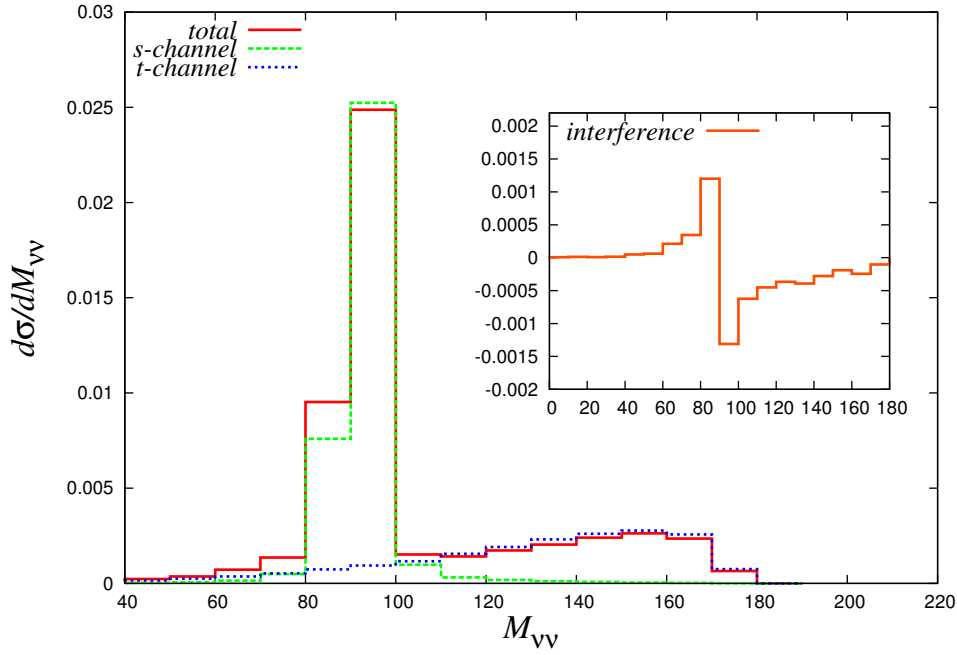


Figure 6.2: Invariant mass distributions of $\nu\bar{\nu}$ of the process $e^+e^- \rightarrow \nu\bar{\nu}H$ at $\sqrt{s} = 300$ GeV and for the benchmark point BP1 ($\kappa = 1, f_{WW} = -3, f_W = 8, f_{BB} = -4, f_B = 3$). The red, green, blue histograms are for the total ($s + t + \text{interference}$), s and t channels respectively. The inset (orange) plot shows the interference ($\text{total} - s - t$) contribution.

$HZ\gamma$ vertex through the W -loop in the effective $HZ\gamma$ vertex. The amplitude for the process $e^+e^- \rightarrow ZH/\nu\bar{\nu}H$ is a linear combination of $x_i \in \{\kappa, f_{WW}, f_W, f_{BB}, f_B\}$ and therefore, the cross-section can always be expressed as a bi-linear form, $\sigma(S, x_i) = \sum_{i,j=1}^5 x_i C_{ij}(S) x_j$, where $C_{ij}(S)$ is the i th element of the coefficient matrix $\mathcal{M}(\sqrt{s})$ at a CME of \sqrt{s} . Hence, the cross-section can be written in the following closed form

$$\sigma(\sqrt{s}) = \mathcal{X} \cdot \mathcal{M}(\sqrt{s}) \cdot \mathcal{X}^T, \quad (6.6)$$

where $\mathcal{X} = (\kappa, f_{WW}, f_W, f_{BB}, f_B)$ is a row vector.

The matrices of coefficients for the $e^+e^- \rightarrow ZH$ process at $\sqrt{s} = 250$ GeV and 300 GeV are

$$\mathcal{M}_{250}^{s,ZH} = \begin{pmatrix} 241.32 & -7.11 & -2.29 & -0.55 & -0.51 \\ -7.11 & 0.35 & 0.13 & -0.02 & -0.05 \\ -2.29 & 0.13 & 0.06 & -0.01 & -0.03 \\ -0.55 & -0.02 & -0.01 & 0.01 & 0.02 \\ -0.51 & -0.05 & -0.03 & 0.02 & 0.04 \end{pmatrix}; \mathcal{M}_{300}^{s,ZH} = \begin{pmatrix} 181.67 & -6.43 & -2.99 & -0.51 & -0.71 \\ -6.43 & 0.46 & 0.18 & -0.03 & -0.08 \\ -2.99 & 0.18 & 0.14 & -0.02 & -0.06 \\ -0.51 & -0.03 & -0.02 & 0.02 & 0.03 \\ -0.71 & -0.08 & -0.06 & 0.03 & 0.08 \end{pmatrix} \quad (6.7)$$

Similar matrices for the t -channel process (after the E_H^c -cut) for the channel $e^+e^- \rightarrow \nu\bar{\nu}H$ at $\sqrt{s} = 250$ GeV and 300 GeV are

$$\mathcal{M}_{250}^{t,\nu\bar{\nu}H} = \begin{pmatrix} 4.63 & 5.2 \times 10^{-3} & 0.02 \\ 5.2 \times 10^{-3} & 2.9 \times 10^{-4} & -1.2 \times 10^{-4} \\ 0.02 & -1.2 \times 10^{-4} & 1.6 \times 10^{-4} \end{pmatrix}; \mathcal{M}_{300}^{t,\nu\bar{\nu}H} = \begin{pmatrix} 15.36 & 0.04 & 0.07 \\ 0.04 & 1.2 \times 10^{-3} & -7.7 \times 10^{-4} \\ 0.07 & -7.7 \times 10^{-4} & 4.6 \times 10^{-4} \end{pmatrix} \quad (6.8)$$

We must mention here that the matrices in Eq. 6.8 are three-dimensional compared to the five-dimensional matrices in Eq. 6.7 because the t -channel only involves the HWW vertex which is not affected by the operators \mathcal{O}_{BB} and \mathcal{O}_B (Eqs. 4.5, 4.6). We also observe that in Eq. 6.7, the coefficients of the matrix related to either f_{BB} or f_B are much less pronounced compared to the coefficients involving the other three parameters, *viz.* κ , f_{WW} and f_W . Also from Eq. 6.8 we see that barring the (1,1) entry in the matrices, all the other coefficients are small implying that the

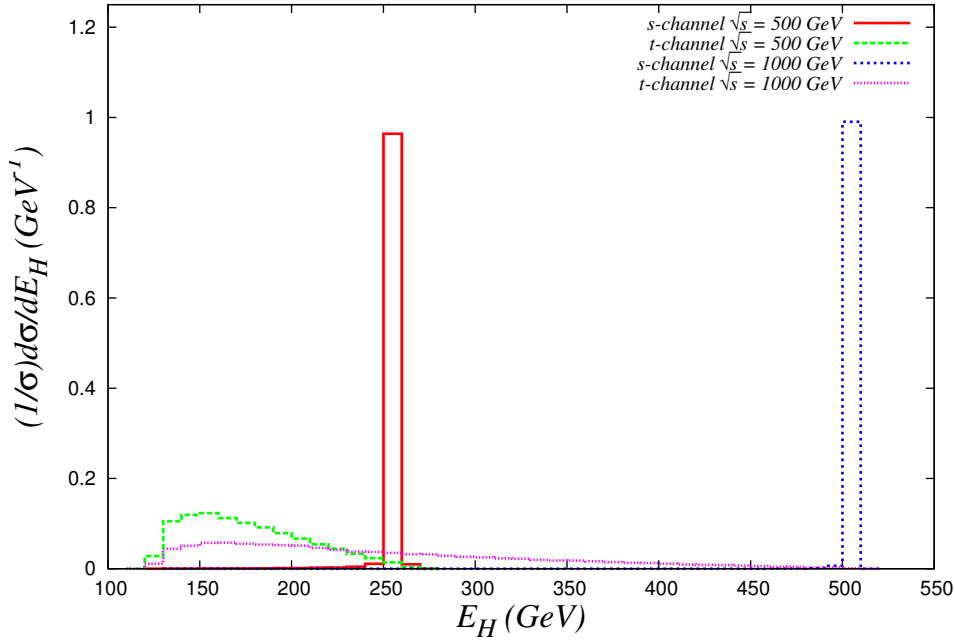


Figure 6.3: Normalised distributions of the Higgs energy (E_H) for the s -channel (red : $\sqrt{s} = 500$ GeV and blue : $\sqrt{s} = 1$ TeV) and t -channel (green : $\sqrt{s} = 500$ GeV and magenta : $\sqrt{s} = 1$ TeV) for the benchmark point BP1.

HDOs will have small but non-negligible effects on the t -channel cross-sections for energies at the Higgs factories.

An explanation of relatively less dependence of the t -channel cross-section compared to the s -channel on the anomalous operators can also be understood from Fig. 6.3. The plots reveal that, for the former process (essentially a vector boson fusion channel), the Higgs emerges with much smaller energy. The higher-dimensional couplings, on the other hand, contain derivatives which translate into a direct dependence on the energy of the Higgs, thus putting the t -channel process at a relative disadvantage. The Higgs energy distribution shows a longer tail for higher centre-of-mass energies, thus offering a partial recompense to the t -channel process for an energy as high as a TeV.

In this study we also consider the process $e^+e^- \rightarrow W^+W^-$ which involves the triple-gauge boson vertices $WW\gamma$ and WWZ . These are concomitantly affected by the operators \mathcal{O}_W and \mathcal{O}_B . Besides, as mentioned in section 4.2, such vertices are also affected by the operator \mathcal{O}_{WWW} which does not affect the Higgs sector. In the basis of $x_i^{WW} \in \{1, f_W, f_B, f_{WWW}\}$, the coefficient

matrix at $\sqrt{s} = 300$ GeV is given by

$$\mathcal{M}_{300}^{WW} = \begin{pmatrix} 13.48 & 1.10 \times 10^{-2} & 5.65 \times 10^{-3} & 4.24 \times 10^{-3} \\ 1.10 \times 10^{-2} & 4.98 \times 10^{-4} & 5.27 \times 10^{-5} & 2.02 \times 10^{-4} \\ 5.65 \times 10^{-3} & 5.27 \times 10^{-5} & 1.17 \times 10^{-4} & 1.96 \times 10^{-5} \\ 4.24 \times 10^{-3} & 2.02 \times 10^{-4} & 1.96 \times 10^{-5} & 8.18 \times 10^{-4} \end{pmatrix}. \quad (6.9)$$

As we can see above, all the C_{ij} s are very small when compared to C_{11} , which gives us the SM cross-section. We will discuss this channel in more details later in this chapter.

6.3.3 Energy dependence of s and t -channel cross-sections

It is well-known that in SM, the cross-section for the s -channel falls with the CME as $1/S$ and that for the t -channel, rises as $\ell n S$ [20]. However, for sets of values of our parameters, different from the SM, the nature of the s -channel curve can be completely different from its SM-counterpart. The t -channel cross-section however is not affected so significantly on the introduction of HDOs as has been discussed in detail in the previous sub-section. We show the variation of the s and t -channel processes for \sqrt{s} ranging from 250 GeV to 900 GeV. In contrast to the SM nature of a fall in the s -channel cross-section with energy, the introduction of HDOs does in no way ensure such a nature which can be seen in Fig.6.4 (a) for two benchmark points (BP2 ($x_i \in \{1, 0, 5, 0, 0\}$) and BP3 ($x_i \in \{1, 0, -5, 0, 0\}$)) alongside the SM. The above two benchmark points have been chosen as the cross-sections are quite sensitive to f_W and the two points are allowed from EWPT constraints. On the whole it is clear from the diagrams that the ratio of the s and t -channel cross-sections in some channel at a particular energy can be an important probe to the nature of new Higgs couplings³

6.3.4 More information from the total rates

The total rates and their ratios at different CMEs can be important probes to identify the tensor structure of the HVV couplings. We show how the total rates for the s and t -channel processes are affected on the introduction of the effective operators (Eqs. 6.7 and 6.8).

³The visible rise with \sqrt{s} (in Fig.6.4(a) for the benchmark points BP2 and BP3) does not threaten unitarity, since the additional degrees of freedom responsible for the effective operators take care of it when \sqrt{s} approaches Λ . The rise is not noticeable if one has the operators O_{WW}/O_{BB} instead of O_W/O_B . The different momentum dependence in the former case tames the rise with \sqrt{s} as can be verified from the corresponding Feynman rules in [13].

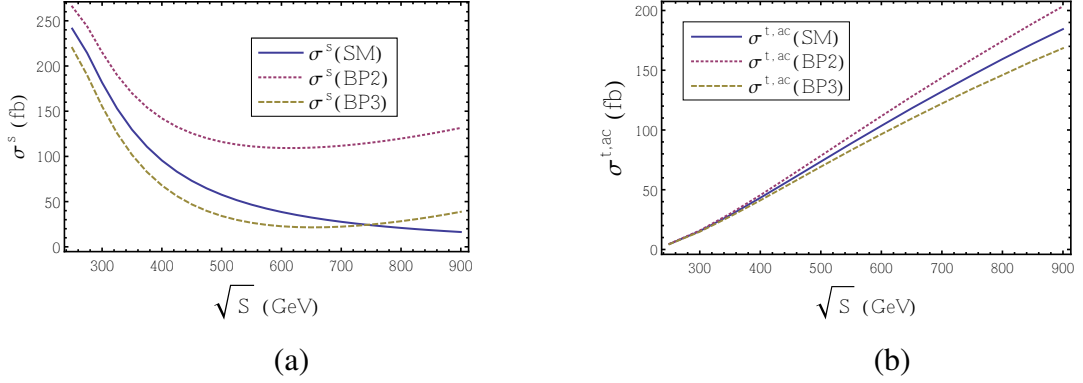


Figure 6.4: (a) : σ^s (in fb) for the channel $e^+e^- \rightarrow ZH$ and (b) : $\sigma^{t,ac}$ (in fb) for the channel $e^+e^- \rightarrow \nu\bar{\nu}H$ as functions of the CME, \sqrt{s} . The cross-sections have been computed for three benchmark points, viz. SM ($x_i \in \{1, 0, 0, 0, 0\}$), BP2 ($x_i \in \{1, 0, 5, 0, 0\}$) and BP3 ($x_i \in \{1, 0, -5, 0, 0\}$). The superscript ac denotes the after cut scenario.

We must make a statement about the values of the coefficients, f_i/Λ^2 (i is the index of the operator under consideration) chosen in the rest of the chapter. In most cases, f_i/Λ^2 is allowed to vary in the range $[-20, 20] \text{ TeV}^{-2}$. Now, a reasonable criterion for the validity of the effective field theory [21] is $f_i x(g) E^2 / \Lambda^2 < 1$, where $x(g)$ are the $SU(2)_L/U(1)_Y$ factors for the operators under study and E is the scale of the process. For the production case, it is the centre of mass energy of the e^+e^- colliding beams, which is 250 – 300 GeV, while for decays, it is the mass of the Higgs boson. For the production case, we perform a rough calculation taking $g \approx 0.65$, $g' \approx 0.74$ and the cut-off scale $\Lambda = 1 \text{ TeV}$. Hence, for the operator O_W , $f_W x(g) E^2 / \Lambda^2 \approx f_W \frac{0.65}{2} 300^2 / 1000^2 \approx 0.029 f_W$, which can take f_W to values ≈ 34 . Similarly, for O_B , the reach will be around $f_B \approx 30$. For O_{WW} , we have two factors of g and two factors of $\frac{1}{2}$, which can take f_{WW} to an even larger value. Thus the values chosen in our scan approximately conforms to the requirement of a valid effective theory.

One parameter at a time

In Figs. 6.5 and 6.6, we show the variations of the $e^+e^- \rightarrow ZH$ and $e^+e^- \rightarrow \nu\bar{\nu}H$ (t -channel) cross-sections as functions of a single parameter by keeping all other parameters fixed at their SM values. We show that even for small values of the operator coefficients, the cross-sections can vary significantly from the SM expectations. We also show that the ratios of the cross sections at two different energies can vary non-trivially with these parameters. If there is no new tensor structure in the HVV couplings, the ratio plots will be flat horizontal curves. Any

departure from a horizontal nature of such curves will shed light on new tensor structure in such HVV vertices. The main sources of departure are the interference terms between the SM and HDO contributions. Such terms, occurring in both the numerator and the denominator of the ratio, carry the dependence on f as well as \sqrt{s} .

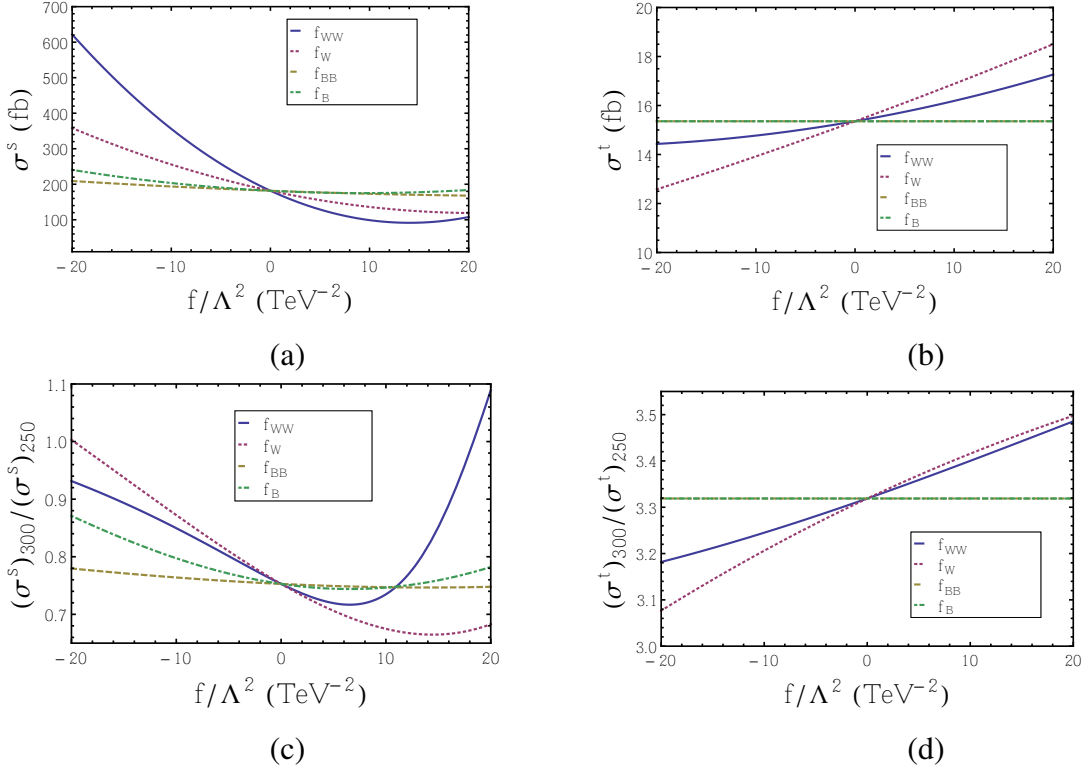


Figure 6.5: Variations of (a) $\sigma_{ZH}^s(300)$ (fb) and (c) $\sigma_{ZH}^s(300)/\sigma_{ZH}^s(250)$ for $e^+e^- \rightarrow ZH$ and of (b) $\sigma_{\nu\bar{\nu}H}^{t,ac}(300)$ (fb) and (d) $\sigma_{\nu\bar{\nu}H}^t(300)/\sigma_{\nu\bar{\nu}H}^{t,ac}(250)$ for $e^+e^- \rightarrow \nu\bar{\nu}H$ with f_{WW}, f_W, f_{BB}, f_B . $\kappa = 1$ for all the cases. The superscript ac denotes the cut in Eq.6.4. The numbers in the brackets are the CMEs.

We also remind the reader that the use of gauge invariant higher-dimensional operators implies a correlated modification in triple gauge boson couplings (Eqs. 4.7, 4.8). f_W and f_B are thus responsible for altering the rates of $e^+e^- \rightarrow W^+W^-$ concomitantly with those for Higgs boson production. Such a concomitance, if verified in an e^+e^- collision experiment, should point rather unmistakably at one or the other of the gauge invariant operators mentioned here. We show the modified rates of the WW final state in Fig. 6.7 where we also show the effects of the operator driven by f_{WW} (which does not affect the Higgs couplings).

It should however be mentioned that the actual presence of anomalous couplings in

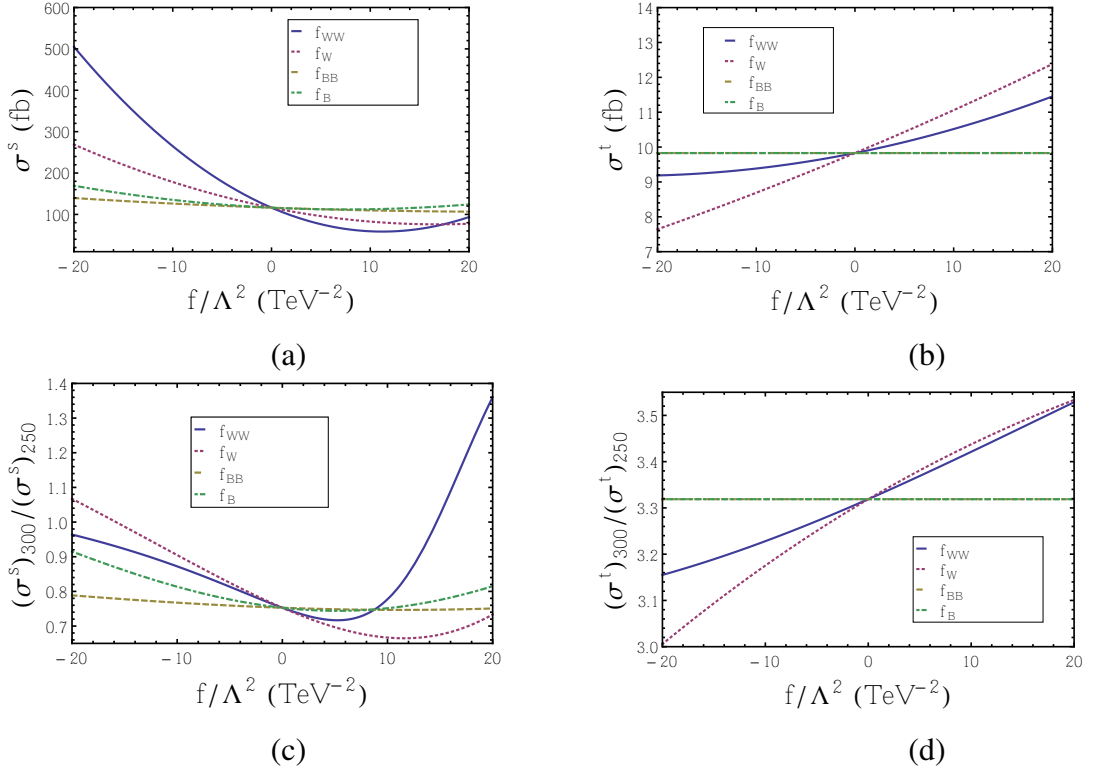


Figure 6.6: Variations of (a) $\sigma_{ZH}^s(300)$ (fb) and (c) $\sigma_{ZH}^s(300)/\sigma_{ZH}^s(250)$ for $e^+e^- \rightarrow ZH$ and of (b) $\sigma_{\nu\bar{\nu}H}^{t,ac}(300)$ (fb) and (d) $\sigma_{\nu\bar{\nu}H}^t(300)/\sigma_{\nu\bar{\nu}H}^{t,ac}(250)$ for $e^+e^- \rightarrow \nu\bar{\nu}H$ with $f_{WW}, f_W, f_{BB}, f_B \cdot \kappa = 0.8$ for all the cases. The superscript ac denotes the cut in Eq.6.4. The numbers in the brackets are the CMEs.

$e^+e^- \rightarrow W^+W^-$ is best reflected in a detailed study of various kinematic regions [22]. Such a study, however is not the subject of the present work.

The main conclusion emerging from Figs. 6.5, 6.6 and 6.7 are as follows :

- In Figs. 6.5(a) and 6.6(a), for the process $e^+e^- \rightarrow ZH$, we find that the operator \mathcal{O}_{WW} changes the cross section from its SM expectation by $\sim 30\%$ even in the range $-5 < f_{WW} < 5$. The major contribution to the cross section modification comes from the operators \mathcal{O}_{WW} and \mathcal{O}_W . \mathcal{O}_B and \mathcal{O}_{BB} have lesser contributions to the cross section.
- In Figs. 6.5(b) and 6.6(b), for the cut-applied t -channel contribution in the process $e^+e^- \rightarrow \nu\bar{\nu}H$, the operator \mathcal{O}_W maximally affects the cross-section. The effect of \mathcal{O}_{WW} is comparatively less pronounced. \mathcal{O}_{BB} and \mathcal{O}_B does not change this cross-section as the HWW vertex is unaffected by these operators. Most importantly, it should be noted that

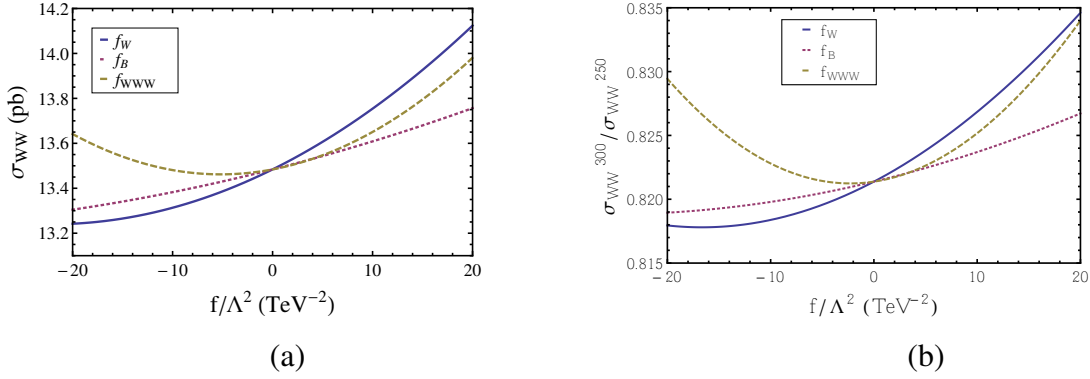


Figure 6.7: (a) Cross section (σ (in pb)) for the process $e^+e^- \rightarrow W^+W^-$ for $\sqrt{s} = 300$ GeV and (b) ratio of cross sections ($\sigma_{300}/\sigma_{250}$) for the same process as functions of f 's.

the effect of these operators on the t -channel process is much less pronounced than its s -channel counterpart (Eqs. 6.7, 6.8).

- In Figs. 6.5(c) and 6.6(c), the ratio of the cross sections for the $e^+e^- \rightarrow ZH$ channel at $\sqrt{s} = 300$ GeV and $\sqrt{s} = 250$ GeV shows a different nature. In the range $-20 < f_i < 20$ for the four operators discussed above, the ratio changes by $\sim 33\%$ for O_W . The effect of O_{WW} is less than this. The change in the ratio is the least for O_{BB} .
- In Figs. 6.5(d) and 6.6(d), the ratio of cross-sections for the cut-applied t -channel process varies in the range $\sim [3.1, 3.5]$ for $-20 < f_i < 20$.
- We see that in Fig. 6.7, the cross-sections do not vary significantly with the operator coefficients. This is because the $e^+e^- \rightarrow W^+W^-$ channel has a strong ν_e mediated t -channel contribution which does not involve the triple-gauge boson vertex. This has a significant interference with the s -channel. In order to bring out the feature of the triple gauge boson vertices, we need to devise some strategy which will tame down the t -channel effect, such as using right-polarised electrons if one uses a linear collider.

Two parameters at the same time

In Figs. 6.8 and 6.9, we show some fixed cross-section contours in the planes of two parameters varied at the same time. In Figs. 6.8 and 6.9, all the parameters apart from the ones shown in the axes, are kept fixed. In each of these figures, we have marked regions in brown where the cross-section is $\sigma(SM) \pm 10\% \times \sigma(SM)$. Hence, we see that for each of these plots, some

regions even with large values of the parameters can closely mimic the SM cross-section. The above statement for the ranges of the coefficients of the HDOs will be somewhat modified if we consider the Higgs decays. This is because then we will have branching ratios depending on the effects of the HDOs. Even for fermionic decays of the Higgs, which are independent of the operators under study, the BR will have non-trivial effects on the operator couplings through the total decay width. But, we must mention here that unless we go to very high values of the operator coefficients, the total decay width remains close to the SM expectation and hence fermionic decay channels would show similar features as these plots. Of course, when we study the effects of all the operators in the basis that we have considered by considering every possible decay mode of the Higgs, then the higher-dimensional operators will come to play at the HVV decay vertices also. Hence, we will get modified bounds on the operator coefficients from a similar approach. We should mention that these operators are also constrained by the electroweak precision observables, viz. S , T and U parameters. An important observation which is carried forward from Fig. 6.5 (a) is that the HZZ and $H\gamma Z$ vertices are very less affected by the operators O_{BB} and O_B . This fact is corroborated in Fig.6.8 (e). The above mentioned pair of operators thus allow a wide region of parameter space which has cross-sections within 10% of the SM value.

Some salient features of Figs. 6.8 and 6.9 are :

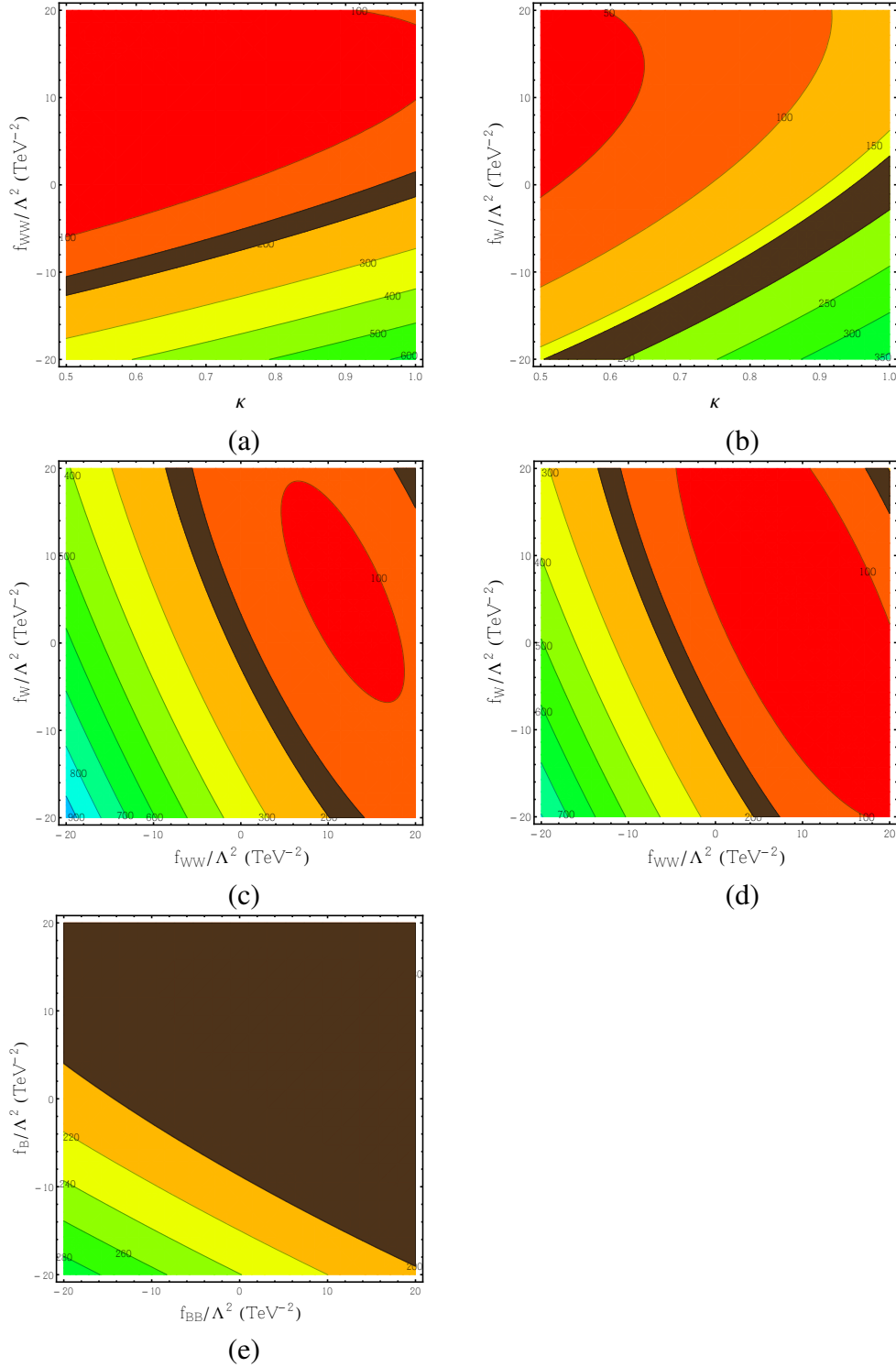


Figure 6.8: Variations of σ_s^{300} for $e^+e^- \rightarrow Zh$ with (a) κ and f_{WW} , (b) κ and f_W , (c) f_{WW} and f_W for $\kappa = 1$, (d) f_{WW} and f_W for $\kappa = 0.8$ and (e) f_{BB} and f_B for $\kappa = 1$. For each case all the other f s are set to zeroes. Brown patches signify cross-sections within $\pm 10\%$ of the SM expectation.

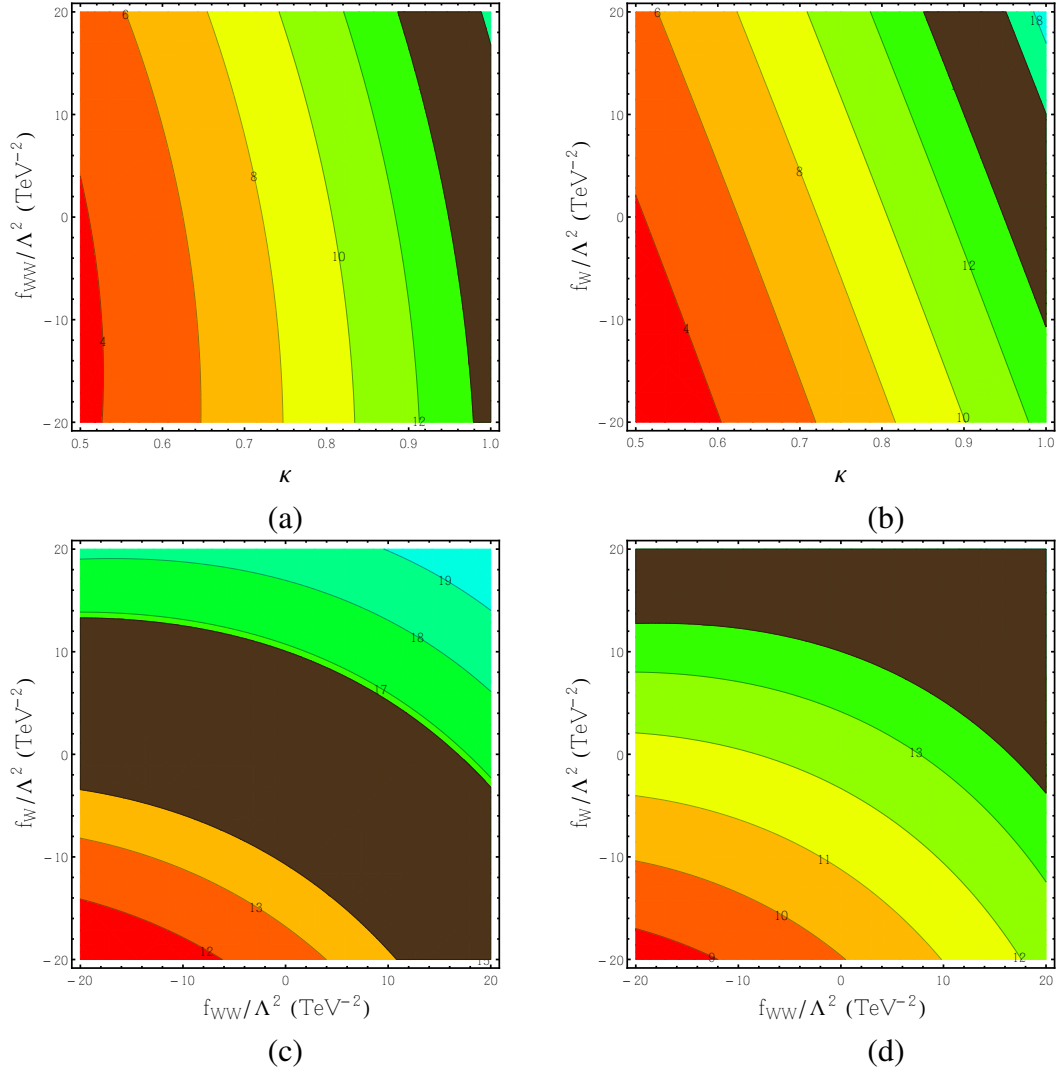


Figure 6.9: Variations of $\sigma_t^{300,ac}$ for $e^+e^- \rightarrow \nu\bar{\nu}h$ with (a) κ and f_{WW} , (b) κ and f_W , (c) f_{WW} and f_W for $\kappa = 1$, (d) f_{WW} and f_W for $\kappa = 0.9$. For each case all the other f s are set to zeroes. Brown patches signify cross-sections within $\pm 10\%$ of the SM expectation.

- Fig. 6.8 shows the variation of the total rate for the channel $e^+e^- \rightarrow ZH$ as functions of two parameters taken together. All the other parameters are fixed for these plots. In Figs. 6.8(a)-(d), the cross-section varies significantly from the SM value for the allowed ranges of the parameters. However, Fig. 6.8(e) shows a large region of the parameter space to have cross-sections similar to the SM (within 10%).
- Fig. 6.9 shows the variation of the cross-sections for the t -channel process in $e^+e^- \rightarrow \nu\bar{\nu}H$

as functions of two parameters varied at the same time. Figs. 6.9(c) and 6.9(d) shows a substantial amount of parameter space agreeing with the SM cross-section.

All parameters at the same time

The most general case will be to vary all the parameters simultaneously to obtain the most realistic parameter space. Here, we demonstrate this scenario for the cut-applied t -channel cross section in the $e^+e^- \rightarrow \nu\bar{\nu}H$ channel. In Figs.6.10 (a), (b) and (c) we present three slices of the 3-dimensional hyper-surface. For each of these plots, there is a third parameter which has been varied. We see that a very large parameter space is allowed which can mimic the SM cross section within its 10% value. Of course these plots are for illustrative purposes only. In Fig. 6.10 (d), we have shown one such slice of the five-dimensional hyper-surface in the space of $(\kappa, f_{WW}, f_W, f_{BB}$ and $f_B)$ for the s -channel process.

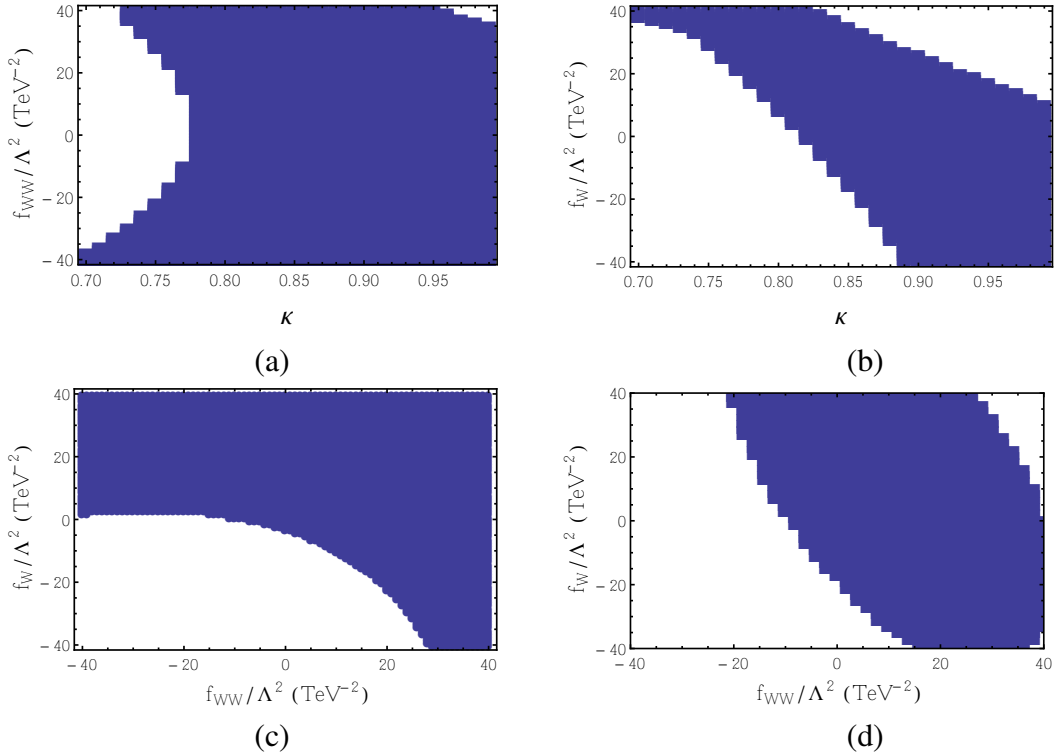


Figure 6.10: Allowed parameter space for $\sigma_{\nu\bar{\nu}H}^{t,ac}$ within 10% of its SM value : (a) f_{WW} vs κ (f_W varied), (b) f_W vs κ (f_{WW} varied), (c) f_W vs f_{WW} (κ varied) and for σ_{ZH}^s within 10% of its SM value : (d) f_W vs f_{WW} (κ, f_{BB} and f_B varied). $\sqrt{s} = 300$ GeV.

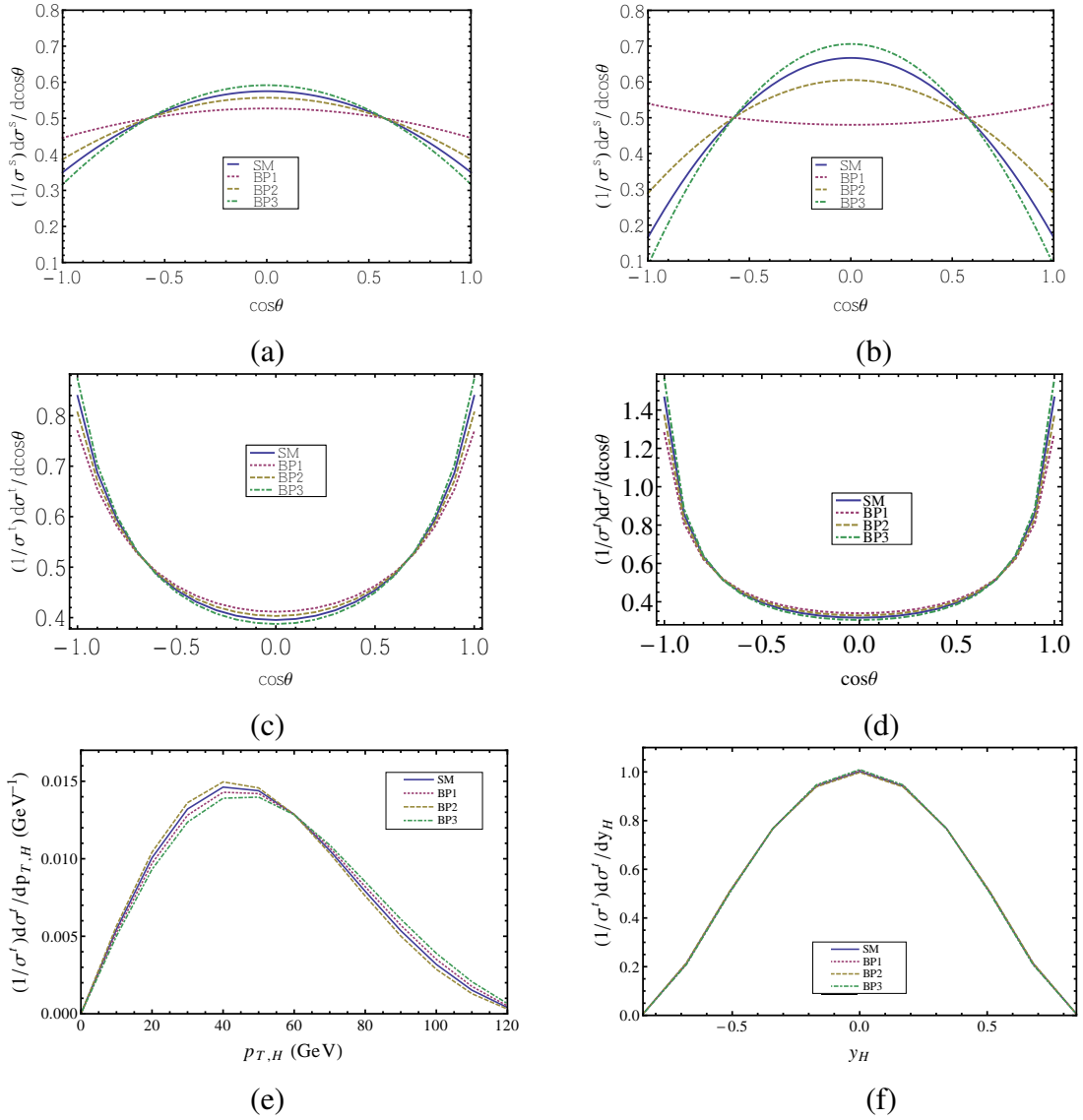


Figure 6.11: Normalised kinematic distributions $(1/\sigma^s)d\sigma^s/d\cos\theta$ for the channel $e^+e^- \rightarrow ZH$ for (a) $\sqrt{s} = 300$ GeV and (b) $\sqrt{s} = 500$ GeV. Normalised kinematic distributions $(1/\sigma^t)d\sigma^t/d\cos\theta$ for the t -channel process in $e^+e^- \rightarrow \nu\bar{\nu}H$ for (c) $\sqrt{s} = 300$ GeV and (d) $\sqrt{s} = 500$ GeV. Distributions for (e) $(1/\sigma^t)d\sigma^t/dp_{T,H}$ and (f) $(1/\sigma^t)d\sigma^t/dy_H$ for the t -channel process in $e^+e^- \rightarrow \nu\bar{\nu}H$ at $\sqrt{s} = 300$ GeV. Benchmark points, viz. SM ($x_i \in \{1, 0, 0, 0, 0\}$), BP1 ($x_i \in \{1, -3, 8, -4, 3\}$), BP2 ($x_i \in \{1, 0, 5, 0, 0\}$) and BP3 ($x_i \in \{1, 0, -5, 0, 0\}$).

Discussion on EWPT constraints : All the benchmark points chosen throughout this chapter are consistent with all constraints available till date [5, 6]. However, if one looks at the contour plots in Figs. 6.8, 6.9 and 6.10, there may exist certain points which are disfavoured by

the precision constraints.

6.3.5 The effects on kinematic distributions

The presence of anomalous HVV vertex can in principle also affect the shapes of various kinematic distributions. In Figs. 6.11(a) and 6.11(b) [Figs. 6.11(c) and (d)], we show the normalised angular (angle of Higgs with the z -axis) distributions for the s -channel (t -channel) processes for $\sqrt{s} = 300$ GeV and 500 GeV respectively. We find that the angular dependence for the s -channel is very sensitive in some regions of the parameter space allowed by the EWPT constraints and the LHC data. We also find the $\cos\theta$ dependence can be completely opposite as we increase the CME. This can be seen in Figs. 6.11(a) and 6.11(b), if we compare the curves for BP1. In contrast, the t -channel is not significantly affected by the inclusion of HDOs. The angular dependence of the differential cross-sections can be expressed as

$$\frac{d\sigma(\sqrt{s}, x_i)}{d\cos\theta} = a(\sqrt{s}, x_i) + b(\sqrt{s}, x_i) \cos^2\theta \quad (6.10)$$

It is found that, between coefficients a and b above, a is more affected by the anomalous couplings rather than b , unless \sqrt{s} is 500 GeV or well above that. As a result, angular distributions are insensitive to the new interactions at the proposed energy scale of a Higgs factory.

In Figs. 6.11(e) and 6.11(f), we show the normalised $d\sigma/dp_{T,h}$ and $d\sigma/dy_h$ distributions respectively for the t -channel where $p_{T,h}$ is the transverse momentum of the Higgs and y_h is its rapidity. We want to emphasise that it is very difficult to see any significant differences in the various kinematic distributions in most of the parameter space allowed by the LHC and EWPT constraints while performing experiments with smaller CME. In both the channels, we do not consider the final decay products of the Higgs. If we consider the Higgs boson decaying to fermionic final states, then the HDOs under consideration will not affect these decay vertices and the above normalised distributions will remain intact. However, if we consider the bosonic decay modes of the Higgs, then the HDOs will affect these distributions non-trivially.

We end this subsection with the following admission. Various kinematical distributions are canonically emphasized as the best places to find the signature of non-standard Lorentz structures in interaction terms. While this expectation is not completely belied in the present case as well, we note that the anomalous couplings are reflected in distributions *at relatively high CMEs*. The reason behind this has already been explained above. While this prospect is

encouraging, electron-positron colliders, especially those designed as Higgs factories, are likely to start operating at energies as low as 250 – 300 GeV. Our observation is that the imprint of anomalous couplings can be found even at such low energies at the level of total rates and their ratios. A detailed study involving all possible decay products and their various correlations can in principle go further in revealing traces of anomalous couplings. We will take up such a study in a subsequent work.

6.3.6 Discussion on relevant backgrounds

We wish to see the effects of anomalous HVV couplings on the Higgs production alone. Therefore, we do not look at bosonic decay modes of Higgs and limit our discussion only to those signal processes where H decays maximally to a $b\bar{b}$ pair. For the $e^+e^- \rightarrow ZH$ process, the Z can either decay visibly to $b\bar{b}$, jj , $\ell^+\ell^-$ (here $j = g, u, d, c, s$ and $\ell = e, \mu$) modes or invisibly to a $\nu\bar{\nu}$ pair. So the dominant backgrounds relevant for these final states are the non-Higgs $e^+e^- \rightarrow b\bar{b}b\bar{b}, b\bar{b}jj, b\bar{b}\ell^+\ell^-, b\bar{b} + \cancel{E}$. The non-Higgs $e^+e^- \rightarrow b\bar{b} + \cancel{E}$ process can also act as the dominant background for the $e^+e^- \rightarrow \nu\bar{\nu}H$ channel. We select events after the following kinematic cuts:

Trigger cuts : $p_T(b, j) > 20$ GeV, $p_T(\ell) > 10$ GeV, $|y(b, j)| < 5.0$, $|y(\ell)| < 2.5$, $\Delta R(bb, bj, jj, b\ell, j\ell) > 0.4$, $\Delta R(\ell\ell) > 0.2$.

Finally we estimate two of the aforementioned backgrounds by applying the cuts below:

- Non-Higgs $e^+e^- \rightarrow b\bar{b}\ell\ell$

We demand the two b 's to fall within the Higgs-mass window and the two ℓ 's to fall within the Z -mass window as follows:

$$|M(bb) - M_h| < 10 \text{ GeV} \quad \text{AND} \quad |M(\ell\ell) - M_Z| < 10 \text{ GeV} \quad (6.11)$$

Finally the total background cross-section for the $b\bar{b}\ell\ell$ final state is defined as, $\mathcal{B}_{b\bar{b}\ell\ell} = \eta_b^2 \sigma_{b\bar{b}\ell\ell}$ where η_b is the b -tagging efficiency which we take as 0.6 for our analysis. The signal is also scaled by the same factor, η_b^2 .

- Non-Higgs $e^+e^- \rightarrow bb + \cancel{E}$

We demand the two b 's to fall within the Higgs-mass window, $|M(bb) - M_h| < 10$ GeV.

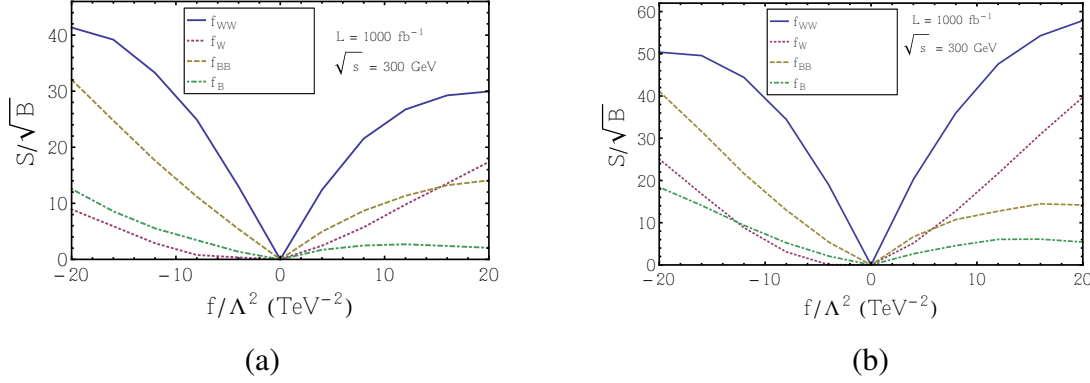


Figure 6.12: Significance ($S/\sqrt{\mathcal{B}}$) as functions of f_i/Λ^2 for $\kappa = 1$ at $\sqrt{s} = 300$ GeV for (a) $e^+e^- \rightarrow bb\ell\ell$ and (b) $e^+e^- \rightarrow bb + \cancel{E}$.

Here the background is $\mathcal{B}_{bb+\cancel{E}} = \eta_b^2 \sigma_{bb+\cancel{E}}$. The signal⁴ has also been scaled by the b -tagging efficiency.

Final states	\sqrt{s} (GeV)	$\sigma_{SM,tc}^{sig}$ (fb)	$\sigma_{SM,ac}^{sig}$ (fb)	$\sigma_{BP1,tc}^{sig}$ (fb)	$\sigma_{BP1,ac}^{sig}$ (fb)	σ_{tc}^{bkg} (fb)	σ_{ac}^{bkg} (fb)
$b\bar{b}l^+l^-$	250	2.68	2.46	2.76	2.52	10.33	0.09
	300	2.33	1.91	2.31	1.83	9.17	0.07
$b\bar{b} + \cancel{E}$	250	12.25	10.31	12.36	10.53	20.53	0.33
	300	13.67	9.79	13.26	9.62	18.00	0.29

Table 6.2: We show the signal and backgrounds for two different final states, *viz.* $b\bar{b}l^+l^-$ and $b\bar{b} + \cancel{E}$. σ_{tc} 's are the cross-sections after the basic trigger cuts mentioned above and σ_{ac} 's are the cross-sections after the channel-specific cuts. The analysis has been done for the SM and the benchmark point BP1 ($x_i \in \{1, -3, 8, -4, 3\}$).

Alongside the issue of distinctness of the presence of the anomalous couplings, it is of interest to find out about the reach of a Higgs factory, or to know down to what strength the anomalous couplings can be detected. This information can be found in Fig. 6.12. There we have plotted the quantities $\mathcal{S} = |\sigma_{BSM}^H - \sigma_{SM}^H|$ and $\mathcal{B} = \sigma_{SM}^H + \sigma_{SM}^{NH}$ for computing the significance. Here, H (NH) signifies sub-processes which involve (does not involve) the Higgs.

In Table 6.2, we show the cross-sections for both the signal and background scenarios. For the signal we have considered two benchmark points, *viz.* SM and BP1 ($x_i \in \{1, -3, 8, -4, 3\}$).

⁴The channel $e^+e^- \rightarrow H + \cancel{E} \rightarrow b\bar{b} + \cancel{E}$ also includes diagrams involving the triple-gauge boson vertices. These effects are almost nullified when the selection cuts for this channel are employed.

We show the cross-sections once after applying just the trigger cuts (designated with the subscript tc) and next by applying the channel-specific selection cuts (written with a subscript ac) along with the basic trigger cuts. All the numbers have been multiplied by η_b^2 . We see that the effects of the invariant mass selection cuts on the signal cross-sections are negligible whereas these are very effective in reducing the backgrounds almost completely.

The study performed here is at parton level. Shower, hadronization and detector effects are expected to have an impact on the effective cross-sections reported in Table 6.2. That said, these effects will not change the conclusions of this work.

6.4 Likelihood Analysis for t -channel

The kinematics of the final state associated to the s -channel production has been studied extensively in the past. As pointed out in section 6.1, the t -channel production provides limited phase-space because the momenta of the outgoing neutrinos cannot be disentangled experimentally. This leaves the Higgs boson kinematics as the only handle to explore the nature of the HWW coupling. Studies are documented in the literature with the use of the Higgs boson momentum as a means to gain sensitivity. Here we attempt to fully exploit the kinematics of the Higgs boson by means of a correlated two-dimensional likelihood analysis. The primary intent of this section is to shed light on the relative improvement of this two-dimensional approach, rather than determining absolute sensitivity to the size of anomalous couplings. The latter requires a detailed study that carefully incorporates experimental effects. This is beyond the scope of this work.

We use a test-statistic (TS) to distinguish the BSM hypothesis from its SM counterpart by defining the logarithm of a profile likelihood ratio ($q_{ij} = \ln \lambda_{ij}$) for two different hypotheses i and j defined as

$$q_{ij} = \ln \lambda_{ij} = \ln \frac{L(P_i|D_i)}{L(P_j|D_i)}, \quad (6.12)$$

where λ_{ij} is the ratio of two likelihood functions $L(P_i|D_i)$ and $L(P_j|D_i)$ describing two different hypotheses ⁵, D_i is the data set used and $P_{i,j}$ are the probability density functions. Due to

⁵Alternatively, its reciprocal is also sometimes used, depending on the analysis required. It should be noted here that both likelihoods are constructed using the same D_i , but different P_i s.

the discrete nature of the probabilities in this analysis, the likelihood functions are defined as products of binned Poisson probabilities over all channels and bins [23]. From the TS, a p -value can be calculated to quantify the extent to which a hypothesis can be rejected. In general, a p -value is a portion of the area under a normalised TS which, after calculation, is the percentage confidence level (CL) by which a hypothesis can be rejected.

In Monte Carlo (MC) studies, these TSs emerge as binned peaks which show up on running pseudo-experiments, each of which returns a value for the TS based on a randomly generated set of pseudo-data. The number of pseudo-data points generated is fixed by the cross-section of the process being studied. The TSs concerned in this analysis are always produced in pairs, in order to discriminate between the SM and BSM hypotheses. This pair of TSs is represented as

$$q_U = \ln \frac{L(P_{SM}|D_{SM})}{L(P_{BSM}|D_{SM})} \quad \text{and} \quad q_L = \ln \frac{L(P_{SM}|D_{BSM})}{L(P_{BSM}|D_{BSM})}. \quad (6.13)$$

The q_U TS tends to have a more positive value due to its ordering, and we refer to it as the *upper* TS for our purposes, while we refer to q_L as the *lower* TS. A hypothesis can be rejected by calculating the associated p -value as follows

$$p = \int_{m_{q_U}}^{\infty} q_L(q) dq, \quad (6.14)$$

where m_{q_U} is the median of the upper TS, q_U . The confidence by which a hypothesis can be rejected, can alternatively be quantified by knowing the *significance* of the separation between the two TSs. The median-significance, Z_{med} , is defined as the number of standard deviations between the median of q_L and the left edge of the p -value area, that is, the median of q_U .

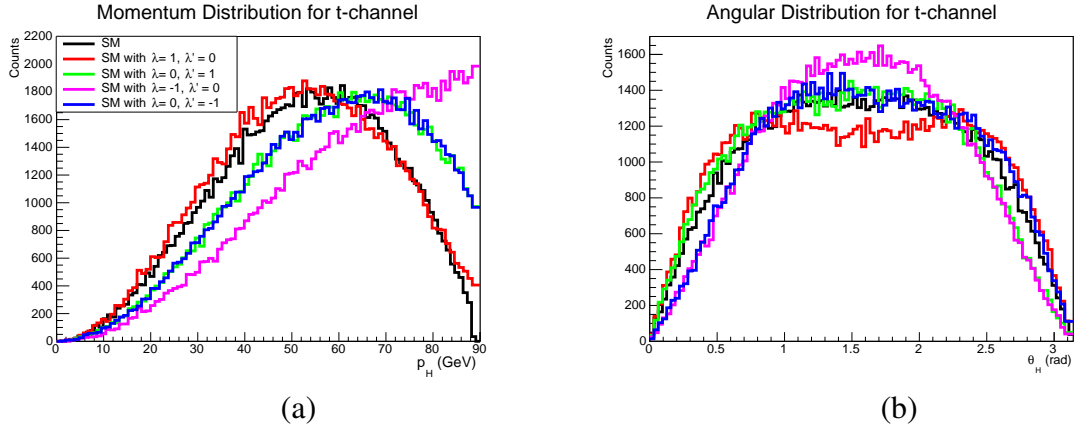


Figure 6.13: Normalised kinematic distributions of (a) Higgs momentum, p_H and (b) the angle of the Higgs with the beam-axis, θ_H for different benchmark points for the t -channel process at $\sqrt{s} = 250$ GeV.

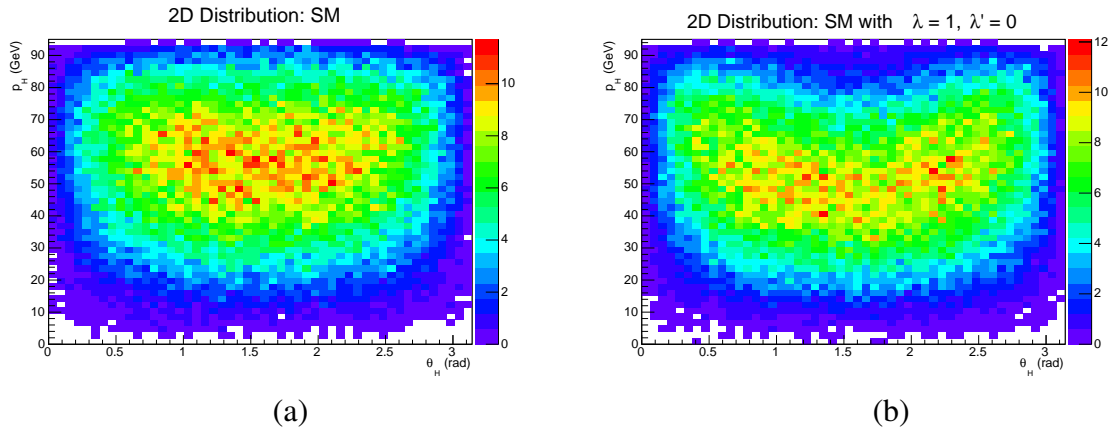


Figure 6.14: Two dimensional histograms showing the correlation of the t -channel Higgs momentum, p_H and the angle of the Higgs with the beam-axis, θ_H at $\sqrt{s} = 250$ GeV. The z -axis is an indication of the frequency of events, in arbitrary units. The effect of the correlation can be seen by noting how the BSM parameter λ affects the distribution.

As stated above, we focus on the t -channel process (in $e^+e^- \rightarrow \nu\bar{\nu}H$) which has not been studied as extensively as the s -channel. The s -channel (t -channel) contributions can be separated out from the $\nu\bar{\nu}H$ events by applying the E_H -cut (E_H^c -cut) in Eq. 6.4. For this purpose, we work with the phenomenological parametrization of anomalous HWW interaction characterised by λ and λ' , as defined in Eq. 6.3.

In our analysis, the vertices for the Lagrangians in the SM and in BSM with spin-0 bosons

are calculated in FEYNRULES [15] and passed to the event-generator MADGRAPH [17], which is used for the generation of the matrix elements for Higgs production in the t - and s -channels. MC samples are produced at parton level. Effects related to detector resolution are taken into account when defining requirements to suppress the contamination from the s -channel process (see Eq. 6.4).

We set the stage for the likelihood analysis by showing some plots for distributions in terms of λ and λ' . In Figs. 6.13(a) and (b), we show the p_H (Higgs momentum) and θ_H (the angle of the Higgs with the beam-axis) distributions respectively for the t -channel at $\sqrt{s} = 250$ GeV. We see that significant deviations from the SM can be seen. This is in contrast to what was shown for the gauge invariant formulation (in Fig. 6.11) because there we stick to moderate values of the parameter coefficients, whereas for example, here, $\{\lambda = 1, \lambda' = 0\} \Rightarrow x_i \approx \{1, 77, 0, 0, 0\}$. In Figs. 6.14(a) and (b), two dimensional histograms in p_H - θ_H plane are shown for the SM and a BSM (SM with $\lambda = 1, \lambda' = 0$) benchmark point respectively at $\sqrt{s} = 250$ GeV.

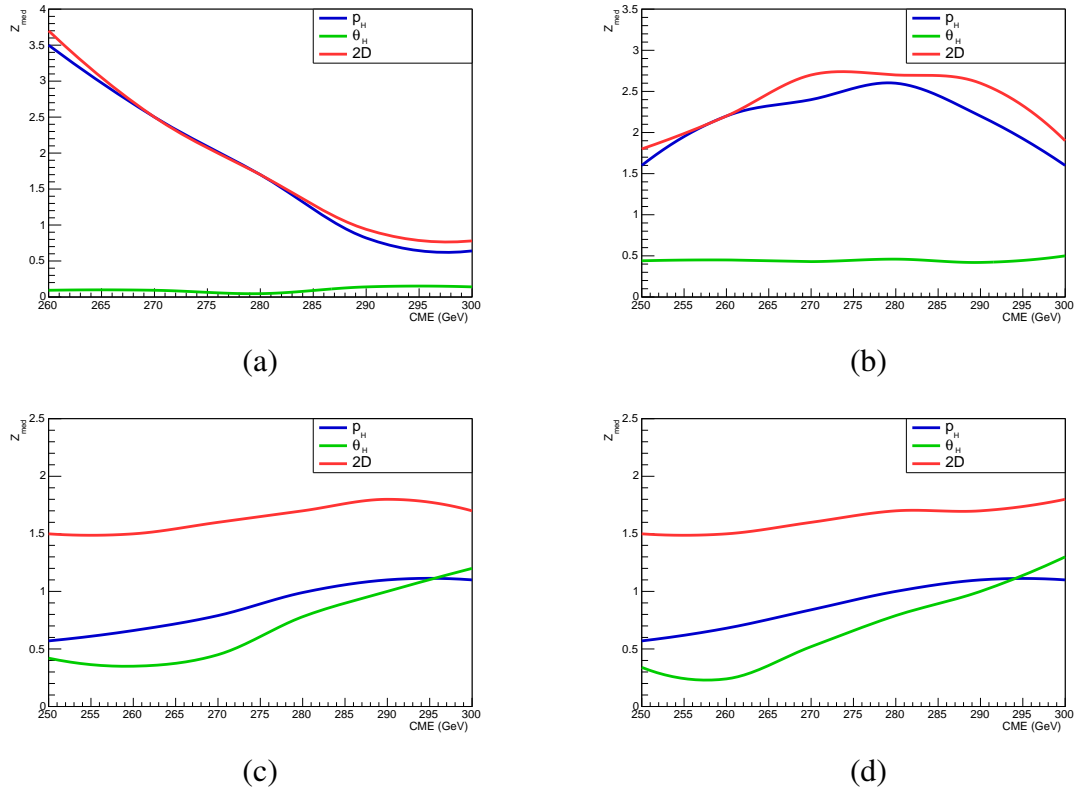


Figure 6.15: Median significance values for likelihood analyses done with both one dimensional and two dimensional distributions. (a) SM with $\lambda = 1$, (b) SM with $\lambda = -1$, (c) SM with $\lambda' = 1$ and (d) SM with $\lambda' = -1$. Results are obtained with 1 fb^{-1} of integrated luminosity.

A likelihood analysis for each BSM hypothesis is performed for integrated luminosities of 1 fb^{-1} , 5 fb^{-1} and 10 fb^{-1} . The number of pseudo-data points in each analysis is determined from the SM cross section. The Z_{med} for the 1 fb^{-1} case are plotted as functions of the CME for each hypothesis as shown in Fig. 6.15. These plots show the power of using two dimensional distributions in likelihood analysis. The likelihood analysis is performed using a total number of 100,000 pseudo-experiments for each TS. The two dimensional distributions, examples of which are shown in Fig. 6.14, are also included in the likelihood analysis to demonstrate the effect of the correlation between the two variables, p_H and θ_H .

Fig. 6.15 displays the significance for one-dimensional analyses using the Higgs boson momentum and the polar angle separately. Results are shown for illustration purposes for 1 fb^{-1} of integrated luminosity. Conclusions drawn here are found not to depend on the integrated luminosity in the range studied here. The corresponding results for the combined 2D likelihood

are shown. The upper two plots correspond to admixtures with the CP-even term. The sensitivity of the polar angle is significantly less than that of the Higgs boson momentum. The lower plots display the corresponding results for admixtures with the CP-odd term. In this case the sensitivity of the polar angle is similar to that of the momentum. As a result, the improvement from the 2D analysis is significant, to the extent that the sensitivity can be enhanced by about a factor of two. The sensitivity of the angular variable grows with the CME.

The results provide a good motivation for the role of an electron positron collider in understanding the nature of the HVV couplings. The plots in Fig. 6.15 show the utility in using two dimensional distributions in discerning the rejection of hypotheses. That is, using the same accrued data from two separate one dimensional distributions, one can enhance the confidence in rejecting hypotheses. The correlation of the two dimensional distributions thus carries vital information about the dynamics of the processes which are studied in e^+e^- collisions.

6.5 Summary and Conclusions

We have attempted to demonstrate the efficacy as well as limitations of an e^+e^- Higgs factory operating at 250 – 300 GeV in probing anomalous, higher-dimensional couplings of a Higgs to W -and Z -pairs, suppressed by a scale $O(\text{TeV})$. For this purpose, we have mostly adhered to the set of gauge-invariant operators that can lead to such interactions, since it is such terms that are expected to emerge on integrating out physics above the electroweak symmetry breaking scale. We have utilised the consequent correlation of the anomalous HWW , HZZ and $HZ\gamma$ couplings, and also the concomitant effect on $ZWW/\gamma WW$ interactions, as reflected in gauge boson pair-production rates.

The general conclusion reached by this study is that the total rates can be quite useful as probes of higher-dimensional operators. Based on this, we have performed a detailed analysis of the cross-sections for s -and t -channel Higgs production, specifying event selection criteria for minimising their mutual contamination. A general scheme of computing the rates with more than one gauge-invariant operators has been outlined. Based on such an analysis, we conclude that, even with the additional operators well within the erstwhile experimental bounds (including those from the LHC), a number of observations can probe them at a Higgs factory. These include not only the individual total cross-sections but also their ratios at different values of \sqrt{s} and also the ratio of the s -and the t -channel Higgs production rates at fixed energies. We

also indicate the correlated variation of W -pair production rates. The Higgs production rate contours with more than one type of anomalous gauge-invariant operators are also presented. Finally, using some illustrative values of anomalous HWW couplings in a more phenomenological parametrization, we indicate the viability of a correlated two-dimensional likelihood analysis to fully exploit the kinematics of the Higgs boson. The latter is particularly relevant to disentangle the SM from CP-violating admixtures.

In the previous chapter, we saw that the high luminosity runs at the LHC can also be efficient in constraining these operators. However, since the LHC environment is plagued with backgrounds, an e^+e^- Higgs factory will have an added advantage of constraining such operator coefficients, in a relatively *clean* situation. The cleanliness of environment may provide an extra handle in probing HVV anomalous couplings. This is especially true when the numerical reach roughly matches that in the high-energy, high-luminosity run of the LHC, as is evident from a comparison of Fig. 6.12 with the results in Chapter 5.

Chapter 7

Conclusions

Ever since the formulation of the standard model (SM) of particle physics, various experiments have confirmed its robustness and predictive power. The $SU(3)_C \times SU(2)_L \times U(1)_Y$ group structure was confirmed through several experiments. Finally, in 2012, the discovery of a Higgs-like boson at the Large Hadron Collider (LHC) generated a lot of excitement in the particle physics community. The mass of the Higgs boson raises questions about the stability of the vacuum. It also raises questions whether this boson is part of a larger gauge group. In chapter 1, we have reviewed the SM and have provided motivations for physics beyond the standard model (BSM). In chapter 2, we discussed some technical aspects of high energy colliders and several basic kinematic variables used in collider studies.

Since 2012, several searches have tried to study the exact nature of this boson and yet have not found any significant deviations from the SM expectations. It is observed from several studies done by CMS and ATLAS, that a spin zero, even parity state is favoured over other hypotheses. One of the most crucial checks to ascertain the fact that the discovered boson is the SM Higgs, is to measure its self-coupling. This is a challenging task. However, till such a measurement is made possible, it is necessary to be certain whether the Higgs couplings to fermions and gauge bosons have any possible *non-standard* behaviour. It is also necessary to establish whether this boson has any *non-standard* decays to *invisible* particles. In this thesis, we have attempted to show how much the Higgs couplings to the SM particles can deviate

from their standard expectations. We have also predicted the significance with which such non-standard couplings may be seen at the high luminosity run of the LHC at 14 TeV or at future e^+e^- colliders. We briefly summarise below the work done in this thesis.

- In chapter 3, we performed a multi-parameter global analysis of all data available till date from the ATLAS, CMS and Tevatron experiments, on the signals of a Higgs boson, to investigate how much scope exists for departure from the standard model prediction. We adopted a very general and model-independent scenario, where separate deviations from standard model values were made possible for couplings of the observed scalar with *up*- and *down*-type fermions, *W*- and *Z*-boson pairs, as well as *gluon* and *photon* pair effective interactions. An arbitrary phase in the coupling with the top-pair, and the provision for an invisible decay width for the scalar were also introduced. After performing a global fit with seven parameters, we found that their values at 95% confidence level can be somewhat different from standard model expectations. Moreover, rather striking implications of the phase in top-quark coupling were noticed. We also noted that the invisible branching ratio can be sizeable, at 95% confidence level.
- In chapter 4, we showed that the inclusion of higher-dimensional gauge invariant operators induces new Lorentz structures in Higgs couplings with electroweak gauge boson pairs. This in principle affects the kinematics of Higgs production and decay, thereby modifying the efficiencies of the experimental cuts compared to what simulations based on the standard model interactions yield. Taking some sample cases, we performed a rigorous analysis of how the efficiencies differ for various strengths of the additional operator *vis-a-vis* the standard model interactions, scanning over the values of both of them. While the response to cuts was shown to be markedly different in some regions, we found that the sensitivity to new operator structures is relatively limited, so long as we remain confined to the 2-sigma regions around the best fit signal strengths measured at the LHC. We also showed modifications to certain kinematical distributions including the new operators in the diphoton final state.
- In chapter 5, we suggested techniques for faithful extraction of the limits on dimension-6 CP-conserving HVV interactions ($V = W, Z, \gamma$), from the LHC data on the Higgs boson to be available in the 14 TeV run. We found that the ratios of total rates in different channels can be quite useful in this respect. We constructed ratios of rates in (a) different channels

for the Higgs produced in the same subprocess, and (b) the same decay channel from two different production modes. We showed that, while most theoretical uncertainties cancel in the former, the latter helps in the case of those operators which shift the numerator and denominator in opposite directions. Our analysis, incorporating theoretical, systematic and statistical errors, led to projected limits that improve upon the strongest ones obtained so far from precision electroweak as well as LHC Higgs data, by factors of 3-4 approximately. Moreover, form-factors which are allowed in disjoint intervals, had their ranges narrowed down remarkably in our approach.

- Probing signatures of anomalous interactions of the Higgs boson with pairs of weak vector bosons is an important goal of an e^+e^- collider commissioned as a Higgs factory. In chapter 6, we performed a detailed analysis of such potential of a collider operating at 250-300 GeV. Mostly using higher dimensional operators in a gauge-invariant framework, we showed that substantial information on anomalous couplings can be extracted from the total rates of s - and t -channel Higgs production. We showed that the most obvious kinematic distributions, based on angular dependence of matrix elements, are relatively less sensitive with moderate coefficients of anomalous couplings, unless one goes to higher centre-of-mass energies. We used the total event rates and their ratios at different energies, ratios of s - and t -channel rates at fixed energies, and under some fortunate circumstances, found the correlated changes in the rates for W -boson pair-production. A general scheme of calculating rates with as many as four gauge-invariant operators was outlined in this chapter. At the end, we performed a likelihood analysis using phenomenological parametrization of anomalous HWW interaction, and indicated their distinguishability for illustrative values of the strength of such interactions.

References for Chapter 1

- [1] For an introduction, see, for example, F. Halzen and A.D. Martin, *Quarks and Leptons: An introductory course in modern particle physics*, (John Wiley, 1984); J. F. Donoghue, E. Golowic and B.R. Holstein, *Dynamics of the Standard Model*, (Cambridge Monographs on Particle Physics, Nuclear Physics and Cosmology, 1994); T.P. Cheng and L.F. Li, *Gauge theory of elementary particle physics*, (Oxford Univ. Press, 1984), and references therein
- [2] Y. Nambu and G. Jona-Lasinio, *Phys. Rev.* **122**, 345 (1961); Y. Nambu and G. Jona-Lasinio, *Phys. Rev.* **124**, 246 (1961); J. Goldstone, *Nuovo Cim.* **19**, 154 (1961); J. Goldstone, A. Salam and S. Weinberg, *Phys. Rev.* **127**, 965 (1962);
- [3] G. 't Hooft, *Nucl. Phys. B* **35**, 167 (1971); G. 't Hooft and M. J. G. Veltman, *Nucl. Phys. B* **44**, 189 (1972).
- [4] S. L. Glashow, *Nucl. Phys.* **22**, 579 (1961); S. Weinberg, *Phys. Rev. Lett.* **19**, 1264 (1967); A. Salam, *Conf. Proc. C* **680519**, 367 (1968); A. Salam, *Weak and electromagnetic interactions - in Elementary particle theory: relativistic groups and analyticity*, N. Svartholm, ed p. 367. Almqvist and Wiksell, 1968. Proceedings of the eighth Nobel symposium.
- [5] F. Englert and R. Brout, *Phys. Rev. Lett.* **13**, 321 (1964); P. W. Higgs, *Phys. Rev. Lett.* **13**, 508 (1964); G. S. Guralnik, C. R. Hagen and T. W. B. Kibble, *Phys. Rev. Lett.* **13**,

585 (1964); P. W. Higgs, Phys. Rev. **145**, 1156 (1966); T. W. B. Kibble, Phys. Rev. **155**, 1554 (1967).

- [6] A. Djouadi, Phys. Rept. **457**, 1 (2008) [hep-ph/0503172].
- [7] S. Dawson, hep-ph/9901280;
- [8] T. Plehn, http://www.thphys.uni-heidelberg.de/~plehn/includes/notes/hunting_higgs/hunting_higgs.pdf.
- [9] K. G. Wilson and J. B. Kogut, Phys. Rept. **12**, 75 (1974).
- [10] T. P. Cheng, E. Eichten and L. F. Li, Phys. Rev. D **9**, 2259 (1974); M. A. B. Beg, C. Panagiotakopoulos and A. Sirlin, Phys. Rev. Lett. **52**, 883 (1984).
- [11] See for example, J. R. Espinosa and M. Quiros, Phys. Lett. B **353**, 257 (1995) [hep-ph/9504241]; J. Elias-Miro, J. R. Espinosa, G. F. Giudice, G. Isidori, A. Riotto and A. Strumia, Phys. Lett. B **709**, 222 (2012) [arXiv:1112.3022 [hep-ph]].
- [12] ATLAS, CMS, CDF and DØ collaborations, <http://cds.cern.ch/record/1669819?ln=en>
- [13] G. Aad *et al.* [ATLAS and CMS Collaborations], Phys. Rev. Lett. **114**, 191803 (2015) [arXiv:1503.07589 [hep-ex]].
- [14] T. Hambye and K. Riesselmann, Phys. Rev. D **55**, 7255 (1997) [hep-ph/9610272].
- [15] D. A. Dicus and V. S. Mathur, Phys. Rev. D **7**, 525 (1973); B. W. Lee, C. Quigg and H. B. Thacker, Phys. Rev. Lett. **38**, 883 (1977); H. A. Weldon, Phys. Rev. D **30**, 1547 (1984); M. S. Chanowitz, M. Golden and H. Georgi, Phys. Rev. Lett. **57**, 2344 (1986).
- [16] W. J. Marciano and S. S. D. Willenbrock, Phys. Rev. D **37**, 2509 (1988); S. Dawson and S. Willenbrock, Phys. Rev. Lett. **62**, 1232 (1989).
- [17] T. Appelquist and C. W. Bernard, Phys. Rev. D **22**, 200 (1980); A. C. Longhitano, Nucl. Phys. B **188**, 118 (1981).
- [18] R. Barate *et al.* [LEP Working Group for Higgs boson searches and ALEPH and DELPHI and L3 and OPAL Collaborations], Phys. Lett. B **565**, 61 (2003) [hep-ex/0306033].

- [19] [Tevatron New Physics Higgs Working Group and CDF and D0 Collaborations], arXiv:1207.0449 [hep-ex].
- [20] T. Aaltonen *et al.* [CDF and D0 Collaborations], Phys. Rev. Lett. **109**, 071804 (2012) [arXiv:1207.6436 [hep-ex]].
- [21] J. N. Bahcall and R. Davis, Jr., BNL-8217; J. N. Bahcall, R. Davis, P. Parker, A. Smirnov and R. Ulrich, Reading, USA: Addison-Wesley (1995) 440 p. (Frontiers in physics. 92)
- [22] Y. Fukuda *et al.* [Super-Kamiokande Collaboration], Phys. Rev. Lett. **81**, 1158 (1998) [Phys. Rev. Lett. **81**, 4279 (1998)] [hep-ex/9805021].
- [23] Q. R. Ahmad *et al.* [SNO Collaboration], Phys. Rev. Lett. **87**, 071301 (2001) [nucl-ex/0106015].
- [24] For an introduction, see, for example, C. Giunti, C. W. Kim, *Fundamentals of Neutrino Physics and Astrophysics*, (Oxford Univ. Press, 2007); R. N. Mohapatra, P. B. Pal, *Massive Neutrinos in Physics and Astrophysics*, (World Scientific, 2004)
- [25] T. Araki *et al.* [KamLAND Collaboration], Phys. Rev. Lett. **94**, 081801 (2005) [hep-ex/0406035].
- [26] F. P. An *et al.* [Daya Bay Collaboration], Phys. Rev. Lett. **108**, 171803 (2012) [arXiv:1203.1669 [hep-ex]].
- [27] F. Zwicky, Astrophys. J. **86**, 217 (1937).
- [28] V. C. Rubin and W. K. Ford, Jr., Astrophys. J. **159**, 379 (1970).
- [29] P. J. E. Peebles and B. Ratra, Rev. Mod. Phys. **75**, 559 (2003) [astro-ph/0207347].
- [30] A. D. Sakharov, Sov. Phys. JETP **49**, 594 (1979) [Zh. Eksp. Teor. Fiz. **76**, 1172 (1979)].
- [31] M. J. G. Veltman, Acta Phys. Polon. B **12**, 437 (1981).
- [32] M. B. Einhorn and D. R. T. Jones, Phys. Rev. D **46**, 5206 (1992).
- [33] S. P. Martin, Adv. Ser. Direct. High Energy Phys. **21**, 1 (2010) [hep-ph/9709356].
- [34] S. Kraml, In *Karlsruhe 2007, SUSY 2007* 132-139 [arXiv:0710.5117 [hep-ph]].

References for Chapter 2

- [1] G. Aad *et al.* [ATLAS Collaboration], arXiv:0901.0512 [hep-ex].
- [2] G. L. Bayatian *et al.* [CMS Collaboration], CERN-LHCC-2006-001, CMS-TDR-008-1.
- [3] <http://scipp.ucsc.edu/personnel/atlas.html>
- [4] <http://cms.web.cern.ch/news/cms-detector-design>
- [5] G. 't Hooft, Nucl. Phys. B **79**, 276 (1974).
- [6] <http://cds.cern.ch/record/1181486?ln=no>; K. Bendtz, A. Katre, D. Lacarre, P. Mermod, D. Milstead, J. Pinfold and R. Soluk, arXiv:1311.6940 [physics.ins-det].
- [7] T. Han, hep-ph/0508097.
- [8] <http://pdg.lbl.gov/>
- [9] Y. Nambu, Phys. Rev. D **10**, 4262 (1974); S. Mandelstam, Phys. Rept. **23**, 245 (1976).
- [10] W. W. Armstrong *et al.* [ATLAS Collaboration], CERN-LHCC-94-43.
- [11] *Private communication with Bruce Mellado*
- [12] J. de Favereau *et al.* [DELPHES 3 Collaboration], JHEP **1402**, 057 (2014) [arXiv:1307.6346 [hep-ex]].

- [13] *Private communication with Satyaki Bhattacharya*
- [14] D. Acosta *et al.* [CDF Collaboration], Phys. Rev. Lett. **94**, 091803 (2005) [hep-ex/0406078].
- [15] G. P. Salam, Eur. Phys. J. C **67**, 637 (2010) [arXiv:0906.1833 [hep-ph]].

References for Chapter 3

- [1] S. L. Glashow, Nucl. Phys. **22**, 579 (1961); S. Weinberg, Phys. Rev. Lett. **19**, 1264 (1967); A. Salam, Proceedings of 8th Nobel Symposium, Ed. N. Svartholm (1968).
- [2] F. Englert and R. Brout, Phys. Rev. Lett. **13** (1964) 321; P. W. Higgs, Phys. Rev. Lett. **13** (1964) 508; P. W. Higgs, Phys. Lett. **12** (1964) 132; G. S. Guralnik, C. R. Hagen and T. W. B. Kibble, Phys. Rev. Lett. **13** (1964) 585; P. W. Higgs, Phys. Rev. **145** (1966) 1156-1163; T. W. B. Kibble, Phys. Rev. **155** (1967) 1554-1561.
- [3] J. Incandela, talk on behalf of the CMS Collaboration at CERN, 4th July, 2012, <https://cms-docdb.cern.ch/cgi-bin/PublicDocDB//ShowDocument?docid=6125>.
- [4] F. Gianotti, talk on behalf of the ATLAS Collaboration at CERN, 4th July, 2012, <https://cms-docdb.cern.ch/cgi-bin/PublicDocDB//ShowDocument?docid=6126>.
- [5] USSR **60**, 207 (1948); Phys. Rev. **77**, 242 (1950).
- [6] arXiv:1411.3441 [hep-ex]; Phys. Lett. B **726**, 120 (2013)
- [7] <https://atlas.web.cern.ch/Atlas/GROUPS/PHYSICS/CONFNOTES/ATLAS-CONF-2015-008/>; G. Aad *et al.* [ATLAS Collaboration], arXiv:1503.03643 [hep-ex].

- [8] A. Azatov, R. Contino and J. Galloway, *JHEP* **1204**, 127 (2012).
- [9] M. Farina, C. Grojean, E. Salvioni, arXiv:1205.0011 [hep-ph];
- [10] For similar studies in this direction before the Higgs discovery, see, F. Bonnet, M. B. Gavela, T. Ota and W. Winter, *Phys. Rev. D* **85**, 035016 (2012); J. R. Espinosa, C. Grojean, M. Muhlleitner and M. Trott, *JHEP* **1205**, 097 (2012) P. P. Giardino, K. Kannike, M. Raidal and A. Strumia, *JHEP* **1206**, 117 (2012); T. Li, X. Wan, Y. -k. Wang and S. -h. Zhu, *JHEP* **1209**, 086 (2012); M. Rauch, arXiv:1203.6826 [hep-ph]; J. R. Espinosa, M. Muhlleitner, C. Grojean and M. Trott, *JHEP* **1209**, 126 (2012); J. Ellis and T. You, *JHEP* **1206** (2012) 140; D. Carmi, A. Falkowski, E. Kuflik and T. Volansky, *JHEP* **1207**, 136 (2012); M. Duhrssen, S. Heinemeyer, H. Logan, D. Rainwater, G. Weiglein and D. Zeppenfeld, *Phys. Rev. D* **70** (2004) 113009; R. Lafaye, T. Plehn, M. Rauch, D. Zerwas and M. Duhrssen, *JHEP* **0908** (2009) 009; M. Klute, R. Lafaye, T. Plehn, M. Rauch and D. Zerwas, *Phys. Rev. Lett.* **109**, 101801 (2012); A. Azatov, R. Contino, D. Del Re, J. Galloway, M. Grassi and S. Rahatlou, *JHEP* **1206**, 134 (2012).
- [11] I. Low, J. Lykken and G. Shaughnessy, *Phys. Rev. D* **86**, 093012 (2012); T. Corbett, O. J. P. Eboli, J. Gonzalez-Fraile and M. C. Gonzalez-Garcia, *Phys. Rev. D* **86**, 075013 (2012); P. P. Giardino, K. Kannike, M. Raidal and A. Strumia, *Phys. Lett. B* **718**, 469 (2012); J. Baglio, A. Djouadi and R. M. Godbole, *Phys. Lett. B* **716**, 203 (2012); J. Ellis and T. You, *JHEP* **1209**, 123 (2012); M. Montull and F. Riva, *JHEP* **1211**, 018 (2012); J. R. Espinosa, C. Grojean, M. Muhlleitner and M. Trott, *JHEP* **1212**, 045 (2012); D. Carmi, A. Falkowski, E. Kuflik, T. Volansky and J. Zupan, *JHEP* **1210** (2012) 196; S. Banerjee, S. Mukhopadhyay and B. Mukhopadhyaya, *JHEP* **1210**, 062 (2012); F. Bonnet, T. Ota, M. Rauch and W. Winter, *Phys. Rev. D* **86**, 093014 (2012); T. Plehn and M. Rauch, *Europhys. Lett.* **100**, 11002 (2012); A. Djouadi, arXiv:1208.3436 [hep-ph]; B. Batell, S. Gori and L. -T. Wang, *JHEP* **1301** (2013) 139; G. Moreau, *Phys. Rev. D* **87**, 015027 (2013); G. Bhattacharyya, D. Das and P. B. Pal, *Phys. Rev. D* **87**, 011702 (2013); D. Choudhury, R. Islam and A. Kundu, arXiv:1212.4652 [hep-ph].
- [12] G. Belanger, B. Dumont, U. Ellwanger, J. F. Gunion and S. Kraml, *JHEP* **1302**, 053 (2013).
- [13] M. Klute, R. Lafaye, T. Plehn, M. Rauch and D. Zerwas, *Europhys. Lett.* **101** (2013) 51001; C. Grojean, E. E. Jenkins, A. V. Manohar and M. Trott, *JHEP* **1304**, 016 (2013);

- K. Cheung, J. S. Lee and P. -Y. Tseng, JHEP **1305**, 134 (2013); K. Cheung, J. S. Lee and P. Y. Tseng, Phys. Rev. D **90**, 095009 (2014) [arXiv:1407.8236 [hep-ph]].
- J. Elias-Mir, J. R. Espinosa, E. Masso and A. Pomarol, JHEP **1308**, 033 (2013); J. Ellis, V. Sanz and T. You, arXiv:1303.0208 [hep-ph]; P. P. Giardino, K. Kannike, I. Masina, M. Raidal and A. Strumia, arXiv:1303.3570 [hep-ph]; R. Contino, M. Ghezzi, C. Grojean, M. Muhlleitner and M. Spira, JHEP **1307**, 035 (2013); J. Ellis and T. You, JHEP **1306**, 103 (2013); A. Djouadi and G. Moreau, arXiv:1303.6591 [hep-ph]; W. -F. Chang, W. -P. Pan and F. Xu, Phys. Rev. D **88**, 033004 (2013); T. Corbett, O. J. P. Eboli, J. Gonzalez-Fraile and M. C. Gonzalez-Garcia, arXiv:1304.1151 [hep-ph]; B. Dumont, S. Fichet and G. von Gersdorff, JHEP **1307**, 065 (2013); J. Elias-Miro, J. R. Espinosa, E. Masso and A. Pomarol, arXiv:1308.1879 [hep-ph]; M. B. Einhorn and J. Wudka, arXiv:1308.2255 [hep-ph]; A. Pomarol and F. Riva, arXiv:1308.2803 [hep-ph].
- [14] Talk given by Michael Duehrssen on behalf of the ATLAS collaboration, <https://indico.cern.ch/getFile.py/access?contribId=231&sessionId=15&resId=0&materialId=slides&confId=218030>;
G. Aad *et al.* [ATLAS Collaboration], arXiv:1307.1432 [hep-ex].
- [15] G. Aad *et al.* [ATLAS Collaboration], arXiv:1307.1427 [hep-ex].
- [16] Talk given by Josh Bendavid on behalf of the CMS collaboration, <https://indico.cern.ch/getFile.py/access?contribId=430&sessionId=15&resId=0&materialId=slides&confId=218030>;
CMS conference note,
<http://cds.cern.ch/record/1542387?ln=en>
- [17] V. Khachatryan *et al.* [CMS Collaboration], Eur. Phys. J. C **74**, no. 10, 3076 (2014) [arXiv:1407.0558 [hep-ex]].
- [18] S. Chatrchyan *et al.* [CMS Collaboration], Phys. Rev. D **89**, no. 9, 092007 (2014) [arXiv:1312.5353 [hep-ex]].
- [19] S. Chatrchyan *et al.* [CMS Collaboration], JHEP **1401**, 096 (2014) [arXiv:1312.1129 [hep-ex]].

- [20] S. Chatrchyan *et al.* [CMS Collaboration], Phys. Rev. D **89**, no. 1, 012003 (2014) [arXiv:1310.3687 [hep-ex]].
- [21] S. Chatrchyan *et al.* [CMS Collaboration], JHEP **1405**, 104 (2014) [arXiv:1401.5041 [hep-ex]].
- [22] V. Khachatryan *et al.* [CMS Collaboration], Eur. Phys. J. C **75**, no. 5, 212 (2015) [arXiv:1412.8662 [hep-ex]].
- [23] G. Aad *et al.* [ATLAS Collaboration], Phys. Rev. D **90**, no. 11, 112015 (2014),
- [24] G. Aad *et al.* [ATLAS Collaboration], Phys. Rev. D **91**, no. 1, 012006 (2015),
- [25] G. Aad *et al.* [ATLAS Collaboration], arXiv:1412.2641 [hep-ex],
- [26] G. Aad *et al.* [ATLAS Collaboration], JHEP **1501**, 069 (2015),
- [27] G. Aad *et al.* [ATLAS Collaboration], arXiv:1501.04943 [hep-ex],
- [28] The ATLAS collaboration, ATLAS-CONF-2015-007, ATLAS-COM-CONF-2015-011.
- [29] T. Aaltonen *et al.* [CDF and D0 Collaborations], Phys. Rev. D **88**, no. 5, 052014 (2013).
- [30] K. Hagiwara, S. Ishihara, R. Szalapski and D. Zeppenfeld, Phys. Lett. B **283**, 353 (1992);
K. Hagiwara, S. Ishihara, R. Szalapski and D. Zeppenfeld, Phys. Rev. D **48**, 2182 (1993).
- [31] M. C. Gonzalez-Garcia, Int. J. Mod. Phys. A **14**, 3121 (1999).
- [32] S. Dittmaier *et al.* [LHC Higgs Cross Section Working Group Collaboration], arXiv:1101.0593 [hep-ph]; S. Dittmaier *et al.*, arXiv:1201.3084 [hep-ph];
<https://twiki.cern.ch/twiki/bin/view/LHCPhysics/CrossSections>
- [33] J. Beringer *et al.* (Particle Data Group), Phys. Rev. D **86**, 010001 (2012).
- [34] G. Aad *et al.* [ATLAS and CMS Collaborations], arXiv:1503.07589 [hep-ex].
- [35] B. Bhattacharjee, A. Chakraborty and A. Choudhury, arXiv:1504.04308 [hep-ph].
- [36] The ATLAS collaboration, ATLAS-CONF-2014-011, ATLAS-COM-CONF-2014-004,
V. Khachatryan *et al.* [CMS Collaboration], arXiv:1502.02485 [hep-ex],
<http://cds.cern.ch/record/1547579?ln=en>.

- [37] A. Djouadi, Phys. Rept. **457**, 1 (2008).
- [38] P. Bolzoni, F. Maltoni, S. -O. Moch and M. Zaro, Phys. Rev. Lett. **105**, 011801 (2010); Phys. Rev. D **85**, 035002 (2012); <http://vbf-nnlo.phys.ucl.ac.be/vbf.html>
- [39] Phys. Lett. B **726**, 587 (2013),
<https://atlas.web.cern.ch/Atlas/GROUPS/PHYSICS/CONFNOTES/ATLAS-CONF-2013-009/>
- [40] F. James, private communication.
- [41] J. Baglio and A. Djouadi, JHEP **1010**, 064 (2010).
- [42] <http://seal.web.cern.ch/seal/snapshot/work-packages/mathlibs/minuit/>
- [43] W. H. Press *et al.*, Numerical Recipes in Fortran, Cambridge University Press (2005).
- [44] Steven G. Johnson, The NLOpt nonlinear-optimization package, <http://ab-initio.mit.edu/nlopt>
- [45] M. J. D. Powell, "A direct search optimization method that models the objective and constraint functions by linear interpolation," in Advances in Optimization and Numerical Analysis, eds. S. Gomez and J.-P. Hennart (Kluwer Academic: Dordrecht, 1994), p. 51-67;
M. J. D. Powell, "Direct search algorithms for optimization calculations," Acta Numerica **7**, 287-336 (1998).
- [46] CMS Collaboration [CMS Collaboration], CMS-PAS-HIG-14-015; CMS Collaboration [CMS Collaboration], CMS-PAS-HIG-14-001.
- [47] E. Gabrielli, B. Mele and M. Raidal, arXiv:1202.1796 [hep-ph], and references therein.
- [48] CMS Collaboration [CMS Collaboration], CMS-PAS-HIG-14-002.

References for Chapter 4

- [1] G. Aad *et al.* [ATLAS Collaboration], Phys. Lett. B **716** (2012) 1.
- [2] S. Chatrchyan *et al.* [CMS Collaboration], Phys. Lett. B **716** (2012) 30.
- [3] For similar studies in this direction before the Higgs discovery, see,
F. Bonnet, M. B. Gavela, T. Ota and W. Winter, Phys. Rev. D **85**, 035016 (2012); J. R. Espinosa, C. Grojean, M. Muhlleitner and M. Trott, JHEP **1205**, 097 (2012) P. P. Giardino, K. Kannike, M. Raidal and A. Strumia, JHEP **1206**, 117 (2012); T. Li, X. Wan, Y. -k. Wang and S. -h. Zhu, JHEP **1209**, 086 (2012); M. Rauch, arXiv:1203.6826 [hep-ph]; J. R. Espinosa, M. Muhlleitner, C. Grojean and M. Trott, JHEP **1209**, 126 (2012); J. Ellis and T. You, JHEP **1206** (2012) 140; D. Carmi, A. Falkowski, E. Kuflik and T. Volansky, JHEP **1207**, 136 (2012); M. Duhrssen, S. Heinemeyer, H. Logan, D. Rainwater, G. Weiglein and D. Zeppenfeld, Phys. Rev. D **70** (2004) 113009; R. Lafaye, T. Plehn, M. Rauch, D. Zerwas and M. Duhrssen, JHEP **0908** (2009) 009; M. Klute, R. Lafaye, T. Plehn, M. Rauch and D. Zerwas, Phys. Rev. Lett. **109**, 101801 (2012); A. Azatov, R. Contino, D. Del Re, J. Galloway, M. Grassi and S. Rahatlou, JHEP **1206**, 134 (2012).
- [4] I. Low, J. Lykken and G. Shaughnessy, Phys. Rev. D **86**, 093012 (2012); T. Corbett, O. J. P. Eboli, J. Gonzalez-Fraile and M. C. Gonzalez-Garcia, Phys. Rev. D **86**, 075013 (2012); P. P. Giardino, K. Kannike, M. Raidal and A. Strumia, Phys. Lett. B **718**, 469 (2012); J. Baglio, A. Djouadi and R. M. Godbole, Phys. Lett. B **716**, 203 (2012); J. Ellis and T. You, JHEP **1209**, 123 (2012); M. Montull and F. Riva, JHEP **1211**, 018

- (2012); J. R. Espinosa, C. Grojean, M. Muhlleitner and M. Trott, JHEP **1212**, 045 (2012); D. Carmi, A. Falkowski, E. Kuflik, T. Volansky and J. Zupan, JHEP **1210** (2012) 196; S. Banerjee, S. Mukhopadhyay and B. Mukhopadhyaya, JHEP **1210**, 062 (2012); F. Bonnet, T. Ota, M. Rauch and W. Winter, Phys. Rev. D **86**, 093014 (2012); T. Plehn and M. Rauch, Europhys. Lett. **100**, 11002 (2012); A. Djouadi, arXiv:1208.3436 [hep-ph]; B. Batell, S. Gori and L. -T. Wang, JHEP **1301** (2013) 139; G. Moreau, Phys. Rev. D **87**, 015027 (2013); G. Bhattacharyya, D. Das and P. B. Pal, Phys. Rev. D **87**, 011702 (2013); D. Choudhury, R. Islam and A. Kundu, arXiv:1212.4652 [hep-ph]. G. Belanger, B. Dumont, U. Ellwanger, J. F. Gunion and S. Kraml, JHEP **1302**, 053 (2013).
- [5] M. Klute, R. Lafaye, T. Plehn, M. Rauch and D. Zerwas, Europhys. Lett. **101** (2013) 51001; C. Grojean, E. E. Jenkins, A. V. Manohar and M. Trott, JHEP **1304**, 016 (2013); K. Cheung, J. S. Lee and P. -Y. Tseng, JHEP **1305**, 134 (2013); J. Elias-Mir, J. R. Espinosa, E. Masso and A. Pomarol, JHEP **1308**, 033 (2013); J. Ellis, V. Sanz and T. You, arXiv:1303.0208 [hep-ph]; P. P. Giardino, K. Kannike, I. Masina, M. Raidal and A. Strumia, arXiv:1303.3570 [hep-ph]; R. Contino, M. Ghezzi, C. Grojean, M. Muhlleitner and M. Spira, JHEP **1307**, 035 (2013); J. Ellis and T. You, JHEP **1306**, 103 (2013); A. Djouadi and G. Moreau, arXiv:1303.6591 [hep-ph]; W. -F. Chang, W. -P. Pan and F. Xu, Phys. Rev. D **88**, 033004 (2013); T. Corbett, O. J. P. Eboli, J. Gonzalez-Fraile and M. C. Gonzalez-Garcia, arXiv:1304.1151 [hep-ph]; B. Dumont, S. Fichet and G. von Gersdorff, JHEP **1307**, 065 (2013); J. Elias-Miro, J. R. Espinosa, E. Masso and A. Pomarol, arXiv:1308.1879 [hep-ph]; M. B. Einhorn and J. Wudka, arXiv:1308.2255 [hep-ph]; A. Pomarol and F. Riva, arXiv:1308.2803 [hep-ph].
- [6] Talk given by Michael Duehrssen on behalf of the ATLAS collaboration, <https://indico.cern.ch/getFile.py/access?contribId=231&sessionId=15&resId=0&materialId=slides&confId=218030>;
G. Aad *et al.* [ATLAS Collaboration], arXiv:1307.1432 [hep-ex].
- [7] G. Aad *et al.* [ATLAS Collaboration], arXiv:1307.1427 [hep-ex].
- [8] Talk given by Josh Bendavid on behalf of the CMS collaboration, <https://indico.cern.ch/getFile.py/access?contribId=430&sessionId=15&resId=0&materialId=slides&confId=218030>;

- CMS conference note,
<http://cds.cern.ch/record/1542387?ln=en>
- [9] ATLAS conference note,
<https://atlas.web.cern.ch/Atlas/GROUPS/PHYSICS/CONFNOTES/ATLAS-CONF-2013-013/>
- [10] W. Buchmuller and D. Wyler, Nucl. Phys. B **268**, 621 (1986).
- [11] B. Grzadkowski, M. Iskrzynski, M. Misiak and J. Rosiek, JHEP **1010**, 085 (2010).
- [12] K. Hagiwara, R. Szalapski and D. Zeppenfeld, Phys. Lett. B **318**, 155 (1993).
- [13] M. C. Gonzalez-Garcia, Int. J. Mod. Phys. A **14**, 3121 (1999).
- [14] M. E. Peskin and T. Takeuchi, Phys. Rev. Lett. **65**, 964 (1990); M. E. Peskin and T. Takeuchi, Phys. Rev. D **46**, 381 (1992).
- [15] G. Altarelli, R. Barbieri and F. Caravaglios, Nucl. Phys. B **405**, 3 (1993).
- [16] E. Masso and V. Sanz, Phys. Rev. D **87**, no. 3, 033001 (2013).
- [17] T. Corbett, O. J. P. Eboli, J. Gonzalez-Fraile and M. C. Gonzalez-Garcia, Phys. Rev. D **87**, 015022 (2013);
- [18] T. Corbett, O. J. P. Eboli, J. Gonzalez-Fraile and M. C. Gonzalez-Garcia, arXiv:1306.0006 [hep-ph].
- [19] A. Falkowski, F. Riva and A. Urbano, arXiv:1303.1812 [hep-ph].
- [20] T. Plehn, D. L. Rainwater and D. Zeppenfeld, Phys. Rev. Lett. **88**, 051801 (2002).
- [21] A. Djouadi, R. M. Godbole, B. Mellado and K. Mohan, Phys. Lett. B **723**, 307 (2013).
- [22] Y. Gao, A. V. Gritsan, Z. Guo, K. Melnikov, M. Schulze and N. V. Tran, Phys. Rev. D **81**, 075022 (2010); P. Avery, D. Bourilkov, M. Chen, T. Cheng, A. Drozdetskiy, J. S. Gainer, A. Korytov and K. T. Matchev *et al.*, Phys. Rev. D **87**, 055006 (2013).
- [23] J. S. Gainer, J. Lykken, K. T. Matchev, S. Mrenna and M. Park, Phys. Rev. Lett. **111**, 041801 (2013).

- [24] J. F. Gunion, H. E. Haber and J. Wudka, Phys. Rev. D **43**, 904 (1991).
- [25] D. Choudhury, R. Islam and A. Kundu, Phys. Rev. D **88**, 013014 (2013); M. Dahiya, S. Dutta and R. Islam, arXiv:1311.4523 [hep-ph].
- [26] G. Aad *et al.* [ATLAS Collaboration], arXiv:1412.2641 [hep-ex].
- [27] N. D. Christensen and C. Duhr, Comput. Phys. Commun. **180**, 1614 (2009).
- [28] J. Alwall, M. Herquet, F. Maltoni, O. Mattelaer and T. Stelzer, JHEP **1106**, 128 (2011).
- [29] T. Sjostrand, S. Mrenna and P. Z. Skands, JHEP **0605**, 026 (2006).
- [30] A. Djouadi, Phys. Rept. **457**, 1 (2008).
- [31] LHC Higgs working group,
<https://twiki.cern.ch/twiki/bin/view/LHCPhysics/CrossSections>
- [32] ATLAS conference note,
<https://atlas.web.cern.ch/Atlas/GROUPS/PHYSICS/CONFNOTES/ATLAS-CONF-2013-012/>
- [33] ATLAS conference note,
<https://atlas.web.cern.ch/Atlas/GROUPS/PHYSICS/CONFNOTES/ATLAS-CONF-2013-072/>
- [34] ATLAS conference note,
<https://atlas.web.cern.ch/Atlas/GROUPS/PHYSICS/CONFNOTES/ATLAS-CONF-2012-091/>

References for Chapter 5

- [1] J. S. Gainer, J. Lykken, K. T. Matchev, S. Mrenna and M. Park, *Phys. Rev. Lett.* **111**, 041801 (2013) [arXiv:1304.4936 [hep-ph]].
- [2] S. Banerjee, S. Mukhopadhyay and B. Mukhopadhyaya, *Phys. Rev. D* **89**, no. 5, 053010 (2014) [arXiv:1308.4860 [hep-ph]].
- [3] N. Desai, D. K. Ghosh, and B. Mukhopadhyaya, *CP-violating HWW couplings at the Large Hadron Collider*, *Phys.Rev.* **D83** (2011) 113004, [arXiv:1104.3327].
- [4] E. Masso and V. Sanz, *Limits on anomalous couplings of the Higgs boson to electroweak gauge bosons from LEP and the LHC*, *Phys.Rev.* **D87** (2013), no. 3 033001, [arXiv:1211.1320].
- [5] T. Corbett, O. Eboli, J. Gonzalez-Fraile, and M. Gonzalez-Garcia, *Robust Determination of the Higgs Couplings: Power to the Data*, *Phys.Rev.* **D87** (2013) 015022, [arXiv:1211.4580].
- [6] A. Falkowski, F. Riva, and A. Urbano, *Higgs at last*, *JHEP* **1311** (2013) 111, [arXiv:1303.1812].
- [7] T. Corbett, O. boli, J. Gonzalez-Fraile, and M. Gonzalez-Garcia, *Determining Triple Gauge Boson Couplings from Higgs Data*, *Phys.Rev.Lett.* **111** (2013) 011801, [arXiv:1304.1151].

- [8] B. Dumont, S. Fichet, and G. von Gersdorff, *A Bayesian view of the Higgs sector with higher dimensional operators*, *JHEP* **1307** (2013) 065, [[arXiv:1304.3369](#)].
- [9] S. Banerjee, S. Mukhopadhyay, and B. Mukhopadhyaya, *New Higgs interactions and recent data from the LHC and the Tevatron*, *JHEP* **1210** (2012) 062, [[arXiv:1207.3588](#)].
- [10] T. Corbett, O. boli, J. Gonzalez-Fraile, and M. Gonzalez-Garcia, *Robust determination of the scalar boson couplings*, [arXiv:1306.0006](#).
- [11] J. Elias-Miro, J. Espinosa, E. Masso, and A. Pomarol, *Higgs windows to new physics through $d=6$ operators: constraints and one-loop anomalous dimensions*, *JHEP* **1311** (2013) 066, [[arXiv:1308.1879](#)].
- [12] A. Pomarol and F. Riva, *Towards the Ultimate SM Fit to Close in on Higgs Physics*, *JHEP* **1401** (2014) 151, [[arXiv:1308.2803](#)].
- [13] M. B. Einhorn and J. Wudka, *Higgs-Boson Couplings Beyond the Standard Model*, *Nucl.Phys.* **B877** (2013) 792–806, [[arXiv:1308.2255](#)].
- [14] S. Willenbrock and C. Zhang, *Effective Field Theory Beyond the Standard Model*, *Ann.Rev.Nucl.Part.Sci.* **64** (2014) 83–100, [[arXiv:1401.0470](#)].
- [15] J. Ellis, V. Sanz, and T. You, *Complete Higgs Sector Constraints on Dimension-6 Operators*, *JHEP* **1407** (2014) 036, [[arXiv:1404.3667](#)].
- [16] H. Belusca-Maito, *Effective Higgs Lagrangian and Constraints on Higgs Couplings*, [arXiv:1404.5343](#).
- [17] R. S. Gupta, A. Pomarol, and F. Riva, *BSM Primary Effects*, *Phys.Rev.* **D91** (2015), no. 3 035001, [[arXiv:1405.0181](#)].
- [18] E. Masso, *An Effective Guide to Beyond the Standard Model Physics*, *JHEP* **1410** (2014) 128, [[arXiv:1406.6376](#)].
- [19] A. Biekter, A. Knochel, M. Krmer, D. Liu, and F. Riva, *Vices and virtues of Higgs effective field theories at large energy*, *Phys.Rev.* **D91** (2015) 055029, [[arXiv:1406.7320](#)].
- [20] C. Englert and M. Spannowsky, *Effective Theories and Measurements at Colliders*, *Phys.Lett.* **B740** (2015) 8–15, [[arXiv:1408.5147](#)].

- [21] J. Ellis, V. Sanz, and T. You, *The Effective Standard Model after LHC Run I*, *JHEP* **1503** (2015) 157, [arXiv:1410.7703].
- [22] R. Edezhath, *Dimension-6 Operator Constraints from Boosted VBF Higgs*, arXiv:1501.00992.
- [23] M. Gorbahn, J. M. No, and V. Sanz, *Benchmarks for Higgs Effective Theory: Extended Higgs Sectors*, arXiv:1502.07352.
- [24] Z. Han and W. Skiba, *Effective theory analysis of precision electroweak data*, *Phys.Rev.* **D71** (2005) 075009, [hep-ph/0412166].
- [25] M. Ciuchini, E. Franco, S. Mishima, and L. Silvestrini, *Electroweak Precision Observables, New Physics and the Nature of a 126 GeV Higgs Boson*, *JHEP* **1308** (2013) 106, [arXiv:1306.4644].
- [26] J. de Blas, *Electroweak limits on physics beyond the Standard Model*, *EPJ Web Conf.* **60** (2013) 19008, [arXiv:1307.6173].
- [27] C.-Y. Chen, S. Dawson, and C. Zhang, *Electroweak Effective Operators and Higgs Physics*, *Phys.Rev.* **D89** (2014), no. 1 015016, [arXiv:1311.3107].
- [28] R. Alonso, E. E. Jenkins, A. V. Manohar, and M. Trott, *Renormalization Group Evolution of the Standard Model Dimension Six Operators III: Gauge Coupling Dependence and Phenomenology*, *JHEP* **1404** (2014) 159, [arXiv:1312.2014].
- [29] C. Englert, A. Freitas, M. Mhlleitner, T. Plehn, M. Rauch, et al., *Precision Measurements of Higgs Couplings: Implications for New Physics Scales*, *J.Phys.* **G41** (2014) 113001, [arXiv:1403.7191].
- [30] M. Trott, *On the consistent use of Constructed Observables*, *JHEP* **1502** (2015) 046, [arXiv:1409.7605].
- [31] A. Falkowski and F. Riva, *Model-independent precision constraints on dimension-6 operators*, *JHEP* **1502** (2015) 039, [arXiv:1411.0669].
- [32] B. Henning, X. Lu, and H. Murayama, *How to use the Standard Model effective field theory*, arXiv:1412.1837.

- [33] J. de Blas, M. Chala, M. Perez-Victoria, and J. Santiago, *Observable Effects of General New Scalar Particles*, arXiv:1412.8480.
- [34] L. Berthier and M. Trott, *Towards consistent Electroweak Precision Data constraints in the SMEFT*, arXiv:1502.02570.
- [35] A. Efrati, A. Falkowski, and Y. Soreq, *Electroweak constraints on flavorful effective theories*, arXiv:1503.07872.
- [36] B. Bhattacharjee, T. Modak, S. K. Patra, and R. Sinha, *Probing Higgs couplings at LHC and beyond*, arXiv:1503.08924.
- [37] S. Dwivedi, D. Ghosh, B. Mukhopadhyaya, and A. Shivaji, *Constraints on CP-Odd Gauge-Higgs Operators*, arXiv:1505.05844.
- [38] G. Amar, S. Banerjee, S. von Buddenbrock, A. S. Cornell, T. Mandal, et al., *Exploration of the tensor structure of the Higgs boson coupling to weak bosons in $e^+ e^-$ collisions*, *JHEP* **1502** (2015) 128, [arXiv:1405.3957].
- [39] S. Kumar and P. Poullose, *Influence of anomalous VVH and VVHH on determination of Higgs self couplings at ILC*, arXiv:1408.3563.
- [40] N. Craig, M. Farina, M. McCullough, and M. Perelstein, *Precision Higgsstrahlung as a Probe of New Physics*, *JHEP* **1503** (2015) 146, [arXiv:1411.0676].
- [41] M. Beneke, D. Boito, and Y.-M. Wang, *Signatures of anomalous Higgs couplings in angular asymmetries of $H \rightarrow Zl+l^-$ and $e^+e^- \rightarrow HZ$* , arXiv:1411.3942.
- [42] S. Kumar, P. Poullose, and S. Sahoo, *Study of Higgs-gauge boson anomalous couplings through $e^- e^+ \rightarrow W^- W^+ H$ at ILC*, arXiv:1501.03283.
- [43] H.-Y. Ren, *New Physics Searches with Higgs-photon associated production at the Higgs Factory*, arXiv:1503.08307.
- [44] S. S. Biswal, R. M. Godbole, B. Mellado, and S. Raychaudhuri, *Azimuthal Angle Probe of Anomalous HWW Couplings at a High Energy ep Collider*, *Phys.Rev.Lett.* **109** (2012) 261801, [arXiv:1203.6285].

- [45] J. S. Gainer, J. Lykken, K. T. Matchev, S. Mrenna, and M. Park, *Geolocating the Higgs Boson Candidate at the LHC*, *Phys.Rev.Lett.* **111** (2013) 041801, [arXiv:1304.4936].
- [46] T. Plehn, D. L. Rainwater, and D. Zeppenfeld, *Determining the structure of Higgs couplings at the LHC*, *Phys.Rev.Lett.* **88** (2002) 051801, [hep-ph/0105325].
- [47] C. Bernaciak, M. S. A. Buschmann, A. Butter, and T. Plehn, *Fox-Wolfram Moments in Higgs Physics*, *Phys.Rev.* **D87** (2013) 073014, [arXiv:1212.4436].
- [48] C. Bernaciak, B. Mellado, T. Plehn, P. Schichtel, and X. Ruan, *Improving Higgs plus Jets analyses through Fox–Wolfram Moments*, *Phys.Rev.* **D89** (2014), no. 5 053006, [arXiv:1311.5891].
- [49] A. Djouadi, R. Godbole, B. Mellado, and K. Mohan, *Probing the spin-parity of the Higgs boson via jet kinematics in vector boson fusion*, *Phys.Lett.* **B723** (2013) 307–313, [arXiv:1301.4965].
- [50] **ATLAS** Collaboration, G. Aad et al., *Search for Higgs boson decays to a photon and a Z boson in pp collisions at $\sqrt{s}=7$ and 8 TeV with the ATLAS detector*, *Phys.Lett.* **B732** (2014) 8–27, [arXiv:1402.3051].
- [51] **CMS** Collaboration, S. Chatrchyan et al., *Search for a Higgs boson decaying into a Z and a photon in pp collisions at $\sqrt{s} = 7$ and 8 TeV*, *Phys.Lett.* **B726** (2013) 587–609, [arXiv:1307.5515].
- [52] A. Alloul, N. D. Christensen, C. Degrande, C. Duhr, and B. Fuks, *FeynRules 2.0 - A complete toolbox for tree-level phenomenology*, *Comput.Phys.Commun.* **185** (2014) 2250–2300, [arXiv:1310.1921].
- [53] C. Degrande, C. Duhr, B. Fuks, D. Grellscheid, O. Mattelaer, et al., *UFO - The Universal FeynRules Output*, *Comput.Phys.Commun.* **183** (2012) 1201–1214, [arXiv:1108.2040].
- [54] J. Alwall, R. Frederix, S. Frixione, V. Hirschi, F. Maltoni, et al., *The automated computation of tree-level and next-to-leading order differential cross sections, and their matching to parton shower simulations*, *JHEP* **1407** (2014) 079, [arXiv:1405.0301].

- [55] T. Sjostrand, S. Mrenna, and P. Z. Skands, *PYTHIA 6.4 Physics and Manual*, *JHEP* **0605** (2006) 026, [[hep-ph/0603175](#)].
- [56] **DELPHES 3** Collaboration, J. de Favereau et al., *DELPHES 3, A modular framework for fast simulation of a generic collider experiment*, *JHEP* **1402** (2014) 057, [[arXiv:1307.6346](#)].
- [57] <https://twiki.cern.ch/twiki/bin/view/LHCPhysics/CrossSections>
- [58] **ATLAS** Collaboration, G. Aad et al., “Projections for measurements of Higgs boson cross sections, branching ratios and coupling parameters with the ATLAS detector at a HL-LHC.” <https://atlas.web.cern.ch/Atlas/GROUPS/PHYSICS/PUBNOTES/ATL-PHYS-PUB-2013-014/>, 2013.
- [59] **ATLAS** Collaboration, G. Aad et al., “HL-LHC projections for signal and background yield measurements of the $H \rightarrow \gamma\gamma$ when the Higgs boson is produced in association with t quarks, W or Z bosons.” <http://atlas.web.cern.ch/Atlas/GROUPS/PHYSICS/PUBNOTES/ATL-PHYS-PUB-2014-012/>, 2014.
- [60] **ATLAS** Collaboration, G. Aad et al., *Measurement of Higgs boson production in the diphoton decay channel in pp collisions at center-of-mass energies of 7 and 8 TeV with the ATLAS detector*, *Phys.Rev.* **D90** (2014), no. 11 112015, [[arXiv:1408.7084](#)].
- [61] **ATLAS** Collaboration, G. Aad et al., *Observation and measurement of Higgs boson decays to WW^* with the ATLAS detector*, [arXiv:1412.2641](#).
- [62] **CMS** Collaboration, V. Khachatryan et al., *Observation of the diphoton decay of the Higgs boson and measurement of its properties*, *Eur.Phys.J.* **C74** (2014), no. 10 3076, [[arXiv:1407.0558](#)].
- [63] **CMS** Collaboration, S. Chatrchyan et al., “Precise determination of the mass of the Higgs boson and studies of the compatibility of its couplings with the standard model.” <http://cds.cern.ch/record/1728249>, 2014.
- [64] **CMS** Collaboration, V. Khachatryan et al., *Precise determination of the mass of the Higgs boson and tests of compatibility of its couplings with the standard model predictions using proton collisions at 7 and 8 TeV*, [arXiv:1412.8662](#).

- [65] I. W. Stewart and F. J. Tackmann, *Theory Uncertainties for Higgs and Other Searches Using Jet Bins*, *Phys.Rev.* **D85** (2012) 034011, [[arXiv:1107.2117](#)].
- [66] S. Banerjee, S. Mukhopadhyay, and B. Mukhopadhyaya, *Higher dimensional operators and the LHC Higgs data: The role of modified kinematics*, *Phys.Rev.* **D89** (2014), no. 5 053010, [[arXiv:1308.4860](#)].
- [67] A. Kruse, A. S. Cornell, M. Kumar, B. Mellado, and X. Ruan, *Probing the Higgs boson via vector boson fusion with single jet tagging at the LHC*, *Phys.Rev.* **D91** (2015), no. 5 053009, [[arXiv:1412.4710](#)].

References for Chapter 6

- [1] S. S. Biswal, R. M. Godbole, R. K. Singh and D. Choudhury, Phys. Rev. D **73**, 035001 (2006) [Erratum-ibid. D **74**, 039904 (2006)] [hep-ph/0509070].
- [2] T. Han and B. Mellado, Phys. Rev. D **82**, 016009 (2010) [arXiv:0909.2460 [hep-ph]].
- [3] S. S. Biswal, R. M. Godbole, B. Mellado and S. Raychaudhuri, Phys. Rev. Lett. **109**, 261801 (2012) [arXiv:1203.6285 [hep-ph]].
- [4] T. Corbett, O. J. P. boli, J. Gonzalez-Fraile and M. C. Gonzalez-Garcia, Phys. Rev. Lett. **111**, no. 1, 011801 (2013) [arXiv:1304.1151 [hep-ph]].
- [5] T. Corbett, O. J. P. boli, J. Gonzalez-Fraile and M. C. Gonzalez-Garcia, arXiv:1306.0006 [hep-ph].
- [6] E. Masso and V. Sanz, Phys. Rev. D **87**, no. 3, 033001 (2013) [arXiv:1211.1320 [hep-ph]].
- [7] T. Corbett, O. J. P. Eboli, J. Gonzalez-Fraile and M. C. Gonzalez-Garcia, Phys. Rev. D **87**, 015022 (2013) [arXiv:1211.4580 [hep-ph]].
- [8] A. Falkowski, F. Riva and A. Urbano, JHEP **1311**, 111 (2013) [arXiv:1303.1812 [hep-ph]].
- [9] S. Banerjee, S. Mukhopadhyay and B. Mukhopadhyaya, Phys. Rev. D **89**, 053010 (2014) [arXiv:1308.4860 [hep-ph]].

- [10] W. Buchmuller and D. Wyler, Nucl. Phys. B **268**, 621 (1986).
- [11] B. Grzadkowski, M. Iskrzynski, M. Misiak and J. Rosiek, JHEP **1010**, 085 (2010) [arXiv:1008.4884 [hep-ph]].
- [12] K. Hagiwara, R. Szalapski and D. Zeppenfeld, Phys. Lett. B **318**, 155 (1993) [hep-ph/9308347].
- [13] M. C. Gonzalez-Garcia, Int. J. Mod. Phys. A **14**, 3121 (1999) [hep-ph/9902321].
- [14] A. Djouadi, R. M. Godbole, B. Mellado and K. Mohan, Phys. Lett. B **723**, 307 (2013) [arXiv:1301.4965 [hep-ph]].
- [15] A. Alloul, N. D. Christensen, C. Degrande, C. Duhr and B. Fuks, Comput. Phys. Commun. **185**, 2250 (2014) [arXiv:1310.1921 [hep-ph]].
- [16] C. Degrande, C. Duhr, B. Fuks, D. Grellscheid, O. Mattelaer and T. Reiter, Comput. Phys. Commun. **183**, 1201 (2012) [arXiv:1108.2040 [hep-ph]].
- [17] J. Alwall, M. Herquet, F. Maltoni, O. Mattelaer and T. Stelzer, JHEP **1106**, 128 (2011) [arXiv:1106.0522 [hep-ph]].
- [18] J. A. M. Vermaseren, math-ph/0010025.
- [19] S. Heinemeyer, S. Kanemura, H. Logan, A. Raspereza, T. M. P. Tait, H. Baer, E. L. Berger and A. Birkedal *et al.*, hep-ph/0511332.
- [20] G. Altarelli, B. Mele and F. Pitolli, Nucl. Phys. B **287**, 205 (1987).
- [21] Private communications with Alex Pomarol, Dieter Zeppenfeld and Maxim Perelstein.
- [22] K. Hagiwara, R. D. Peccei, D. Zeppenfeld and K. Hikasa, Nucl. Phys. B **282**, 253 (1987).
- [23] G. Aad *et al.* [ATLAS Collaboration], Phys. Lett. B **716**, 1 (2012) [arXiv:1207.7214 [hep-ex]].